Gaofeng Pan
Xiaqing Miao
Xuanhe Yang
Ziyi Yang *Editors*

UAV Communications: Modeling and Analyses

Springer

UAV Communications: Modeling and Analyses

Gaofeng Pan · Xiaqing Miao · Xuanhe Yang ·
Ziyi Yang
Editors

UAV Communications: Modeling and Analyses

Springer

Editors
Gaofeng Pan
School of Cyberspace Science
and Technology
Beijing Institute of Technology
Beijing, China

Xiaqing Miao
School of Cyberspace Science
and Technology
Beijing Institute of Technology
Beijing, China

Xuanhe Yang
School of Cyberspace Science
and Technology
Beijing Institute of Technology
Beijing, China

Ziyi Yang
School of Cyberspace Science
and Technology
Beijing Institute of Technology
Beijing, China

ISBN 978-981-97-0382-1 ISBN 978-981-97-0383-8 (eBook)
https://doi.org/10.1007/978-981-97-0383-8

This Springer imprint is published by the registered company Springer Nature Singapore Pte Ltd.
The registered company address is: 152 Beach Road, #21-01/04 Gateway East, Singapore 189721, Singapore

Paper in this product is recyclable.

Contents

Chapter 1
Introduction to UAV Communications

Gaofeng Pan, Xiaqing Miao, Xuanhe Yang, and Ziyi Yang

Abstract Unmanned Aerial Vehicles (UAVs), also known as drones, have experienced a remarkable surge in popularity across diverse sectors, including military, civilian, and commercial domains. Their expansive array of applications promises transformative benefits, but to harness this potential, UAVs rely critically on reliable, efficient communication systems that enable real-time functionality. However, UAV communication systems face several challenges, including limited bandwidth, unreliable connectivity, and susceptibility to interference. In response to these challenges, researchers have diligently explored innovative techniques. Concepts like cognitive radio (CR), cooperative communication, and multiple-input multiple-output (MIMO) systems have emerged as promising strategies to overcome these hurdles, ensuring UAVs can fulfill their missions effectively. Here, we will provide a comprehensive overview of UAV communication systems, delving into the realm of UAV communication systems, exploring their diverse applications, the hurdles they confront, and the cutting-edge solutions proposed to conquer them. Additionally, we spotlight the latest advancements in UAV communications, encompassing the integration of 5G technologies and the emergence of satellite-based communication systems. These cutting-edge technologies hold the potential to redefine the capabilities and reach of UAVs, promising to elevate the landscape of unmanned aerial vehicle technology.

1.1 Development of UAV Communications

Unmanned Aerial Vehicles (UAVs), more commonly referred to as drones, have rapidly gained popularity in recent years. These autonomous aircraft operate without a human pilot on board, offering exceptional versatility and the capability to tackle tasks that are often too perilous or technically demanding for manned flight. UAVs find applications in a wide range of fields, including military reconnaissance, com-

G. Pan (✉) · X. Miao · X. Yang · Z. Yang
Beijing Institute of Technology, Beijing, China
e-mail: gfpan@bit.edu.cn

Z. Yang
e-mail: yziyi@bit.edu.cn

G. Pan et al. (eds.), *UAV Communications: Modeling and Analyses*,
https://doi.org/10.1007/978-981-97-0383-8_1

mercial photography and videography, environmental monitoring, package delivery, agricultural surveys, and search and rescue operations. The proliferation of UAVs continues to transform industries and redefine what is achievable in various domains. Yet, beneath the surface of their impressive capabilities lies a pivotal factor essential to their functionality and success UAV communications. This vital aspect allows these unmanned systems to seamlessly interact with operators, enabling real-time control, data transmission, and situational awareness.

UAV communications encompass two vital categories: control link communications and data link communications, each serving distinct but interconnected purposes.

- **Control Link Communications**: These communications primarily involve transmitting commands from the Control Station (CS) to the UAV. Through the control link, operators provide instructions, adjust flight paths, and ensure safe and precise maneuvering. This real-time connection is essential for maintaining control over the UAV's movements and actions.
- **Data Link Communications**: In contrast, data link communications focus on the exchange of information, data, and feedback between the UAV and the CS. This two-way data flow enables the transmission of critical data, such as telemetry information, payload data (such as images and sensor readings), and situational awareness updates. These data links provide operators with a comprehensive view of the UAV's status and the environment in which it operates.

Collectively, UAV communications empower operators and autonomous systems to remotely control UAVs, continuously monitor their operational status, and receive real-time data updates. This comprehensive approach fosters precise control, efficient data transmission, and effective coordination among UAVs and their associated communication systems.

As UAVs are inherently mobile and can operate in various environments, including remote or hard-to-reach locations, UAV communications harness wireless communication technologies to establish and sustain connectivity, facilitating seamless interactions between UAVs and various devices, such as ground terminals, satellites, and even other UAVs. The methods utilized within UAV communications encompass a range of communication technologies, including radio frequency (RF) communication, such as Wi-Fi, Bluetooth, and dedicated RF links, as well as satellite communication for beyond-line-of-sight (BLOS) operations. Additionally, UAV communication systems may employ networking protocols and technologies like mesh or ad-hoc networks to establish robust and resilient communication links, particularly in scenarios involving multiple UAVs or challenging and remote environments.

While UAVs have transformed numerous applications with their capabilities, they also bring forth a set of security challenges, particularly in the realm of wireless communications. As UAVs become increasingly integrated into everyday operations, ensuring the security of these communication systems is paramount. Here are some key security concerns:

(1) Frequency Interference: UAVs rely on wireless communication systems that operate in specific frequency bands. Frequency interference from other devices or communication systems can disrupt or degrade UAV communication signals, leading to loss of control or compromised data transmission. Proper frequency allocation, spectrum management, and interference mitigation techniques are essential to address this safety problem. The contribution of [1] is to explore the vulnerability of UAVs to deceptive Global Positioning System (GPS) signals. It investigate the potential risks and impacts of spoofing or jamming GPS signals on UAV navigation and operation.
(2) Signal Loss and Link Failure: UAVs may experience signal loss or link failures due to obstructions, radio signal propagation limitations, or technical issues. Loss of communication links can result in losing control over the UAV. Implementing robust communication protocols, redundancy mechanisms, and fail-safe procedures is crucial to ensure UAVs can safely return to a pre-defined state or execute contingency plans during communication loss. Ref. [2] provided path loss exponents for an open field and a campus scenario. Path loss exponent is a parameter used to model the attenuation of wireless signals as they propagate through a medium. This paper is likely to contain empirical measurements and signal propagation analysis specific to these environments.
(3) Cybersecurity Vulnerabilities: UAV communication systems are susceptible to cybersecurity threats, including unauthorized access, data breaches, and cyber-attacks. Malicious actors may attempt to intercept or manipulate UAV communication, leading to unauthorized control, tampering with data transmission, or disrupting the UAV's operation. Strong encryption, authentication protocols, intrusion detection systems, and secure communication standards are necessary to mitigate cybersecurity risks and safeguard UAV communication.
(4) Spectrum Congestion: As the number of UAVs in operation increases, airspace congestion, and spectrum overcrowding can occur, especially in densely populated areas or during large-scale events. Spectrum congestion can lead to communication delays, decreased reliability, and compromised UAV operations. Implementing effective spectrum management strategies, dynamic spectrum allocation techniques and traffic control mechanisms can help alleviate this safety problem [3, 4].
(5) Human Error and Operator Training: UAV communications' safety also depends on the proficiency and training of the UAV operators. Human errors in managing communication systems, misinterpretation of data, or failure to respond to communication issues can impact the safety of UAV operations. Proper training, certification, and adherence to standard operating procedures are crucial to minimize human-related safety risks.
(6) Environmental Factors: UAV communication is not immune to environmental factors, which can include weather disturbances, electromagnetic interference, or geographical obstacles. These external conditions, such as high winds, severe

weather events, or signal reflection, have the potential to disrupt communication links or lead to signal degradation [5]. Recognizing and addressing these environmental limitations is crucial for maintaining the safety and reliability of UAV communications [6]. Implementing robust communication systems that can withstand such challenges ensures that UAV operations remain secure and effective, even in adverse conditions. By proactively considering environmental factors and engineering solutions to mitigate their impact, UAV operators can enhance the resilience and overall performance of their communication systems.

Addressing these safety problems requires a holistic approach that combines technical solutions, regulatory frameworks, operator training, and industry collaboration. Ongoing research, development of standardized protocols, and adherence to safety guidelines are essential to enhance UAV communications' safety and foster the safe integration of UAVs into airspace systems [7, 8].

These innovative solutions not only bolster security but also significantly expand the capabilities of UAVs across a diverse range of applications. Below, we highlight a selection of remarkable UAV-based communication systems that have gained prominence in recent years. In the realm of relay networks, UAVs assume a pivotal role as intermediate nodes, facilitating signal transmission between source and destination nodes. Reference [9], the authors focus on a UAV relay network where UAVs serve as amplify-and-forward relays. This pioneering approach capitalizes on UAVs' exceptional mobility, which offers an enticing opportunity to enhance the performance of wireless communication systems. Within the context of data collection, UAVs play a transformative role. In [10] delves into a UAV-enabled data collection framework, where UAVs are dispatched to acquire specific data volumes from fixed ground terminals. The paper navigates critical facets such as data scheduling, energy efficiency, and data quality, crucial considerations in optimizing UAV-enabled data collection scenarios. The concept of non-orthogonal multiple access (NOMA) takes center stage in Ref. [11], presenting a novel framework for UAV networks with massive access capabilities. This paper explores the application of NOMA techniques in UAV networks, with the primary objective of enhancing spectral efficiency and accommodating an extensive array of connected devices. These cutting-edge UAV-based communication systems exemplify the ongoing commitment to advancing UAV capabilities while simultaneously addressing the challenges posed by security and performance. By harnessing UAVs' unique attributes and integrating state-of-the-art technologies, these systems pave the way for more robust, versatile, and efficient UAV operations across numerous domains, ranging from telecommunications to data collection and beyond. As research in this field continues to evolve, so too will the possibilities for enhancing the potential of unmanned aerial vehicles.

1.2 Basic Concept and Features

1.2.1 Composition of UAV Communications

UAV communications can be broadly categorized into different types based on the communication links involved. Here are the four categories you mentioned:

(1) Satellite to UAV Communications: This refers to the communication link between a satellite and a UAV, as shown in Fig. 1.1. Satellites can provide BLOS communication capabilities, enabling UAVs to operate over long distances and in remote areas where direct ground-based communication is limited. Satellite-to-UAV communications typically utilize satellite links for data transmission, control commands, and real-time telemetry, enabling UAVs to access global communication coverage.
(2) UAV to UAV Communications: UAV to UAV communications involve communication links established between multiple UAVs, as shown in Fig. 1.2. This type of communication is essential for tasks such as collaborative missions, swarm operations, coordinated surveillance, or distributed sensing. UAV-to-UAV communications allow for the exchange of information, coordination of actions, and sharing of data among the UAVs, enabling them to work together efficiently and achieve common objectives.

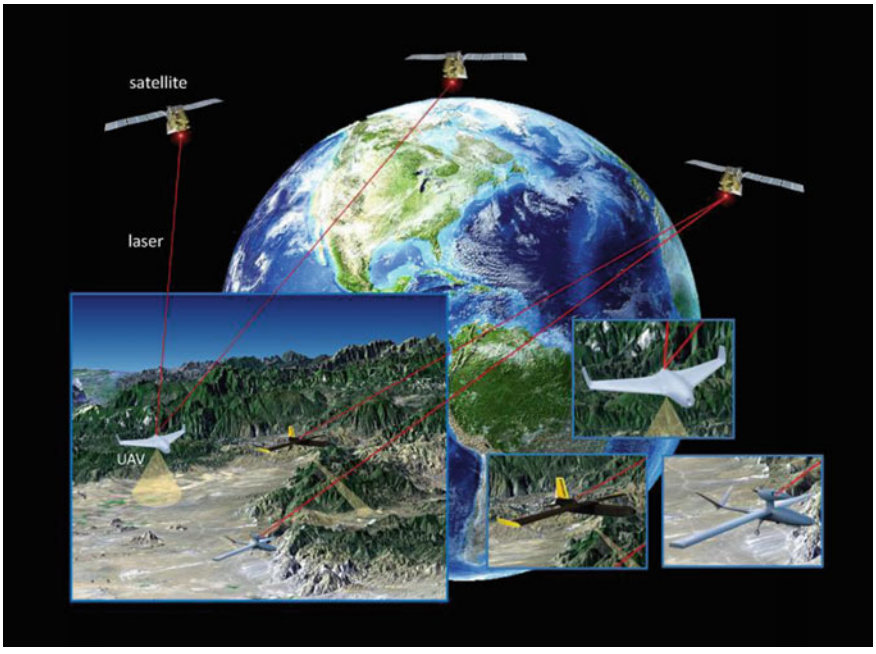

Fig. 1.1 Satellite to UAV communications

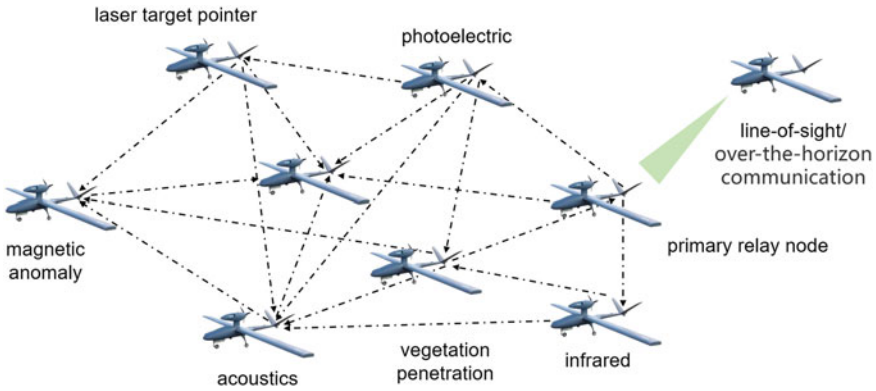

Fig. 1.2 UAV to UAV communications

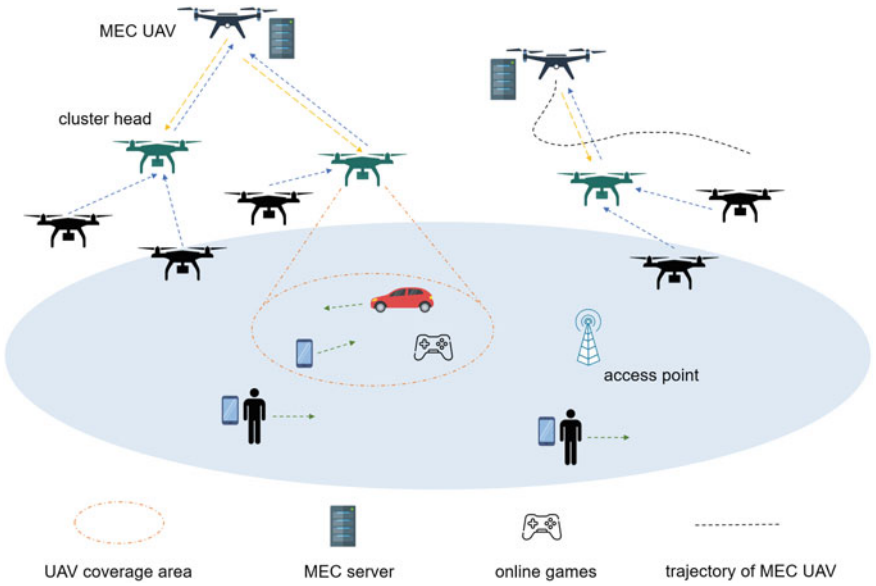

Fig. 1.3 UAV to ground communications

(3) UAV to Ground Communications: UAV-to-ground communications refer to the communication link between a UAV and a ground station or control center, as shown in Fig. 1.3. This link is vital for real-time control, command and control functions, data transmission, and mission monitoring. UAV-to-ground communication allows operators or ground-based systems to control the UAV remotely, receive telemetry data, and exchange commands, ensuring seamless operation and monitoring of the UAV.

(4) Hybrid Communications: Hybrid communications represent an integration of the above-mentioned three communication types, as illustrated in Fig. 1.4. This innovative approach creates a comprehensive communication network, facilitating the seamless exchange of data and control commands between satellites, UAVs, and ground stations. The result is a robust infrastructure that empowers BLOS operations, long-range communication, and uninterrupted connectivity across various platforms. This, in turn, significantly augments the range, versatility, and overall capabilities of UAV communication systems, marking a significant advancement in the field.

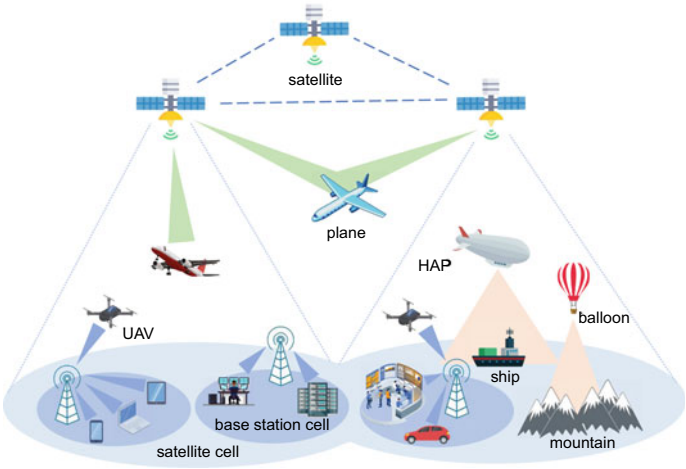

Fig. 1.4 Satellite-UAV-ground communications

These different types of UAV communications serve specific purposes and have their own challenges and requirements. Advancements in technology, such as satellite communication systems, networking protocols, and ground-based infrastructure, improve the efficiency, reliability, and safety of UAV communications across these different linkages.

1.2.2 Features of UAV Communications

UAV communication possesses several distinct characteristics that differentiate it from traditional communication systems. Here are some critical attributes of UAV communication:

(1) Wireless and Remote: UAV communications rely on wireless communication technologies to establish and maintain links between the UAV and the ground

station or other communication nodes. This wireless nature enables UAVs to operate in remote areas, over challenging terrains, and in environments that may be inaccessible or hazardous for humans. Moreover, UAVs can operate on various communication frequencies, including radio frequencies (RF) and satellite communication. The choice of frequency affects factors like data transmission speed, range, and susceptibility to interference.

(2) LOS and BLOS communication: In the realm of UAV communication, two distinct modes exist, LOS and NLOS, each with its own unique characteristics and implications. LOS communication is a fundamental concept in UAV operations, where a direct, unobstructed LOS between the UAV and its control station is required. This type of communication is widely used for remote piloting and real-time data transmission. In LOS scenarios, UAVs typically operate within the visual LOS of their ground stations or operators. This requirement is driven by the nature of RF communication, which relies on a direct path between the UAV and receiver. Any physical obstacles or interference in the LOS can disrupt the RF signals, affecting communication reliability. Consequently, LOS constraints naturally limit the range and operational capabilities of UAVs. In contrast, Beyond-Line-of-Sight (BLOS) communication represents a significant advancement that empowers UAVs to operate beyond the visual line of sight of their operators. BLOS communication harnesses a range of technologies, including satellite communication and long-range radio links, to overcome the limitations of LOS. These technologies enable UAVs to establish communication over extended distances and across obstacles, making them essential for applications requiring long-range surveillance and autonomous package delivery.

(3) Bandwidth Limitations: UAVs often have limited bandwidth available for communication due to frequency spectrum allocation, RF hardware limitations, or the need to conserve power. Therefore, communication protocols and data transmission techniques for UAVs are designed to optimize the utilization of available bandwidth while meeting the specific requirements of the mission or application.

(4) Reliability and Resilience: UAV communication systems must be reliable and resilient to ensure consistent connectivity between the UAV and the ground station. Since UAVs may operate in dynamic and challenging environments, communication systems must handle interference, signal degradation, and other obstacles while maintaining a reliable and stable link. Encryption ensures that the data transmitted between the UAV and the ground control station remains secure and cannot be intercepted by unauthorized parties. This is crucial for maintaining the privacy and integrity of sensitive information. To enhance reliability, some UAVs incorporate redundant communication systems. If one communication link fails, the UAV can seamlessly switch to a backup link to maintain control and data transmission.

(5) Low Latency Requirements: Some UAV applications, such as real-time surveillance or autonomous operations, require low-latency communication. The ability to transmit and receive data with minimal delay is crucial for timely decision-making and responsiveness of UAV systems.

(6) Multi-hop and Mesh Networks: UAVs can form multi-hop or mesh networks, where data is relayed from one UAV to another until it reaches the destination. This enables UAVs to extend their communication range and overcome LOS limitations by leveraging intermediate UAVs as relays. Multi-hop and mesh networking also enhance the resilience and fault tolerance of the communication system.

These characteristics highlight the unique aspects of UAV communications and the challenges involved in establishing reliable, efficient, and secure communication links for UAVs.

1.2.3 Basic Aspects of UAV Communications

1.2.3.1 UAV Communication Channels

In UAV communication, the establishment of connectivity between two devices generally relies on wireless methods, primarily due to the mobility of UAV terminals. Consequently, an in-depth examination of the wireless propagation channel assumes paramount significance as it significantly influences the overall system performance. Numerous existing resources comprehensively encompass the characteristics, ongoing research advancements, as well as the persisting challenges within UAV communication channel modeling. For a more detailed exploration, readers are encouraged to consult [12, 13]. In this section, we will provide an overview of the prevalent channel models widely adopted in the existing literature.

Finding a unified channel model that can accurately represent the propagation characteristics of various UAV communication applications is a challenging task. The end-to-end channel experience for the transmitted signals is contingent upon several factors, such as the selected frequency bands, the scattering properties within the propagation environments, antenna configurations, and the Doppler effects induced by UAV movements. To effectively characterize propagation behavior while operating under specific assumptions and parameters, two primary modeling approaches are commonly embraced: deterministic modeling, stochastic modeling, and geometry-based stochastic modeling.

- **Deterministic Model** This approach operates under the premise that environmental obstructions are arranged in specific layouts, making it particularly suitable for situations where the size of environmental objects greatly exceeds the wavelength. It can accurately depict the realistic behavior of electromagnetic wave propagation but is heavily reliant on the availability of environment-specific databases. In other words, the accuracy of deterministic models hinges on the quality of information pertaining to the environment, including details about terrain topography, electrical properties of buildings, and other obstructive materials. Typically, this type of model is implemented using 3D ray-tracing software. For example, in [14,

15], analytical aerial-ground propagation models are proposed for urban environments, covering frequencies ranging from 200 MHz to 5 GHz and altitudes ranging from 100 to 2000 m. Additionally, a generic path loss model is introduced in [16] using statistical parameters recommended by the International Telecommunication Union at 700, 2000, and 5800 MHz. However, it's important to note that these models may not be readily applicable to different environments and often overlook fading effects caused by small-scale variations.

- **Stochastic Model** These models are constructed on the premise that wireless channel behavior is inherently uncertain, shaped by a multitude of influencing factors that include both large-scale fading and small-scale fading as critical components. Large-scale fading encompasses factors like path loss, which quantifies how signal strength diminishes with distance, and shadowing, which accounts for the effects of obstacles and terrain by introducing random variations in signal strength. The primary contributors to large-scale fading in UAV communication are the dynamics of the UAV itself, including variables such as altitude, distance, and elevation angle, as indicated in [13]. Small-scale fading, on the other hand, refers to rapid and short-term signal strength fluctuations caused by the constructive and destructive interference of multipath components. This phenomenon is typically represented as a complex stochastic process. Small-scale fading is more localized and changes rapidly, often occurring over a limited spatial or temporal scale. In UAV communications, small-scale fading can follow various statistical distributions such as the Loo model, Rayleigh, Rician, or Nakagami, contingent on the specific characteristics of the wireless channel. Stochastic models are valuable for analyzing the time-varying attributes of the UAV channel. However, many existing results primarily offer numerical analyses and often lack validation through measured data. Developing effective stochastic frameworks tailored to the unique characteristics of UAV channels is crucial to advancing our understanding of these systems.

It is worthy to mention that the integration of both deterministic and stochastic models can yield more comprehensive and versatile UAV propagation models. Given the popularity of stochastic models in the performance analysis and system optimization of UAV communications, we will provide a more in-depth introduction to this approach, covering both its widely utilized large-scale and small-scale components.

(1) Large-Scall Fading Models: The large-scall fading occurs when the Line-of-Sight (LOS) path between UAV communication terminals is obstructed by an object that is significantly large relative to the wavelength. In situations where the LOS path remains unobstructed, the only other substantial large-scale effect is the two-ray variation stemming from multipath components. Numerous measurement campaigns have been conducted in the existing literature to study this. One of the most well-known models for this behavior is the log-distance free space path loss model, which can be expressed as:

$$PL(d) = PL_0 + 10\gamma \log_{10}\left(\frac{d}{d_0}\right) + X, \tag{1.1}$$

where, PL_0 represents the path loss at the reference distance d_0 in free space and is given by $10 \log \left[\left(\frac{4\pi d_0}{\lambda}\right)\right]$, λ is the wavelength, γ denotes the path loss exponential, which is determined through minimum mean square error best fit and typically falls within the range of 1.5–4. The aerial-aerial channel is generally better than aerial-ground channel in terms of path loss exponent. The variable X accounts for random effects, such as shadowing, or, in the case of LOS channels, variations around the linear fit. The reference distance in the free space path loss model mentioned above can be eliminated and represented by two additional parameters, the slope (α) and the intercept (β). This yields the following expression:

$$PL(d) = 10\alpha \log_{10}(d) + \beta + X. \tag{1.2}$$

This modified model is commonly referred to as the "floating intercept model." In this model, the path loss is determined without the need for a reference distance, and linear least square error regression is employed to fit the data. It's worth noting that while the floating intercept model offers increased flexibility, it may not be as accurate as the free space path loss model at both short and long distances. To improve accuracy, further evaluation of the slope parameter may be required, particularly for different distance ranges. Furthermore, various models take into account shadowing for NLOS paths, as well as additional losses incurred due to other obstacles, as described in [17]. Additionally, modified free-space path loss models that factor in the altitude of UAVs are developed to account for the three-dimensional motion of UAVs, as discussed in [18, 19]. These models offer a more comprehensive understanding of the path loss characteristics in UAV communication systems by considering various environmental factors and UAV dynamics.

Another commonly used model for path loss in UAV communication systems is one that averages the path loss over the probabilities of LOS and NLOS conditions, as presented in [20]. It can be expressed as:

$$PL = \Pr(LOS) \times PL_{LOS} + (1 - \Pr(LOS)) \times PL_{NLOS}, \tag{1.3}$$

where PL_{LOS} and PL_{NLOS} represent the path loss in LOS and NLOS conditions, respectively, while $\Pr(LOS)$ denotes the probability of having a LOS link between the communication terminals. This mixture path loss model calculates an average path loss over a large number of potential LOS and NLOS link possibilities. It's important to exercise caution when using this model in system-level analysis, especially when calculating end metrics such as throughput and outage. The accuracy of this approach relies on the appropriate estimation of LOS probabilities and path loss values in both LOS and NLOS conditions, which can be influenced by the specific characteristics of the environment and the UAV communication system.

In summary, the free space path loss model is the most widely used due to its simplicity and its ability to provide a standard platform for comparing measurements in various environments using a reference distance. However, in scenarios where the reference free space path loss model is not applicable, alternative forms of large-scale models may be employed. The choice of an appropriate path loss model for a given

UAV propagation scenario is of paramount importance, as it significantly impacts the accuracy of system performance predictions and analysis. Careful consideration of the specific environmental and operational conditions is essential in selecting the most suitable model for the task at hand.

(2) Small-Scale Fading Models: Small-scale fading models are typically applied to narrow-band channels or to individual multipath components, often referred to as "taps" in tapped delay line wide-band models, within a certain bandwidth. These stochastic fading models can be derived through various means, including theoretical analysis, empirical data collection, or geometric analysis and simulation. In the following section, we will explore several commonly used models for small-scale fading in the context of UAV communication. These models are crucial for understanding how signal strength fluctuates rapidly over short distances due to factors like multipath propagation, interference, and scattering.

Rayleigh Fading Model: Rayleigh fading is a widely used fading model that assumes a purely scattered propagation environment without a dominant LOS component. It occurs when multiple uncorrelated paths exist between the transmitter and receiver, resulting in a random and fluctuating signal strength. Rayleigh fading is typically observed in urban and dense environments with significant multipath reflections [21, 22]. The samples for the Rayleigh flat-fading samples are drawn in Fig. 1.5 from the following random variable $\mathbf{h} = \|X + jY\|$ where $X \sim N\left(0, \sigma^2/2\right)$ and $Y \sim N\left(0, \sigma^2/2\right)$. The average power in the distribution is $P_a v = \sigma^2$. Therefore to model a channel with $P_a v = 1$, the normal random variables X and Y should have the standard deviation $\sigma = 1/\sqrt{(2)}$. Rayleigh models was theoretically proved to be accurate for cooperative relay based UAV systems, multiple-access ground-aerial channels, and channels for the field measurements with large elevation angles in a mixed-urban environment.

Rician Fading Model: Rayleigh distribution is well suited for the absence of a dominant LOS path between the transmitter and the receiver. However when a LOS path does exist, Rician is more preferred to approximate the fluctuations in the fading channels. Rician fading is a multipath fading model that accounts for a dominant LOS component and scattered or reflected paths. It assumes the received signal combines a dominant signal and multiple weaker scattered signals. Rician fading is applicable in scenarios with a strong LOS path, such as in open areas with limited obstacles [23–25]. Specifically, the fading process can be represented as the sum of a complex exponential and a narrowband complex Gaussian process $g(t)$. If the LOS component arrives at the receiver at an Angle of Arrival (AoA) θ, phase ϕ and with the maximum Doppler frequency f_D, the fading process in baseband can be represented as

$$h(t) = \underbrace{\sqrt{\frac{K\Omega}{K+1}}}_{\text{A:=}} e^{(j2\pi f_D \cos(\theta)t + \phi)} + \underbrace{\sqrt{\frac{\Omega}{K+1}}}_{\text{S:=}} g(t), \tag{1.4}$$

where K represents the Rician K factor given as the ratio of power of LOS component $\left(A^2\right)$ to the power of scattered components $\left(S^2\right)$ marked in the equation above, that is, $K = \frac{A^2}{S^2}$. The received signal power Ω is the sum of power in the LOS component and the power in scattered components, given as $\Omega = A^2 + S^2$. In fact, the severity of the multipath fading in a Rician channel is quantified using the Rician K factor. In Rician fading, the best-case scenario occurs when $K = \infty$, representing a channel with a strong LOS path where the signal behaves like a Gaussian channel. On the other hand, the worst-case Rician fading channel corresponds to $K = 0$, indicating a Rayleigh channel with no LOS path. In practical terms, a high K value signifies a more dominant LOS component, while a low K value implies that the signal is primarily affected by scattered components and lacks a strong LOS path.

Nakagami-*m* Fading Model: Nakagami-*m* fading is a statistical fading model that characterizes the wireless channel as a gamma distribution, which are appropriate for characterizing teh UAV fading channels intended for high altitude applications. It represents a generalization of the Rayleigh fading model, accounting for different levels of severity or fading depth. The parameter m determines the severity of fading, with higher values indicating less severe fading and approaching a non-fading channel [26, 27].

Loo Model: The Loo model is a composite channel model that combines elements of both Rician and Log-Normal distributions. Specifically, it uses a Log-Normal distribution to model the LOS component and typically employs the Rician model for the multipath components. This model is designed to provide a more accurate representation of fading statistics in wireless communication channels. The results given in [28] show that Loo model is effective in capturing the statistical behavior of the channel, particularly in urban settings where multipath and LOS components play crucial roles in signal propagation.

As summarized in [13], fading channel statistics for most UAV communication cases reported in the literature are analyzed with the Nakagami-m and Rician distributions. These fading models are essential for analyzing the performance of UAV communication systems, as shown in Fig. 1.5. They help in designing efficient modulation and coding schemes, evaluating link quality, estimating channel capacity, and optimizing communication strategies to compensate for the variations in signal strength caused by fading effects.

When undertaking theoretical analyses of UAV communication systems, the choice of communication channel model is a critical decision that should align with various factors. These factors include the operational range, data transfer needs, regulatory stipulations, and the existing communication infrastructure specific to the scenarios under consideration. Ensuring this alignment is essential for constructing accurate theoretical models and predictions. Furthermore, strict adherence to local regulations is imperative. This includes securing the requisite licenses or permissions for utilizing particular frequency bands or communication channels in UAV operations. Compliance with these regulations not only fosters legality but also promotes responsible and interference-free UAV communication practices, contributing to the overall safety and reliability of unmanned aerial vehicle operations.

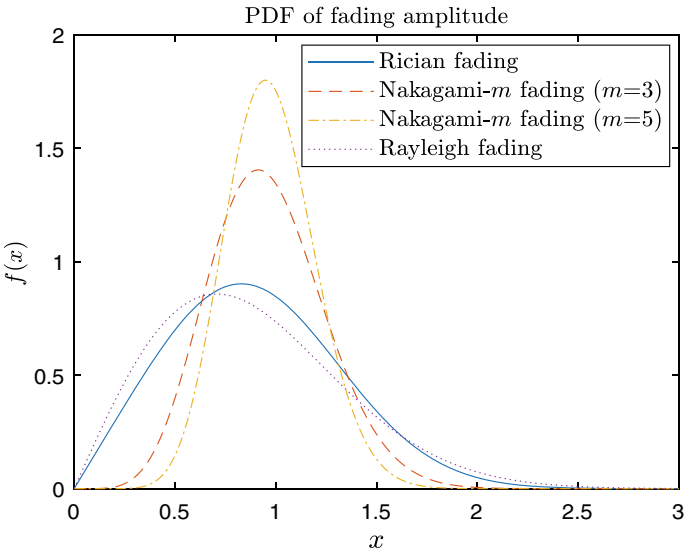

Fig. 1.5 PDF for different fading channels

1.2.3.2 Performance Metrics

Several metrics are commonly used when assessing the performance of UAV communication systems. Here are three key performance indicators:

- **Outage Probability (OP)**: OP measures the probability that the UAV communication system fails to meet a specified quality of service (QoS) threshold, as shown in Fig. 1.6. It is typically defined as a desired data rate or signal-to-noise ratio (SNR) level. A lower OP indicates better system performance, implying a higher likelihood of meeting the desired QoS target.
- **Ergodic Capacity (EC)**: EC represents a UAV communication system's average achievable data rate over a long-term duration, considering fading channel conditions as shown in Fig. 1.7. It captures the channel's statistical behavior and estimates the system's capacity for data transmission. Higher EC implies better overall performance in terms of achievable data rates.
- **Packet Error Rate (PER) or Bit Error Rate (BER)**: PER or BER measures the ratio of erroneous packets or bits to the total transmitted packets or bits, respectively, as shown in Fig. 1.8. These metrics quantify the quality of the received data and assess the impact of errors in the communication system. Lower PER or BER values indicate better system performance and higher reliability in terms of data transmission.

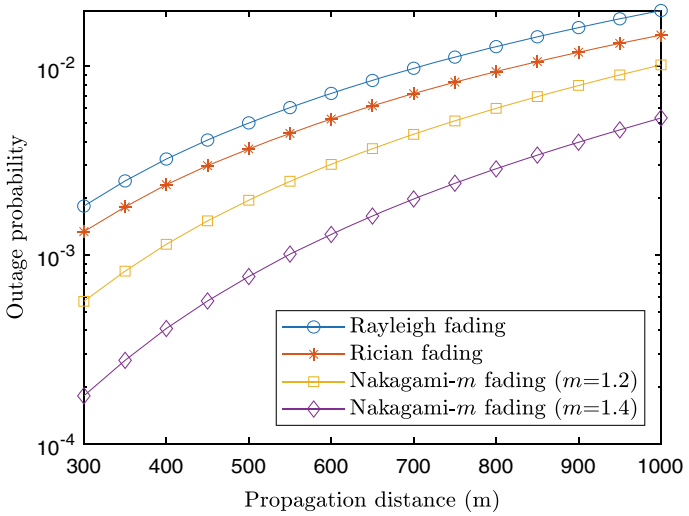

Fig. 1.6 OP for different fading channels

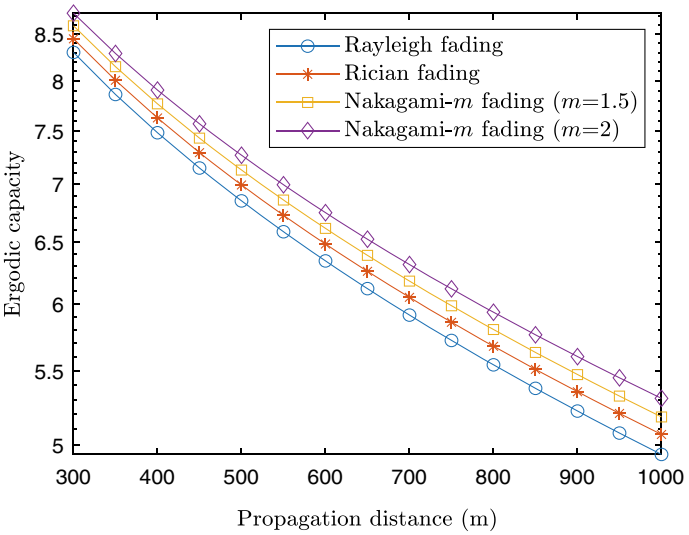

Fig. 1.7 EC for different fading channels

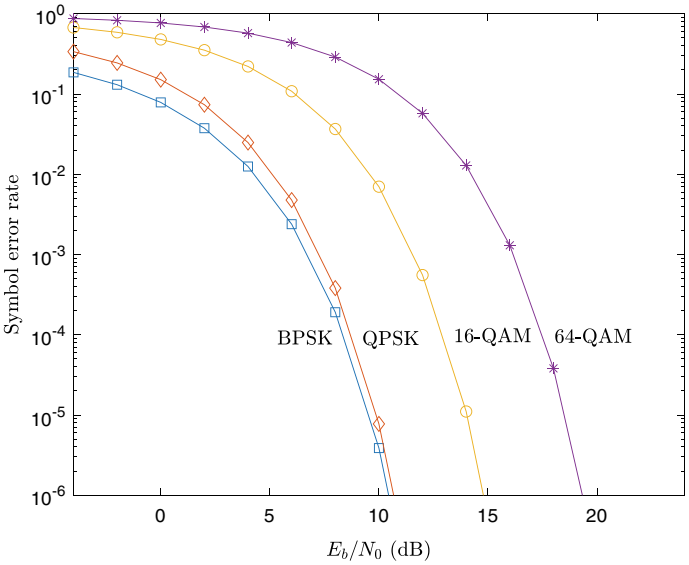

Fig. 1.8 Symbol error rate for different fading channels

These performance metrics are commonly used to evaluate and optimize the performance of UAV communication systems. By analyzing OP, EC, and PER/BER, system designers can make informed decisions about communication protocols, modulation schemes, coding techniques, transmit power control, and other system parameters to ensure reliable and efficient communication between the UAV and the ground station or other communication devices.

The transmission of data in UAV communications unfolds within the expansive three-dimensional aerial space, presenting acute concerns regarding information security. Within this context, the concept of PLS takes center stage, serving as a linchpin for safeguarding the confidentiality and integrity of data as it traverses the physical layer of communication. It utilizes the properties of the wireless channel, such as channel fading, noise, and interference, to provide secure and confidential communication. Through techniques such as beamforming, artificial noise injection, cooperative communication, and the implementation of secure coding schemes, PLS not only enhances the security of UAV communications but also effectively thwarts unauthorized access and eavesdropping attempts. Here, we delve into two pivotal components integral to the domain of PLS:

- **Secrecy Outage Probability (SOP)**: SOP is a metric used to evaluate the level of secrecy or confidentiality achieved in a communication system, as shown in Fig. 1.9. It represents the probability that an eavesdropper can decode the transmitted information above a certain threshold. A lower SOP indicates better protection against eavesdropping and higher confidentiality.

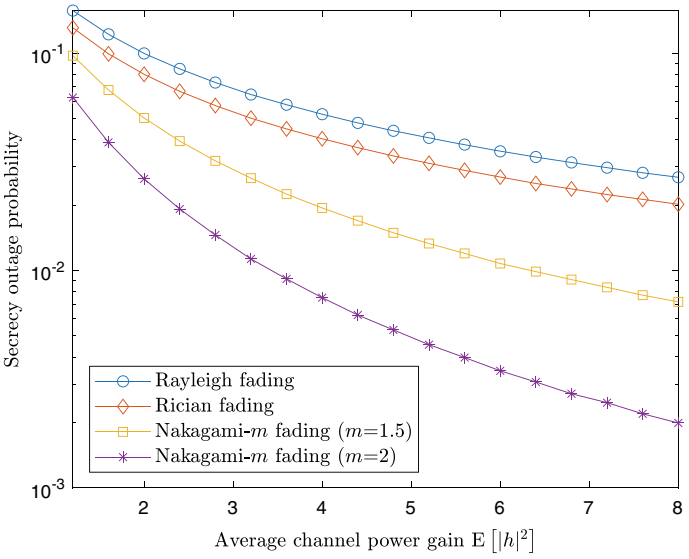

Fig. 1.9 SOP for different fading channels

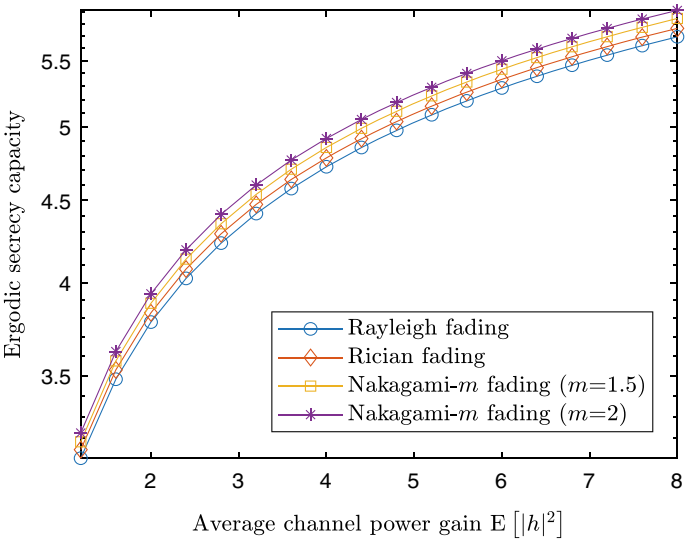

Fig. 1.10 ASC for different fading channels

- **Average Secrecy Capacity (ASC)**: ASC measures a communication system's maximum achievable secrecy rate or information-theoretic security over a long-term average, as shown in Fig. 1.10. It considers both the legitimate receiver's quality of service and the secrecy requirement against eavesdroppers. ASC quantifies the maximum secure communication rate sustained over time, considering the channel conditions and system constraints.

By considering SOP and ASC and leveraging PLS techniques, UAV communication systems can achieve improved confidentiality, integrity, and protection against eavesdropping attacks. These measures safeguard sensitive information transmitted between the UAV, ground station, or other communication devices.

1.2.3.3 A Useful Tool of Modeling the Randomness of Nodes

Stochastic geometry serves as a robust mathematical framework employed to analyze and model the random or probabilistic spatial distribution and behavior of objects. In the context of UAV communication, stochastic geometry plays a pivotal role in both the study and optimization of UAV networks. This branch of mathematics specializes in elucidating spatial patterns and structures that emerge from random geometric processes, encompassing the examination of random point patterns, random tessellations, and various related objects. To provide a deeper understanding of this mathematical discipline, we delve into fundamental formulas and concepts commonly applied in stochastic geometry:

(1) Point process intensity: A point process represents a random collection of points in a given space within stochastic geometry. The intensity of a point process refers to the average number of points per unit area or volume. This parameter serves as a foundational measure for quantifying the spatial distribution of objects within a stochastic framework.
(2) Pair correlation function: The pair correlation function, denoted as $g(r)$, stands as a critical tool for measuring the relative density of points at a distance r from a reference point compared to a random distribution. This function offers valuable insights into the spatial clustering or repulsion characteristics present within a point process.
(3) K-function: Another pivotal measure of spatial clustering or dispersion in a point process is the K-function, denoted as $K(r)$. This function quantifies the expected number of points located within a distance r of a typical point in the process, relative to a random distribution. It provides a complementary perspective on spatial arrangement patterns.
(4) Void probability: The void probability, symbolized as $V(r)$, represents the probability that a randomly chosen point in a point process lies at a distance greater than r from the nearest neighboring point. This measure characterizes the degree of clustering present in a point pattern.
(5) Second-order characteristics: Stochastic geometry often centers on exploring the second-order characteristics of point processes, including the pair correla-

tion function ($g(r)$), the K-function ($K(r)$), and other related measures. These characteristics offer invaluable insights into the spatial organization of points within a given context. They find application in modeling and analyzing diverse phenomena, encompassing the distribution of objects, network connectivity, and coverage within wireless communication systems.

Stochastic geometry provides indispensable tools and techniques for modeling the locations and movements of UAVs, the distribution of ground users or devices, and the intricate characteristics of the communication environment. It enables the consideration of random spatial distributions, movement patterns, and environmental factors, thereby enhancing the understanding and performance of UAV networks. Here are some key applications:

(1) Coverage Analysis: Stochastic geometry is harnessed to assess the coverage probability of UAVs within a designated area. By modeling the spatial arrangements of UAVs, ground users, and potential obstacles, engineers can estimate the likelihood that a ground user will establish a reliable communication link with a nearby UAV. This analysis proves invaluable in optimizing network coverage, particularly in applications such as remote sensing or disaster response.
(2) Interference Modelling: In the complex landscape of UAV networks, interference is a significant concern. Stochastic geometry allows for the in-depth analysis of interference patterns, taking into account the spatial distribution of UAVs and their respective transmit powers. By evaluating interference levels experienced by different users, engineers can strategize optimal deployment approaches to mitigate interference and enhance network reliability.
(3) Path Loss Modeling: Stochastic geometry excels in modeling path loss and signal propagation dynamics, even in intricate and unpredictable environments. This modeling accounts for factors such as terrain, obstacles, and atmospheric conditions, thereby enabling precise predictions of signal strength and the optimization of communication range. Path loss modeling is instrumental in ensuring reliable communication across varying landscapes.
(4) Capacity Analysis: The estimation of network capacity is a crucial aspect of UAV communication systems. Stochastic geometry allows for the modeling of the spatial distribution of UAVs, ground users, communication requirements, and constraints. This comprehensive analysis yields valuable insights into the maximum achievable data rates and overall network capacity, guiding network dimensioning efforts.
(5) Trajectory Planning: Stochastic geometry plays a pivotal role in planning UAV trajectories to optimize various tasks, including data collection, surveillance, and communication. It accounts for diverse factors such as terrain characteristics, obstacles, communication range constraints, and the spatial distribution of targets or points of interest. Through trajectory planning, engineers ensure efficient UAV paths, minimize travel time, and conserve energy resources.

In summary, stochastic geometry provides a powerful mathematical foundation for designing, analyzing, and optimizing UAV communication systems. It is essential

to note that the specific mathematical formulations within stochastic geometry vary according to the unique problem or model under consideration. Advanced topics within this discipline delve into models such as Poisson point processes, random tessellations (e.g., Voronoi tessellations), and more intricate spatial structures. Stochastic geometry's versatility and ability to address the spatial challenges inherent in UAV operations make it an invaluable tool for ensuring the reliability, efficiency, and effectiveness of UAV communication networks across diverse real-world scenarios.

References

1. K.P. Valavanis, G.J., Vachtsevanos *Handbook of Unmanned Aerial Vehicles* (Springer, Dordrecht, Switzerland, 2011)
2. E. Yanmaz, R. Kuschnig, C. Bettstetter, Channel measurements over 802.11a-based UAV-to-ground Links, in *2011 IEEE Globecom Workshops (GC WKSHPS)* (2011), pp. 1280–1284
3. D. Yang, W. Qingqing, Y. Zeng, R. Zhang, Energy tradeoff in ground-to-UAV communication via trajectory design. IEEE Trans. Veh. Technol. **67**(7), 6721–6726 (2018)
4. Z. Feng, L. Ji, Q. Zhang, W. Li, Spectrum management for MmWave enabled UAV swarm networks: challenges and opportunities. IEEE Commun. Mag. **57**(1), 146–153 (2019)
5. S. Zhang, H. Zhang, B. Di, L. Song, Cellular UAV-to-X communications: design and optimization for multi-UAV networks. IEEE Trans. Wireless Commun. **18**(2), 1346–1359 (2018)
6. A.J. Kerns, D.P. Shepard, J.A. Bhatti, T.E. Humphreys, Unmanned aircraft capture and control via GPS spoofing. J. Field Robot. **31**(4), 617–636 (2014)
7. Y. Liu, Z. Qin, Y. Cai, Y. Gao, G.Y. Li, A. Nallanathan, UAV communications based on non-orthogonal multiple access. IEEE Wirel. Commun. **26**(1), 52–57 (2018)
8. Y. Du, K. Yang, K. Wang, G. Zhang, Y. Zhao, D. Chen, Joint resources and workflow scheduling in UAV-enabled wirelessly-powered MEC for IoT systems. IEEE Trans. Veh. Technol. **68**(10), 10187–10200 (2019)
9. J. Tian, L. Wang, X. Li, H. Gong, C. Shi, R. Zhong, X. Liu, Comparison of UAV and world view-2 imagery for mapping leaf area index of mangrove forest. Int. J. Appl. Earth Obs. Geoinf. **61**, 22–31 (2017)
10. S. Zhang, H. Zhang, Q. He, K. Bian, L. Song, Joint trajectory and power optimization for UAV relay networks. IEEE Commun. Lett. **22**(1), 161–164 (2017)
11. A.A. Khuwaja, Y. Chen, N. Zhao, M.-S. Alouini, P. Dobbins, A survey of channel modeling For UAV communications. IEEE Commun. Surv. Tutor. **20**(4), 2804–2821 (2018)
12. A.A. Khuwaja, Y. Chen, N. Zhao, M.-S. Alouini, P. Dobbins, A survey of channel modeling for UAV communications. IEEE Commun. Surv. Tutor. **20**(4), 2804–2821 (2018). Fourthquarter
13. W. Khawaja, I. Guvenc, D.W. Matolak, U.-C. Fiebig, N. Schneckenburger, A survey of air-to-ground propagation channel modeling for unmanned aerial vehicles. IEEE Commun. Surv. Tutor. **21**(3), 2361–2391 (2019), thirdquarter
14. Q. Feng, J. McGeehan, E.K. Tameh, A.R. Nix, Path loss models for air-to-ground radio channels in urban environments, in *IEEE 63rd Vehicular Technology Conference*, vol. 2006 (Melbourne, VIC, Australia 2006), pp. 2901–2905
15. Q. Feng, E.K. Tameh, A.R. Nix, J. McGeehan, WLCp2-06: modelling the likelihood of line-of-sight for air-to-ground radio propagation in urban environments, in *IEEE Globecom*, vol. 2006 (San Francisco, CA, USA, 2006), pp. 1–5
16. A. Al-Hourani, S. Kandeepan, A. Jamalipour, Modeling air-to-ground path loss for low altitude platforms in urban environments, in *IEEE Global Communications Conference*, vol. 2014 (Austin, TX, USA, 2014), pp. 2898–2904
17. J. Holis, P. Pechac, Elevation dependent shadowing model for mobile communications via high altitude platforms in built-up areas. IEEE Trans. Antennas Propag. **56**(4), 1078–1084 (2008). (April)

18. A. Al-Hourani, S. Kandeepan, A. Jamalipour, Modeling air-to-ground path loss for low altitude platforms in urban environments, in *IEEE Global Communications Conference*, vol. 2014 (Austin, TX, USA, 2014), pp. 2898–2904
19. T. Tavares, et al., Generalized LUI propagation model for UAVs communications using terrestrial cellular networks, in *IEEE 82nd Vehicular Technology Conference (VTC2015-Fall)*, vol. 2015 (Boston, MA, USA, 2015), pp. 1–6
20. A. Al-Hourani, S. Kandeepan, S. Lardner, Optimal LAP altitude for maximum coverage. IEEE Wirel. Commun. Lett. **3**(6), 569–572 (2014). (Dec.)
21. C. Xiao, Y.R. Zheng, N.C. Beaulieu, Statistical simulation models for Rayleigh and Rician fading, in *IEEE International Conference on Communications*, vol. 5 (2003), pp. 3524–3529
22. G. Vikas, N. Deepak, N-Rayleigh distribution in mobile computing over flat-fading channel, in *2009 Proceeding of International Conference on Methods and Models in Computer Science (ICM2CS)* (2009), pp. 1–3
23. O. Ozdogan, E. Bjornson, E.G. Larsson, Massive MIMO with spatially correlated Rician fading channels. IEEE Trans. Commun. **67**(5), 3234–3250 (2019)
24. K.A. Hamdi, Capacity of MRC on correlated Rician fading channels. IEEE Trans. Commun. **56**(5), 708–711 (2008)
25. S.K. Jayaweera, H.V. Poor, On the capacity of multiple-antenna systems in Rician fading. IEEE Trans. Wireless Commun. **4**(3), 1102–1111 (2005)
26. N.C. Beaulieu, C. Cheng, Efficient Nakagami-m fading channel simulation. IEEE Trans. Veh. Technol. **54**(2), 413–424 (2005)
27. S. Ikki, M.H. Ahmed, Performance analysis of cooperative diversity wireless networks over Nakagami-m fading channel. IEEE Commun. Lett. **11**(4), 334–336 (2007)
28. M. Simunek, F.P. Fontán, P. Pechac, The UAV low elevation propagation channel in urban areas: statistical analysis and time-series generator. IEEE Trans. Antennas Propag. **61**(7), 3850–3858 (2013). (July)

Chapter 2
UAV-Terrestrial Communications

Gaofeng Pan, Tingting Li, Jinhui Fang, Hongjiang Lei, Jia Ye, and Sheng Ke

2.1 Secure UAV-Terrestrial Communication with Linear Trajectory

By observing the fact that moving in a straight line is a common flying behavior of UAVs in normal applications, e.g., power line inspections and air patrols along with highway/streets/borders, in this section we investigate the secrecy outage performance of a UAV system with linear trajectory, where a UAV (S) flies in a straight line and transmits its information over the downlink to a legitimate ground station (G) while an eavesdropping UAV (E) trying to overhear the information delivery between S and G. Meanwhile, some information is delivered to S over the uplink from G, such as commanding messages to control S's detecting operations, which can also be eavesdropped by E. The locations of S, G, and E are randomly distributed. We first characterize the statistical characteristics, including cumulative distribution functions (CDF) and probability density function (PDF), of the received SNR over both downlink and uplink. Then, the closed-form analytical expressions for the lower boundary of the SOP of both downlink and uplink have also been derived accordingly. Finally, Monte Carlo simulations are given to testify to our proposed analytical models.

G. Pan (✉) · J. Fang · S. Ke
Beijing Institute of Technology, Beijing, China
e-mail: gfpan@bit.edu.cn

T. Li
Southwest University, Chongqing, China

H. Lei
Chongqing University of Posts and Telecommunications, Chongqing, China

J. Ye
Chongqing University, Chongqing, China

G. Pan et al. (eds.), *UAV Communications: Modeling and Analyses*,
https://doi.org/10.1007/978-981-97-0383-8_2

The main contributions of this section are summarized as follows:

(1) We characterize the statistical characteristics (including CDF and PDF) of the received SNR at E, G over the downlink, and S over the uplink, respectively;
(2) We derive the closed-form analytical expressions for the lower boundary of the secrecy SOP of uplink and downlink, respectively;
(3) We systematically study and summarize the impacts of the radius of the coverage space of S and G, the transmit SNR at S and G, and the height of UAV on the secrecy performance of the considered system.

The rest of this section is organized as follows. In Sect. 2.1.1, the considered power-line inspection UAV system is described. In Sects. 2.1.2 and 2.1.3 the secrecy outage analysis is conducted for both the uplink and the downlink, respectively. Also, closed-form analytical expressions for the lower boundary of the SOP of both uplink and downlink are derived in Sects. 2.1.2 and 2.1.3. In Sect. 2.1.4 numerical results for the secrecy outage are presented and discussed. Finally, we conclude the section with some remarks in Sect. 2.1.5.

2.1.1 System Model

In this section, a UAV system with linear trajectory is considered, in which S is adopted to perform inspection/supervision. In particular, S moves in a straight line (e.g., power line inspections and air patrols along with highway/streets/borders) and sends back inspection data to G. Simultaneously, E tries to overhear the information transmissions between S and G. In other words, E can eavesdrop on the information delivery over the uplink link from G to S and the downlink from S to G. To facilitate the illustration, we take power line inspection as an example of the considered system, shown in Fig. 2.1. Furthermore, an omnidirectional transmission antenna is assumed to be employed at S and G. In Sect. 2.1 we also assume that all links suffer independent Rayleigh fading to reflect the effects of small-scale fading, namely, the channel gain $h_{jk} \sim \mathcal{CN}\left(0, g_{jk}\right)$, where $g_{jk} = E\left(\left|h_{jk}\right|^2\right)$ and $j, k \in \{G, S, E\}$.[1]

Section 2.1 assumes that the trajectory of S is in a straight line for tractability purposes. This assumption is reasonable, as S normally flies along highways/streets/borders to inspect/monitor and gather the state information. Furthermore, we also assume that E is uniformly distributed in the airspace to eavesdrop the information delivery between S and G.[2]

[1] In Sect. 2.1 non-line-of-sight (NLOS) propagation scenarios (e.g., UAVs are employed to patrol and monitor the urban streets) are considered to facilitate presenting the technical road map on analyzing the SOP of the considered system, which can readily serve as a useful reference to study the performance of similar systems, no matter in NLOS or LOS propagation scenarios.

[2] In Sect. 2.1 passive eavesdropping is considered, which can realize the optimal eavesdropping from E's side. If the operating space of legitimate users is open, E can share this space with legitimate

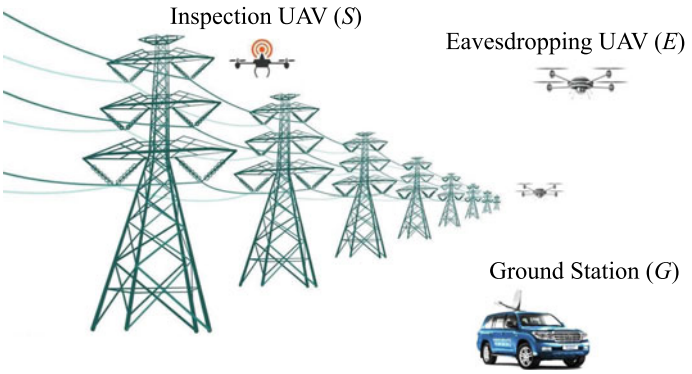

Fig. 2.1 Automatic power-line inspection UAV system

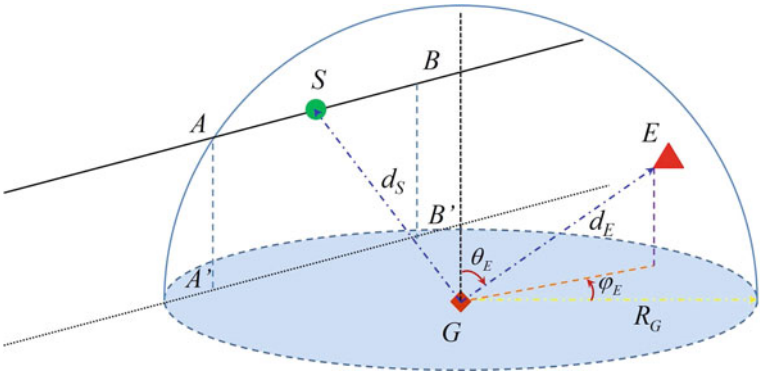

Fig. 2.2 Uplink model

As depicted in Fig. 2.2, during the uplink transmission stage, the coverage space of G is a hemisphere with radius R_G, the center of which is G.[3] As presented in Fig. 2.3, in the downlink delivery stage, the coverage space of S is a spherical cap with height $R_S + h$ (where $R_C = \sqrt{R_S^2 - h^2}$) and the radius of the base R_C (where $0 \leq h \leq R_S$). Moreover, it is easy to obtain the volumes of the coverage spaces of G and S as $V_G = \frac{2}{3}\pi R_G^3$ and $V_{S_1} = \frac{\pi}{3}\left(4R_S^3 - 3R_S h^2 + h^3\right)$, respectively.

The following two sections will present a secrecy outage analysis for the information delivery over uplink and downlink.

users and pretend to be legal users. Then, it can approach legitimate users with no doubts. Therefore, here, we do not consider the minimum distance between E and legitimate users for simplification.

[3] In practical, UAVs suffer their minimum flying heights ranging from meters or more, which depends on the designs and application purposes. Similar to the analysis on traditional wireless systems, to facilitate theoretical analysis, in Sect. 2.1 the minimum operating heights of the UAVs and the height of the transceiver antennas at G are ignored.

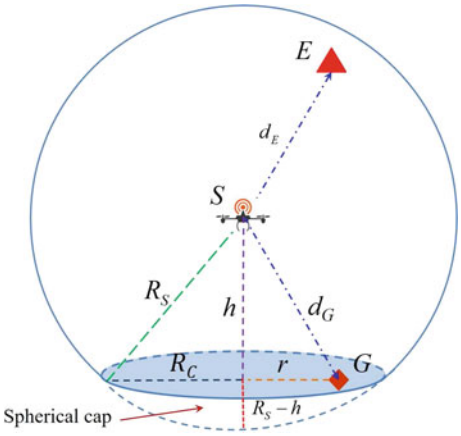

Fig. 2.3 Downlink model

2.1.2 Secrecy Outage Analysis for the Uplink

As depicted in Fig. 2.2, it is assumed that S is uniformly distributed in a straight-line segment AB, the length of which l $(0 < l \leq 2R_G)$ is determined by the juncture points of power-line and the coverage space of G. E is uniformly distributed in the hemisphere with radius R_G and center G.

2.1.2.1 Signal Model

The received signals at S and E can be respectively written as

$$y_S = \sqrt{P_G d_S^{-n}} h_{GS} s_G + z_S \tag{2.1}$$

and

$$y_E = \sqrt{P_G d_E^{-n}} h_{GE} s_G + z_E, \tag{2.2}$$

where P_G is the transmit power at G, s_G denotes the transmitted symbols from G, d_S is the distance between G and S, d_E is the distance between G and E, n is the path-loss exponent, z_S and z_E denote the independent complex Gaussian noise at S and E, respectively. In Sect. 2.1 to simplify the analysis, we assume that z_S and z_E are with zero means and the same variances, N_0.

Therefore, the received SNR at S and E can be further given as

$$\gamma_S = \frac{P_G |h_{GS}|^2}{d_S^n N_0} = \lambda_G \frac{|h_{GS}|^2}{d_S^n} \tag{2.3}$$

and

$$\gamma_E = \frac{P_G |h_{GE}|^2}{d_E^n N_0} = \lambda_G \frac{|h_{GE}|^2}{d_E^n}, \tag{2.4}$$

respectively, where $\lambda_G = \frac{P_G}{N_0}$.

As in Sect. 2.1 all links suffer independent Rayleigh fading, we can obtain the PDF of $\left|h_{jk}\right|^2$ $(j, k \in \{G, S, E\})$ as

$$f_{|h_{jk}|^2}(x) = \frac{1}{g_{jk}} \exp\left(-\frac{x}{g_{jk}}\right), \tag{2.5}$$

where g_{jk} is the mean value of the power gain, $\left|h_{jk}\right|^2$.

2.1.2.2 The Derivation of the CDF of γ_S

To facilitate the following analysis, we first give a useful Theorem (2.1.1) to characterize the statistical characteristics of d_S as follows:

Theorem 2.1.1 *As shown in Fig. 2.4, given an isosceles triangle $\triangle GAB$, in which $GA = GB = b$, $AB = l$, S is uniformly distributed over AB, C is the midpoint of AB, $AS = x$ $(0 \le x \le l)$ and $GS = y$ $(c = \sqrt{b^2 - \frac{l^2}{4}} \le y \le b)$. Thus, the PDF of y can be written as*

$$f_Y(y) = \begin{cases} \frac{4y}{l\sqrt{4y^2 + l^2 - 4b^2}}, & \text{if } \sqrt{b^2 - \frac{l^2}{4}} \le y \le b \\ 0, & \text{else} \end{cases}. \tag{2.6}$$

Proof Please refer to Appendix 1. □

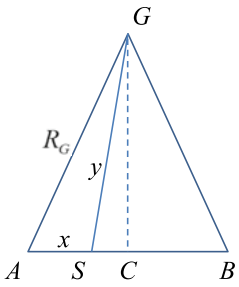

Fig. 2.4 An isosceles triangle

Corollary 2.1 *As shown in Fig. 2.2, S is uniformly distributed in AB and G is at the centra of the hemisphere. Then, the the PDF of the distance between S and G, d_S, can be given as*

$$f_{d_S}(x) = \begin{cases} \frac{4x}{l\sqrt{4x^2+l^2-4b^2}}, & \text{if } \sqrt{b^2-\frac{l^2}{4}} \le x \le b; \\ 0, & \text{else} \end{cases}. \tag{2.7}$$

Proof Equation (2.7) can be easily achieved by applying Theorem (2.1.1). □

Corollary 2.2 *Considering the randomness of the position of S, the PDF of d_S^n/λ_G can be presented as*

$$f_{\frac{d_S^n}{\lambda_G}}(x) = \begin{cases} \frac{2\lambda_G}{nl}\frac{(\lambda_G x)^{\frac{2}{n}-1}}{\sqrt{(\lambda_G x)^{\frac{2}{n}}-c}}, & \text{if } \frac{1}{\lambda_G}c^{\frac{n}{2}} < x < \frac{b^n}{\lambda_G}; \\ 0, & \text{else} \end{cases}. \tag{2.8}$$

Proof Using Corollary 2.1, the CDF of d_S can be given as

$$\begin{aligned} F_{d_S}(x) &= \int_0^x f_{d_S}(y)dy \\ &= \begin{cases} 0, & \text{if } x < \sqrt{c}; \\ \frac{2\sqrt{x^2-c}}{l}, & \text{elseif } \sqrt{c} < x < b; \\ 1, & \text{else} \end{cases}, \end{aligned} \tag{2.9}$$

where $c = b^2 - \frac{l^2}{4}$.

So, one can have the CDF of d_S^n/λ_G as

$$\begin{aligned} F_{\frac{d_S^n}{\lambda_G}}(x) &= \left\{\frac{d_S^n}{\lambda_G} \le x\right\} \\ &= \left\{d_S \le \sqrt[n]{\lambda_G x}\right\} \\ &= \begin{cases} 0, & \text{if } x < \frac{1}{\lambda_G}c^{\frac{n}{2}}; \\ \frac{2\sqrt{(x\lambda_G)^{\frac{2}{n}}-c}}{l}, & \text{elseif } \frac{1}{\lambda_G}c^{\frac{n}{2}} < x < \frac{b^n}{\lambda_G}; \\ 1, & \text{else} \end{cases}. \end{aligned} \tag{2.10}$$

Therefore, the PDF of d_S^n/λ_G can be obtained, as it is the derivation of Eq. (2.10). Then, the proof is completed. □

Observing Eq. (2.3), and using Eqs. (2.5) and (2.8), the CDF of γ_S can be calculated as

$$
\begin{aligned}
F_{\gamma_S}(\gamma) &= \Pr\left\{\lambda_G \frac{|h_{GS}|^2}{d_S^n} < \gamma\right\} \\
&= \Pr\left\{|h_{GS}|^2 < \frac{d_S^n}{\lambda_G}\gamma\right\} \\
&= \int_0^{\infty} F_{|h_{GS}|^2}(t\gamma)\, f_{\frac{d_S^n}{\lambda_G}}(t)\, dt \\
&= 1 - \frac{2\lambda_G}{nl} \int_{\frac{c^2}{\lambda_G}}^{\frac{b^n}{\lambda_G}} \exp\left(-\frac{t\gamma}{g_{GS}}\right) \frac{(\lambda_G t)^{\frac{2}{n}-1}}{\sqrt{(\lambda_G t)^{\frac{2}{n}} - c}} dt.
\end{aligned} \tag{2.11}
$$

For analytical tractability, in Sect. 2.1 we only consider cases that the path loss factor is $n = 2$, which is suitable for the case of infinite space and matches the open-air space scenarios considered in Sect. 2.1 as suggested in [1].

Then, we can further calculate the CDF of γ_S as

$$
\begin{aligned}
F_{\gamma_S}(\gamma) &= 1 - \frac{\lambda_G}{l} \int_{\frac{c}{\lambda_G}}^{\frac{b^2}{\lambda_G}} \exp\left(-\frac{t\gamma}{g_{GS}}\right) \frac{1}{\sqrt{\lambda_G t - c}} dt \\
&= 1 - \frac{\sqrt{\lambda_G}}{l} \int_{\frac{c}{\lambda_G}}^{\frac{b^2}{\lambda_G}} \exp\left(-\frac{t\gamma}{g_{GS}}\right) \frac{1}{\sqrt{t - \frac{c}{\lambda_G}}} dt \\
&= 1 - A_S \gamma^{-\frac{1}{2}} \exp(-B_S\gamma)\ \mathrm{erf}\left(C_S \gamma^{\frac{1}{2}}\right),
\end{aligned} \tag{2.12}
$$

where $A_S = \frac{2\sqrt{\pi g_{GS}\lambda_G}}{l}$, $B_S = \frac{c}{g_{GS}\lambda_G}$, and $C_S = \sqrt{\frac{b^2-c}{g_{GS}\lambda_G}}$.

2.1.2.3 The Derivation of the PDF of γ_E

Lemma 2.1 *As E is uniformly distributed in the coverage space of S, the PDF of d_E can be written as*

$$
f_{d_E}(x) = \begin{cases} \frac{3x^2}{R_G^3}, & \text{if } 0 \le x \le R_G; \\ 0, & \text{else} \end{cases}. \tag{2.13}
$$

Proof The PDF of the distance between E and S can be easily calculated as $f_D(x) = \frac{3}{2\pi R_G^3}$. Therefore, we can have the CDF of d_E as

$$F_{d_E}(x) = \int_0^x \int_0^{\pi/2} \int_0^{2\pi} \frac{3}{2\pi R_G^3} \sin\phi_i d_i^2 \mathrm{d}\theta_i \mathrm{d}\phi_i \mathrm{d}(d_i)$$

$$= \begin{cases} 0, & \text{if } x < R_G; \\ \frac{x^3}{R_G^3}, & \text{elseif } 0 \le x \le R_G; \\ 1, & \text{else} \end{cases}. \tag{2.14}$$

Thus, one can easily achieve the PDF of d_E as the derivative of Eq. (2.14). Then, the proof is completed. □

So, it is easy to have the CDF of d_E^n/λ_G as

$$\begin{aligned} F_{\frac{d_E^n}{\lambda_G}}(x) &= \left\{ \frac{d_E^n}{\lambda_G} \le x \right\} \\ &= \left\{ d_E \le \sqrt[n]{\lambda_G x} \right\} \\ &= \begin{cases} 0, & \text{if } x \le 0; \\ \frac{\lambda_G{}^{\frac{3}{n}} x^{\frac{3}{n}}}{R_G^3}, & \text{elseif } 0 < x \le \frac{R_G{}^n}{\lambda_G}; \\ 1, & \text{else} \end{cases}. \end{aligned} \tag{2.15}$$

Accordingly, the PDF of d_E^n/λ_G can be derived as

$$f_{\frac{d_E^n}{\lambda_G}}(x) = \begin{cases} \frac{3\lambda_G{}^{\frac{3}{n}} x^{\frac{3}{n}-1}}{nR_G^3}, & \text{if } 0 < x \le \frac{R_G{}^n}{\lambda_G}; \\ 0, & \text{else} \end{cases}. \tag{2.16}$$

Observing Eq. (2.4), and using [2, Eq. (3.351.1)] and Eqs. (2.5) and (2.16), the PDF of γ_E can be calculated as

$$\begin{aligned} f_{\gamma_E}(x) &= \int_0^\infty y f_{|h_{GE}|^2}(yx) f_{\frac{d_E^n}{\lambda_G}}(y)\, dy \\ &= \frac{3\lambda_G{}^{\frac{3}{n}}}{nR_G^3 g_{GE}} \int_0^{\frac{R_G{}^n}{\lambda_G}} y \exp\left(-\frac{yx}{g_{GE}}\right) y^{\frac{3}{n}-1} dy \\ &= \eta x^{-\frac{3}{n}-1} \Upsilon\left(1+\frac{3}{n}, \frac{R_G{}^n}{\lambda_G g_{GE}} x\right), \end{aligned} \tag{2.17}$$

where $\eta = \frac{3\lambda_G{}^{\frac{3}{n}} g_{GE}{}^{\frac{3}{n}}}{nR_G^3}$ and $\Upsilon(\alpha, x) = \int_0^x e^{-t} t^{\alpha-1} dt$ is the lower incomplete gamma function, as defined by [2, (8.350.1)].

2.1.2.4 The Calculation of SOP

Therefore, the instantaneous secrecy capacity of the uplink transmission can be presented as

$$C_{s,\text{up}}\left(\gamma_S, \gamma_E\right) = \max\left\{\log_2\left(1+\gamma_S\right) - \log_2\left(1+\gamma_E\right), 0\right\}. \tag{2.18}$$

In Sect. 2.1 SOP is defined as the probability that the secrecy capacity is less than an outage threshold R_s, which can be written as

$$\begin{aligned} P_{out,\text{up}} &= \Pr\left\{C_{s,\text{up}}\left(\gamma_S, \gamma_E\right) \le R_s\right\} \\ &= \Pr\left\{\log_2\left(1+\gamma_S\right) - \log_2\left(1+\gamma_E\right) \le R_s\right\} \\ &= \Pr\left\{\gamma_S \le \Theta\gamma_E + \Theta - 1\right\}, \end{aligned} \tag{2.19}$$

where $\Theta = 2^{R_s}$.

It must be noted that obtaining a closed-form result for Eq. (2.19) is almost impossible and/or too complex. Therefore in the subsequent section, the lower bound of the SOP is considered,[4] which has been utilized in many works [3, 4], as

$$\begin{aligned} P^{\text{L}}_{out,\text{up}} &= \Pr\left\{\gamma_S \leqslant \Theta\gamma_E\right\} \\ &= \int_0^\infty F_{\gamma_S}\left(\Theta\gamma_E\right) f_{\gamma_E}\left(\gamma_E\right) d\gamma_E. \end{aligned} \tag{2.20}$$

Then, using Eqs. (2.12) and (2.17), $\Upsilon\left(a,z\right) = G^{1,1}_{1,2}\left[z\left|{}^{1}_{a,0}\right.\right]$, $\text{erf}\left(x\right) = \pi^{-0.5}G^{1,1}_{1,2}\left[x^2\left|{}^{1}_{0.5,0}\right.\right]$, $\exp\left(-x\right) = G^{1,0}_{0,1}\left[x\left|{}^{-}_{0}\right.\right]$, and utilizing the integral equation presented in [5, (20)], we can calculate SOP as

$$\begin{aligned} P^{\text{L}}_{out,\text{up}} &= \int_0^\infty F_{\gamma_S}\left(\Theta x\right) f_{\gamma_E}\left(x\right) dx \\ &= 1 - \frac{A_S\eta}{\sqrt{\Theta}}\int_0^\infty x^{-3}\exp\left(-B_S\Theta x\right)\text{erf}\left(C_S\sqrt{\Theta}x^{\frac{1}{2}}\right)\Upsilon\left(\frac{5}{2}, \frac{R_G^2}{\lambda_G g_{GE}}x\right) dx \\ &= 1 - \frac{A_S\eta}{\sqrt{\Theta\pi}}\int_0^\infty x^{-3}G^{1,0}_{0,1}\left[B_S\Theta x\left|{}^{-}_{0}\right.\right]G^{1,1}_{1,2}\left[C_S^2\Theta x\left|{}^{1}_{0.5,0}\right.\right] \\ &\quad \times G^{1,1}_{1,2}\left[\frac{R_G^2}{\lambda_G g_{GE}}x\left|{}^{1}_{2.5,0}\right.\right] dx \\ &= 1 - \frac{A_S\eta\left(C_S^2\Theta\right)^3}{\sqrt{\Theta\pi}}\int_0^\infty G^{1,0}_{0,1}\left[B_S\Theta x\left|{}^{-}_{0}\right.\right]G^{1,1}_{1,2}\left[C_S^2\Theta x\left|{}^{-2}_{-2.5,-3}\right.\right] \end{aligned}$$

[4] In Sect. 2.1 the lower bound of SOP is considered by exploiting the fact that, compared with $\Theta\gamma_E + \Theta - 1$, a lower outage threshold, $\Theta\gamma_E$, represents a more rigorous outage request for γ_S and is more useful from the engineering perspective.

$$\times G_{1,2}^{1,1}\left[\frac{R_G^2}{\lambda_G g_{GE}}x\,\middle|\,\begin{matrix}1\\2.5,0\end{matrix}\right]dx$$
$$=1-\frac{A_S\eta C_S^6\Theta^2}{B_S\sqrt{\Theta\pi}}G_{0,1:1,2:1,2}^{1,0:1,1:1,1}\left(\begin{matrix}1\\-\end{matrix}\middle|\begin{matrix}-2\\-2.5,-3\end{matrix}\middle|\begin{matrix}1\\2.5,0\end{matrix}\middle|\frac{C_S^2}{B_S},\frac{R_G^2}{B_S\Theta\lambda_G g_{GE}}\right), \quad (2.21)$$

where $G_{p,q}^{m,n}\left[x\,\middle|\,\begin{matrix}a_1,\ldots,a_p\\b_1,\ldots,b_q\end{matrix}\right]=\frac{1}{2\pi i}\int\frac{\prod_{j=1}^{m}\Gamma(b_j-s)\prod_{j=1}^{n}\Gamma(1-a_j+s)}{\prod_{j=m+1}^{q}\Gamma(1-b_j+s)\prod_{j=n+1}^{p}\Gamma(a_j-s)}x^s ds$ is the Meijer's G-function, as defined by [2, Eq. (9.301)], and $G_{p_1,q_1:p_2,q_2:p_3,q_3}^{m_1,n_1:m_2,n_2:m_3,n_3}[\cdot]$ is the EGBMGF function, which can be easily realized see Table 1 in [6].

2.1.3 Secrecy Outage Analysis for Downlink

As shown in Fig. 2.3, it is assumed that G is uniformly distributed in the base of the cap with height (R_S+h), which is a circle with radius $R_C=\sqrt{R_S^2-h^2}$. In the following, we name the spherical cap shown in Fig. 2.3 as S_1 and its volume as $V_{S_1}=\frac{\pi}{3}\left(4R_S^3-3R_S h^2+h^3\right)$.

Therefore, similar to the last section, we can obtain the SOP for the downlink transmission as

$$P_{out,\mathrm{dn}}^{\mathrm{L}}=\int_0^{\infty}F_{\gamma_G}(\Theta x)\,f_{\gamma_E}(x)\,dx, \quad (2.22)$$

where $\gamma_G=\frac{P_S|h_{SG}|^2}{d_G^n N_0}=\lambda_S\frac{|h_{SG}|^2}{d_G^n}$ is the received SNR at G, P_S is the transmit power at S, $\lambda_S=\frac{P_S}{N_0}$, $\gamma_E=\frac{P_S|h_{SE}|^2}{d_E^n N_0}=\lambda_S\frac{|h_{SE}|^2}{d_E^n}$ is the received SNR at E.

As depicted in Fig. 2.3 and considering the randomness of the positions of G and E, one can have

$$\begin{aligned}P_{out,\mathrm{dn}}^{\mathrm{L}}&=\int_{V_{S_1}}\Pr\{\gamma_G\le\Theta\gamma_E\}dV_{S_1}\\&=\int_{V_{Sp}}\Pr\{\gamma_G\le\Theta\gamma_E\}dV_{S_1}-\frac{V_{S_2}}{V_{S_p}}\int_{V_{S_2}}\Pr\{\gamma_G\le\Theta\gamma_E\}dV_{S_2}\\&=I_{Sp}-\frac{h^2(3R_S-h)}{4{R_S}^3}I_{S_2},\end{aligned} \quad (2.23)$$

where $I_{Sp}=\int_{V_{Sp}}\Pr\{\gamma_G\le\Theta\gamma_E\}dV_{S_1}$, $I_{S_2}=\int_{V_{S_2}}\Pr\{\gamma_G\le\Theta\gamma_E\}dV_{S_2}$, S_p is the sphere with radius R_S and volume as $V_{Sp}=\frac{4}{3}\pi{R_S}^3$, the spherical cap (S_2) with the height (R_S-h) and volume $V_{S_2}=\pi h^2\left(R_S-\frac{h}{3}\right)$.

In the following, we will calculate I_{Sp} and I_{S_2}, respectively.

2.1.3.1 The Derivation of I_{Sp}

Lemma 2.2 *When E is uniformly distributed in the ball with the centra, S, the PDF of d_E^n/λ_S can presented as*

$$f_{\frac{d_E^n}{\lambda_S}}(x) = \begin{cases} \frac{3\lambda_S{}^{\frac{3}{n}}}{nR_S^3} x^{\frac{3}{n}-1}, & \text{if } 0 \le x \le \frac{R_S{}^n}{\lambda_S}; \\ 0, & \text{else} \end{cases}. \tag{2.24}$$

Proof As suggested in [7], when E is randomly distributed in S_p,the CDF of d_E can be given as

$$\begin{aligned} F_{d_E}(x) &= \int_0^x \int_0^\pi \int_0^{2\pi} \frac{3}{4\pi {R_S}^3} d_E^2 \sin\phi_E d\theta_E d\phi_E d(d_E) \\ &= \begin{cases} 0, & \text{if } x < 0; \\ \frac{x^3}{R_S^3}, & \text{elseif } 0 \le x \le R_S; \\ 1, & \text{else} \end{cases}. \end{aligned} \tag{2.25}$$

So, one can have the CDF of d_E^n/λ_S as

$$\begin{aligned} F_{\frac{d_E^n}{\lambda_S}}(x) &= \left\{ \frac{d_E^n}{\lambda_S} \le x \right\} \\ &= \left\{ d_E \le \sqrt[n]{\lambda_S x} \right\} \\ &= \begin{cases} 0, & \text{if } x < 0; \\ \frac{\lambda_S{}^{\frac{3}{n}}}{R_S^3} x^{\frac{3}{n}}, & \text{elseif } 0 \le x \le \frac{R_S{}^n}{\lambda_S}; \\ 1, & \text{else} \end{cases}. \end{aligned} \tag{2.26}$$

Thus, one can easily obtain the PDF of d_E^n/λ_S as it is the derivative of Eq. (2.24). Then, the proof is completed. □

Observing Eq. (2.4), and using Eqs. (2.5) and (2.24), the PDF of γ_E can be calculated as

$$\begin{aligned} f_{\gamma_E}(x) &= \int_0^\infty y f_{|h_{SE}|^2}(yx) f_{\frac{d_E^n}{\lambda_S}}(y) dy \\ &= \frac{3\lambda_S{}^{\frac{3}{n}}}{nR_S^3 g_{SE}} \int_0^{\frac{R_S{}^n}{\lambda_S}} y^{\frac{3}{n}} \exp\left(-\frac{yx}{g_{SE}}\right) dy \end{aligned}$$

$$= \frac{3(\lambda_S g_{SE})^{\frac{3}{n}}}{nR_S^3} x^{-\frac{3}{n}-1} \gamma\left(1+\frac{3}{n}, \frac{{R_S}^n}{\lambda_G g_{SE}} x\right)$$
$$= B_E x^{-\frac{3}{n}-1} G_{1,2}^{1,1}\left[C_E x \left|{}^{1}_{1+\frac{3}{n},0}\right.\right], \tag{2.27}$$

where $B_E = \frac{3(\lambda_S g_{SE})^{\frac{3}{n}}}{nR_S^3}$ and $C_E = \frac{{R_S}^n}{\lambda_S g_{SE}}$.

Lemma 2.3 *When G is uniformly distributed in the circle with radius R_C, the PDF of d_G^n/λ_S can presented as*

$$f_{\frac{d_G^n}{\lambda_S}}(x) = \begin{cases} \frac{2\lambda_S^{\frac{2}{n}}}{nR_C^2} x^{\frac{2}{n}-1}, & \text{if } \frac{h^n}{\lambda_S} \le x \le \frac{\left({R_C}^2+h^2\right)^{\frac{n}{2}}}{\lambda_S}; \\ 0, & \text{else} \end{cases}. \tag{2.28}$$

Proof When G is uniformly distributed in the circle with radius R_C, as shown in [8], one can have the PDF of r as

$$f_r(x) = \frac{2x}{R_C^2}. \tag{2.29}$$

As $d_G^2 = h^2 + r^2$ and using Eq. (2.29), the CDF of $d_G = \sqrt{h^2+r^2}$ can be presented as

$$F_{d_G}(x) = \frac{x^2}{R_C^2} - \frac{h^2}{R_C^2}, \quad h \le x \le \sqrt{{R_C}^2 + h^2} = R_G. \tag{2.30}$$

Therefore, one can have the CDF of d_G^n/λ_S as

$$\begin{aligned} F_{\frac{d_G^n}{\lambda_S}}(x) &= \left\{\frac{d_G^n}{\lambda_S} \le x\right\} \\ &= \left\{d_G \le \sqrt[n]{\lambda_S x}\right\} \\ &= \begin{cases} 0, & \text{if } x \le \frac{h^n}{\lambda_S}; \\ \frac{\lambda_S^{\frac{2}{n}}}{R_C^2} x^{\frac{2}{n}} - \frac{h^2}{R_C^2}, & \text{elseif } \frac{h^n}{\lambda_S} \le x \le \frac{\left({R_C}^2+h^2\right)^{\frac{n}{2}}}{\lambda_S}; \\ 1 & \text{else} \end{cases}. \end{aligned} \tag{2.31}$$

So, the PDF of d_G^n/λ_S can be obtained as it is the derivative of Eq. (2.31). Then, the proof is completed. □

So, using [2, Eq. (3.351.1)], and Eqs. (2.5) and (2.28), the PDF of γ_G can be calculated as

$$
\begin{aligned}
f_{\gamma_G}(x) &= \int_0^{\infty} y f_{|h_{SG}|^2}(yx) f_{\frac{d_G^n}{\lambda_S}}(y)\, dy \\
&= \frac{1}{g_{SG}} \int_{\frac{h^n}{\lambda_S}}^{\frac{\left(R_C{}^2+h^2\right)^{\frac{n}{2}}}{\lambda_S}} y \exp\left(-\frac{yx}{g_{SG}}\right) \frac{2\lambda_S{}^{\frac{2}{n}}}{nR_C^2} y^{\frac{2}{n}-1} dy \\
&= \frac{2\lambda_S{}^{\frac{2}{n}}}{nR_C^2 g_{SG}} \int_0^{\frac{\left(R_C{}^2+h^2\right)^{\frac{n}{2}}}{\lambda_S}} y^{\frac{2}{n}} \exp\left(-\frac{yx}{g_{SG}}\right) dy - \frac{2\lambda_S{}^{\frac{2}{n}}}{nR_C^2 g_{SG}} \int_0^{\frac{h^n}{\lambda_S}} y^{\frac{2}{n}} \exp\left(-\frac{yx}{g_{SG}}\right) dy \\
&= C_G x^{-\frac{2}{n}-1} \gamma\left(\frac{2}{n}+1, \frac{\left(R_C{}^2+h^2\right)^{\frac{n}{2}}}{\lambda_S g_{SG}} x\right) - C_G x^{-\frac{2}{n}-1} \gamma\left(\frac{2}{n}+1, \frac{h^n}{\lambda_S g_{SG}} x\right) \\
&= C_G x^{-\frac{2}{n}-1} G_{1,2}^{1,1}\left(\frac{\left(R_C{}^2+h^2\right)^{\frac{n}{2}}}{\lambda_S g_{SG}} x \,\middle|\, \begin{matrix} 1 \\ 1+\frac{2}{n}, 0 \end{matrix}\right) \\
&\quad - C_G x^{-\frac{2}{n}-1} G_{1,2}^{1,1}\left(\frac{h^n}{\lambda_S g_{SG}} x \,\middle|\, \begin{matrix} 1 \\ 1+\frac{2}{n}, 0 \end{matrix}\right),
\end{aligned} \tag{2.32}
$$

where $C_G = \frac{2(\lambda_S g_{SG})^{\frac{2}{n}}}{nR_C^2}$.

Accordingly, the CDF of γ_G can be easily obtained as

$$
\begin{aligned}
F_{\gamma_G}(x) &= \int_0^x f_{\gamma_G}(y) dy \\
&= C_G \int_0^x y^{-\frac{2}{n}-1} G_{1,2}^{1,1}\left(\frac{\left(R_C{}^2+h^2\right)^{\frac{n}{2}}}{\lambda_S g_{SG}} y \,\middle|\, \begin{matrix} 1 \\ 1+\frac{2}{n}, 0 \end{matrix}\right) dy \\
&\quad - C_G \int_0^x y^{-\frac{2}{n}-1} G_{1,2}^{1,1}\left(\frac{h^n}{\lambda_S g_{SG}} y \,\middle|\, \begin{matrix} 1 \\ 1+\frac{2}{n}, 0 \end{matrix}\right) dy \\
&= C_G x^{-\frac{2}{n}} G_{2,3}^{1,2}\left(\frac{\left(R_C{}^2+h^2\right)^{\frac{n}{2}}}{\lambda_S g_{SG}} x \,\middle|\, \begin{matrix} 1+\frac{2}{n}, 1 \\ 1+\frac{2}{n}, 0, \frac{2}{n} \end{matrix}\right) \\
&\quad - C_G x^{-\frac{2}{n}} G_{2,3}^{1,2}\left(\frac{h^n}{\lambda_S g_{SG}} x \,\middle|\, \begin{matrix} 1+\frac{2}{n}, 1 \\ 1+\frac{2}{n}, 0, \frac{2}{n} \end{matrix}\right) \\
&= C_G x^{-\frac{2}{n}} G_{2,3}^{1,2}\left[A_G x \,\middle|\, \begin{matrix} 1+\frac{2}{n}, 1 \\ 1+\frac{2}{n}, 0, \frac{2}{n} \end{matrix}\right] - C_G x^{-\frac{2}{n}} G_{2,3}^{1,2}\left[B_G x \,\middle|\, \begin{matrix} 1+\frac{2}{n}, 1 \\ 1+\frac{2}{n}, 0, \frac{2}{n} \end{matrix}\right],
\end{aligned} \tag{2.33}
$$

where $A_G = \frac{\left(R_C^2+h^2\right)^{\frac{n}{2}}}{\lambda_S g_{SG}}$ and $B_G = \frac{h^n}{\lambda_S g_{SG}}$.

Therefore, utilizing Eqs. (2.27) and (2.33), $I_{Sp} = \int\limits_{V_{Sp}} \Pr\{\gamma_G \le \gamma_E\} dV_{S_1}$ can be further derived as

$$\begin{aligned}
I_{SP} &= \int\limits_{V_{Sp}} \Pr\{\gamma_G \le \Theta\gamma_E\} dV_{S_1} \\
&= \int\limits_0^\infty F_{\gamma_G}(\Theta x) f_{\gamma_E}(x)\, dx \\
&= C_G \Theta^{-\frac{2}{n}} \int\limits_0^\infty x^{-\frac{2}{n}} G_{2,3}^{1,2}\left[A_G \Theta x \left| \begin{matrix} 1+\frac{2}{n}, 1 \\ 1+\frac{2}{n}, 0, \frac{2}{n} \end{matrix} \right. \right] f_{\gamma_E}(x)\, dx \\
&\quad - C_G \int\limits_0^\infty x^{-\frac{2}{n}} G_{2,3}^{1,2}\left[B_G \Theta x \left| \begin{matrix} 1+\frac{2}{n}, 1 \\ 1+\frac{2}{n}, 0, \frac{2}{n} \end{matrix} \right. \right] f_{\gamma_E}(x)\, dx \\
&= C_G B_E \Theta^{\frac{3}{n}} A_G{}^{\frac{5}{n}} G_{4,4}^{3,2}\left[\frac{C_E}{A_G \Theta} \left| \begin{matrix} 1, \frac{3}{n}, 1+\frac{5}{n}, 1+\frac{3}{n} \\ 1+\frac{3}{n}, \frac{3}{n}, \frac{5}{n}, 0 \end{matrix} \right. \right] \\
&\quad - C_G B_E \Theta^{\frac{3}{n}} B_G{}^{\frac{5}{n}} G_{4,4}^{3,2}\left[\frac{C_E}{B_G \Theta} \left| \begin{matrix} 1, \frac{3}{n}, 1+\frac{5}{n}, 1+\frac{3}{n} \\ 1+\frac{3}{n}, \frac{3}{n}, \frac{5}{n}, 0 \end{matrix} \right. \right]
\end{aligned} \tag{2.34}$$

2.1.3.2 The Derivation of I_{S_2}

Lemma 2.4 *As shown in Fig. 4.17, when E is uniformly distributed in the spherical cap with height $(R_S - h)$, the PDF of d_E^n/λ_S can presented as*

$$f_{\frac{d_E^n}{\lambda_S}}(x) = \begin{cases} \frac{2\pi}{nV_S}\left({\lambda_S}^{\frac{3}{n}} x^{\frac{3}{n}-1} - h{\lambda_S}^{\frac{2}{n}} x^{\frac{2}{n}-1} \right), & \text{if } \frac{h^n}{\lambda_S} \le x \le \frac{R_G^n}{\lambda_S}; \\ 0, & \text{else} \end{cases}. \tag{2.35}$$

Proof When E is randomly distributed in S_2, the CDF of d_E can be given as

$$\begin{aligned}
F_{d_E}(x) &= \frac{1}{V_S} \int_0^{\arccos\left(\frac{h}{x}\right)} \int_{\frac{h}{\cos(\phi)}}^{x} \int_0^{2\pi} \delta^2 \sin(\phi)\, d\theta d\delta d\phi \\
&= \frac{2\pi}{V_S} \int_0^{\arccos\left(\frac{h}{x}\right)} \int_{\frac{h}{\cos(\phi)}}^{x} \delta^2 \sin(\phi)\, d\delta d\phi \\
&= \frac{2\pi}{3V_S} \int_0^{\arccos\left(\frac{h}{x}\right)} \left[x^3 - h^3 \sec^3(\phi) \right] \sin(\phi)\, d\phi \\
&= \frac{\pi}{3V_S}\left(2x^3 - 3hx^2 + h^3 \right).
\end{aligned} \tag{2.36}$$

So, the CDF of d_E^n/λ_S can be obtained as

$$\begin{aligned} F_{\frac{d_E^n}{\lambda_S}}(x) &= \Pr\left\{\frac{d_E^n}{\lambda_S} < x\right\} \\ &= \Pr\left\{d_E < (\lambda_S x)^{\frac{1}{n}}\right\} \\ &= \frac{\pi}{3V_S}\left[2\left((\lambda_S x)^{\frac{1}{n}}\right)^3 - 3h\left((\lambda_S x)^{\frac{1}{n}}\right)^2 + h^3\right] \\ &= \frac{\pi}{3V_S}\left(2\lambda_S{}^{\frac{3}{n}}x^{\frac{3}{n}} - 3h\lambda_S{}^{\frac{2}{n}}x^{\frac{2}{n}} + h^3\right). \end{aligned} \tag{2.37}$$

Thus, the PDF of d_E^n/λ_S can be derived via performing differential operation on Eq. (2.37).

Then, the proof is completed. □

Observing Eq. (2.4), and using [2, Eq. (3.351.1)], Eqs. (2.5) and (2.35), the PDF of γ_E can be calculated as

$$\begin{aligned} f_{\gamma_E}(x) &= \int_0^\infty y f_{|h_{SE}|^2}(yx) f_{\frac{d_E^n}{\lambda_S}}(y)\, dy \\ &= \frac{2\pi}{nV_S g_{SG}} \int_{\frac{h^n}{\lambda_S}}^{\frac{R_S^n}{\lambda_S}} y \exp\left(-\frac{yx}{g_{SG}}\right)\left(\left(\lambda_S{}^{\frac{3}{n}} y^{\frac{3}{n}-1} - h\lambda_S{}^{\frac{2}{n}} y^{\frac{2}{n}-1}\right)\right) dy \\ &= \frac{2\pi\lambda_S{}^{\frac{3}{n}}}{nV_S g_{SG}} \int_{\frac{h^n}{\lambda_S}}^{\frac{R_S^n}{\lambda_S}} y^{\frac{3}{n}} \exp\left(-\frac{yx}{g_{SG}}\right) dy - \frac{2\pi h\lambda_S{}^{\frac{2}{n}}}{nV_S g_{SG}} \int_{\frac{h^n}{\lambda_S}}^{\frac{R_S^n}{\lambda_S}} y^{\frac{2}{n}} \exp\left(-\frac{yx}{g_{SG}}\right) dy \\ &= E_1 \int_{\frac{h^n}{\lambda_S}}^{\frac{R_G^n}{\lambda_S}} y^{\frac{3}{n}} \exp\left(-\frac{yx}{g_{SE}}\right) dy - E_2 \int_{\frac{h^n}{\lambda_S}}^{\frac{R_G^n}{\lambda_S}} y^{\frac{2}{n}} \exp\left(-\frac{yx}{g_{SE}}\right) dy \\ &= E_1 g_{SE}{}^{\frac{3}{n}+1} f_1\left(\frac{3}{n}\right) - E_2 g_{SE}{}^{\frac{2}{n}+1} f_1\left(\frac{2}{n}\right), \end{aligned} \tag{2.38}$$

where $E_1 = \frac{2\pi\lambda_S{}^{\frac{3}{n}}}{nV_S g_{SG}}$, $E_2 = \frac{2\pi h\lambda_S{}^{\frac{2}{n}}}{nV_S g_{SG}}$, and $f_1(a) = \int_{\frac{h^n}{\lambda_S}}^{\frac{R_S^n}{\lambda_S}} y^a \exp\left(-\frac{yx}{g_{SG}}\right) dy$.

Therefore, using Eqs. (2.33) and (2.38), and the integral equation of Meijer's G-function presented in [9], $I_{S_2} = \int_{V_{S_2}} \Pr\{\gamma_G \le \gamma_E\} dV_{S_2}$ can be further derived as

$$
\begin{aligned}
I_{S_2} &= \int_0^{\infty} F_{\gamma_G}(\Theta x) f_{\gamma_E}(x)\, dx \\
&= C_G \Theta^{-\frac{2}{n}} \int_0^{\infty} x^{-\frac{2}{n}} G_{2,3}^{1,2}\left[A_G \Theta x \left| {1+\frac{2}{n}, 1 \atop 1+\frac{2}{n}, 0, \frac{2}{n}} \right. \right] f_{\gamma_E}(x)\, dx \\
&- C_G \Theta^{-\frac{2}{n}} \int_0^{\infty} x^{-\frac{2}{n}} G_{2,3}^{1,2}\left[B_G \Theta x \left| {1+\frac{2}{n}, 1 \atop 1+\frac{2}{n}, 0, \frac{2}{n}} \right. \right] f_{\gamma_E}(x)\, dx \\
&= C_G \Theta^{-\frac{2}{n}} \left[f_2(A_G) - f_2(B_G) \right], \qquad (2.39)
\end{aligned}
$$

where

$$
\begin{aligned}
f_2(t) &= \int_0^{\infty} x^{-\frac{2}{n}} G_{2,3}^{1,2}\left[t\Theta x \left| {1+\frac{2}{n}, 1 \atop 1+\frac{2}{n}, 0, \frac{2}{n}} \right. \right] f_{\gamma_E}(x)\, dx \\
&= E_1 g_{SG}{}^{\frac{3}{n}+1} \int_0^{\infty} f_1\left(\frac{3}{n}\right) x^{-\frac{2}{n}} G_{2,3}^{1,2}\left[t\Theta x \left| {1+\frac{2}{n}, 1 \atop 1+\frac{2}{n}, 0, \frac{2}{n}} \right. \right] dx \\
&- E_2 g_{SG}{}^{\frac{2}{n}+1} \int_0^{\infty} f_1\left(\frac{2}{n}\right) x^{-\frac{2}{n}} G_{2,3}^{1,2}\left[t\Theta x \left| {1+\frac{2}{n}, 1 \atop 1+\frac{2}{n}, 0, \frac{2}{n}} \right. \right] dx \\
&= E_1 g_{SG}{}^{\frac{3}{n}+1} \left[f_3\left(\frac{3}{n}, t, C_E\right) - f_3\left(\frac{3}{n}, t, D_E\right) \right] \\
&- E_2 g_{SG}{}^{\frac{2}{n}+1} \left[f_3\left(\frac{2}{n}, t, C_E\right) - f_3\left(\frac{2}{n}, t, D_E\right) \right] \qquad (2.40)
\end{aligned}
$$

and

$$
\begin{aligned}
f_3(s, t, b) &= \int_0^{\infty} x^{-s-1-\frac{2}{n}} G_{1,2}^{1,1}\left[bx \left| {1 \atop s+1, 0} \right. \right] G_{2,3}^{1,2}\left[t\Theta x \left| {1+\frac{2}{n}, 1 \atop 1+\frac{2}{n}, 0, \frac{2}{n}} \right. \right] dx \\
&= b^{s+\frac{2}{n}} G_{4,4}^{2,3}\left[\frac{t\Theta}{b} \left| {1+\frac{2}{n}, 1, \frac{2}{n}, 1+s+\frac{2}{n} \atop 1+\frac{2}{n}, s+\frac{2}{n}, 0, \frac{2}{n}} \right. \right]. \qquad (2.41)
\end{aligned}
$$

Finally, the SOP over the downlink, $P_{out,\mathrm{dn}}$, can be obtained by inserting Eqs. (2.34) and (2.39) into Eq. (2.23).

2.1.4 Numerical Results

In this section, Monte Carlo simulations are carried out to validate our proposed analytical expressions for the SOP over both downlink and uplink. The main adopted parameters are set as $R_S = 20$ m, $h = 10$ m, $R_G = 15$ m, $R_s = 0.1$ bits/s/Hz, $\lambda_S = 5$ dB, $\lambda_G = 1.25$ dB and $g_{GE} = g_{SE} = 1.1$. Moreover, the coverage distance of the source UAV is set from tens of meters to hundreds of meters to reflect the practical scenarios of UAVs in civil applications. During each case, we run 10^5 trials for the Monte Carlo simulations and also consider 10^5 times the realizations of the

considered systems. Furthermore, all following numerical results are given while the mean value of the power gain over the link between S and G (g_{GS} or g_{SG}) increasing, to show the system performance that can be achieved in each potential channel situations.

2.1.4.1 Secrecy Outage Over the Uplink

In this subsection, we will investigate the secrecy outage performance over the uplink of the considered system shown in Fig. 2.2.

In Fig. 2.5, numerical results are presented to address the influence of g_{GE} on the secrecy outage performance of the considered system. We can see that the mean value of the power gain over $G - E$ link (g_{GE}) shows a negative effect on the secrecy outage, as a large g_{GE} leads to degraded secrecy outage performance. Because a large g_{GE} represents a high channel gain for the eavesdropping link from G to E.

The effect of λ_G (the transmit SNR at G) on the secrecy outage performance of the considered system is studied in Fig. 2.6. λ_G does not exhibit a significant influence on the secrecy outage performance, while a large λ_G incurs improved secrecy outage performance. Moreover, as presented in Fig. 2.6, the lines for the lower boundary of the SOP with $\lambda_G = 0$ and 5 dB are almost overlapping. Then, we can conclude that increasing λ_G is not an effective way to improve the secrecy outage performance of the considered system. Because the changing of λ_G will show the same trend and scale on the received SNR at S and E, which can be proved by Eqs. (2.3) and (2.4).

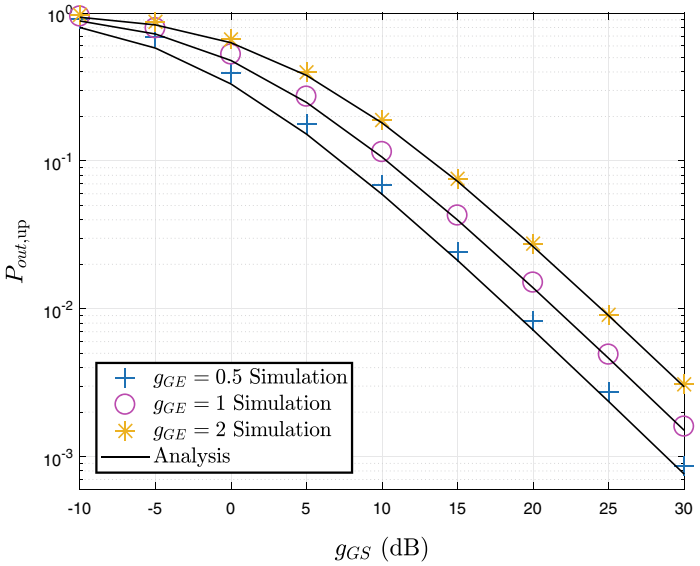

Fig. 2.5 Secrecy outage versus g_{GS} for various g_{GE}

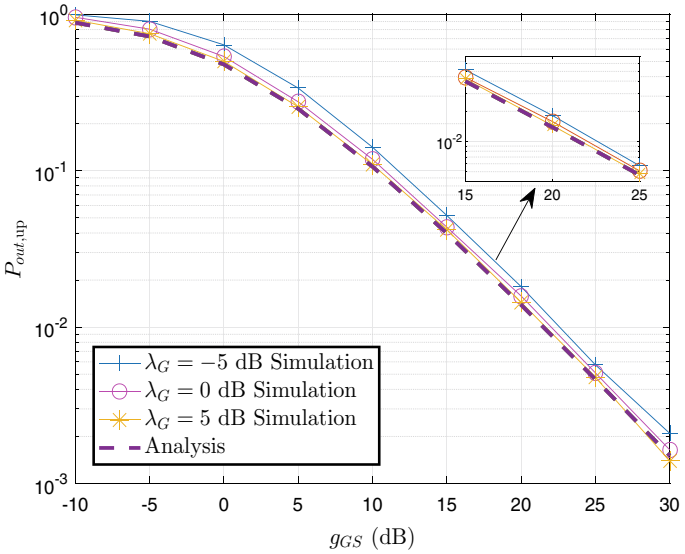

Fig. 2.6 Secrecy outage versus g_{GS} for various λ_S

Figure 2.7 presents the secrecy outage performance of the considered system. In contrast, the radius of the coverage space of G, $R_G = 1000$, 2000 and 3000 m.[5] One can easily observe that the $P_{out,\mathrm{up}}$ with various R_G is similar. Moreover, we can also find that R_G (the radius of the coverage space of the ground receiver, G) negatively affects the secrecy outage performance, which is more apparent when R_G is small. This comes from the fact that a large R_G leads to a large coverage space of G, and then the probability that the distance d_{GE} gets large increases, resulting in bad channel quality of the eavesdropping link.

In Fig. 2.8, the secrecy outage performance of the considered system with various outage thresholds (R_s) is studied. A large R_s shows a large $P_{out,\mathrm{up}}$, which means the secrecy outage performance of the considered system gets worse. This is because a large R_s represents a large outage threshold.

Furthermore, it can be seen from Figs. 2.5, 2.6, 2.7 and 2.8 that increasing g_{GS} can improve the secrecy outage performance of the considered system. Because a large g_{GS} represents a high channel gain for the main link from G to S. Also, simulation and analysis results match very well with each other, which verifies the correctness of our proposed analytical model.

[5] In Sect. 2.1 he effects of the radius of the coverage space of S and G on the secrecy outage performance are considered. Because the radius of the coverage space of a transmitter not only depends on the transmit power at the transmitter but also is determined by the sensitivity of the receiver.

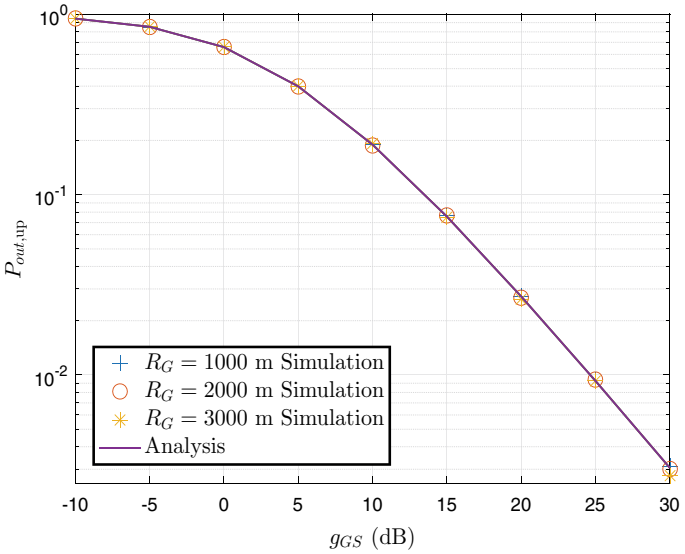

Fig. 2.7 Secrecy outage versus g_{GS} for various R_G

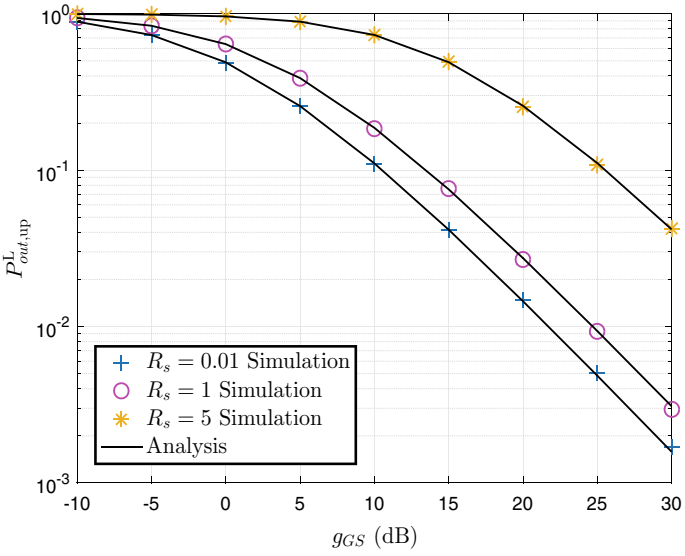

Fig. 2.8 Secrecy outage versus g_{GS} for various R_s

2.1.4.2 Secrecy Outage Over the Downlink

In this subsection, the secrecy outage performance over the uplink of the considered system (shown in Fig. 2.3) will be studied.

Figure 2.9 depicts the numerical results of the secrecy outage performance with various mean values of the power gain over $S - E$ link, g_{SE}, while g_{SG} increasing. One can observe that the secrecy outage performance with a small g_{SE} outperforms that with a large g_{SE}, as a large g_{SE} means better channel gain for the eavesdropping link, which leads to more information being overheard.

In Fig. 2.10, we investigate how the secrecy outage performance is influenced by λ_S (the transmit SNR at S). The secrecy outage lines for different λ_S (namely, -5, 0, and 5 dB) overlap, indicating that adjusting λ_S cannot improve the secrecy outage performance of the considered system. This observation is similar to the one obtained for the uplink from Fig. 2.6. Also, it can be explained that increasing λ_S will improve the received SNR at both G and E, and then the secrecy outage performance of the considered system cannot be improved anymore.

The impact of R_S (the radius of the coverage space of S) on the secrecy outage performance of the considered system is shown in Fig. 2.11, while g_{SG} is increasing. It is shown that the curves of $P_{out,\mathrm{dn}}$ for $R_S = 1000, 2000$ and 3000 m fully overlap with each other, which reveals that R_S does not influence the secrecy outage performance of the considered system, because adjusting R_s exhibits a same influence on the transmission distances of $S - E$ and $S - G$ links. This finding is similar to the one achieved from Fig. 2.7, both of which demonstrate that enlarging the coverage space of the transmitter cannot improve the secrecy outage performance.

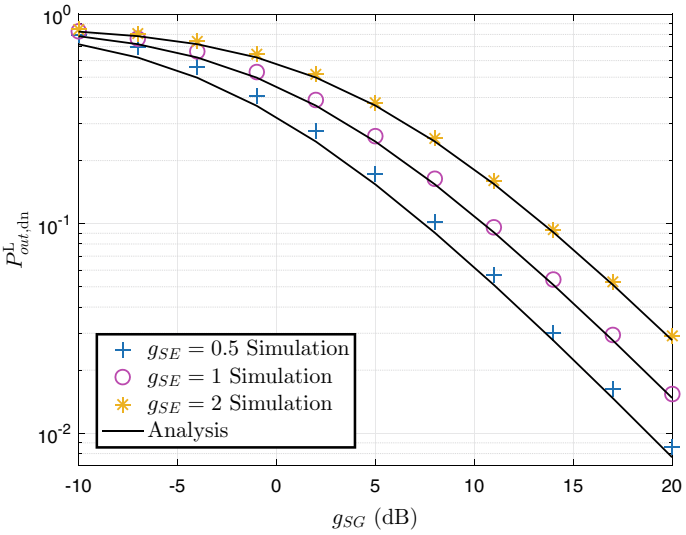

Fig. 2.9 Secrecy outage versus g_{SG} for various g_{GE}

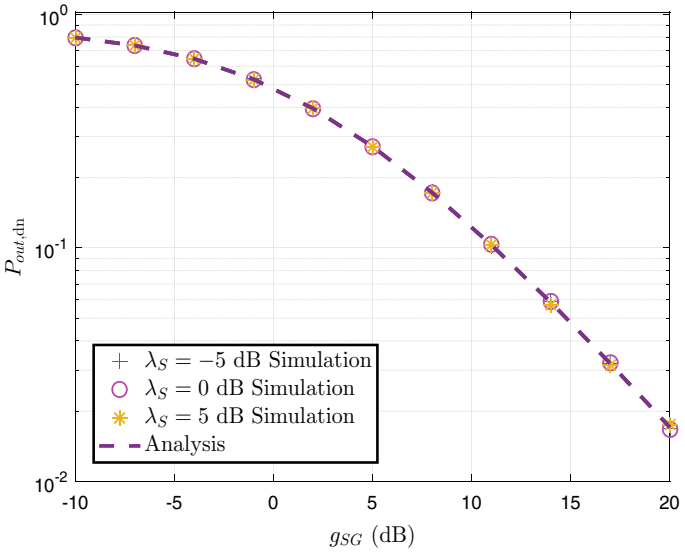

Fig. 2.10 Secrecy outage versus g_{SG} for various λ_S

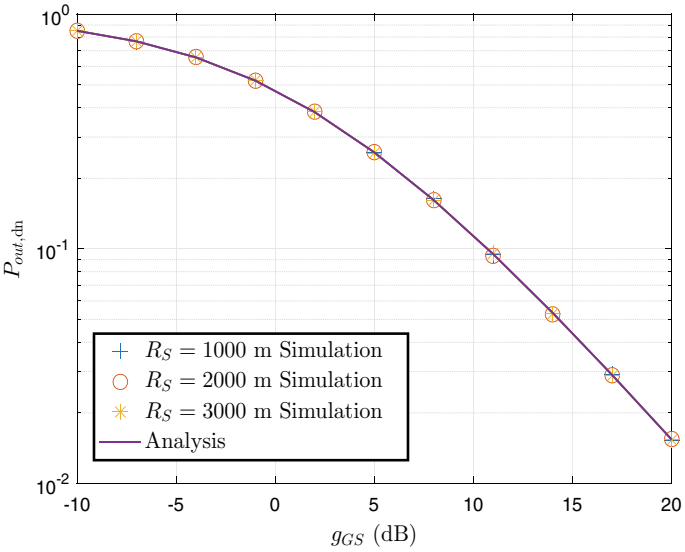

Fig. 2.11 Secrecy outage versus g_{SG} for various R_S

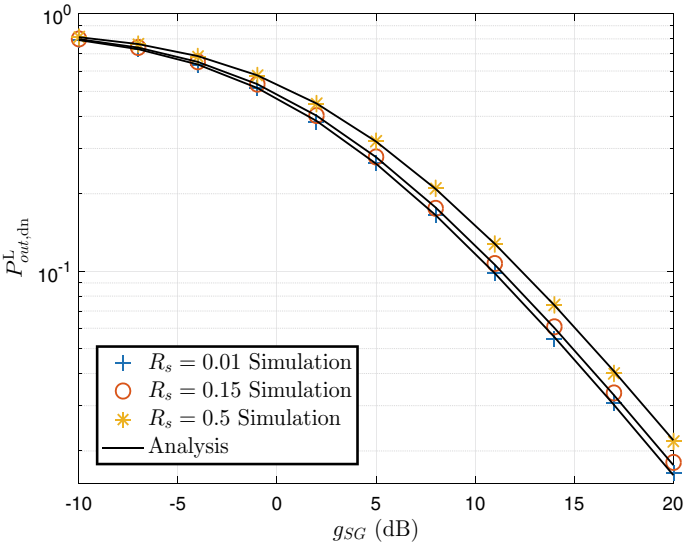

Fig. 2.12 Secrecy outage versus g_{SG} for various R_s

Figure 2.12 presents the secrecy outage performance of the considered system with various outage threshold (R_s). The results show that $P_{out,\mathrm{dn}}$ with a small R_s outperforms that with a large R_s. Because a large R_s implies that the probability that the secrecy capacity of the considered system is less than the threshold will increase, this observation is the same as the one seen in Fig. 2.8 for the uplink.

In Fig. 2.13, the SOP lines for various heights of S, h, are depicted while $R_S = 1000$ m. The height of S, h, negatively affects SOP because a large h leads to a low received SNR at the ground receiver, G, and further incurs the degraded secrecy outage performance. Though the secrecy performance will degrade while the height of the UAV increases, optimizations can be set up to realize optimal secrecy performance vis choosing suitable heights for the UAV, and some schemes can be designed to safeguard the security of UAV system, e.g., jamming and artificial noise schemes.

Finally, as presented in Figs. 2.9, 2.10, 2.11, 2.12 and 2.13, it is noted that g_{SG} exhibits a similar effect on the secrecy outage performance of the considered system as g_{GS} does in Figs. 2.5, 2.6, 2.7 and 2.8. This can also be explained by the idea of the reason given at the end of the last subsection. Moreover, simulation and analysis results show perfect matching with each other, which demonstrates the accuracy of the proposed analysis model.

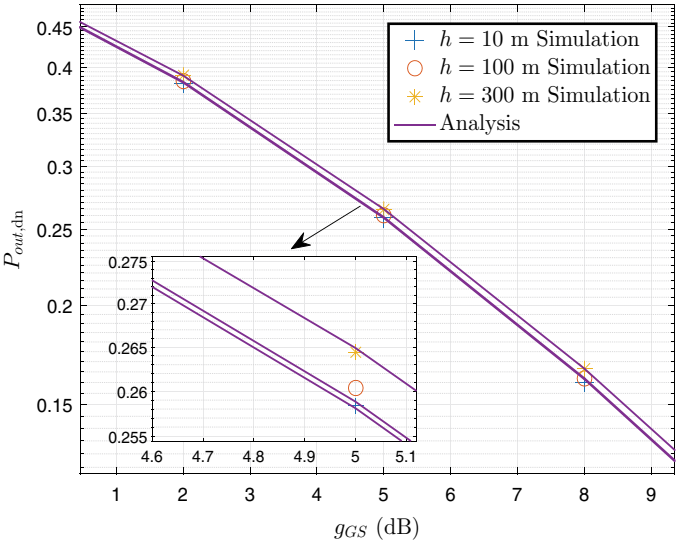

Fig. 2.13 Secrecy outage versus g_{SG} for various h

2.1.5 Conclusion

In this section, we have studied the secrecy outage performance of a UAV system with linear trajectory and derived the closed-form analytical expressions for the lower boundary of the SOP of both downlink and uplink. We consider the randomness of the positions of all UAVs and the ground receiver to make the system more practical.

Observing from the numerical results, we can reach some remarks as follows:

(1) The radius of the coverage space of S does not exhibit an apparent impact on the secrecy outage performance over the downlink, and that of G shows a weak influence on the secrecy outage performance over the uplink.
(2) The transmit SNR at S and G provides a very weak impact on the secrecy outage performance over the downlink and the uplink, respectively.
(3) The height of S negatively affects the secrecy outage performance of the considered system.

Appendix 1: Proof of Theorem (2.1.1)

As C is the midpoint of AB, obtaining $AC = l/2$ is easy. Then, we can have $\cos A = \frac{l}{2b}$. According to the Cosine theorem, we can also achieve

$$\cos A = \frac{b^2 + x^2 - y^2}{2bx}. \tag{2.42}$$

Solving this quadric equation leads

$$\begin{aligned} x &= \frac{l \pm \sqrt{4y^2 + l^2 - 4b^2}}{2} \\ &= g(y). \end{aligned} \tag{2.43}$$

Since S is uniformly distributed over AB, the PDF of x is given as

$$f_x(x) = \frac{1}{l}, \quad 0 \le x \le l. \tag{2.44}$$

Using the transformation of a random variable, we can obtain the PDF of y as

$$\begin{aligned} f_y(y) &= f_x(g(y)) \left| g'(y) \right| \\ &= \begin{cases} \frac{2y}{l\sqrt{4y^2+l^2-4b^2}}, & \text{if } \sqrt{b^2 - \frac{l^2}{4}} \le y \le b; \\ 0, & \text{else} \end{cases}. \end{aligned} \tag{2.45}$$

Then, the proof is completed.

2.2 Secure UAV-to-Vehicle Communications

UAV communications have been widely exploited daily, leading to rising concerns about security. Section 2.2 investigates the secrecy performance of a UAV-to-vehicle (UAV-2-V) communication system, where the information delivered over both downlink and uplink between a UAV (S) acting as a temporary aerial BS and a legitimate vehicle (D) moving along a road is overheard by an eavesdropping vehicle (E) on the same route. The location of S is assumed to be uniformly distributed in the sky, while the locations of D and E are uniformly distributed on the highway. The statistical characteristics, including the CDF and PDF of the received SNR over both downlink and uplink, are characterized, respectively. Closed-form expressions for the approximate and asymptotic SOP of the downlink experiencing Rician fading channels have been derived accordingly. Moreover, the secrecy outage performance of the uplink is investigated by deriving the closed-form expression of the exact and asymptotic SOP in two cases: the eavesdropping channel suffers Rician and Weibull fading, respectively. Finally, Monte Carlo simulations are shown to verify our proposed analytical models.

The main contributions of Sect. 2.2 are summarized as follows:

(1) We characterize the statistical characteristics, including CDF and PDF of the received SNR at D, E over the downlink, at S over the uplink, and E from D under different channel propagation, respectively.

(2) We derive the approximate and asymptotic analytical expressions for the SOP over the uplink, assuming all channels experience Rician fading.
(3) We derive closed-form analytical expressions for the exact and asymptotic SOP over the downlink while two different kinds of channel fading between D and E (namely, Rician and Weibull fading) are respectively considered.
(4) We systematically investigate the impacts of the radius of the coverage space of S and the height of the UAV on the secrecy outage performance of the considered UAV-2-V system.

2.2.1 System Model

In Sect. 2.2 we consider a UAV-2-V communication system shown in Fig. 2.14,[6] in which a UAV (S) plays as a temporary aerial BS to deliver/collect information to/from a legitimate vehicle (D). In contrast, an eavesdropping vehicle (E) moves on the same linear road with D and tries to overhear the information exchange between S and D. Moreover, $S-D$ and $S-E$ links are assumed to suffer from independent and identically distributed Rician fading.

One of the advantages of UAVs is the flexibility for quick deployment. In Sect. 2.2 UAV is used to substitute for the on-ground BSs that are out of service due to some emergency (e.g., earthquake) or fulfill the blind coverage area without any terrestrial infrastructure. Then, we assume that the location of S is uniformly distributed in the sky. Without loss of generality, in Sect. 2.2 it is also believed that D and E are uniformly distributed on the highway, which is modeled as a straight line here to facilitate the following analysis.

As depicted in Fig. 2.15, the coverage area of S on the ground is a circle with radius R_S and center O (in other words, the projection of S is the node O). We denote the height of S as h, and let the length of OD and OE be l_{OD} and l_{OE}, respectively. Then, it is easy to obtain the distances between S and D/E as

$$d_{SD} = \sqrt{h^2 + l_{OD}^2} \tag{2.46}$$

and

$$d_{SE} = \sqrt{h^2 + l_{OE}^2}, \tag{2.47}$$

respectively.

[6] There are some practical application scenarios for the considered model presented in Fig. 2.14, e.g., during patrols or pursuit missions, UAVs are usually used to aid the police on the road/highway to set up communications with the command center. However, due to the openness of the application scenarios, eavesdropping cannot be totally prohibited. Moreover, for simplification purposes, in Sect. 2.2 we consider the simplest scenario depicted in Fig. 2.14 to propose our analytical method, which can serve as a valuable reference to investigate the performance of similar UAV communication systems.

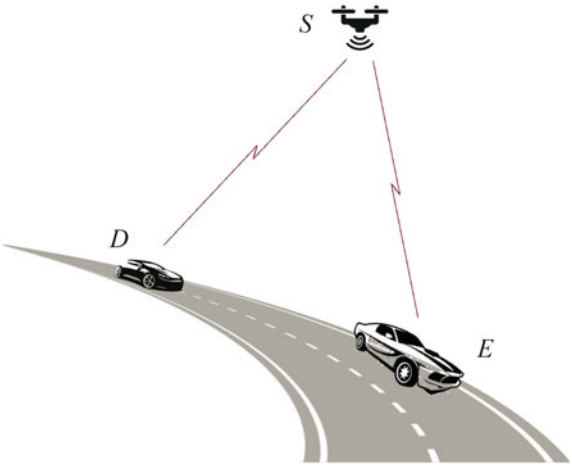

Fig. 2.14 UAV-2-V communication scenarios

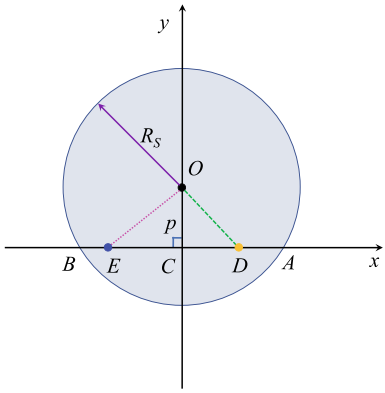

Fig. 2.15 2-dimensional model for UAV-2-V link

Also, the PDF of h can be presented as

$$f_h(x) = \frac{1}{H_{\max} - H_{\min}}, H_{\min} \leq h \leq H_{\max}, \tag{2.48}$$

where $H_{\max}$ and $H_{\min}$ are the maximum and minimum heights that S can reach, respectively.

To characterize the statistical characteristics of l_{OD} and l_{OE}, we use Fig. 2.16 to address the geometric relationships in the 3D space. As S is uniformly distributed in the 3D space, it is easy to obtain that O is uniformly distributed in the interval $[0, R_S]$ on the Y-axis. Then, we can easily achieve that the vertical distance from the project of S, O, to the highway AB is a uniformly distributed variable, the PDF of p, which can be given as

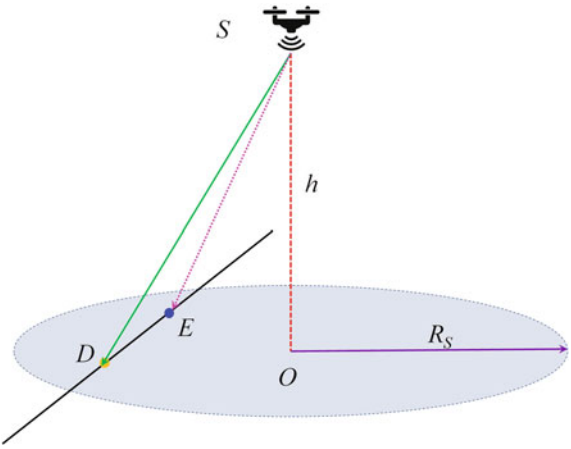

Fig. 2.16 3D model for UAV-2-V link

$$f_p(x) = \begin{cases} \frac{1}{R_S}, & \text{if } 0 < x \le R_S; \\ 0, & \text{else} \end{cases}. \tag{2.49}$$

In Fig. 2.16, we let the middle point of AB, C, as the origin, and AB as the horizontal axis to facilitate the following analysis. Then, the coordinates of A and B can be written as $\left(\sqrt{R_S^2 - p^2}, 0\right)$ and $\left(-\sqrt{R_S^2 - p^2}, 0\right)$, respectively.

Therefore, when D and E are uniformly distributed on the line AB, conditioned on p, the conditional PDF of the length of CD and CE, t and w, can be presented as

$$f_{j|p}(x) = \begin{cases} \frac{1}{\sqrt{R_S^2 - p^2}}, & \text{if } 0 < x \le \sqrt{R_S^2 - p^2}; \\ 0, & \text{else} \end{cases}, \tag{2.50}$$

where $j \in \{t, w\}$.

2.2.2 *Secrecy Outage Analysis over Downlink*

The received signal at D and E can be written as[7] The received signal at D and E can be written as[8]

$$y_i = \sqrt{P_S / d_{Si}^{\alpha}} h_{Si} x_S + z_i, \tag{2.51}$$

[7] As the main purpose of Sect. 2.2 is to uncover the impacts of the randomness of the positions of the UAV and vehicles, and small-scale fading on the secrecy outage performance of the considered system, the influence of Doppler shift is ignored for simplification purposes, which will be investigated in the future work.

[8] As the main purpose of Sect. 2.2 is to uncover the impacts of the randomness of the positions of the UAV and vehicles, and small-scale fading on the secrecy outage performance of the consid-

where $i \in \{D, E\}$, P_S is the transmit power at S, d_{Si} is the distance between S and node i, h_{Si} is the channel gain over the link between S and node i, α is the path-loss factor. x_S is the information bit transmitted by S, z_i denotes the additive Gaussian white noise (AWGN) at node i with average power N_0.

The SNR at node i ($i \in \{D, E\}$) can be written as

$$\gamma_i = \frac{P_S |h_{Si}|^2}{N_0 d_{Si}^{\alpha}} = \frac{\lambda_{Si}}{d_{Si}^{\alpha}}, \tag{2.52}$$

where $\lambda_{Si} = \rho_S |h_{Si}|^2$ and $\rho_S = \frac{P_S}{N_0}$.

In Sect. 2.2 it is assumed that the channel between S and node i ($i \in \{D, E\}$) follows independent and identical Rician distribution. Then, the PDF and CDF of λ_{Si} can be expressed as

$$f_{\lambda_{Si}}(x) = \exp(-\mu_i x) \sum_{n=0}^{\infty} A_i x^n \tag{2.53}$$

and

$$F_{\lambda_{Si}}(x) = 1 - \exp(-\mu_i x) \sum_{l=0}^{\infty} \sum_{n=0}^{l} B_i x^n, \tag{2.54}$$

respectively, where $A_i = a_i \mu_i \exp(-K_i)$, $a_i = \frac{1}{(n!)^2} (K_i \mu_i)^n$, $\mu_i = \frac{1+K_i}{\Omega_{Si} \rho_S}$, $B_i = \frac{(K_i)^l (\mu_i)^n}{\exp(K_i) l! n!}$, Ω_{Si} is the fading power, and K_i is the Rician factor corresponding to the ratio of the LOS (specular) component's power to the scattered component's average power. Although there is an infinite summation in Eqs. (2.53) and (2.54), the expression of the CDF in Eq. (2.54) bukqi converges quickly to the finite series of summation.

Therefore, the instantaneous secrecy capacity of the downlink transmission is

$$C_{\text{dn}}(\gamma_D, \gamma_E) = \max\left\{\log_2(1 + \gamma_D) - \log_2(1 + \gamma_E), 0\right\}. \tag{2.55}$$

In Sect. 2.2 passive eavesdropping is assumed to reflect the most common eavesdropping scenario for the eavesdropper to achieve the best eavesdropping and to keep itself from being uncovered. In other words, S has no channel state information (CSI) of the eavesdropping channel, and SOP is investigated. Based on [10], SOP is defined as the probability that the secrecy capacity is smaller than a threshold R_{th}, which can be written as

---

ered system, the influence of Doppler shift is ignored for simplification purposes, which will be investigated in the future work.

$$\begin{aligned} P_{\text{out,dn}} &= \Pr\left\{C_{\text{dn}}\left(\gamma_D, \gamma_E\right) \leq R_{\text{th}}\right\} \\ &= \Pr\left\{\gamma_D \leq \Theta\gamma_E + \Theta - 1\right\} \\ &\geq \Pr\left\{\gamma_D \leq \Theta\gamma_E\right\} \\ &= P_{\text{out,dn}}^{\text{L}}, \end{aligned} \tag{2.56}$$

where $\Theta = 2^{R_{\text{th}}}$.

2.2.2.1 Exact Secrecy Outage Analysis

Using Eqs. (2.46), (2.47), and (2.52), one can rewrite the lower bound of SOP as

$$\begin{aligned} P_{\text{out,dn}}^{\text{L}} &= \Pr\left\{\gamma_D \leq \Theta\gamma_E\right\} \\ &= \Pr\left\{\frac{\lambda_{SD}}{d_{SD}^{\alpha}} \leq \Theta\frac{\lambda_{SE}}{d_{SE}^{\alpha}}\right\} \\ &= \Pr\left\{\frac{\lambda_{SD}}{\lambda_{SE}} \leq \Theta\frac{\left(h^2 + p^2 + t^2\right)^{\frac{\alpha}{2}}}{\left(h^2 + p^2 + w^2\right)^{\frac{\alpha}{2}}}\right\} \\ &= \Pr\left\{X \leq \Theta^{\frac{2}{\alpha}} Y\right\} \\ &= \int_0^{\infty} F_X\left(\Theta^{\frac{2}{\alpha}} y\right) f_Y\left(y\right) dy, \end{aligned} \tag{2.57}$$

where $X = \left(\frac{\lambda_{SD}}{\lambda_{SE}}\right)^{\frac{2}{\alpha}} = \left(\frac{|h_{SD}|^2}{|\lambda_{SE}|^2}\right)^{\frac{2}{\alpha}}$ and $Y = \frac{h^2+p^2+t^2}{h^2+p^2+w^2}$.

Remark 2.1 On can easily find that the lower bound of SOP given in Eq. (2.56) has nothing to do with the transmit SNR at S. In other words, increasing the transmit SNR at S is not a feasible way to improve the secrecy outage performance of the considered system.

Utilizing [2, Eq. (3.326.2)], we can derive the CDF of X as

$$
\begin{aligned}
\Pr\{X \le x\} &= \Pr\left\{\left(\frac{\lambda_{SD}}{\lambda_{SE}}\right)^{\frac{2}{\alpha}} \le x\right\} \\
&= \Pr\left\{\lambda_{SD} \le x^{\frac{\alpha}{2}}\lambda_{SE}\right\} \\
&= \int_0^{\infty} F_{\lambda_{SD}}\left(x^{\frac{\alpha}{2}}y\right) f_{\lambda_{SE}}(y)\, dy \\
&= \int_0^{\infty} \left(1 - e^{-\mu_D x^{\frac{\alpha}{2}} y} \sum_{l=0}^{\infty}\sum_{n=0}^{l} B_D\left(x^{\frac{\alpha}{2}}y\right)^n\right) \exp(-\mu_E y) \sum_{s=0}^{\infty} A_E y^s dy \\
&= 1 - \int_0^{\infty} e^{-\mu_D x^{\frac{\alpha}{2}} y} \sum_{l=0}^{\infty}\sum_{n=0}^{l} B_D\left(x^{\frac{\alpha}{2}}y\right)^n \exp(-\mu_E y) \sum_{s=0}^{\infty} A_E y^s dy \\
&= 1 - \sum_{l=0}^{\infty}\sum_{n=0}^{l} B_D\left(x^{\frac{\alpha}{2}}\right)^n \sum_{s=0}^{\infty} A_E \int_0^{\infty} y^{n+s} e^{-\left(\mu_E + \mu_D x^{\frac{\alpha}{2}}\right)y} dy \\
&= 1 - \sum_{l=0}^{M}\sum_{n=0}^{l} B_D\left(x^{\frac{\alpha}{2}}\right)^n \sum_{s=0}^{T} A_s \frac{\Gamma(n+s+1)}{\left(\mu_e + \mu_D x^{\frac{\alpha}{2}}\right)^{n+s+1}} \\
&= 1 - \sum_{l=0}^{\infty}\sum_{n=0}^{l}\sum_{s=0}^{\infty} B_D A_E \left(x^{\frac{\alpha}{2}}\right)^n \frac{\Gamma(n+s+1)}{\left(\mu_E + \mu_D x^{\frac{\alpha}{2}}\right)^{n+s+1}}.
\end{aligned}
\tag{2.58}
$$

Observing from Figs. 2.15 and 2.16, one can obtain $\phi_1 = \frac{H_{\min}^2}{H_{\min}^2 + R_S^2} \le Y \le \phi_1^{-1}$. A useful theorem (2.2.1) is given as follows to characterize the statistical characteristics of Y.

Theorem 2.2.1 *The PDF of* $Y = \frac{h^2+p^2+t^2}{h^2+p^2+w^2}$ *can be derived as*

$$
f_Y(y) = \frac{1}{\Xi y^{1.5}} \begin{cases}
\int_{H_{\min}}^{\sqrt{\frac{y}{1-y}}R_S} \int_0^{\sqrt{c_1 y - h^2}} g_1(p,h,y)\, dp dh, & \phi_1 \le y < \phi_2; \\
\int_{H_{\min}}^{H_{\max}} \int_0^{\sqrt{c_1 y - h^2}} g_1(p,h,y)\, dp dh, & \phi_2 \le y < 1; \\
\int_{H_{\min}}^{H_{\max}} \int_0^{\sqrt{\frac{c_1}{y} - h^2}} g_2(p,h,y)\, dp dh, & 1 < y \leqslant \frac{1}{\phi_2}; \\
\int_{H_{\min}}^{\sqrt{\frac{R_S^2}{y-1}}} \int_0^{\sqrt{\frac{c_1}{y} - h^2}} g_2(p,h,y)\, dp dh, & \frac{1}{\phi_2} < y \leqslant \frac{1}{\phi_1}
\end{cases},
\tag{2.59}
$$

where $g_1(p,h,y) = \frac{a_1(y+1)}{b_1}\log\frac{\sqrt{b_1 y}+\sqrt{c_1 y - a_1}}{\sqrt{a_1(1-y)}} + \sqrt{\frac{c_1 y^2 - a_1 y}{b_1}}$, $g_2(p,h,y) = \frac{a_1(y+1)}{b_1}\log\frac{\sqrt{b_1}+\sqrt{c_1 - a_1 y}}{\sqrt{a_1(y-1)}} + \sqrt{\frac{c_1 - a_1 y}{b_1}}$, $\Xi = 4R_S(H_{\max} - H_{\min})$, $a_1 = h^2 + p^2$, $b_1 = R_S^2 - p^2$, $c_1 = R_S^2 + h^2$, *and* $\phi_2 = \frac{H_{\max}^2}{H_{\max}^2 + R_S^2}$.

Proof Please refer to the Appendix 2. □

Substituting Eqs. (2.58) and (2.59) into Eq. (2.57), we obtain

$$P_{\text{out,dn}}^{\text{L}} = 1 - \sum_{l=0}^{\infty}\sum_{n=0}^{l}\sum_{s=0}^{\infty} B_D A_E \Gamma(n+s+1)\Theta\psi, \tag{2.60}$$

where $\psi = \int_0^{\infty} \frac{y^{\iota_1}}{\tau^{n+s+1}} f_Y(y)\,dy$ with $\tau = \mu_E + \mu_D \Theta y^{\frac{\alpha}{2}}$ and $\iota_1 = \frac{\alpha n}{2}$. ψ can be written as

$$\begin{aligned}
\psi =& \frac{1}{\Xi}\int_{\phi_1}^{\phi_2} \frac{y^{\iota_1 - 1.5}}{\tau^{n+s+1}} \int_{H_{\min}}^{\sqrt{\frac{R_S^2 y}{1-y}}} \int_0^{\sqrt{c_1 y - h^2}} g_1(p,h,y)\,dpdhdy \\
&+ \frac{1}{\Xi}\int_{\phi_2}^{1} \frac{y^{\iota_1 - 1.5}}{\tau^{n+s+1}} \int_{H_{\min}}^{H_{\max}} \int_0^{\sqrt{c_1 y - h^2}} g_1(p,h,y)\,dpdhdy \\
&+ \frac{1}{\Xi}\int_{1}^{\frac{1}{\phi_2}} \frac{y^{\iota_1 - 1.5}}{\tau^{n+s+1}} \int_{H_{\min}}^{H_{\max}} \int_0^{\sqrt{\frac{c_1}{y} - h^2}} g_2(p,h,y)\,dpdhdy \\
&+ \frac{1}{\Xi}\int_{\frac{1}{\phi_2}}^{\frac{1}{\phi_1}} \frac{y^{\iota_1 - 1.5}}{\tau^{n+s+1}} \int_{H_{\min}}^{\sqrt{\frac{R_S^2}{y-1}}} \int_0^{\sqrt{\frac{c_1}{y} - h^2}} g_2(p,h,y)\,dpdhdy.
\end{aligned} \tag{2.61}$$

Using Chebyshev-Gauss quadrature method [11, Eq. (25.4.30)], we can have the approximated analytical expression of (2.61) as

$$\psi \approx \frac{\hbar_1}{8\Xi}\sum_{k=1}^{N_3}\frac{\bar{\chi}_1\eta_k\varepsilon_{k,1}{}^{\iota_1-1.5}}{T_{k,1}{}^{n+s+1}}\sum_{j=1}^{N_2}\upsilon_j\ell_1\sum_{i=1}^{N_1}\xi_i G_1\left(\zeta_{i,1},\vartheta_{j,1},\varepsilon_{k,1}\right)$$
$$+\frac{\hbar_2}{8\Xi}\sum_{k=1}^{N_3}\frac{\bar{\chi}_2\eta_k\varepsilon_{k,2}{}^{\iota_1-1.5}}{T_{k,2}{}^{n+s+1}}\sum_{j=1}^{N_2}\upsilon_j\ell_2\sum_{i=1}^{N_1}\xi_i G_1\left(\zeta_{i,2},\vartheta_{j,2},\varepsilon_{k,2}\right)$$
$$+\frac{\hbar_3}{8\Xi}\sum_{k=1}^{N_3}\frac{\bar{\chi}_3\eta_k\varepsilon_{k,3}{}^{\iota_1-1.5}}{T_{k,3}{}^{n+s+1}}\sum_{j=1}^{N_2}\upsilon_j\ell_3\sum_{i=1}^{N_1}\xi_i G_2\left(\zeta_{i,3},\vartheta_{j,3},\varepsilon_{k,3}\right)$$
$$+\frac{\hbar_4}{8\Xi}\sum_{k=1}^{N_3}\frac{\bar{\chi}_4\eta_k\varepsilon_{k,4}{}^{\iota_1-1.5}}{T_{k,4}{}^{n+s+1}}\sum_{j=1}^{N_2}\upsilon_j\ell_4\sum_{i=1}^{N_1}\xi_i G_2\left(\zeta_{i,4},\vartheta_{j,4},\varepsilon_{k,4}\right), \tag{2.62}$$

where N_1, N_2, and N_3 are the parameters for the summation item, which reflects accuracy versus complexity, $\hbar_1 = \phi_2 - \phi_1$, $\hbar_2 = 1 - \phi_2$, $\hbar_3 = \frac{1}{\phi_2} - 1$, $\hbar_4 = \frac{1}{\phi_1} - \frac{1}{\phi_2}$, $\bar{\chi}_1 = \sqrt{\frac{R_S^2\varepsilon_{k,1}}{1-\varepsilon_{k,1}}} - H_{\min}, \bar{\chi}_2 = \bar{\chi}_3 = H_{\max} - H_{\min}, \bar{\chi}_4 = \sqrt{\frac{R_S^2}{\varepsilon_{k,4}-1}} - H_{\min}$, η_k, υ_j, ξ_i are the Gaussian weights, which are constants and given in [12, Table (25.4)], $\varepsilon_{k,s} = \frac{\hbar_s}{2}z_s + \varrho_s, s = 1, 2, 3, 4, \varrho_1 = \frac{\phi_1+\phi_2}{2}, \varrho_2 = \frac{1+\phi_2}{2}, \varrho_3 = \frac{1}{2}(1 + \frac{1}{\phi_2}), \varrho_4 = \frac{1}{2}(\frac{1}{\phi_1} + \frac{1}{\phi_2})$, $T_{k,s} = \mu_E + \mu_D\Theta\varepsilon_{k,s}{}^{\frac{\alpha}{2}}$, $C_{1,s} = R_S^2 + \vartheta_{j,s}{}^2$, $\vartheta_{j,s} = \frac{\bar{\chi}_s}{2}y_s + \chi_s$, $\chi_1 = \frac{1}{2}(H_{\min} + \sqrt{\frac{R_S^2\varepsilon_{k,1}}{1-\varepsilon_{k,1}}})$, $\chi_2 = \chi_3 = \frac{1}{2}(H_{\min} + H_{\max})$, $\chi_4 = \frac{1}{2}(H_{\min} + \sqrt{\frac{R_S^2}{\varepsilon_{k,4}-1}})$, $\ell_t = \sqrt{C_{1,t}\varepsilon_{k,t} - \vartheta_{j,t}{}^2}$, $t = 1, 2$;
$\ell_t = \sqrt{\frac{C_{1,t}}{\varepsilon_{k,t}} - \vartheta_{j,t}{}^2}, t = 3, 4, \zeta_{i,s} = \frac{\ell_s}{2}x_s + \frac{\ell_s}{2}, G_1\left(\zeta_{i,s},\vartheta_{j,s},\varepsilon_{k,s}\right) = \sqrt{\frac{C_{1,s}\varepsilon_{k,s}{}^2 - A_{1,s}\varepsilon_{k,s}}{B_{1,s}}}$ $+\frac{A_{1,s}(\varepsilon_{k,s}+1)}{B_{1,s}}\log\frac{\sqrt{B_{1,s}\varepsilon_{k,s}}+\sqrt{C_{1,s}\varepsilon_{k,s}-A_{1,s}}}{\sqrt{A_{1,s}(1-\varepsilon_{k,s})}}$, $G_2\left(\zeta_{i,s},\vartheta_{j,s},\varepsilon_{k,s}\right) = \frac{A_{1,s}(\varepsilon_{k,s}+1)}{B_{1,s}}\log$ $\frac{\sqrt{B_{1,s}}+\sqrt{C_{1,s}-A_{1,s}\varepsilon_{k,s}}}{\sqrt{A_{1,s}(\varepsilon_{k,s}-1)}} + \sqrt{\frac{C_{1,s}-A_{1,s}\varepsilon_{k,s}}{B_{1,s}}}$ with $A_{1,s} = \vartheta_{j,s}{}^2 + \zeta_{i,s}{}^2$, $B_{1,s} = R_S^2 - \zeta_{i,s}{}^2$, x_s, y_s, z_s are the sth zeros of Legendre polynomials, which are given in [11, Table (25.4)].

2.2.2.2 Asymptotic Secrecy Outage Analysis

To obtain a simplified expression for SOP, in this section, we analyze the asymptotic SOP of the UAV-2-V communication systems in the high-Ω_D regime. When $\Omega_D \to \infty$, applying [13, Eq. (26)], we obtain the asymptotic CDF of λ_{SD} as

$$F_{\lambda_{SD}}^{\infty}(x) = \mu_D \exp\left(-K_D\right) x\exp(-\mu_D x). \tag{2.63}$$

Utilizing [2, Eq. (3.326.2)], the asymptotic CDF of X is expressed as

$$F_X^{\infty}(x) = \mu_D \exp\left(-K_D\right) x^{\frac{\alpha}{2}}\sum_{s=0}^{\infty}\frac{A_E\Gamma\left(s+2\right)}{\left(\mu_E+\mu_D x^{\frac{\alpha}{2}}\right)^{s+2}}. \tag{2.64}$$

Thus, the asymptotic SOP is obtained as

$$P_{\text{out,dn}}^{\text{L},\infty} = \int_0^{\infty} F_X^{\infty}\left(\Theta^{\frac{2}{\alpha}} y\right) f_Y(y)\, dy$$
$$= \mu_D \exp(-K_D)\, \Theta \sum_{s=0}^{\infty} \frac{A_E \Gamma(s+2)}{(\mu_E)^{s+2}} \psi^{\infty}, \tag{2.65}$$

where ψ^{∞} is shown as

$$\psi^{\infty} = \frac{1}{\Xi} \int_{\phi_1}^{\phi_2} y^{\frac{\alpha-3}{2}} \int_{H_{\min}}^{\sqrt{\frac{R_S^2 y}{1-y}}} \int_0^{\sqrt{c_1 y - h^2}} g_1(p,h,y)\, dpdhdy$$
$$+ \frac{1}{\Xi} \int_{\phi_2}^{1} y^{\frac{\alpha-3}{2}} \int_{H_{\min}}^{H_{\max}} \int_0^{\sqrt{c_1 y - h^2}} g_1(p,h,y)\, dpdhdy$$
$$+ \frac{1}{\Xi} \int_{1}^{\frac{1}{\phi_2}} y^{\frac{\alpha-3}{2}} \int_{H_{\min}}^{H_{\max}} \int_0^{\sqrt{\frac{c_1}{y} - h^2}} g_2(p,h,y)\, dpdhdy$$
$$+ \frac{1}{\Xi} \int_{\frac{1}{\phi_2}}^{\frac{1}{\phi_1}} y^{\frac{\alpha-3}{2}} \int_{H_{\min}}^{\sqrt{\frac{R_S^2}{y-1}}} \int_0^{\sqrt{\frac{c_1}{y} - h^2}} g_2(p,h,y)\, dpdhdy. \tag{2.66}$$

Similar to Eq. (2.62), we can finally derive ψ^{∞} as

$$\psi^{\infty} \approx \frac{\hbar_1}{8\Xi} \sum_{k=1}^{N_3} \bar{\lambda}_1 \eta_k \varepsilon_{k,1}{}^{0.5\alpha-1.5} \sum_{j=1}^{N_2} \upsilon_j \ell_1 \sum_{i=1}^{N_1} \xi_i G_1\left(\zeta_{i,1}, \vartheta_{j,1}, \varepsilon_{k,1}\right)$$
$$+ \frac{\hbar_2}{8\Xi} \sum_{k=1}^{N_3} \bar{\lambda}_2 \eta_k \varepsilon_{k,2}{}^{0.5\alpha-1.5} \sum_{j=1}^{N_2} \upsilon_j \ell_2 \sum_{i=1}^{N_1} \xi_i G_1\left(\zeta_{i,2}, \vartheta_{j,2}, \varepsilon_{k,2}\right)$$
$$+ \frac{\hbar_3}{8\Xi} \sum_{k=1}^{N_3} \bar{\lambda}_3 \eta_k \varepsilon_{k,3}{}^{0.5\alpha-1.5} \sum_{j=1}^{N_2} \upsilon_j \ell_3 \sum_{i=1}^{N_1} \xi_i G_2\left(\zeta_{i,3}, \vartheta_{j,3}, \varepsilon_{k,3}\right)$$
$$+ \frac{\hbar_4}{8\Xi} \sum_{k=1}^{N_3} \bar{\lambda}_4 \eta_k \varepsilon_{k,4}{}^{0.5\alpha-1.5} \sum_{j=1}^{N_2} \upsilon_j \ell_4 \sum_{i=1}^{N_1} \xi_i G_2\left(\zeta_{i,4}, \vartheta_{j,4}, \varepsilon_{k,4}\right). \tag{2.67}$$

2.2.3 Secrecy Outage Analysis over Uplink

In Fig. 2.17, we present the 3D model for the transmission over V-2-UAV link to aid the following analysis in this section. The coverage space of D is a hemisphere with the centre C and radius $R_D = AD = DB$.

To address the randomness of the positions of both D and E, we take D as the origin, and it is assumed that E is uniformly distributed on the line segment AB with length L_{AB}. Then, the PDF of d_{DE} can be presented as

$$f_{d_{DE}}(x) = \begin{cases} \frac{1}{R_D}, & \text{if } 0 < x \leq R_D; \\ 0, & \text{else} \end{cases}. \tag{2.68}$$

During the uplink transmission stage, S is uniformly distributed in the coverage space of D. Therefore, the PDF of the distance between D and S can be written as

$$f_{d_{DS}}(x) = \begin{cases} \frac{3x^2}{R_D^3}, & \text{if } 0 < x \leq R_D; \\ 0, & \text{else} \end{cases}. \tag{2.69}$$

The received signal at S/E can be written as

$$y_j = \sqrt{P_D / d_{Dj}^{\alpha}} h_{Dj} x_D + z_j, \tag{2.70}$$

where $j \in \{S, E\}$, P_D is the transmit power at D, d_{Di} is the distance between D and node j, h_{Dj} is the channel gain over the link between D and node j, x_D is the information bits transmitted by D, z_j is the AWGN at node j with average power N_0. For simplification purposes, in Sect. 2.2 we assume that h_{DS} has the same statistical characteristics as h_{SD} due to the reciprocity of the wireless channels.

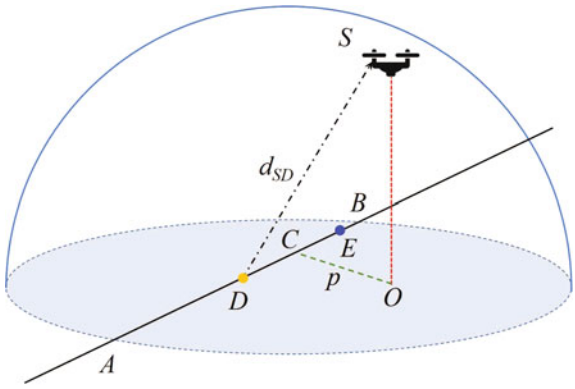

Fig. 2.17 3D model for V-2-UAV link

Accordingly, the received SNR at node j ($j \in \{S, E\}$) can be written as

$$\gamma_j = \frac{P_D \left|h_{Dj}\right|^2}{N_0 d_{Di}^{\alpha}} = \frac{\lambda_{Di}}{d_{Di}^{\alpha}}, \tag{2.71}$$

where $\lambda_{Dj} = \rho_D \left|h_{Dj}\right|^2$ and $\rho_D = \frac{P_D}{N_0}$.

Moreover, we also have $\lambda_{DS} = \lambda_{SD}$ by considering the reciprocity of the wireless channels.

Similarly, the SOP over the uplink is given as

$$\begin{aligned} P_{\text{out,up}}^{\text{L}} &= \Pr\left\{\gamma_S \leq \Theta \gamma_E\right\} \\ &= \Pr\left\{\frac{\lambda_{DS}}{d_{DS}^{\alpha}} \leq \Theta \frac{\lambda_{DE}}{d_{DE}^{\alpha}}\right\}. \end{aligned} \tag{2.72}$$

In this case, the link between D and E is a vehicle-to-vehicle (V2V) link. As discussed in [32], Rician fading is used to statistically describe the V2V communication in urban, suburban, and highway environments when the distance between communicating vehicles is small and a strong LOS component is present. However, the fading gradually transits from Rician to Rayleigh when the vehicle separation increases. Moreover, when the distance exceeds 70–100 m, the fading becomes worse than Rayleigh, modeled as Weibull fading. Hence, for V2V communications, it is reasonable and practical that different fading models may be applicable according to the surrounding environment and vehicle density.

To fully cover all potential cases, in Sect. 2.2 we will conduct our analysis work for two cases: (1) $D - E$ link suffers Rician fading; (2) $D - E$ link suffers Weibull fading.

2.2.3.1 $D - E$ Link Suffering Rician Fading

In this case, the SNR at S and E can be expressed as $\gamma_S = \frac{\rho_D |h_{DS}|^2}{d_{DS}^{\alpha}} = \frac{\lambda_{DS}}{d_{DS}^{\alpha}}$ and $\gamma_E = \frac{\rho_D |h_{DE}|^2}{d_{DE}^{\alpha}} = \frac{\lambda_{DE}}{d_{DE}^{\alpha}}$, respectively, where $\lambda_{DS} = \rho_D |h_{DS}|^2$ and $\lambda_{DE} = \rho_D |h_{DE}|^2$.

Using [14, Eq. (5)], we have the PDF of d_{DS}^{α} as

$$f_{d_{DS}^{\alpha}}(t) = \frac{\varpi}{R_D^3} t^{\varpi - 1}, \ 0 < t \leq R_D^{\alpha}, \tag{2.73}$$

where $\varpi = \frac{3}{\alpha}$.

Utilizing [2, Eq. (3.351.1)], the CDF of γ_S is obtained as

$$
\begin{aligned}
F_{\gamma_S}(x) &= \Pr\{\gamma_S < x\} \\
&= \Pr\left\{\lambda_{DS} < d_{DS}^{\alpha} x\right\} \\
&= \int_0^{\infty} F_{\lambda_{DS}}(tx)\, f_{d_{DS}^{\alpha}}(t)\, dt \\
&= 1 - \sum_{l=0}^{\infty} \sum_{n=0}^{l} B_S x^n \int_0^{\infty} t^n \exp(-\mu_S t x)\, f_{d_{DS}^{\alpha}}(t)\, dt \\
&= 1 - \frac{3}{\alpha R_D^3} \sum_{l=0}^{\infty} \sum_{n=0}^{l} B_S x^n \int_0^{R_D^{\alpha}} t^{n+\varpi-1} \exp(-\mu_S t x)\, dt \\
&= 1 - \sum_{l=0}^{\infty} \sum_{n=0}^{l} \beta_S x^{-\varpi} \Upsilon(n+\varpi, \phi_S x), \qquad (2.74)
\end{aligned}
$$

where $\beta_S = \frac{\varpi B_S}{(\mu_S)^{n+\varpi} R_D^3}$, $\phi_S = \mu_S R_D^{\alpha}$, $\mu_S = \frac{1+K_S}{\Omega_{DS}\rho_S}$, $B_S = \frac{(K_S)^l (\mu_S)^n}{\exp(K_S) l! n!}$, and Ω_{DS} is the fading power.

Similarly, unitizing [2, Eq. (3.351.1)], we have the PDF of γ_E as

$$
\begin{aligned}
f_{\gamma_E}(x) &= \int_0^{\infty} f_{\lambda_{DE}}(xy)\, f_{d_{DE}^{\alpha}}(y)\, y dy \\
&= \sum_{s=0}^{\infty} A_E x^s \frac{\gamma}{R_D} \int_0^{R_D^{\alpha}} y^{s+\gamma} \exp(-\mu_E x y)\, dy \\
&= \sum_{s=0}^{\infty} \beta_E x^{-\gamma-1} \Upsilon(s+\gamma+1, \phi_E x), \qquad (2.75)
\end{aligned}
$$

where $\gamma = \frac{1}{\alpha}$, $\beta_E = \frac{\tau A_E (\mu_E)^{-s-\gamma-1}}{R_D}$, $\mu_E = \frac{1+K_E}{\Omega_{DE}\rho_D}$, $A_E = a_E \mu_E \exp(-K_E)$, $a_E = \frac{1}{(s!)^2}(K_E \mu_E)^s$, and $\phi_E = \mu_E R_D^{\alpha}$.

Employing [15, Eq. (8.4.16.1)] and [16, Eq. (12)], the SOP in this case, is obtained as

$$
\begin{aligned}
P_{\text{out,up}}^{\text{L}} &= \Pr\{\gamma_S \le \Theta \gamma_E\} = \int_0^{\infty} F_{\gamma_S}(\Theta x)\, f_{\gamma_E}(x)\, dt \\
&= 1 - \sum_{l=0}^{M} \sum_{n=0}^{l} \beta_s \Theta^{-\varpi} \int_0^{\infty} x^{-\varpi} \Upsilon(n+\varpi, \phi_s \Theta x) \sum_{s=0}^{T} \beta_e x^{-\tau-1}
\end{aligned}
$$

$$
\begin{aligned}
&\times \Upsilon\left(s+\tau+1, \phi_e x\right) dx \\
&= 1-\sum_{l=0}^{\infty} \sum_{n=0}^{l} \beta_S \Theta^{-\varpi} \sum_{s=0}^{\infty} \beta_E \int_0^{\infty} x^{-\varpi-\gamma-1} \Upsilon\left(s+\gamma+1, \phi_E x\right) \\
&\times \Upsilon\left(n+\varpi, \Theta \phi_S x\right) dx \\
&= 1-\sum_{l=0}^{M} \sum_{n=0}^{l} \beta_s \Theta^{-\varpi} \sum_{s=0}^{T} \beta_e \int_0^{\infty} x^{-\varpi-\tau-1} G_{1,2}^{1,1}\left[\phi_e x \left|{}_{s+\tau+1,0}^{1}\right.\right] \\
&\times G_{1,2}^{1,1}\left[\Theta \phi_s x \left|{}_{n+\varpi,0}^{1}\right.\right] dx \\
&= 1-\sum_{l=0}^{\infty} \sum_{n=0}^{l} \beta_S \Theta^{-\varpi} \sum_{s=0}^{\infty} \beta_E {\phi_E}^{\varpi+\gamma} G_{3,3}^{2,2}\left[\frac{\Theta \phi_S}{\phi_E} \middle| \begin{matrix} 1, \varpi-s, 1+\varpi+\gamma \\ n+\varpi, \varpi+\gamma, 0 \end{matrix}\right],
\end{aligned}
\tag{2.76}
$$

where $G_{p,q}^{m,n}\left[x \left|{}_{b_1,\ldots,b_q}^{a_1,\ldots,a_p}\right.\right]$ is the Meijer's G-function, as defined by [2, Eq. (9.301)].

Using [2, Eq. (1.4.13)] and $\lim_{z\to 0^+} {}_pF_q\left(a, b, z\right) = 1$ [17], for Meijer-G function, it is known that

$$
\begin{aligned}
&\lim_{x\to 0} G_{p,q}^{m,n}\left[x \left|{}_{b_1,\ldots,b_q}^{a_1,\ldots,a_p}\right.\right] \\
&\quad = \sum_{k=1}^{m} \frac{\prod_{j=1, j\neq k}^{m} \Gamma\left(b_j-b_k\right) \prod_{j=1}^{n} \Gamma\left(1+b_k-a_j\right)}{\prod_{j=n+1}^{p} \Gamma\left(a_j-b_k\right) \prod_{j=m+1}^{q} \Gamma\left(1+b_k-b_j\right)} x^{b_k} + o\left(x^{b_k}\right),
\end{aligned}
\tag{2.77}
$$

if $p \leq q$ and for $1 \leq j, k \leq m$, $j \neq k, b_j - b_k \notin \mathbb{Z}$ hold. Then, when $x \to 0$, we can have

$$
\begin{aligned}
&G_{3,3}^{2,2}\left[x \left| \begin{matrix} 1, \varpi-s, 1+\varpi+\gamma \\ n+\varpi, \varpi+\gamma, 0 \end{matrix}\right.\right] \\
&\quad = \begin{cases} \frac{s!}{\gamma \varpi} x^{\varpi} + \frac{\Gamma(-\gamma)\Gamma(1+s+\gamma)}{\varpi+\gamma} x^{\varpi+\gamma} + o(x^{\varpi+\gamma}), & n=0; \\ \frac{\Gamma(n-\gamma)\Gamma(1+s+\gamma)}{\varpi+\gamma} x^{\varpi+\gamma} + o(x^{\varpi+\gamma}), & n \neq 0 \end{cases}.
\end{aligned}
\tag{2.78}
$$

Thus, when $\Omega_S \to \infty$, the asymptotic SOP, in this case, is obtained as

$$
P_{\text{out,up}}^{\text{L},\infty} = 1-\sum_{l=0}^{\infty} \sum_{n=0}^{l} \beta_S \Theta^{-\varpi} \sum_{s=0}^{\infty} \beta_E {\phi_E}^{\varpi+\gamma} \times G_{3,3}^{2,2}\left[\frac{\Theta \phi_S}{\phi_E} \middle| \begin{matrix} 1, \varpi-s, 1+\varpi+\gamma \\ n+\varpi, \varpi+\gamma, 0 \end{matrix}\right]
$$

$$= 1 - \underbrace{\sum_{l=0}^{\infty} \beta_S \Theta^{-\varpi} \sum_{s=0}^{\infty} \beta_E \phi_E{}^{\varpi+\gamma} \times G_{3,3}^{2,2}\left[\frac{\Theta\phi_S}{\phi_E} \middle| \begin{matrix} 1, \varpi - s, 1 + \varpi + \gamma \\ \varpi, \varpi + \gamma, 0 \end{matrix}\right]}_{n=0}$$

$$- \underbrace{\sum_{l=1}^{\infty} \sum_{n=1}^{l} \beta_S \Theta^{-\varpi} \sum_{s=0}^{\infty} \beta_E \phi_E{}^{\varpi+\gamma} \times G_{3,3}^{2,2}\left[\frac{\Theta\phi_S}{\phi_E} \middle| \begin{matrix} 1, \varpi - s, 1 + \varpi + \gamma \\ n + \varpi, \varpi + \gamma, 0 \end{matrix}\right]}_{n \neq 0}$$

$$\overset{Eq.(2.78)}{=} -\left(\frac{\Theta\phi_S}{\phi_E}\right)^{\gamma} \sum_{l=0}^{\infty} \sum_{n=0}^{l} \sum_{s=0}^{\infty} \frac{\gamma \varpi (K_S)^l (K_E)^s \Gamma(n-\gamma) \Gamma(1+s+\gamma)}{\exp(K_S + K_E)\, l! n! (s!)^2 (\varpi + \gamma)}$$

$$+ o\left((\phi_S)^{\gamma}\right) \tag{2.79}$$

Based on the definition of the secrecy diversity order (SDO) presented in [18], we can derive the SDO in this case as

$$G_d = \gamma = \frac{1}{\alpha}. \tag{2.80}$$

2.2.3.2 $D - E$ Link Suffering Weibull Fading

In this case, we have $\gamma_E = \frac{\rho_D |h_{DE}|^2}{d_{DE}^{\alpha}} = \frac{\lambda_{DE}}{d_{DE}^{\alpha}}$. The PDF of the power gain over $D - E$ link $|h_{DE}|^2$ is

$$f_{|h_{DE}|^2}(x) = \frac{b}{a^b} x^{b-1} \exp\left(-\frac{x^b}{a^b}\right), \tag{2.81}$$

where a is the scale parameter, b is the Weibull fading parameter.[9] When $b = 1$, the Weibull distribution becomes exponential; $b = 2$ implies the well-known Rayleigh distribution. Then, the PDF of λ_{DE} is obtained as

$$f_{\lambda_{DE}}(x) = \frac{b}{(\rho_D a)^b} x^{b-1} \exp\left(-\frac{x^b}{(\rho_D a)^b}\right). \tag{2.82}$$

Thus, we can further have the CDF of d_{DE}^{α} as

$$F_{d_{DE}^{\alpha}}(x) = \Pr\left\{d_{DE}^{\alpha} \leq x\right\} = \begin{cases} \frac{x^{\gamma}}{R_D}, & \text{if } 0 < x \leq R_D^{\alpha}; \\ 1, & \text{elseif } x > R_D^{\alpha}; \\ 0, & \text{else} \end{cases}. \tag{2.83}$$

Using Eq. (2.83), we obtain the PDF of d_{DE}^{α} as

[9] In Sect. 2.2 we only consider the case that $b \in \mathbb{Z}^+$ for mathematical tractability.

$$f_{d_{DE}^{\alpha}}(x) = \frac{\gamma x^{\gamma-1}}{R_D},\ 0 < x \le R_D^{\alpha}. \tag{2.84}$$

So, the PDF of $\gamma_E = \frac{\rho_D |h_{DE}|^2}{d_{DE}^{\alpha}}$ can be derived as

$$\begin{aligned} f_{\gamma_E}(x) &= \int_0^{\infty} f_{\lambda_{DE}}(xy)\, f_{d_{DE}^{\alpha}}(y)\, y dy \\ &= \frac{b}{(\rho_D a)^b} \frac{\gamma}{R_D} x^{b-1} \int_0^{R_D^{\alpha}} y^{\gamma+b-1} \exp\left(-\frac{x^b}{(\rho_D a)^b} y^b\right) dy \\ &= \frac{(\rho_D a)^{\gamma}\gamma}{R_D} x^{-\gamma-1} \Upsilon\left(\frac{\tau}{b}+1, \frac{x^b}{(\rho_D a)^b}(R_D)^{\frac{\alpha}{b}}\right) \\ &= A_E x^{-\gamma-1} \Upsilon\left(\frac{\gamma}{b}+1, B_E x^b\right), \end{aligned} \tag{2.85}$$

where $A_E = \frac{(\rho_D a)^{\gamma}\gamma}{R_D}$ and $B_E = \frac{R_D^{\frac{\alpha}{b}}}{(\rho_D a)^b}$.

Thus, adopting [16, Eq. (21)], the SOP in this case is finally written as

$$\begin{aligned} P_{\text{out,up}}^{\text{L}} &= \Pr\{\gamma_S \le \Theta\gamma_E\} = \int_0^{\infty} F_{\gamma_S}(\Theta x)\, f_{\gamma_E}(x)\, dt \\ &= 1 - A_E \sum_{l=0}^{\infty}\sum_{n=0}^{l} \beta_S \Theta^{-\varpi} \int_0^{\infty} x^{-\gamma-\varpi-1} \Upsilon(n+\varpi, \phi_S \Theta x)\, \Upsilon\left(\frac{\gamma}{b}+1, B_E x^b\right) dx \\ &= 1 - A_E \sum_{l=0}^{\infty}\sum_{n=0}^{l} \beta_S \Theta^{-\varpi} \int_0^{\infty} x^{-\gamma-\varpi-1} G_{1,2}^{1,1}\left[\phi_S \Theta x \,\middle|\, {}^{1}_{n+\varpi,0}\right] \\ &\quad \times G_{1,2}^{1,1}\left[B_E x^b \,\middle|\, {}^{1}_{\frac{\gamma}{b}+1,0}\right] dx \\ &= 1 - A_E \sum_{l=0}^{M}\sum_{n=0}^{l} \beta_s \Theta^{-\varpi} \int_0^{\infty} x^{-\tau-\varpi-1} G_{1,2}^{1,1}\left[\phi_s \Theta x \,\middle|\, {}^{1}_{n+\varpi,0}\right] \\ &\quad \times G_{1,2}^{1,1}\left[B_E x^b \,\middle|\, {}^{1}_{\frac{\tau}{b}+1,0}\right] dx \\ &= 1 - \frac{A_E \Theta^{\gamma} b^{-\gamma-1.5}}{(2\pi)^{0.5(b-1)}} \sum_{l=0}^{\infty}\sum_{n=0}^{l} b^n \beta_S (\phi_S)^{\gamma+\varpi} \\ &\quad \times G_{1+2b,2+b}^{1+b,1+b}\left[\frac{B_E b^b}{(\phi_S\Theta)^b} \,\middle|\, {}^{1,\Delta(b,1+\gamma-n),\Delta(b,1+\gamma+\varpi)}_{\Delta\left(1,\frac{\gamma}{b}+1\right),\Delta(b,\gamma+\varpi),0}\right], \end{aligned} \tag{2.86}$$

where $\Delta(k,a) = \frac{a}{k}, \frac{a+1}{k}, ..., \frac{a+k-1}{k}$.

For Meijer-G function, as indicated by [19, Eq. (A.1)], when $x \to \infty$, we have

$$\lim_{x\to\infty} G_{p,q}^{m,n}\left[x\left|\begin{matrix}a_1,\ldots,a_p\\ b_1,\ldots,b_q\end{matrix}\right.\right] = \sum_{k=1}^{n} \frac{\prod_{j=1,j\neq k}^{n} \Gamma\left(a_k - a_j\right) \prod_{j=1}^{m} \Gamma\left(1 + b_j - a_k\right)}{\prod_{j=n+1}^{p} \Gamma\left(1 + a_j - a_k\right) \prod_{j=m+1}^{q} \Gamma\left(a_k - b_j\right)} \times x^{a_k - 1}\left(1 + O\left(\frac{1}{x}\right)\right), \tag{2.87}$$

where $p \geq q$ and $a_k - a_l \notin \mathbb{Z}$, $(k, l = 1, 2, \ldots, n, k \neq l)$.

Similar to the derivation of Eq. (2.79), the asymptotic SOP and the SDO, in this case, are obtained as

$$P_{\text{out,up}}^{\text{L},\infty} = -\frac{\varpi A_E (\Theta\phi_S)^{\gamma} b^{-\gamma-0.5}}{(2\pi)^{0.5(b-1)} \exp\left(K_S\right)} \sum_{l=0}^{\infty} \sum_{n=0}^{l} \frac{\Gamma\left(1 - \Delta\left(b, 1 + \gamma - n\right)\right) \Gamma\left(\frac{\gamma}{b} + 1\right)}{b^{-n} (K_S)^{-l} l! n! \left(\gamma + \varpi\right)} + o\left((\phi_S)^{\gamma}\right) \tag{2.88}$$

and

$$G_d = \gamma = \frac{1}{\alpha}, \tag{2.89}$$

respectively.

2.2.4 Numerical Results and Discussion

In this section, Monte Carlo simulations are carried out to validate our proposed analytical expressions for the SOP over both downlink and uplink. The main parameters are set as $H_{\max} = 50$ m, $H_{\min} = 10$ m, $R_S = 100$ m, $\rho_S = 40$ dB, $\Omega_{SE} = 1$, $K_D = K_E = 2$, $\alpha = 3$, $R_{\text{th}} = 1$ bits/s/Hz, $R_D = 100$ m, $a = 0.5$, and $b = 1$. We run 10^5 trials for the Monte Carlo simulations and consider 10^5 times the systems' realizations.

2.2.4.1 Secrecy Outage Analysis of Downlink

In this subsection, the SOP in the downlink of the considered system will be investigated in Figs. 2.18, 2.19, 2.20 and 2.21.

In the first experiment, the impact of the received signal variance at the eavesdropper Ω_{SE} on the SOP was studied and shown in Fig. 2.18. We can see that SOP decreases as Ω_{SE} increases, showing that Ω_{SE} negatively affects SOP. A larger Ω_{SE} gives a better channel condition for the eavesdropping link between S and E. More-

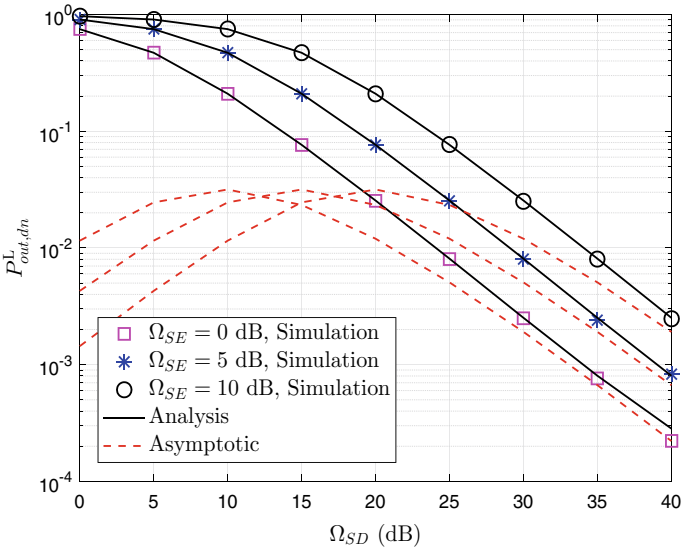

Fig. 2.18 SOP versus Ω_{SD} for various Ω_{SE}

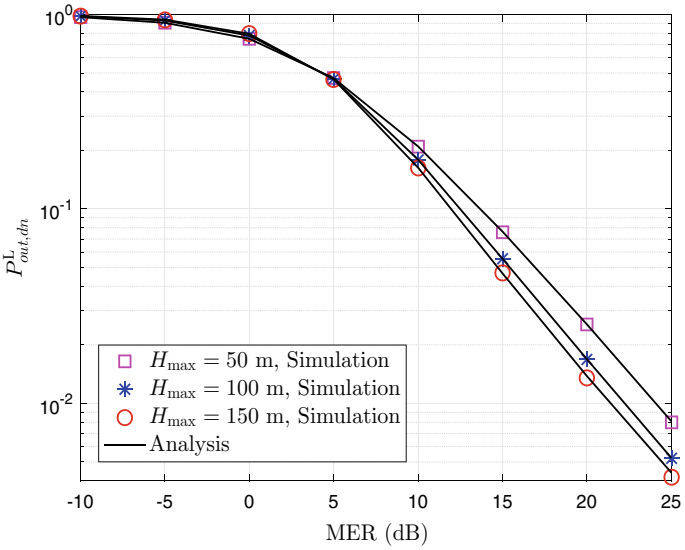

Fig. 2.19 SOP versus MER for various $H_{\max}$

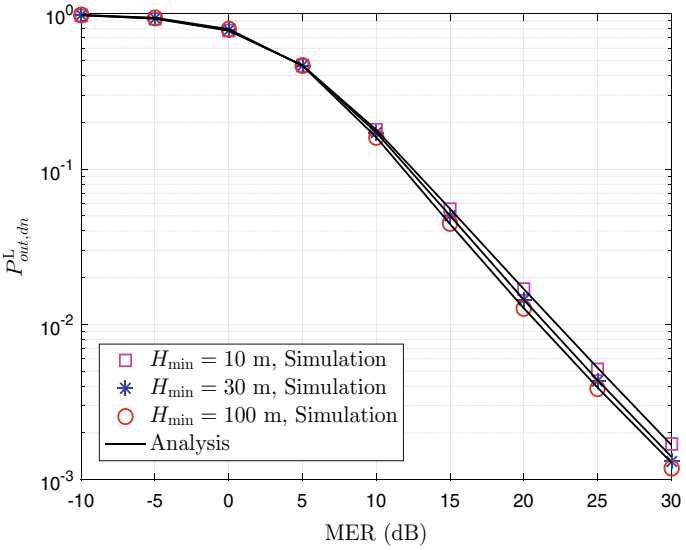

Fig. 2.20 SOP versus MER for various $H_{\min}$

over, the asymptotic SOP of the considered system gets close to the simulation and analysis ones as the average channel gain increases.

In Figs. 2.19 and 2.20, we present simulation and analytical results of SOP versus main-to-eavesdropper ratio (MER), which is defined as Ω_{SD}/Ω_{SE}, to address the impact of the maximum and minimum heights that S can reach, respectively. $H_{\max}$ and $H_{\min}$ do not exhibit a significant influence on SOP, while a large $H_{\max}/H_{\min}$ incurs the improved secrecy outage performance. We can then have that the altitude of S shows a positive effect on SOP but not an effective way.

Figure 2.21 presents the considered system's secrecy outage performance while varying the coverage area's radius on the ground of S, $R_S = 150, 100$, and 50 m. One can find that R_S exhibits a negative effect on SOP, which comes from the fact that a large R_S leads to a large coverage area of S, and then the probability that the distance d_{SE} gets large increases, which results in the received signal power loss at E.

2.2.4.2 *D-E* Link Suffering Rician Fading

Figure 2.22 depicts the SOP with various mean values of the power gain over D-E link, Ω_{DE}, while Ω_{DS} increasing. The SOP with a small Ω_{DE} outperforms that with a large Ω_{DE}, as a large Ω_{DE} represents a higher channel gain for the eavesdropping link. This observation is also similar to the one obtained for the downlink.

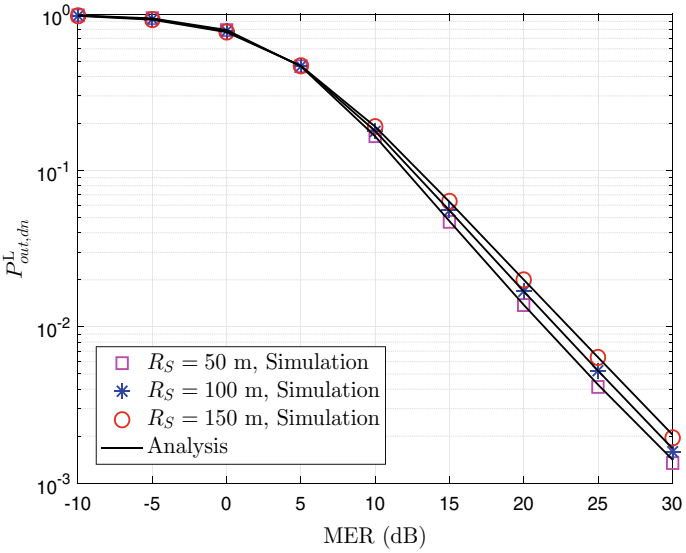

Fig. 2.21 SOP versus MER for various R_S

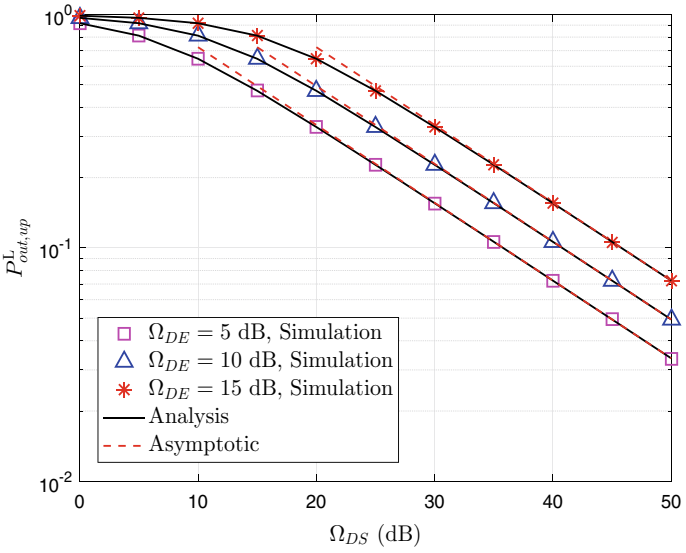

Fig. 2.22 SOP versus Ω_{DS} for various Ω_{DE}

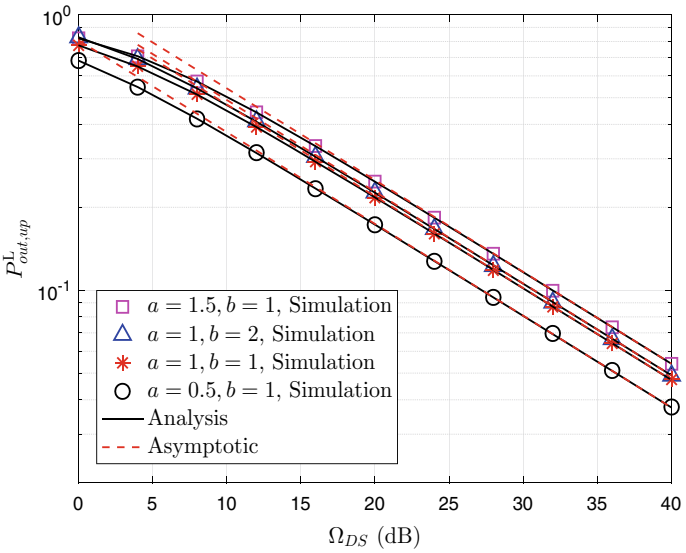

Fig. 2.23 SOP versus Ω_{DS} for various a and b

2.2.4.3 *D-E* Link Suffering Weibull Fading

Considering that the channel between D and E experiences Weibull fading, Fig. 2.23 presents the secrecy outage performance of the considered system with various combinations of channel parameters a and b. The results show that the SOP with a small a outperforms that with a large a because a large a implies more information being overheard by the eavesdropper. However, the secrecy outage lines for different b, namely, $b = 1$ and 2, overlap, indicating that the eavesdropping link's scale parameter does not influence the secrecy outage performance over the uplink of the considered system.

In Fig. 2.24, the SOP lines for various R_D fully overlap with each other, which means that adjusting R_D cannot improve or degrade the SOP of the considered system. It can be explained by the fact that adjusting R_D will influence the received SNR at both S and E, and then the secrecy outage performance will not change anymore.

Furthermore, it can be seen from Figs. 2.22 and 2.23, the derived asymptotic SOP can perfectly match the simulation and analysis ones in the high Ω_{DS} region, which suggests that the proposed asymptotic SOP can be used in practical applications instead of simulation and analysis expressions by exploiting its accuracy in high Ω_{DS} region.

Finally, as presented in Figs. 2.18, 2.19, 2.20, 2.21, 2.22, 2.23 and 2.24, it is noted that Ω_{SD} and Ω_{DS} exhibit the same positive effect on the secrecy outage performance of the considered system. A large Ω_{SD}/Ω_{DS} represents a high channel gain for the

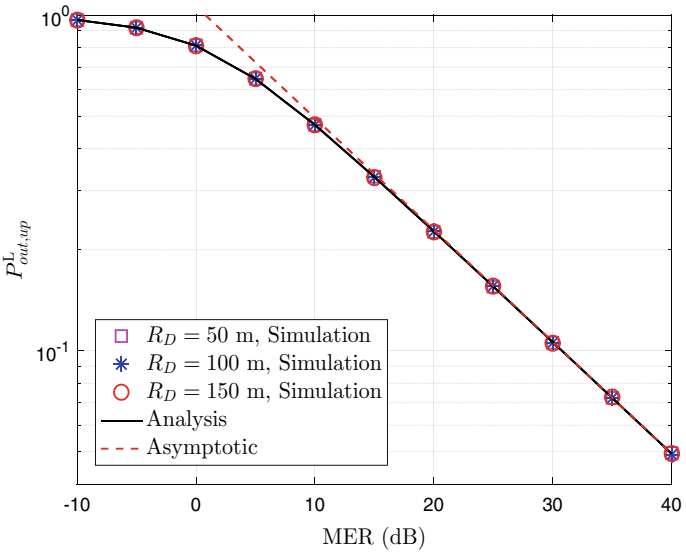

Fig. 2.24 SOP versus MER for various R_D

main link between S and D. Also, simulation and analysis results match very well with each other, which verifies the correctness of our proposed analytical model.

2.2.5 Conclusion

In Sect. 2.2 the secrecy outage performance of the UAV-2-V system has been investigated by deriving the approximated/exact closed-form analytical expressions for the SOP and the asymptotic results of both downlink and uplink. We consider the randomness of the positions of the UAV, the legitimate vehicle, and the eavesdropping vehicle to make our system more realistic and reasonable.

Observing from the simulation results, we can reach some helpful remarks as follows:

(1) The maximum and minimum heights S can weakly influence the secrecy outage performance over the downlink. At the same time, it does not exhibit an evident impact on the secrecy outage performance over the uplink.
(2) The transmit SNR at S weakens the SOP over the downlink, while the transmit SNR at D does not show an apparent impact on the SOP over the uplink.
(3) The radius of S's ground coverage area negatively affects the secrecy outage performance. At the same time, the radius of D also does not exhibit an apparent influence on the secrecy outage performance.

Appendix 2: The proof of Theorem (2.1.1)

Firstly, using Eqs. (2.48) and (2.50), we can obtain the joint PDF of (h, p, t, w) as

$$f_{h,p,w,t}(h, p, w, t) = \frac{\mathbb{I}(\text{con})}{R_S(H_{\max} - H_{\min})\left(R_S^2 - p^2\right)}, \tag{2.90}$$

where $\text{con} = \left(H_{\min} \leqslant h \leqslant H_{\max}, 0 \leqslant p \leqslant R_S, 0 \leqslant w \leqslant \sqrt{R_S^2 - p^2}, 0 \leqslant t \leqslant \sqrt{R_S^2 - p^2}\right)$. $\mathbb{I}(\cdot)$ is the indicator function, i.e., $\mathbb{I}(\text{con}) = 1$ when con is true, or $\mathbb{I}(\text{con}) = 0$ when con is false. Then the joint PDF of (h, p, w, y) is given as

$$f_{h,p,w,y}(h, p, w, y) = f_{h,p,w,t}(h, p, w, g(h, p, w, y))|J|, \tag{2.91}$$

where $g(h, p, w, y) = \sqrt{\frac{1}{y}\left(h^2 + p^2 + w^2\right) - \left(h^2 + p^2\right)}$ and the matrix J is the Jacobian matrix defined as

$$J = \begin{bmatrix} 1 & 0 & 0 & 0 \\ 0 & 1 & 0 & 0 \\ 0 & 0 & 1 & 0 \\ \frac{\partial g(h,p,w,y)}{\partial h} & \frac{\partial g(h,p,w,y)}{\partial p} & \frac{\partial g(h,p,w,y)}{\partial w} & \frac{\partial g(h,p,w,y)}{\partial y} \end{bmatrix}.$$

Substituting J into Eq. (2.91), one can get $f_{h,p,w,y}(h, p, w, y)$ as

$$\begin{aligned} f_{h,p,w,y}(h, p, w, y) = & \frac{1}{R_S(H_{\max} - H_{\min})} \frac{h^2 + p^2 + w^2}{2y^2 g(h, p, w, y)\left(R_S^2 - p^2\right)} \\ & \times \mathbb{I}\Big(H_{\min} \leqslant h \leqslant H_{\max}, 0 \leqslant p \leqslant R_S, 0 \leqslant w \\ & \leqslant \sqrt{R_S^2 - p^2}, 0 \leqslant g(h, p, w, y) \leqslant \sqrt{R_S^2 - p^2}\Big). \end{aligned} \tag{2.92}$$

Then, the PDF of Y is

$$f_Y(y) = \int\int\int f_{h,p,w,y}(h, p, w, y) dh dp dw. \tag{2.93}$$

In the following, let $a_1 = h^2 + p^2$, $b_1 = R_S^2 - p^2$, $c_1 = R_S^2 + h^2$, and $\phi_2 = \frac{{H_{\max}}^2}{{H_{\max}}^2 + R_S^2}$, and recall $\phi_1 = \frac{{H_{\min}}^2}{{H_{\min}}^2 + R_S^2}$ to simplify the analysis.

To deal with the condition in the indicator function of Eq. (2.92), we first consider $y < 1$. Now, we discuss the following two cases:

Case 1: $\phi_1 \leq y < \phi_2$. Thus, the indicator function of Eq. (2.92) can be derived as

$$\mathbb{I}\left(H_{\min} \leqslant h \leqslant \sqrt{\frac{y}{1-y}} R_S,\ 0 \leqslant p \leqslant \sqrt{y(R_S^2+h^2)-h^2},\right.$$
$$\left. 0 \leqslant w \leqslant \sqrt{y(R_S^2+h^2)-h^2-p^2}\right). \tag{2.94}$$

Plugging Eq. (2.92) into Eq. (2.93), we obtain that

$$\begin{aligned} f_Y(y) &= \int_{H\,\min}^{\sqrt{\frac{y}{1-y}}R_S} \int_0^{\sqrt{y(R_S^2+h^2)-h^2}} \int_0^{\sqrt{y(R_S^2+h^2)-h^2-p^2}} \frac{1}{R_S(H_{\max}-H_{\min})} \\ &\quad \times \frac{h^2+p^2+w^2}{2y^2 g(h,p,w,y)\left(R_S^2-p^2\right)} dhdpdw \\ &= \frac{1}{\Xi y^{1.5}} \int_{H_{\min}}^{\sqrt{\frac{y}{1-y}}R_S} \int_0^{\sqrt{c_1 y-h^2}} g_1(p,h,y)\, dpdh, \end{aligned} \tag{2.95}$$

where $g_1(p,h,y) = \frac{a_1(y+1)}{b_1} \log \frac{\sqrt{b_1 y}+\sqrt{c_1 y-a_1}}{\sqrt{a_1(1-y)}} + \sqrt{\frac{c_1 y^2-a_1 y}{b_1}}$ and $\Xi = 4R_S(H_{\max}-H_{\min})$.

Case 2: $\phi_2 \leq y < 1$. Then, the indicator function of Eq. 2.92 can be derived as $\mathbb{I}\left(H_{\min} \leqslant h \leqslant H_{\max}, 0 \leqslant p \leqslant \sqrt{y(R_S^2+h^2)-h^2}, 0 \leqslant w \leqslant \sqrt{y(R_S^2+h^2)-h^2-p^2}\right)$.

Similarly, it gives

$$f_Y(y) = \frac{1}{\Xi y^{1.5}} \int_{H_{\min}}^{H_{\max}} \int_0^{\sqrt{c_1 y-h^2}} g_1(p,h,y)\, dpdh. \tag{2.96}$$

Notice that $Y = \frac{h^2+p^2+t^2}{h^2+p^2+w^2}$ and $1/Y$ are identically distributed thus we can easily derive that the PDF of Y satisfies $f_Y(y) = \frac{1}{y^2} f_Y\left(\frac{1}{y}\right)$.

Therefore, one can derive that, when $y > 1$, the PDF of $Y = \frac{h^2+p^2+t^2}{h^2+p^2+w^2}$ is

$$f_Y(y) = \begin{cases} \frac{1}{\Xi y^{1.5}} \int_{H_{\min}}^{H_{\max}} \int_0^{\sqrt{\frac{c_1}{y}-h^2}} g_2(p,h,y)\, dpdh, & \text{if } 1 < y \leqslant \frac{1}{\phi_2}; \\ \frac{1}{\Xi y^{1.5}} \int_{H_{\min}}^{\sqrt{\frac{R_S^2}{y-1}}} \int_0^{\sqrt{\frac{c_1}{y}-h^2}} g_2(p,h,y)\, dpdh, & \text{elseif } \frac{1}{\phi_2} < y \leqslant \frac{1}{\phi_1} \end{cases}, \tag{2.97}$$

where $g_2(p,h,y) = \frac{a_1(y+1)}{b_1} \log \frac{\sqrt{b_1}+\sqrt{c_1-a_1 y}}{\sqrt{a_1(y-1)}} + \sqrt{\frac{c_1-a_1 y}{b_1}}$.

Thus, combining Eqs. (2.95), (2.96), and (2.97) completes the proof.

2.3 On Power Adaptation Schemes in Aerial-Terrestrial Communications

This section mainly studies the transmission capacity performance of an aerial-terrestrial communication system, in which an unmanned aerial vehicle (S) delivers information bits to a terrestrial receiver (D) by adaptively controlling its transmit power according to the instantaneous CSI. In Sect. 2.3 three adaptive transmission schemes, i.e., optimal simultaneous power and rate adaptation, optimal rate adaptation with constant transmit power, and truncated channel inversion with fixed rate, are considered at S. Closed-form expressions for the EC under these adaptive transmission schemes are derived while considering the randomness of the location of D. Furthermore, some insights are obtained by deriving asymptotic expressions for the EC. Finally, numerical results are proposed to compare the performance of these considered power adaption methods and to confirm the accuracy of the proposed analytical models. Here, making use of Shadowed-Rician (SR) fading channel, we investigate the impacts of the small-scale fading over the aerial-terrestrial channel and the randomness of the position of the terrestrial terminal on the capacity performance of a single-input single-output (SISO) aerial-terrestrial system under three different adaptive transmission schemes: optimal simultaneous power and rate adaptation (OSPRA), optimal rate adaptation with constant transmit power (ORA) schemes and channel inversion with fixed rate (TIFR). The main contributions of Sect. 2.3 can be summarized as follows.

1. We derive the exact and asymptotic expressions for EC while considering the randomness of the location of the terrestrial receiver;
2. Making use of these derived results, the EC performance of these three considered adaptive transmission schemes is studied and compared;
3. The principles of how the fading parameters of SR fading and the randomness of the position of the terrestrial terminal influence the EC performance of the considered system are observed and summarized.

The rest of this section is organized as follows. Section 2.3.1 proposes the capacity analysis of these considered different adaptive transmission schemes. Section 2.3.2 presents the asymptotic analysis of the EC, while Sect. 2.3.3 gives some numerical examples. Section 2.3.4 offers some discussions to show the possible extensions and applications of the proposed analytical method. Finally, Sect. 2.3.5 concludes the work.

2.3.1 Capacity of Aerial-Terrestrial Systems

Here, a SISO aerial-terrestrial system, which consists of a UAV (S) and a terrestrial receiver (D), is considered.[10] By using the instantaneous CSI, S can adaptively adjust its transmit power to realize the optimal EC.[11]

Though, as pointed out in Refs. [21–23], the accuracy of CSI plays a key role in the transmission performance in various wireless communication systems. In Sect. 2.3 the impacts of the imperfect CSI will be ignored to make the presentation more concise, as the main focus of this study is to present the analytical method to investigate the influences of the small-scale fading over the aerial-terrestrial channel and the randomness of the position of the terrestrial terminal on the performance of the considered power adaptation schemes.

Similar to [24] and to study the impact of the randomness of D on the performance of the considered system, it is assumed that D is uniformly distributed in the coverage area of S, which is a circle on the ground with radius R, and the projection of S as the original. Then, one can obtain the transmission distance between S and D as

$$d = \left(r^2 + H^2\right)^{\frac{1}{2}}, \tag{2.98}$$

where r is the distance between D and the original of coverage area of S, H is the height of S from the ground.

Also, it is easy to achieve the PDF of r as

$$f_r(x) = \frac{2x}{R^2},\ 0 \le x \le R, \tag{2.99}$$

and further, we can write the PDF of d as

$$f_d(x) = \frac{2x}{R^2}, \tag{2.100}$$

where $H \le x \le G = (R^2 + H^2)^{\frac{1}{2}}$.

[10] As more computation, memory, and power resources are required to implement complicated signal processing algorithms, which will unavoidably increase the hardware cost of UAVs, it is not reasonable for common commercial UAVs to be equipped with multiple antennas. Moreover, LOS propagation is always available in typical open aerial-terrestrial communication scenarios, leading to better radio quality than traditional cellular networks in urban areas. Therefore, in Sect. 2.3 we only consider a SISO aerial-terrestrial communication system to present the proposed analytical method.

[11] As suggested in [20], spatial channel covariance, defined by long-term statistic information of channels, can be applied in highly mobile mmWave aerial-terrestrial systems to realize the manageability and adaptability of the CSI feedback. Thus, it is reasonable to assume that S can exploit the CSI to adjust its transmit power adaptively.

Furthermore, the SR model is adopted in Sect. 2.3 to describe the statistical distribution of aerial-terrestrial links. Without loss of generality, the PDF of the power gain, $|h|^2$, for a SISO system in the SR fading channel is given by [25, Eq. (6)] as[12]

$$f_{|h|^2}(x) = \alpha \exp(-\beta x)\, {}_1F_1(m; 1; \delta x), \quad x \geq 0, \tag{2.101}$$

where $\alpha = \left(\frac{2bm}{2bm+\Omega}\right)^m / (2b)$, $\beta = \frac{1}{2b}$, and $\delta = \frac{\Omega}{2b(2bm+\Omega)}$, Ω and $2b$ are the average power of the LOS and multipath components, respectively, m is the fading severity parameter, and ${}_1F_1(\cdot;\cdot;\cdot)$ is the confluent hypergeometric function of first kind [2].

Then, the received SNR at D can be given as

$$\gamma = \frac{P_t}{\sigma^2}\frac{|h|^2}{d^n} = \frac{\Lambda}{d^n}, \tag{2.102}$$

where n is the path-loss factor, $\Lambda = P_t|h|^2/\sigma^2$, P_t and σ^2 are the transmit power at S and the average power of the AWGN at D.

By variable substitution, it is easy to obtain the PDF and CDF of Λ as

$$f_\Lambda(x) = \alpha \sum_{k=0}^{m-1} \frac{\varsigma(k)}{\lambda^{k+1}} x^k \exp(-\Psi x) \tag{2.103}$$

and

$$F_\Lambda(x) = 1 - \alpha \sum_{k=0}^{m-1} \frac{\varsigma(k)}{\lambda^{k+1}} \sum_{p=0}^{k} \frac{k!\lambda^{k+1-p}}{p!} \frac{x^p \exp(-\Psi x)}{(\beta-\delta)^{k+1-p}}, \tag{2.104}$$

where $\Psi = \frac{\beta-\delta}{\lambda}$, $\lambda = P_t/\sigma^2$, $\varsigma(k) = \frac{(-1)^k(1-m)_k\delta^k}{(k!)^2}$ and $(t)_k = t(t+1)\cdots(t+k-1)$ is the Pochhammer symbol.

2.3.1.1 Optimal Simultaneous Power and Rate Adaptation (OSPRA) Scheme

Under the OSPRA scheme, SNR is assumed to be well-tracked by D and then sent back to S with no error. Thus, S can adapt its transmit power according to dynamic channel conditions. Namely, making use of the instantaneous CSI, the transmit power at S is adjusted by

$$P_t = \max\left\{\overline{P}_t\left(\gamma_0^{-1} - \gamma^{-1}\right), 0\right\}, \tag{2.105}$$

[12] As shown in [25], the PDF of the power gain is achieved by applying variables substitution in [25, Eq. (3)].

where $\overline{P}_t$ is the average transmit power at S, γ_0 is the optimal cutoff SNR below which S will suspend data transmission and must satisfy

$$\int_H^G \int_{\gamma_0 d^n}^{\infty} \left(1/\gamma_0 - d^n/x\right) f_\Lambda(x) f_d(d) dx d(d) = 1, \tag{2.106}$$

where $f_\gamma(\gamma)$ is the PDF of γ.

It may be impossible in MATLAB to calculate the double integral identity directly in the optimization constraint in Eq. (2.106). Here, we perform some simplifications as

$$\begin{aligned}
&\int_H^G \int_{\gamma_0 d^n}^{\infty} \left(\frac{1}{\gamma_0} - \frac{d^n}{x}\right) f_\Lambda(x) f_d(d) dx d(d) \\
&\quad = \frac{1}{\gamma_0} \alpha \sum_{k=0}^{m-1} \frac{\varsigma(k)}{\lambda^{k+1}} \sum_{p=0}^{k} \frac{k! \lambda^{k+1-p}}{p!} \frac{\gamma_0^p}{(\beta-\delta)^{k+1-p}} \frac{2}{R^2} \\
&\quad \times \int_H^G d^{np+1} \exp\left(-\Psi \gamma_0 d^n\right) d(d) - \frac{2\alpha}{R^2} \sum_{k=0}^{m-1} \frac{\varsigma(k)}{\lambda^{k+1}} \\
&\quad \times (\Psi)^{-k} \int_H^G d^{n+1} \Gamma\left(k, \Psi \gamma_0 d^n\right) d(d).
\end{aligned} \tag{2.107}$$

Further, when $m = 1$, the optimization constraint can be simplified as

$$\frac{2\alpha}{R^2 \gamma_0} \frac{1}{\beta - \delta} \int_H^G d \exp\left(-\Psi \gamma_0 d^n\right) d(d) - \frac{2\alpha}{R^2 \lambda} \int_H^G d^{n+1} \Gamma\left(0, \Psi \gamma_0 d^n\right) d(d) = 1. \tag{2.108}$$

Therefore, the achievable EC (in bits/s/Hz) under the OSPRA scheme can be given as [26]

$$\begin{aligned}
\langle C \rangle_{\text{ospra}} &= \int_{\gamma_0 d^n}^{\infty} \log_2 \left(\frac{x}{\gamma_0 d^n}\right) f_\Lambda(x) dx \\
&= \frac{\alpha}{\ln 2} \sum_{k=0}^{m-1} \frac{\varsigma(k)}{\lambda^{k+1}} \int_{\gamma_0}^{\infty} \ln\left(\frac{x}{\gamma_0 d^n}\right) x^k \exp(-\Psi x) dx,
\end{aligned} \tag{2.109}$$

which can be further written as

$$\langle C\rangle_{\text{ospra}} \overset{y=x-\gamma_0 d^n}{=} \frac{\alpha}{\ln 2}\sum_{k=0}^{m-1}\frac{\varsigma(k)}{\lambda^{k+1}}\exp\left(-\Psi\gamma_0 d^n\right) \times \underbrace{\int_0^{\infty}\ln\left(1+\frac{y}{\gamma_0 d^n}\right)\left(y+\gamma_0 d^n\right)^k\exp\left(-\Psi y\right)dy}_{\mathcal{I}_0}. \tag{2.110}$$

Using binomial expansion and the Appendix 2 in [27], $\mathcal{I}_0$ can be calculated as

$$\mathcal{I}_0 = \sum_{p=0}^{k}\binom{k}{p}p!e^{\frac{(\beta-\delta)\gamma_0 d^n}{\lambda}}\cdot\sum_{q=1}^{p+1}\frac{\lambda^q\Gamma\left(q-p-1,\frac{(\beta-\delta)\gamma_0 d^n}{\lambda}\right)}{(\beta-\delta)^q(\gamma_0 d^n)^{q-k-1}}, \tag{2.111}$$

where $\Gamma(\cdot,\cdot)$ denotes the upper incomplete gamma function [2]. Note that $\Gamma(\cdot,\cdot)$ presented here cannot be calculated directly in MATLAB due to $q-p-1\le 0$, and this can be solved by transforming $\Gamma(\cdot,\cdot)$ into the generalized hypergeometric function form, given by [33]

$$\Gamma(a,z) = z^{a-1}\exp(-z)\,{}_2F_0\left(1-a,1;;-\frac{1}{z}\right), \tag{2.112}$$

where ${}_pF_q(:;:;:)$ is the generalized hypergeometric function as [2, Eq. (9.14.1)].

Therefore, let $\sum_{k,p,q} = \sum_{k=0}^{m-1}\frac{\alpha\varsigma(k)}{\ln 2}\sum_{p=0}^{k}\binom{k}{p}p!\sum_{q=1}^{p+1}$ for simplification, and using Eq. (2.111) into Eq. (2.110), the EC under the OSPRA scheme can be achieved as

$$\langle C\rangle_{\text{ospra}} = \sum_{k,p,q}\frac{\Gamma\left(q-p-1,\frac{(\beta-\delta)\gamma_0 d^n}{\lambda}\right)}{(\beta-\delta)^q\gamma_0^{q-k-1}\lambda^{k+1-q}d^{n(q-k-1)}}. \tag{2.113}$$

Finally, considering the randomness of d, the EC under the OSPRA scheme is given as

$$\langle C\rangle_{\text{ospra}} = \frac{2}{R^2}\sum_{k,p,q}\frac{1}{(\beta-\delta)^q\gamma_0^{q-k-1}\lambda^{k+1-q}} \times\left[g\left(\frac{(\beta-\delta)\gamma_0}{\lambda},q-p-1,1+n(k+1-q),n,G\right)\right. \left.-g\left(\frac{(\beta-\delta)\gamma_0}{\lambda},q-p-1,,1+n(k+1-q),n,H\right)\right], \tag{2.114}$$

where $\vartheta + \phi n > -1$, $\vartheta > -1$, and

$$g(\xi, \phi, \vartheta, n, x) = \int_0^x d^{\vartheta} \Gamma\left(\phi, \xi d^n\right) d(d) = \frac{1}{1+\vartheta} \xi^{-\frac{1+\vartheta}{n}} \left(\gamma\left(\phi + \frac{1+\vartheta}{n}, \xi x^n\right) + \xi^{\frac{1+\vartheta}{n}} x^{1+\vartheta} \Gamma\left(\phi, \xi x^n\right)\right). \tag{2.115}$$

2.3.1.2 Optimal Rate Adaptation with Constant Transmit Power (ORA) Scheme

Under this scheme, S adopts the optimal rate to adapt to channel fading with a constant transmit power. The achievable EC (in bit/s/Hz) can expressed as [26]

$$\langle C \rangle_{\text{ora}} = \int_0^{\infty} \log_2(1+\gamma) f_{\gamma}(\gamma) d\gamma. \tag{2.116}$$

Using Eq. (2.103), the EC of the ORA scheme in the considered SISO aerial-terrestrial system can be written as

$$\langle C \rangle_{\text{ora}} = \alpha \sum_{k=0}^{m-1} \frac{\varsigma(k)}{\lambda^{k+1}} \underbrace{\int_0^{\infty} x^k \log_2\left(1 + \frac{x}{d^n}\right) \exp(-\Psi x)\, dx}_{\mathcal{I}_1}. \tag{2.117}$$

Similar to the calculation of $\mathcal{I}_0$ presented in Eq. (2.110), one can easily derive $\mathcal{I}_1$ as

$$\mathcal{I}_1 = \frac{\Gamma(k+1) \exp(\Psi d^n)}{\ln 2} \sum_{s=1}^{k+1} d^{n(k+1-s)} \frac{\Gamma(s-k-1, \Psi d^n)}{\Psi^s}. \tag{2.118}$$

By using [9], we can have

$$\exp\left(\Psi d^n\right) \Gamma\left(s-k-1, \Psi d^n\right) = \frac{1}{\Gamma(2+k-s)} G_{1,2}^{2,1}\left[\Psi d^n \left|{}^{s-k-1}_{0,s-k-1}\right.\right], \tag{2.119}$$

where $G_{p,q}^{m,n}\left[x \left|{}^{a_1,\ldots,a_p}_{b_1,\ldots,b_q}\right.\right]$ is the Meijer's G-function, as defined by [2, Eq. (9.301)].

Considering the randomness of d and using [16, Eq. (26)], we can further derive $\mathcal{I}_1$ as

$$\mathcal{I}_1 = \frac{2\Gamma(k+1)}{R^2 \ln 2} \sum_{s=1}^{k+1} \frac{h(s,k,G^n) - h(s,k,H^n)}{\Psi^s \Gamma(2+k-s)}, \tag{2.120}$$

where $h(s,k,x) = \frac{1}{n} x^{k+1-s+\frac{2}{n}} G_{2,3}^{2,2}\left[\Psi x \left| \begin{matrix} s-k-1, s-k-\frac{2}{n} \\ 0, s-k-1, s-k-1-\frac{2}{n} \end{matrix} \right.\right]$.

Therefore, substituting Eq. (2.120) in Eq. (2.117), we can easily obtain the EC as

$$\langle C \rangle_{\text{ora}} = \frac{2\alpha}{R^2 \ln 2} \sum_{k=0}^{m-1} \frac{\varsigma(k)\, \Gamma(k+1)}{\lambda^{k+1}} \sum_{s=1}^{k+1} \frac{h(s,k,G^n) - h(s,k,H^n)}{\Psi^s \Gamma(2+k-s)}. \tag{2.121}$$

2.3.1.3 Channel Inversion with Fixed Rate (TIFR) Scheme

Under this scheme, S adapts its transmit power to maintain a constant SNR at D, which inverts the channel fading only above a fixed fade depth. The EC under the TIFR scheme is derived as [26]

$$\langle C \rangle_{\text{tifr}} = \log_2\left(1 + \frac{1}{\mathcal{I}_2}\right) \cdot (1 - P_{\text{out}}), \tag{2.122}$$

where $P_{\text{out}} = 1 - \int_{\gamma_0}^{\infty} f_\gamma(\gamma) d\gamma$ and $\mathcal{I}_2 = \int_{\gamma_0}^{\infty} \gamma^{-1} f_\gamma(\gamma) d\gamma$.

P_{out} can be easily derived by exploiting Eq. (2.104) as

$$P_{\text{out}} = 1 - \alpha \sum_{k=0}^{m-1} \frac{\varsigma(k)}{\lambda^{k+1}} \sum_{p=0}^{k} \frac{k! \lambda^{k+1-p}}{p!} \frac{{\gamma_0}^p d^{np} \exp(-\Psi \gamma_0 d^n)}{(\beta - \delta)^{k+1-p}}. \tag{2.123}$$

Considering the randomness of d, P_{out} can further written as

$$\begin{aligned} P_{\text{out}} = 1 - \frac{2\alpha}{R^2} \sum_{k=0}^{m-1} \varsigma(k) \sum_{p=0}^{k} \frac{k! \lambda^{\frac{2}{n}}}{p!} \frac{{\gamma_0}^{-\frac{2}{n}}}{n(\beta-\delta)^{k+1+\frac{2}{n}}} \\ \times \left[\gamma\left(p + \frac{2}{n}, \Psi\gamma_0 G^n\right) - \gamma\left(p + \frac{2}{n}, \Psi\gamma_0 H^n\right)\right], \end{aligned} \tag{2.124}$$

where $\gamma(\cdot,\cdot)$ denotes the lower incomplete gamma function [2].

Using Eq. (2.103), we can have $\mathcal{I}_2 = \alpha \sum_{k=0}^{m-1} \frac{\varsigma(k)}{\lambda} \frac{d^n \Gamma(k, \Psi\gamma_0 d^n)}{(\beta-\delta)^k}$. Considering the randomness of d, we can further calculate $\mathcal{I}_2$ as

$$\mathcal{I}_2 = \frac{2\alpha}{R^2} \sum_{k=0}^{m-1} \frac{\varsigma(k)}{\lambda(\beta-\delta)^k} \left(u(k,G) - u(k,H)\right), \tag{2.125}$$

where

$$u(k,x) = \int_0^x d^{n+1}\Gamma\left(k, \Psi\gamma_0 d^n\right) d(d)$$
$$= \frac{x^{2+n}\Gamma(k, \Psi\gamma_0 x^n) + (\Psi\gamma_0)^{-\frac{2+n}{n}}\gamma\left(1+k+\frac{2}{n}, \Psi\gamma_0 x^n\right)}{2+n}. \quad (2.126)$$

Therefore, the EC of the TIFR scheme can achieved by inserting Eqs. (2.124) and (2.125) into Eq. (2.122).

2.3.2 Asymptotic Analysis

In this section, the asymptotic analysis is performed in high SNRs, i.e., $\lambda \to \infty$, to achieve some insights and simplify the EC expressions while ignoring the randomness of the position of D.[13] From the previous works [28, 29], the closed-form expression for the asymptotic EC comprises two parts, i.e., the slope and power offset, which govern the EC behaviors in high SNRs. In Sect. 2.3.3 the power offset is the interception on the horizontal axis when λ changes in the dB scale (i.e., log-scale).

2.3.2.1 OSPRA and ORA Schemes

When $\lambda \to \infty$, i.e., $\Phi \to 0$, making use of $\lim_{x\to 0}\frac{\Gamma(s,x)}{x^s} = -\frac{1}{s}$ for $\mathrm{Re}(s) < 0$ and $\lim_{x\to 0}\Gamma(0,x) = -\ln x + \psi(1)$, where $\psi(\cdot)$ denotes the digamma function [2], we have $P = \lim_{\Psi\to 0}\exp(\Psi)\sum_{s=1}^{k+1}\frac{\Gamma(s-k-1,\Psi)}{\Psi^s}$ as

$$P = \underbrace{\lim_{\Psi\to 0}\exp(\Psi)}_{=1}\cdot\lim_{\Psi\to 0}\sum_{s=1}^{k+1}\frac{\Gamma(s-k-1,\Psi)}{\Psi^s}$$
$$= \Psi^{-k-1}\left(\lim_{\Psi\to 0}\sum_{s=1}^{k}\frac{\Gamma(s-k-1,\Psi)}{\Psi^{s-k-1}} + \Gamma(0,\Psi)\right)$$
$$= \Psi^{-k-1}\left(\sum_{s=1}^{k}\frac{1}{k+1-s} - \ln\Psi + \psi(1)\right)$$
$$= \Psi^{-k-1}\left(\psi(k+1) - \ln\Psi\right). \quad (2.127)$$

[13] In this section, we adopt the normalized distance between S and D (namely, $d = 1$) to facilitate the following analysis.

Thus, using Eq. (2.118), the asymptotic EC of the ORA scheme can be given as

$$\langle C\rangle_{\text{ora}}^{\infty}=\frac{\alpha}{\ln 2}\sum_{k=0}^{m-1}\frac{\varsigma\left(k\right)\Gamma\left(k+1\right)}{\left(\beta-\delta\right)^{k+1}}\left(\psi\left(k+1\right)-\ln\Psi\right), \tag{2.128}$$

which can be further simplified as

$$\begin{aligned}\langle C\rangle_{\text{ora}}^{\infty}&\overset{(a)}{=}\frac{1}{\ln 2}\underbrace{\alpha\sum\nolimits_{k=0}^{m-1}\frac{\varsigma\left(k\right)\Gamma\left(k+1\right)}{\left(\beta-\delta\right)^{k+1}}}_{=1}\ln\lambda\\&\quad\times+\frac{\alpha}{\ln 2}\sum\nolimits_{k=0}^{m-1}\frac{\varsigma\left(k\right)\Gamma\left(k+1\right)}{\left(\beta-\delta\right)^{k+1}}\left(\psi\left(k+1\right)-\ln\left(\beta-\delta\right)\right)\\&=\log_2\lambda+\frac{\alpha}{\ln 2}\sum\nolimits_{k=0}^{m-1}\frac{\varsigma\left(k\right)\Gamma\left(k+1\right)}{\left(\beta-\delta\right)^{k+1}}\left(\psi\left(k+1\right)-\ln\left(\beta-\delta\right)\right),\end{aligned} \tag{2.129}$$

where (a) follows $\int_0^{\infty}f_{\gamma}(x)dx=1\Rightarrow\alpha\sum_{k=0}^{m-1}\frac{\varsigma(k)}{\lambda^{k+1}}\int_0^{\infty}x^k\exp\left(-\Psi x\right)dx=1\Rightarrow\alpha\sum_{k=0}^{m-1}\frac{\varsigma(k)\Gamma(k+1)}{(\beta-\delta)^{k+1}}=1$.

By observing Eqs. (2.114) and (2.121), it is easy to find that the EC of the OSPRA and ORA schemes is with a similar format while treating $\frac{(\beta-\delta)\gamma_0}{\lambda}$ in Eq. (2.114) as a variable. Then, the asymptotic EC of the OSPRA scheme can also be derived using the same method presented in this section. In Sect. 2.3 the derivation of the asymptotic EC of the OSPRA scheme is omitted to save the page space.

2.3.2.2 TIFR Scheme

When $\lambda\to\infty$, it is easy to see that $\lim_{\Psi\to 0}\left(1-P_{\text{out}}\right)=1-\lim_{\Psi\to 0}F_{\gamma}\left(\gamma_0\right)=1$ in Eq. (2.122).

Then, the asymptotic result for $\mathcal{I}_2$ as $\lambda\to\infty$ can be derived as

$$\begin{aligned}\mathcal{I}_2&=\alpha\frac{\Gamma\left(0,\Psi\gamma_0\right)}{\lambda}+\alpha\sum_{k=1}^{m-1}\frac{\varsigma\left(k\right)}{\left(\beta-\delta\right)^{k}}\frac{\Gamma\left(k,\Psi\gamma_0\right)}{\lambda}\\&\overset{\lambda\to\infty}{\simeq}\alpha\frac{\psi\left(1\right)+\ln\left(\frac{1}{\Psi\gamma_0}\right)}{\lambda}+\alpha\sum\nolimits_{k=1}^{m-1}\frac{\varsigma\left(k\right)\Gamma\left(k\right)}{\left(\beta-\delta\right)^{k}\lambda}.\end{aligned} \tag{2.130}$$

By using $\log_2(1+x)\approx\log_2(x)$ for $x\gg 1$, the asymptotic EC under TIFR scheme is finally derived as

$$\langle C\rangle_{\text{tifr}}^{\infty} \overset{\lambda\to\infty}{\simeq} \begin{cases} \log_2 \dfrac{\lambda}{\alpha\left(\psi(1)+\ln\left(\frac{1}{\Psi\gamma_0}\right)+\sum\limits_{k=1}^{m-1}\frac{\varsigma(k)\Gamma(k)}{(\beta-\delta)^k}\right)}, & m \geq 2; \\ \log_2\lambda - \log_2\left(\alpha\left(\psi(1)+\ln\left(\frac{1}{\Psi\gamma_0}\right)\right)\right), & m = 1. \end{cases} \tag{2.131}$$

From Eqs. (2.129) and (2.131), we can easily see that the asymptotic ECs under OSPRA and ORA schemes are linear functions to λ in log-scale, where the slope is always unity regardless of any parameter setting. The power offset is independent of λ and only depends on the channel statistics. Although the asymptotic EC under the TIFR scheme is not a linear function concerning λ in log-scale because of the existence of λ in the power offset, the slope changes very slowly in high SNRs, which will be verified in the following simulation results.

2.3.3 Numerical Results

Without loss of generality, we assume that the power of the noise is one and run 10^5 trials for channel state realizations and 10^3 trials for location realizations in the Monte Carlo simulations, by using MATLAB to validate the effectiveness of our proposed analytical models. As the main concern of Sect. 2.3 is to study the impacts of the small-scale fading over the aerial-terrestrial channel and the randomness of the position of the terrestrial terminal on the performance of the considered power adaptation schemes. In this section, the influences of other system factors, e.g., beam width, beam overlapping, and interference, will not be considered. Essentially, such influences can be reflected by the received SNR/signal-to-interference-plus-noise ratio (SINR) at the terrestrial receiver.

Figure 2.25 presents the EC performance of these three adaptive transmission methods in frequent heavy shadowing scenarios. At the same time, D is randomly distributed in the coverage area of S. One can easily see that the EC of three power adaption schemes is improved, while λ increases because the transmitting SNR at S is improved. In the low λ region ($\lambda < 114$ dB), the TIFR scheme has the worst EC performance, and OSPRA is the best one, as the instantaneous CSI is available under the OSPRA scheme. When λ increases to 130 dB, OSPRA and ORA schemes show the same EC performance, which outperforms the TIFR scheme. Because the transmit power under the OSPRA scheme approaches the average transmit power.

In Fig. 2.26, the scenarios of infrequent light shadowing ($m = 20$, which corresponds to open areas with less obstruction of the LOS) and frequent heavy shadowing ($m = 1$, in which there are some more obstructions of the LOS) are both considered. Obviously, the EC of these three schemes in infrequent light shadowing scenarios outperforms the three schemes in frequent heavy shadowing scenarios because of strong LOS components existing in rare light shadowing scenarios.

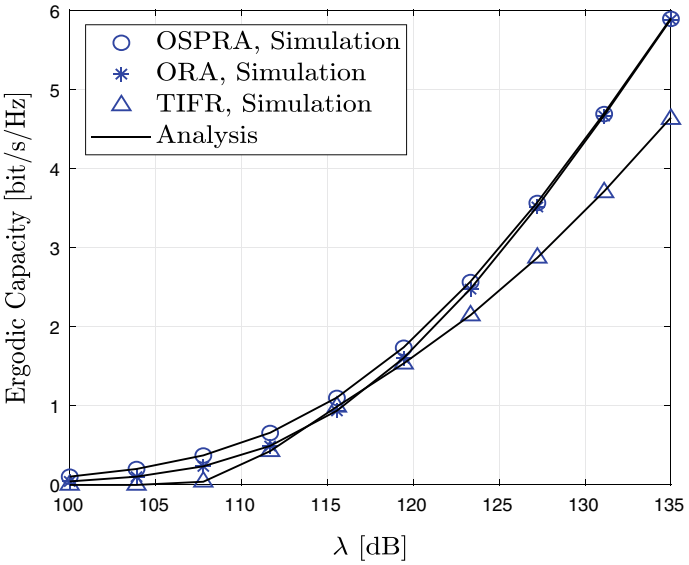

Fig. 2.25 EC versus λ for $m = 1, b = 0.063, \Omega = 8.97 \times 10^{-4}$ (frequent heavy shadowing), $H =$ 200 Km, $R = 10$ Km, $n = 2$, and $\gamma_0 = 1$ in TIFR

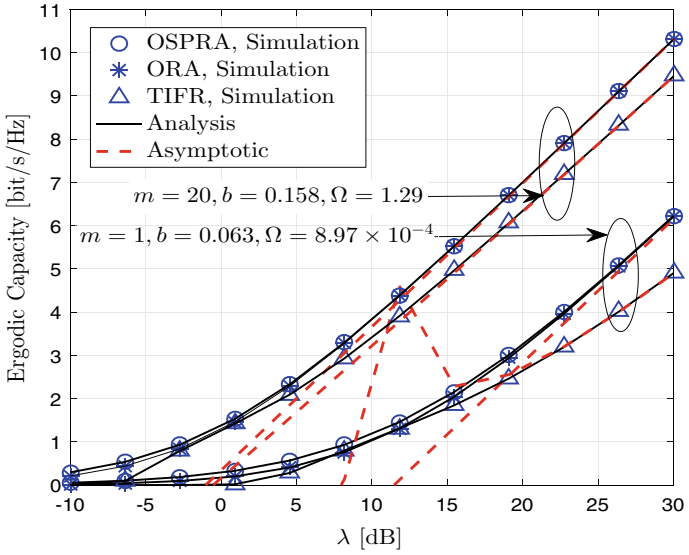

Fig. 2.26 EC versus λ for $\gamma_0 = 1$ in TIFR

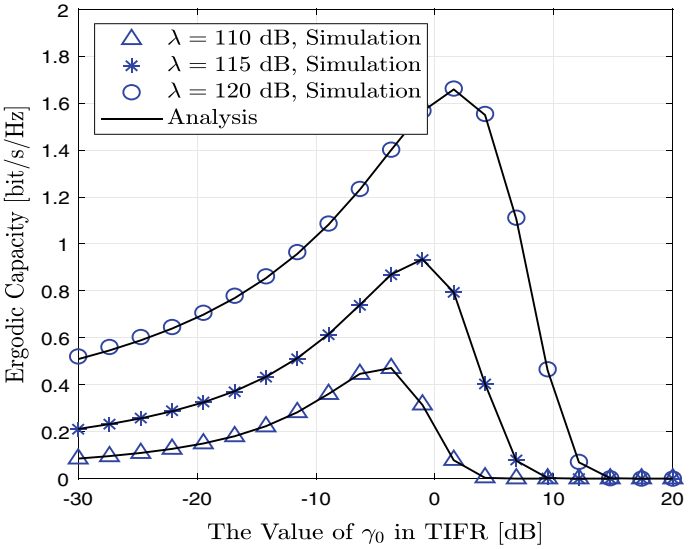

Fig. 2.27 EC versus γ_0 under the TIFR scheme for $m = 1, b = 0.063, \Omega = 8.97 \times 10^{-4}$ (frequent heavy shadowing), $H = 200$ km, $R = 10$ km, and $n = 2$

Figure 2.27 presents the EC performance of the TIFR scheme versus γ_0 in frequent heavy shadowing scenarios. Obviously, the transmitting SNR λ exhibits a positive effect on the EC performance, as increasing λ can improve the received SNR at the ground receiver. Moreover, the EC performance of the TIFR scheme shows various maximum values for different λ, respectively. Therefore, optimal EC can be achieved for the TIFR scheme by setting the values of γ_0. In other words, tradeoffs between outage and EC performance can be designed and realized by carefully choosing the system parameters.

Moreover, in Fig. 2.28, we also depict the EC performance of the TIFR scheme versus λ for various γ_0 in frequent heavy shadowing scenarios. Clearly, the EC performance with a large γ_0 outperforms that with a low γ_0, because a large γ_0 leads to a large P_{out} and a small $\mathcal{I}_2$ as suggested by the definitions of P_{out} and $\mathcal{I}_2$ given after Eq. (2.122).

Finally, it is observed from Figs. 2.26 and 2.28 that asymptotic results match very well with the simulation and analytical ones in the high λ (transmitting SNR) region, and the slope of the EC under OPRA and ORA schemes is always unity concerning $\ln \lambda$, while parameter settings show no impacts. Furthermore, as seen from Figs. 2.26, 2.27 and 2.28, simulation and analysis results match very well with each other, which verifies the correctness of our proposed analysis model.

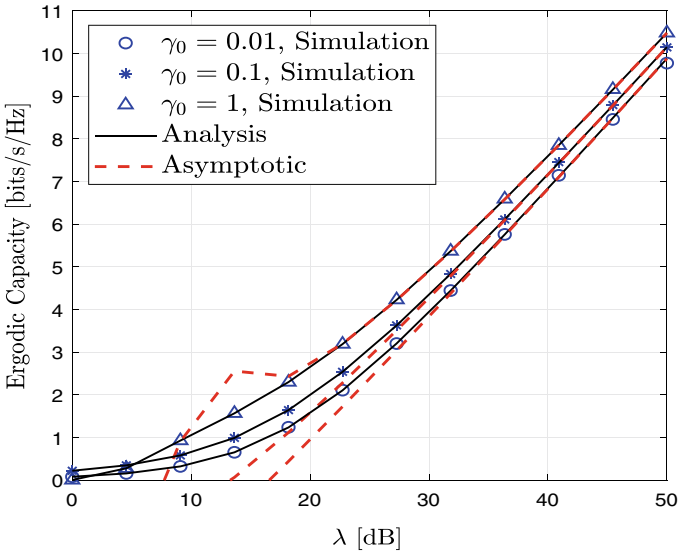

Fig. 2.28 EC versus λ under the TIFR scheme for $m = 1$, $b = 0.063$, and $\Omega = 8.97 \times 10^{-4}$ (frequent heavy shadowing)

2.3.4 Discussions

In Sect. 2.3 we mainly study the impacts of the small-scale fading over the aerial-terrestrial channel and the randomness of the position of the terrestrial terminal on the capacity performance of the three considered power adaptation schemes. To facilitate the modeling and analysis, exact and asymptotic analytical expressions have been derived for the EC of a SISO aerial-terrestrial system. In the following, some discussions will be offered to discuss the possible applications of the proposed modeling and analysis method presented in Sect. 2.3.

2.3.4.1 Extension to Multiple-Input Multiple-Output (MIMO) Systems

As mentioned before, a SISO system is considered to show the proposed modeling and analysis method in Sect. 2.3. In practice, multi-antenna may be applied to achieve better delivery quality due to the diversity gain arising from MIMO technology. This section will give valuable guidelines for extending Sect. 2.3 to MIMO systems.

Referring to the considered system described in Sect. 2, let's assume that D is equipped with M ($M > 1$) receiving antennas to improve its received SNR. Then, suppose the maximum ratio combing scheme is adopted at D to process the multiple copies of the received signal. In that case, one can rewrite the received SNR as

$\gamma = \frac{\Lambda}{d^n}$, where $\Lambda = \frac{P_t}{\sigma^2} \sum_{i=1}^{M} |h_i|^2$, h_i is the channel gain between S and the ith receiving antenna at D. Making use of Eqs. (4) and (5) in [30], we can obtain the PDF of Λ. Therefore, by repeating the derivation process in Sect. 2.3 exact and asymptotic analytical expressions for EC for such a multi-antenna case can be easily derived.

2.3.4.2 Studies of Some More Performance Indices

Section 2.3 has derived exact and asymptotic analytical expressions for EC. The readers and researchers may be interested in other performance indices, e.g., the approximation expression and the bounds of the EC. To make Sect. 2.3 more concise, in the following, we will take the bound of the EC as an example and give the main technical steps to demonstrate the applications of our proposed analytical method for other performance indices.

By exploring the classic inequality of exponential function [31], $1 + x \leq \exp(x)$, one can first replace $\exp(-\beta x)$ in Eq. (2.103) by using $1 - \beta x$, and then repeat the derivation processes of the exact analytical expressions for EC given in Sect. 2, lower bounds for the EC under the considered three different power adaptation schemes can be achieved accordingly.

2.3.5 Conclusions

In this section, we have derived and verified the exact and asymptotic expressions for the EC under three different power adaption schemes over aerial-terrestrial communication links, while considering the randomness of the location of the terrestrial user. Some insights can be deduced from numerical results as follows:

(a) The slope of the EC under OSPRA and ORA scheme concerning $\ln \lambda$ is always unity in high transmit SNR region, despite the parameter settings;
(b) The EC performance of the three power adaptation schemes can be improved by increasing the transmit SNR and shadowing over the satellite-to-terrestrial fading channels exhibits a negative influence on the EC of the three schemes;
(c) OSPRA scheme always shows the best EC performance among the considered three methods, and the EC of OSPRA and ORA schemes converge in high transmit SNR region.
(d) Optimal EC performance can be designed and achieved for the TIFR scheme by suitably setting the values of the system parameters to balance the outage and EC performance.

References

1. T.S. Rappaport, *Wireless Communications: Principles and Practices*, 2nd edn. (Prentice Hall, New Jersey, 2002)
2. I.S. Gradshteyn, I.M. Ryzhik, *Table of Integrals, Series and Products*, 7th edn. (Academic Press, San Diego, 2007)
3. H. Lei, H. Luo, K.-H. Park, G. Pan, Z. Ren, M.-S. Alouini, On secrecy performance of mixed RF-FSO systems with channel imperfection. IEEE Photon. **10**(3), 1–14 (2018)
4. H. Lei, H. Luo, K.-H. Park, I.S. Ansari, W. Lei, G. Pan, M.-S. Alouini, on secure mixed RF-FSO systems with TAS and imperfect CSI. IEEE Trans. Commun. **68**(7), 4461–4475 (2020)
5. H. Lei, C. Gao, I.S. Ansari, Y. Guo, G. Pan, K. Qaraqe, On physical layer security over SIMO generalized-K fading channels. IEEE Trans. Veh. Technol. **65**(9), 7780–7785 (2016)
6. I.S. Ansari, S. Al-Ahmadi, F. Yilmaz, M.S. Alouini, H. Yanikomeroglu, A new formula for the BER of binary modulations with dual-branch selection over generalized-K composite fading channels. IEEE Trans. Commun. **59**(10), 2654–2658 (2011)
7. J. Ye, C. Zhang, H. Lei, G. Pan, Z. Ding, Secure UAV-to-UAV systems with spatially random UAVs. IEEE Wirel. Commun. Lett. **8**(2), 564–567 (2019)
8. G. Pan, J. Ye, Z. Ding, On Secure VLC Systems with Spatially Random Terminals. IEEE Commun. Lett. **21**(3), 492–495 (2017)
9. Explanation of Meijer-G Function. http://functions.wolfram.com/HypergeometricFunctions/MeijerG/21/ShowAll.html
10. M. Bloch, J. Barros, *Physical-Layer Security: From Information Theory to Security Engineering* (Cambridge University Press, Cambridge, 2011)
11. M. Abramowitz, I. Stegun, *Handbook of Mathematical Functions With Formulas, Graphs, and Mathematical Tables*, 9th edn. (American Association of Physics Teachers, New York, 1972)
12. H. Menouar, I. Guvenc, K. Akkaya, A.S. Uluagac, A. Kadri, A. Tuncer, UAV-enabled intelligent transportation systems for the smart city: applications and challenges. IEEE Commun. Mag. **55**(3), 22–28 (2017)
13. H. Lei, D. Wang, K.-H. Park, I.S. Ansari, J. Jiang, G. Pan, M.-S. Alouini, Safeguarding UAV IoT communication systems against randomly located eavesdroppers. IEEE Internet Things J. **7**(2), 1230–1244 (2020)
14. H. Lei, Y. Zhang, K.-H. Park, I.S. Ansari, G. Pan, M.-S. Alouini, Performance analysis of dual-hop RF-UWOC systems. IEEE Photonics J. **12**(2), 1–15 (2020)
15. A.P. Prudnikov, Y.A. Brychkov, O.I. Marichev, *Integrals and Series: More Special Functions*, vol. 3 (Gordon and Breach Science, New York, 1992)
16. V.S. Adamchik, O.I. Marichev, The Algorithm for Calculating Integrals of Hypergeometric Type Functions and Its Realization in REDUCE System, in *Proceedings of the International Symposium on Symbolic and Algebraic Computation* (1990), pp. 212–224
17. M. Di Renzo, A. Guidotti, G.E. Corazza, Average rate of downlink heterogeneous cellular networks over generalized fading channels: a stochastic geometry approach. IEEE Trans. Commun. **61**(7), 3050–3071 (2013)
18. H. Lei, Z. Yang, K.-H. Park, I.S. Ansari, Y. Guo, G. Pan, M.-S. Alouini, Secrecy outage analysis for cooperative NOMA systems with relay selection schemes. IEEE Trans. Commun. **67**(9), 6282–6298 (2019)
19. E. Zedini, M.S. Alouini, on the performance of multihop heterodyne FSO systems with pointing errors. IEEE Photonics **7**(2), 1–10 (2015)
20. J. Yu, X. Liu, H. Qi, Y. Gao, Long-term channel statistic estimation for highly-mobile hybrid MmWave multi-user MIMO systems. IEEE Trans. Veh. Technol. **69**(12), 14277–14289 (2020)
21. K.N. Le, Fundamentals of acute relay CSI severity. IEEE Trans. Wirel. Commun. **19**(11), 7653–7662 (2020)
22. K.N. Le, V.W. Tam, Wireless secrecy under multivariate correlated Nakagami-m fading. IEEE Access. **8**, 33223–33236 (2020)
23. K.N. Le, Distributions of multivariate equal-correlated Nakagami-m fading employing MRC. IEEE Trans. Veh. Technol. **68**(9), 9308–9312 (2019)

24. X. Yan, H. Xiao, K. An, G. Zheng, S. Chatzinotas, Ergodic capacity of NOMA-based uplink satellite networks with randomly deployed users. IEEE Syst. J. **14**(3), 3343–3350 (2020)
25. A. Abdi, W. Lau, M.-S. Alouini, M. Kaveh, A new simple model for land mobile satellite channels: first and second order statistics. IEEE Trans. Wirel. Commun. **2**(3), 519–528 (2003)
26. A.J. Goldsmith, P.P. Varaiya, Capacity of fading channels with channel side information. IEEE Trans. Inf. Theory **43**(6), 1986–1992 (1997)
27. M.-S. Alouini, A.J. Goldsmith, Capacity of Rayleigh fading channels under different adaptive transmission and diversity-combining techniques. IEEE Trans. Veh. Technol. **48**(4), 1165–1181 (1999)
28. H. Zhao, L. Yang, A.S. Salem, M. Alouini, Ergodic capacity under power adaption over Fisher-Snedecor $\mathcal{F}$ fading channels. IEEE Commun. Lett. **23**(3), 546–549 (2019)
29. H. Zhao, Z. Liu, Different power adaption methods on fluctuating two-ray fading channels. IEEE Wirel. Commun. Lett. **8**(2), 592–595 (2019)
30. Y. Zhang, J. Ye, G. Pan, M.-S. Alouini, Secrecy outage analysis for satellite-terrestrial downlink transmissions. IEEE Wirel. Commun. Lett. **9**(10), 1643–1647 (2020)
31. G.H. Hardy, J.E. Littlewood, G. Polya, *Inequalities* (Cambridge University Press, Cambridge, 1975)
32. I. Sen, D.W. Matolak, Vehicle-vehicle channel models for the 5-GHz band. IEEE Trans. Intell. Transp. Syst. **9**(2), 235–245 (2008)
33. H. Zhao, Y. Tan, G. Pan, Ergodic secrecy capacity of MRC/SC in single-input multiple-output wiretap systems with imperfect channel state information. Front. Inf. Technol. Electron. Eng. **18**(4), 578–590 (2017)

Chapter 3
UAV-to-UAV Communications

Jia Ye, Yanci Si, and Gaofeng Pan

3.1 Secure UAV-to-UAV Systems with Spatially Random UAVs

In this section, we investigate the secrecy performance of a UAV-to-UAV system, where a UAV acts as the source (S) transmitting information to a legitimate UAV receiver while a group of UAVs trying to eavesdrop on the information delivery between S and legitimate UAV receiver. The locations of the legitimate UAV receiver and the eavesdropping UAVs are randomly distributed in the coverage space of S. We first characterize the statistical characteristics of the SNR over S to the legitimate UAV receiver links. Then the closed-form analytical expressions for SOP and the average secrecy capacity have also been derived accordingly. Finally, Monte Carlo simulations are carried out to verify our proposed analytical models.

3.1.1 System Model

In Sect. 3.1, we consider an A2A communication system, as shown in Fig. 3.1, where a UAV with a single omni transmitting antenna acts as the source (S) trying to transmit its information to a legitimate UAV.[1] Furthermore, there are also a group of UAVs

[1] In Sect. 3.1, we only consider omni transmitting antenna to introduce the analysis method for A2A systems and the system with directional antenna is a particular case of the one with omni transmitting antenna: the coverage space of directional antenna is a part of the one of omni antenna, leading to a portion of the sphere for eavesdroppers to distribute, as indicated in Fig. 3.1.

J. Ye
Chongqing University, Chongqing, China

Y. Si · G. Pan (✉)
Beijing Institute of Technology, Beijing, China
e-mail: gfpan@bit.edu.cn

G. Pan et al. (eds.), *UAV Communications: Modeling and Analyses*,
https://doi.org/10.1007/978-981-97-0383-8_3

distributed in the coverage space (in which the received signal strength is equal or above the threshold at the receiver to demodulate and decode the received signal) of S trying to eavesdrop the information transmission between S and the legitimate UAV. For tractability purposes, in Sect. 3.1, we treat the coverage space of S as a sphere, $\mathcal{V}$, with radius, D ($D > 0$) m, where S is located at the center of the sphere. Without loss generality, we assume that the legitimate UAV and N ($N \geqslant 1$) eavesdropping UAVs can be modeled as a set of independent and identical uniformly distributed points without cooperation with each other in the sphere $\mathcal{V}$, denoted by W, to protect their eavesdropping activities. The number of the eavesdropping receivers is Poisson distributed with density λ, i.e.,

$$P\{N = k\} = \left(\mu_{\mathcal{V}}^{k}/k!\right) \exp\left(-\mu_{\mathcal{V}}\right), \tag{3.1}$$

where $\mu_{\mathcal{V}} = \frac{4\pi D^3}{3}\lambda$ is the mean measure.

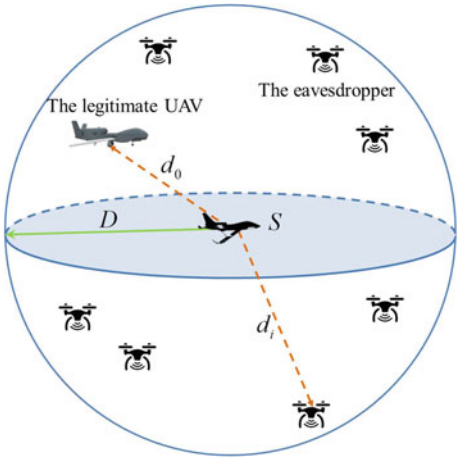

Fig. 3.1 System model

In the following, we name the legitimate receiver as the 0th receiver to facilitate the subsequent analysis. Therefore, the distance between S and UAVs can be calculated from W, the PDF of which can be given by using [1, Eq. (1)] as $f_W(w) = \frac{3}{4\pi D^3}$.

Section 3.1 assumes that the communication channels from S to UAVs are dominated by LoS links rather than other channel impairments in the open airspace, such as shadowing or small-scale fading, as treated in [2]. Thus, the channel power gain from S to the ith ($0 \leqslant i \leqslant N$) UAV follows the free-space path loss model, which can be given by $g_i = \beta d_i^{-2}$, where β denotes the channel power at the reference distance $d = 1$ m, whose value depends on the carrier frequency, antenna gain, etc., and d_i is the link distance between S and the ith UAV.

Let P denote the transmit power at S. The received SNR at the ith UAV from S can be expressed as

$$\gamma_i = \frac{P g_i}{\delta^2} = \frac{\gamma P}{d_i^2}, \tag{3.2}$$

where δ^2 denotes the noise power, and $\gamma = \frac{\beta}{\delta^2}$ represents the reference SNR.

In the following, we also denote $v_{\min} = \frac{\gamma P}{D^2} \leq \gamma_i \leq v_{\max} = \infty$ for simplification, where $v_{\min}$ and $v_{\max}$ means the minimum and maximum values of γ_i, respectively.

Lemma 3.1 *The CDF of $\gamma_i = \frac{\gamma P}{d_i^2}$ can be expressed as*

$$F_{\gamma_i}(x) = \begin{cases} 1 - \frac{\left(\sqrt{\gamma P}\right)^3}{x^{\frac{3}{2}} D^3}, & \text{if } x \geq \frac{\gamma P}{D^2}; \\ 0, & \text{else} \end{cases}. \tag{3.3}$$

Proof Using $f_W(w) = \frac{3}{4\pi D^3}$, we have the CDF of d_i as

$$\begin{aligned} F_{d_i}(x) &= \int_0^x \int_0^{\pi} \int_0^{2\pi} \frac{3}{4\pi D^3} \sin\phi_i d_i^2 \mathrm{d}\theta_i \mathrm{d}\phi_i \mathrm{d}(d_i) \\ &= \begin{cases} 0, & \text{if } x < D; \\ \frac{x^3}{D^3}, & \text{elseif } 0 \leq x \leq D; \\ 1, & \text{else} \end{cases}. \end{aligned} \tag{3.4}$$

Therefore, we can achieve the CDF of γ_i as

$$\begin{aligned} F_{\gamma_i}(x) &= \Pr\{\gamma_i \leq x\} \\ &= 1 - \Pr\left\{d_i \leq \sqrt{\frac{\gamma P}{x}}\right\}. \end{aligned} \tag{3.5}$$

Then, the proof is completed. □

Corollary 3.1 *Accordingly, the PDF of γ_i can be expressed as*

$$f_{\gamma_i}(x) = \begin{cases} \frac{3\left(\sqrt{\gamma P}\right)^3}{2x^{\frac{5}{2}} D^3}, & \text{if } x \geq \frac{\gamma P}{D^2}; \\ 0, & \text{else} \end{cases}. \tag{3.6}$$

Proof The PDF of γ_i is the derivative of Eq. (3.3). □

Lemma 3.2 *The CDF of $\gamma_{\max}$ with N eavesdropping UAVs can be derived as*

$$F_{\gamma_{\max}}^N(x) = \begin{cases} \left[1 - \frac{\left(\sqrt{\gamma P}\right)^3}{x^{\frac{3}{2}} D^3}\right]^N, & \text{if } x \geq \frac{\gamma P}{D^2}; \\ 0, & \text{else} \end{cases}. \tag{3.7}$$

Proof Using probability theory, we have $F_z(z) = \Pr\{\max\{x_1, x_2, \ldots, x_M\} \le z\}$, if $x_1, x_2, \ldots, x_M$ are M ($M > 1$) independent variables. Then, $F_z(z) = \prod_{i=1}^{M} F_{x_i}(z)$, where $F_{x_i}(x)$ is the CDF of x_i. As the eavesdropping channels are independent of each other, we can derive the CDF of $\gamma_{\max}$ as Eq. (3.7). □

Corollary 3.2 *Accordingly, the PDF of $\gamma_{\max}$ with N eavesdropping UAVs can be expressed as*

$$f_{\gamma_{\max}}^{N}(x) = \begin{cases} N\left[1 - \frac{\left(\sqrt{\gamma P}\right)^3}{x^{\frac{3}{2}} D^3}\right]^{N-1} \frac{3\left(\sqrt{\gamma P}\right)^3}{2x^{\frac{5}{2}} D^3}, & \text{if } x \ge \frac{\gamma P}{D^2}; \\ 0, & \text{else} \end{cases}$$
$$= \begin{cases} N\frac{3\left(\sqrt{\gamma P}\right)^3}{2D^3} \sum_{j=0}^{N-1} (-1)^j C_{N-1}^{j} \frac{\left(\sqrt{\gamma P}\right)^{3j}}{x^{\frac{3}{2}j+\frac{5}{2}} D^{3j}}, & \text{if } x \ge \frac{\gamma P}{D^2}; \\ 0, & \text{else} \end{cases}. \quad (3.8)$$

Proof The PDF of $\gamma_{\max}$ is the derivative of Eq. (3.7). □

3.1.2 SOP

Here, SOP is defined as the probability that the instantaneous secrecy capacity is below a threshold secrecy rate, C_{th} ($C_{th} \ge 0$).

Therefore, the instantaneous secrecy capacity from S to the legitimate UAV is

$$C_S(\gamma_0, \gamma_{\max}) = \max\left\{\log_2(1+\gamma_0) - \log_2(1+\gamma_{\max}), 0\right\}, \quad (3.9)$$

where $\gamma_{\max} = \max_{i\in\{1,\ldots,N\}}\{\gamma_i\}$.

Then, let $\nu = 2^{C_{th}}$. SOP can be written as

$$\begin{aligned} P_r(C_{th}) &= \Pr\{C_s \le C_{th}\} \\ &= \Pr\left\{\frac{1+\gamma_0}{1+\gamma_{\max}} \le 2^{C_{th}}\right\} \\ &= \Pr\{\gamma_0 \le \nu\gamma_{\max} + \nu - 1\}. \end{aligned} \quad (3.10)$$

Theorem (3.1.1) *Using the Corollarys 3.1 and 3.2, we can express $P_r(C_{th})$ as*

$$P_r(C_{th}) = \sum_{N=1}^{\infty} \frac{\mu\nu}{N!} e^{-\mu\nu} \left[\sum_{j=0}^{N-1} (-1)^j C_{N-1}^{j} \frac{3N\left(\sqrt{\gamma P}\right)^{3j+6}}{(3j+3)\, v_{\min}^{\frac{3}{2}j+3} D^{3j+6}}\right.$$
$$\left. - \sum_{j=0}^{N-1} (-1)^j C_{N-1}^{j} \frac{3N\left(\sqrt{\gamma P}\right)^{3j+6}}{2\nu^{\frac{3}{2}} D^{3j+6}}\right.$$

$$\times \frac{B\left(\frac{3}{2}j+3,1\right){}_2F_1\left(\frac{3}{2}j+\frac{5}{2},1;\frac{3}{2}j+\frac{3}{2};\frac{3}{2v_{\min}}\right)}{{v_{\min}}^{\frac{3}{2}j+\frac{5}{2}}\sqrt{1-\frac{1}{\nu}+v_{\min}}}\Bigg], \tag{3.11}$$

Proof As the main and eavesdropping channels are independent of each other, we can calculate $P_r\left(C_{th}\right)$ with N eavesdropping UAVs as

$$\begin{aligned} P_r^N\left(C_{th}\right) &= \int_{v_{\min}}^{\infty}\int_{v_{\min}}^{\nu y+\nu-1} f_{\gamma_0}(x)\, f_{\gamma_{\max}}(y)\,\mathrm{d}x\mathrm{d}y \\ &= \int_{v_{\min}}^{\infty} f_{\gamma_{\max}}(y)\int_{v_{\min}}^{\nu y+\nu-1}\frac{3\left(\sqrt{\gamma P}\right)^3}{2x^{\frac{5}{2}}D^3}\mathrm{d}x\mathrm{d}y \\ &= \int_{v_{\min}}^{\infty} f_{\gamma_{\max}}(y)\left[\frac{\left(\sqrt{\gamma P}\right)^3}{{v_{\min}}^{\frac{3}{2}}D^3}-\frac{\left(\sqrt{\gamma P}\right)^3}{(\nu y+\nu-1)^{\frac{3}{2}}D^3}\right]dy \\ &= \sum_{j=0}^{N-1}(-1)^j C_{N-1}^j\int_{v_{\min}}^{\infty}\frac{3N\left(\sqrt{\gamma P}\right)^{3j+6}}{2{v_{\min}}^{\frac{3}{2}}D^{3j+6}y^{\frac{3}{2}j+\frac{5}{2}}}\mathrm{d}y. \end{aligned} \tag{3.12}$$

Using [3, Eq. (3.197.2)] and taking the Poisson distributed number of eavesdroppers into consideration, $P_r\left(C_{th}\right)$ can be obtained as Eq. (3.11). □

3.1.3 The Average Secrecy Capacity

In Sect. 3.1, ASC is defined as the expected value of secrecy capacity as[2]

$$\begin{aligned} \bar{C}_s\left(\gamma_0,\gamma_{\max}\right) &= E\left[C_s\left(\gamma_0,\gamma_{\max}\right)\right] \\ &= \int_{v_{\min}}^{\infty}\int_{v_{\min}}^{\infty} C_s\left(\gamma_0,\gamma_{\max}\right) f\left(\gamma_0,\gamma_{\max}\right)\mathrm{d}\gamma_0\mathrm{d}\gamma_{\max}. \end{aligned} \tag{3.13}$$

As the main and eavesdropping channels are independent of each other, we can rewrite ASC as

$$\bar{C}_s\left(\gamma_0,\gamma_{\max}\right) = \sum_{N=1}^{\infty}\frac{\mu_{\mathcal{V}}}{N!}\exp\left(-\mu_{\mathcal{V}}\right)\left(\bar{C}_{s1}^N-\bar{C}_{s2}^N\right)/\ln 2, \tag{3.14}$$

[2] The ASC aims at a case that the source can gain the CSI of the eavesdropping link and transmits the information only when the legitimate channel outperforms the eavesdropping channel. Therefore, the ESC is a special case of ASC, as ASC is calculated for the case that no matter the CSI of the eavesdropping channel is available or not at the source.

where $\bar{C}_{s1}^{N} = \int_{v_{\min}}^{\infty} \ln(1+x) f_{\gamma_0}(x) \int_{v_{\min}}^{x} f_{\gamma_{\max}}(y)\,\mathrm{d}y\mathrm{d}x$ and $\bar{C}_{s2}^{N} = \int_{v_{\min}}^{\infty} \ln(1+y) f_{\gamma_{\max}}(y) \int_{y}^{\infty} f_{\gamma_0}(x)\mathrm{d}x\mathrm{d}y$.

Thus, we can calculate $\bar{C}_{s1}^{N}$ as

$$\begin{aligned}\bar{C}_{s1}^{N} &= \int_{v_{\min}}^{\infty} \ln(1+x)\, f_0(x) \int_{v_{\min}}^{x} N \frac{3\left(\sqrt{\gamma P}\right)^3}{2D^3} \sum_{j=0}^{N-1} (-1)^j C_{N-1}^{j} \frac{\left(\sqrt{\gamma P}\right)^{3j}}{y^{\frac{3}{2}j+\frac{5}{2}} D^{3j}} \mathrm{d}y\mathrm{d}x \\ &= \sum_{j=0}^{N-1} C_{N-1}^{j} \frac{9N(-1)^j \left(\sqrt{\gamma P}\right)^{3j+6}}{2(3j+3)\, {v_{\min}}^{\frac{3}{2}j+\frac{3}{2}} D^{3j+6}} \int_{v_{\min}}^{\infty} x^{-\frac{5}{2}} \ln(1+x)\mathrm{d}x \\ &\quad - \sum_{j=0}^{N-1} C_{N-1}^{j} \frac{9N(-1)^j \left(\sqrt{\gamma P}\right)^{3j+6}}{2(3j+3)\, D^{3j+6}} \int_{v_{\min}}^{\infty} x^{-\frac{3}{2}j-4} \ln(1+x)\mathrm{d}x. \end{aligned} \tag{3.15}$$

To facilitate the analysis, we define a new function $g_1(m) = \int_{v_{\min}}^{\infty} x^m \ln(1+x)\,\mathrm{d}x$. Using [4, Eq. (2.6.10.47)], one can easily write $g_1(m)$ as

$$\begin{aligned} g_1(m) &= {v_{\min}}^{m+1} B(1, -m-1) \left[\ln(v_{\min}) + \psi(-m) - \psi(-m-1)\right] \\ &\quad + {v_{\min}}^{m} B(1, -m)\, {}_3F_2\left(-m, 1, 1; 2, -m+1; -\frac{1}{v_{\min}}\right). \end{aligned} \tag{3.16}$$

Then, using Eq. (3.16) in Eq. (3.15), $\bar{C}_{s1}^{N}$ can be easily derived as

$$\begin{aligned} \bar{C}_{s1}^{N} &= \sum_{j=0}^{N-1} C_{N-1}^{j} \frac{9N(-1)^j \left(\sqrt{\gamma P}\right)^{3j+6}}{2(3j+3)\, {v_{\min}}^{\frac{3}{2}j+\frac{3}{2}} D^{3j+6}} g_1\left(-\frac{5}{2}\right) \\ &\quad - \sum_{j=0}^{N-1} C_{N-1}^{j} \frac{9N(-1)^j \left(\sqrt{\gamma P}\right)^{3j+6}}{2(3j+3)\, D^{3j+6}} g_1\left(-\frac{3}{2}j-4\right), \end{aligned} \tag{3.17}$$

where $g_1(m) = \int_{v_{\min}}^{\infty} x^m \ln(1+x)\,\mathrm{d}x$.

Similarly, we can also derive $\bar{C}_{s2}^{N}$ by using Eq. (3.16) as

$$\begin{aligned} \bar{C}_{s2}^{N} &= \int_{v_{\min}}^{\infty} \ln(1+y)\, f_{\gamma_{\max}}(y) \int_{y}^{v_{\max}} \frac{3\left(\sqrt{\gamma P}\right)^3}{2x^{\frac{5}{2}} D^3} \mathrm{d}x\mathrm{d}y \\ &= \int_{v_{\min}}^{\infty} \ln(1+y)\, f_{\gamma_{\max}}(y) \frac{\left(\sqrt{\gamma P}\right)^3}{y^{\frac{3}{2}} D^3} dy \end{aligned}$$

$$= \sum_{j=0}^{N-1} (-1)^j C_{N-1}^j \frac{3N\left(\sqrt{\gamma P}\right)^{3j+6}}{2D^{3j+6}} \int_{v_{\min}}^{\infty} y^{-\frac{3}{2}j-4} \ln(1+y)\, \mathrm{d}y$$

$$= \sum_{j=0}^{N-1} (-1)^j C_{N-1}^j \frac{3N\left(\sqrt{\gamma P}\right)^{3j+6}}{2D^{3j+6}} g_1\left(-\frac{3j}{2}-4\right). \tag{3.18}$$

Finally, ASC can be obtained by substituting Eqs. (3.17) and (3.18) into Eq. (3.14).

3.1.4 Numerical Results

In this subsection, Monte Carlo simulations are carried out to validate our proposed analytical expressions for SOP and ASC under dominated LoS fading channels and Nakagami-m fading. The main adopted parameters are set as $\gamma = 80$ dB [5], $P = 10$ dBW, $C_{th} = 1$ bits/s/Hz and the expectation of channel power gain of the Nakagami-m fading channel is 1 dB. Moreover, the coverage distance of the source UAV is set from hundreds of meters to tens of km to reflect the practical scenarios of UAVs in civil and military applications.

Figure 3.2a shows the SOP versus λ for various C_{th} with $D = 500$ m. Since a high threshold secrecy rate means the system requires a large channel secrecy rate, we can see that the systems with a small C_{th} outperform the one with a large C_{th}. Figure 3.2b shows the SOP versus D for various λ. There are more eavesdropping UAVs when λ and/or D increase, resulting in degraded SOP because the diversity gain of the information eavesdropping will increase while the number of eavesdropping UAVs enlarges.

Figure 3.3a presents the ASC versus D for various λ, in which one can see that ASC can be improved in the low λ region and degrades in large λ region when λ decreases or D increases. Because low λ and large D can improve the probability that the distance between S and the legitimate UAV is shorter than the ones among S and the eavesdropping UAVs, then the legitimate UAV will suffer weaker eavesdropping, compared to the case with high λ and small D. However, it is exactly the opposite for ASC in the high λ and/or low D regions since more eavesdropping UAVs will lead to poorer secrecy performance. As shown in Fig. 3.3b with $\lambda = -130$ dB, we can also see that the reference SNR γ cannot play a positive role significantly since the received SNR over the eavesdropping links will also be improved when γ increases.

Moreover, while suffering both LoS and Nakagami-m fading, we also present the SOP performance with $m = 2$ and $m = 3$ in Fig. 3.2a and b, and the ASC with $m = \sqrt{6}$ and $m = \sqrt{2}$ in Fig. 3.3a and b, separately. One can see that the SOP and ASC suffering both LoS propagation and Nakagami-m fading outperform the ones only experiencing LoS propagation. This observation can be explained by the fact that benefiting from the diversity gain of multiple eavesdropping UAVs, the equivalent received SNR at eavesdroppers, $\gamma_{\max}$, will degrade slower compared with the received

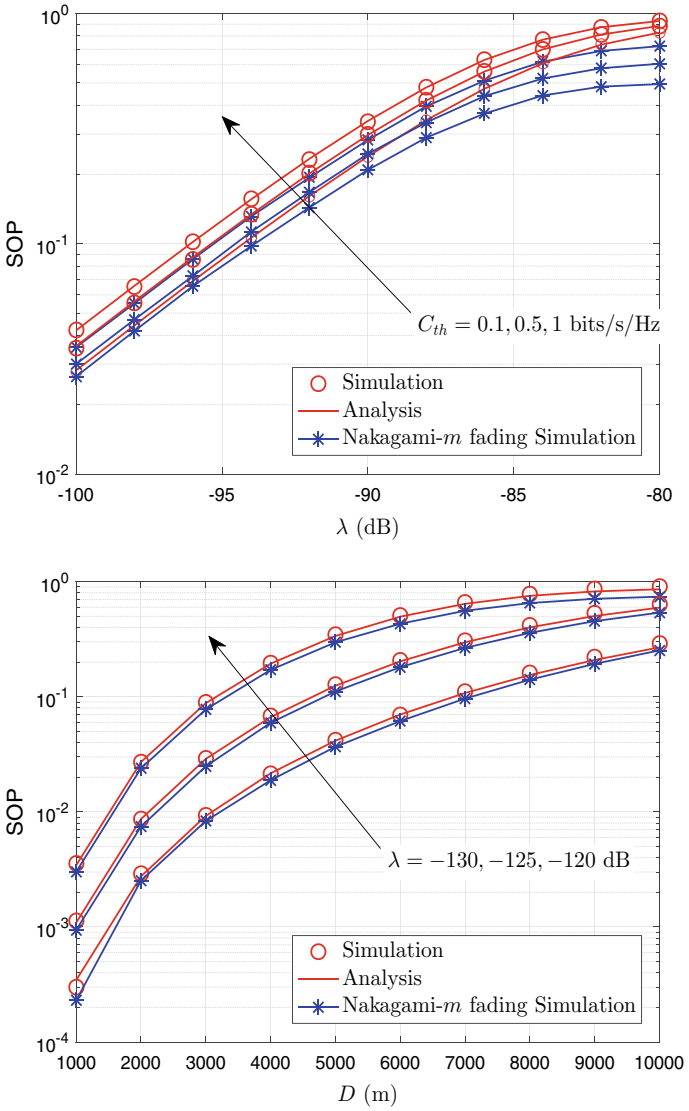

Fig. 3.2 SOP: **a** SOP versus λ; **b** SOP versus D

SNR at the legitimated UAV, γ_0, when the channels get worse. Therefore, we can see that the SOP only suffering LoS fading acts as the upper bound of the SOP, and the ASC only experiencing LoS fading serves as the lower bound of the ASC.

Finally, we can also clearly see from Figs. 3.2 and 3.3 that simulation and analysis results match very well with each other, which can verify the correctness of our proposed analysis models.

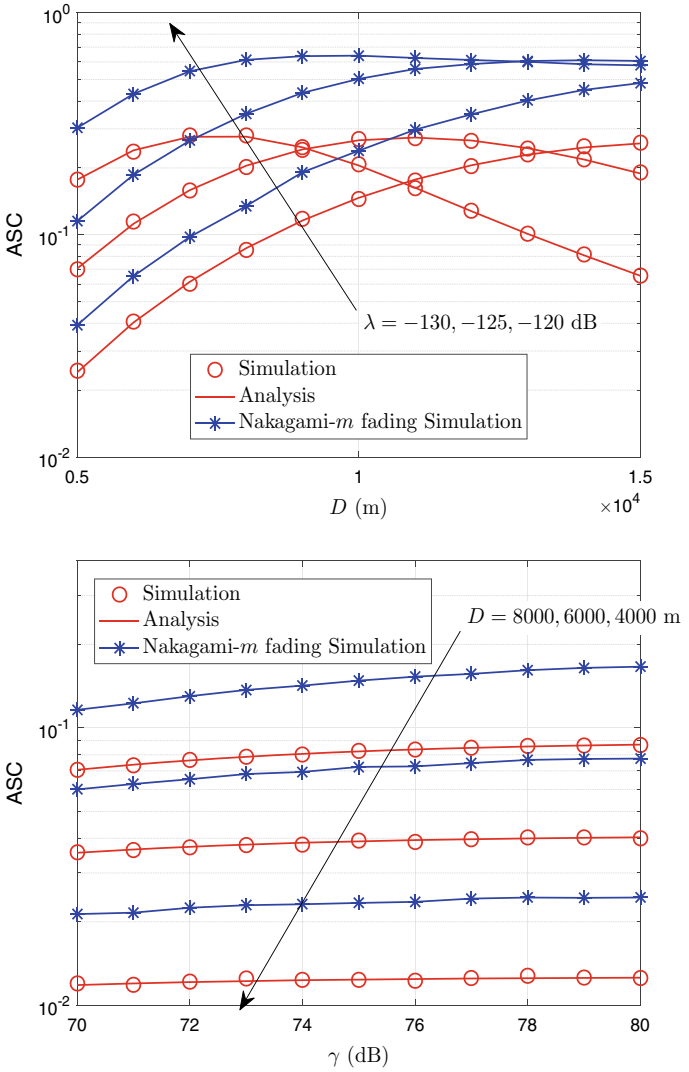

Fig. 3.3 ASC: **a** ASC versus D; **b** ASC versus γ

3.1.5 Conclusion

In this section, we have studied the secrecy performance of an A2A communication system and derived the closed-form analytical expressions for SOP and ASC. We consider the randomness of the number and the positions of all UAVs to make our system more practical. From the numerical results, we can obtain that the density of the eavesdropping UAVs and the radius of the coverage space of S negatively impact SOP. However, the ASC can be improved by increasing the radius of the coverage space of the source UAV.

3.2 Transmission Performance of Direct-Sequence Code Division Multiple Access (DS-CDMA) Drone Swarm

When deploying a drone swarm, the random distribution of vehicles will unavoidably interfere with the transmissions within the drone swarm. Additionally, in practical wireless communication, various factors, such as changes in node positions and the random nature of wireless channel fading, degrade the transmission performance of wireless information. Hence, it is meaningful to study the transmission performance in drone swarms to gain a deeper understanding of the influencing factors and performance characteristics, which is essential for optimizing the cooperative control of drone swarms.

The main objective of this section is to investigate the OP performance of the DS-CDMA drone swarm. In this section, we utilize stochastic geometry theory to establish a reasonable model for the communication scenario of a drone swarm in three-dimensional space, considering the usage requirements of drone swarm communication. Thus, we derive the expression of the SINR by considering the channels that suffer Nakagami-m fading. Next, the exact and asymptotic expressions for the OP are derived while considering the randomness of the drones' position. Finally, we investigate the transmission performance of the considered drone swarm and verify the accuracy of the proposed analysis model.

The main contributions of this section are summarized as follows.

(1) We set up the analysis models for the SINR, the OP of the considered system, and that for asymptotical OP in high SNR regions.
(2) We verify the transmission performance of the system via Monte Carlo simulation. Additionally, we also perform a simulation analysis of the EC performance.

3.2.1 System Model

The main content of this section is to study the information transmission performance of a randomly distributed drone swarm model in three-dimensional space. The system

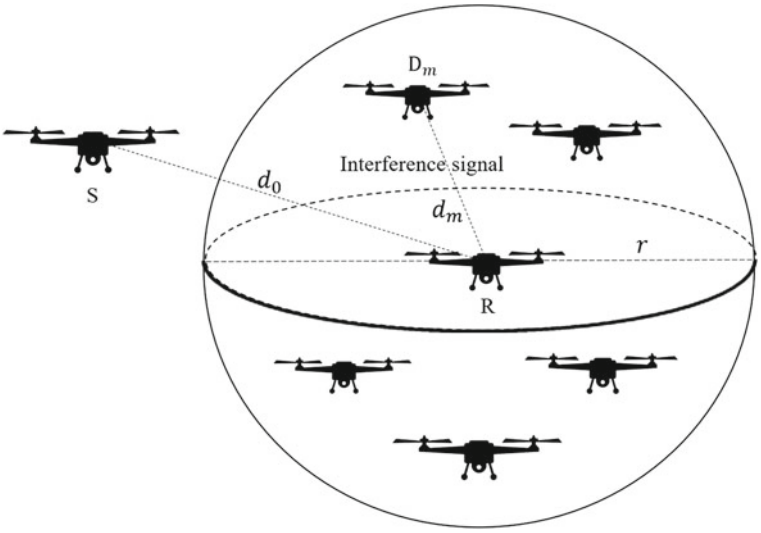

Fig. 3.4 System model of the drone swarm

model studied is shown in Fig. 3.4, where drone S is the source node, drone R is the destination node, and the distance between the two is d_0. In the spherical space with aircraft R as the center and r as the radius, there are M interfering nodes uniformly distributed, in which the distance between the interfering node m and the receiving node R is d_m.

Moreover, the channels between S and the interfering/receiving nodes are subject to independent identical distribution (i.i.d) Nakagami-m fading. It also assumes that the number of interfering nodes follows a Poisson Point Process with a density of λ, denoted as Φ_D.

When S sends its signal to R, the signal transmitted by D becomes the interference signal suffered by R. At a specific time, interfering nodes usually use the same frequency band to transmit information to different receivers. Section 3.2 considers R at the sphere's center as a typical user to make the situation more universal. It analyzes its receiving performance to reflect the transmission performance of the drone swarm.

3.2.1.1 Signal Model

This section adopts the DS-CDMA scheme for signal transmission. Direct-sequence spread spectrum and modulation are performed on the transmitted signal. The signal transmitted by the mth node ($1 \leq m \leq M$) can be expressed as

$$s_m(t) = \sum_{i=-\infty}^{+\infty} \sum_{l=0}^{L-1} \sqrt{P_m} b_m(i) c_m(l) p_c\left(t - lT_c - iT_b\right) \cos\left(2\pi f_c t + \theta_m\right), \quad (3.19)$$

where P_m is the transmission power of the mth transmitting node, $b_m(i)$ and $c_m(l)$ are the binary information of the ith transmitting node and the lth extended code chip, respectively, $p_c(t)$ represents the pulse response of the band-limited code chip pulse integer filter used for pulse shaping of the signal, T_b and T_c respectively represents the symbol duration and chip period, and $T_b = LT_c$. f_c is the base carrier frequency. θ_m is a random phase introduced by the sending node m, which is uniformly distributed on $[0, 2\pi)$.

Assuming the distance d_0 from S to R is fixed, then the received signal at R can be represented as

$$\begin{aligned} r_0(t) &= \frac{h_0}{\sqrt{{d_0}^n}} s_0\left((1+\Delta t)t + \tau_0\right) + \sum_{m=i}^{M} \frac{h_m}{\sqrt{{d_m}^n}} s_m\left((1+\Delta t)t + \tau_m\right) + z \\ &= \frac{h_0}{\sqrt{{d_0}^n}} \sum_{i=-\infty}^{+\infty} \sum_{l=0}^{L-1} \sqrt{P_0} b_0(i) c_0(l) p_c\left((1+\Delta t)t + \tau_0 - lT_c - iT_b\right) \\ &\quad \times \cos\left(2\pi f_c\left((1+\Delta t)t + \tau_0\right) + \theta_0\right) \\ &\quad + \sum_{m=1}^{M} \frac{h_m}{\sqrt{{d_m}^n}} \sum_{i=-\infty}^{+\infty} \sum_{l=0}^{L-1} \sqrt{P_m} b_m(i) c_m(l) p_c\left((1+\Delta t)t + \tau_m - lT_c - iT_b\right) \\ &\quad \times \cos\left(2\pi f_c\left((1+\Delta t)t + \tau_m\right) + \theta_m\right) + z, \end{aligned} \quad (3.20)$$

where h_0 and h_m represent the channel gain from S and the mth interfering node to the receiving node, n represents the path loss factor of the system, $\Delta t = \frac{v}{c}$ is the Doppler factor caused by the relative motion of S and R, v is the relative velocity, c is the speed of light, τ_0 and τ_m respectively represents the transmitter chip delay of the received signal corresponding to S and the interfering node propagating on the channel, and z is the AWGN with the mean value of 0.

The received signal is coherently demodulated on the carrier of S, and the demodulated signal is written as

$$\begin{aligned} y_0(t) &= r_0(t) \cos\left(f_m t\right) \\ &= \frac{h_0}{2\sqrt{{d_0}^n}} \sum_{i=-\infty}^{+\infty} \sum_{l=0}^{L-1} \sqrt{P_0} b_0(i) c_0(l) p_c\left((1+\Delta t)t + \tau_0 - lT_c - iT_b\right) \\ &\quad \times \left[\cos\left(f_0\left((2+\Delta t)t + \tau_0\right) + \theta_0\right) + \cos\left(f_0\left(t\Delta t + \tau_0\right) + \theta_0\right)\right] \\ &\quad + \frac{1}{2} \sum_{m=1}^{M} \frac{h_m}{\sqrt{d_m}} \sum_{i=-\infty}^{+\infty} \sum_{l=0}^{L-1} \sqrt{P_m} b_m(i) c_m(l) \end{aligned}$$

$$\times p_c\left((1+\Delta t)t+\tau_m-lT_c-iT_b\right)\left[\cos\left(f_m\left((2+\Delta t)t+\tau_m\right)+\theta_m\right)\right.$$
$$\left.+\cos\left(f_m\left(t\Delta t+\tau_m\right)+\theta_m\right)\right]+z, \tag{3.21}$$

where $f_m = 2\pi f_c$ is the carrier frequency of the interfering node, and f_0 is the carrier frequency of S.

Pass $y_0(t)$ through a low-pass filter to obtain the following signal

$$\begin{aligned} y_0(t) = {} & \frac{h_0}{2\sqrt{d_0^n}} \sum_{i=-\infty}^{+\infty} \sum_{l=0}^{L-1} \sqrt{P_0} b_0(i) c_0(l) p_c\left((1+\Delta t)t+\tau_0-lT_c-iT_b\right) \\ & \times \cos\left(f_0\left(t\Delta t+\tau_0\right)+\theta_0\right)+\frac{1}{2}\sum_{m=1}^{M}\frac{h_m}{\sqrt{d_m{}^n}}\sum_{i=-\infty}^{+\infty}\sum_{l=0}^{L-1}\sqrt{P_m} \\ & \times b_m(i)c_m(l)p_c\left((1+\Delta t)t+\tau_m-lT_c-iT_b\right) \\ & \times \cos\left(f_m\left(t\Delta t+\tau_m\right)+\theta_m\right)+z. \end{aligned} \tag{3.22}$$

Since the Doppler effect is considered, frequency compensation is carried out at the receiver to eliminate the influence of Doppler frequency shift as far as possible. Then, one can have

$$\begin{aligned} y_0(t) = {} & \left\{ \frac{h_0}{2\sqrt{d_0{}^n}} \sum_{i=-\infty}^{+\infty} \sum_{l=0}^{L-1} \sqrt{P_0} b_0(i) c_0(l) p_c\left((1+\Delta t)t+\tau_0-lT_c-iT_b\right) \right. \\ & \times \cos\left(f_0\left(t\Delta t+\tau_0\right)+\theta_0\right)+\frac{1}{2}\sum_{m=1}^{M}\frac{h_m}{\sqrt{d_m{}^n}}\sum_{i=-\infty}^{+\infty}\sum_{l=0}^{L-1}\sqrt{P_m}b_m(i)c_m(l)p_c \\ & \left. \times \left((1+\Delta t)t+\tau_m-lT_c-iT_b\right)\cos\left(f_m\left(t\Delta t+\tau_m\right)+\theta_m\right)+z \right\} \cdot \cos(\Delta\hat{f}t) \\ = {} & z+\frac{h_0}{4\sqrt{d_0{}^n}} \sum_{i=-\infty}^{+\infty} \sum_{l=0}^{L-1} \sqrt{P_0} b_0(i) c_0(l) p_c\left((1+\Delta t)t+\tau_0-lT_c-iT_b\right) \\ & \times \left[\cos\left(f_0\left(t\Delta t+\tau_0\right)+\theta_0+\Delta\hat{f}t\right)+\cos\left(f_0\tau_0+\theta_0+\delta t\right)\right] \\ & +\frac{1}{4}\sum_{m=1}^{M}\frac{h_m}{\sqrt{d_m{}^n}}\sum_{i=-\infty}^{+\infty}\sum_{l=0}^{L-1}\sqrt{P_m}b_m(i)c_m(l)p_c\left((1+\Delta t)t+\tau_m-lT_c-iT_b\right) \\ & \times \left[\cos\left(f_m\left(t\Delta t+\tau_m\right)+\theta_m+\Delta\hat{f}t\right)+\cos\left(f_m\tau_m+\theta_m+\delta t\right)\right], \end{aligned} \tag{3.23}$$

where $\Delta f = \Delta t \times 2\pi f_c$, $\Delta\hat{f}$ is the compensation frequency, and $\delta = \Delta f - \Delta\hat{f}$ is the compensation error.

The received signal passes through a low-pass filter, yielding

$$y_0(t) = z + \frac{h_0}{4\sqrt{{d_0}^n}} \sum_{i=-\infty}^{+\infty} \sum_{l=0}^{L-1} \sqrt{P_0} b_0(i) c_0(l)\, p_c\left((1+\Delta t)t + \tau_0 - lT_c - iT_b\right) \times \cos\left(f_0\tau_0 + \theta_0 + \delta t\right) + \frac{1}{4} \sum_{m=1}^{M} \frac{h_m}{\sqrt{d_m^n}} \sum_{i=-\infty}^{+\infty} \sum_{l=0}^{L-1} \sqrt{P_m} b_m(i) c_m(l)\, p_c\left((1+\Delta t)t + \tau_m - lT_c - iT_b\right) \times \cos\left(f_m\tau_m + \theta_m + \delta t\right). \tag{3.24}$$

At the receiving end, the signal is received in correlation, and the demodulation signal at R can be further written as

$$y_0(t) = z + \frac{h_0}{4\sqrt{{d_0}^n}} \sum_{i=-\infty}^{+\infty} \sqrt{P_0} b_0(i) c_0 \times \int_0^{T_b} p_c\left((1+\Delta t)t + \tau_0 - lT_c - iT_b\right) \times \cos\left(f_0\tau_0 + \theta_0 + \delta t\right) dt$$

$$\begin{aligned} y_0(t) &= z + \frac{h_0}{4\sqrt{{d_0}^n}} \sum_{i=-\infty}^{+\infty} \sqrt{P_0} b_0(i) c_0 \\ &\quad \times \int_0^{T_b} p_c\left((1+\Delta t)t + \tau_0 - lT_c - iT_b\right) \times \cos\left(f_0\tau_0 + \theta_0 + \delta t\right) dt \\ &\quad + \frac{1}{4} \sum_{m=1}^{M} \frac{h_m}{\sqrt{{d_m}^n}} \sum_{i=-\infty}^{+\infty} \sqrt{P_m} b_m(i) c_m \\ &\quad \times \int_0^{T_b} p_c\left((1+\Delta t)t + \tau_m - lT_c - iT_b\right) \times \cos\left(f_m\tau_m + \theta_m + \delta t\right) dt \\ &= z + \frac{h_0}{4\delta\sqrt{{d_0}^n}} \sum_{i=-\infty}^{+\infty} \sqrt{P_0} b_0(i) c_0 \times \frac{1}{1+\Delta t}\left(1 - \frac{\Delta t}{T_b}\right) \\ &\quad \times \left[\sin\left(\delta T_b + f_0\tau_0 + \theta_0\right) - \sin\left(f_0\tau_0 + \theta_0\right)\right] \\ &\quad + \frac{1}{4\delta} \sum_{m=1}^{M} \frac{h_m}{\sqrt{{d_m}^n}} \sum_{i=-\infty}^{+\infty} \sqrt{P_m} b_m(i) c_m \times \frac{1}{1+\Delta t}\left(1 - \frac{\Delta t}{T_b}\right) \\ &\quad \times \left[\sin\left(\delta T_b + f_m\tau_m + \theta_m\right) - \sin\left(f_m\tau_m + \theta_m\right)\right]. \end{aligned} \tag{3.25}$$

In the above equation, to simplify the calculation, let

$$g\left(f_m, \tau_m, \delta\right) = \sin\left(\delta T_b + f_m\tau_m + \theta_m\right) - \sin\left(f_m\tau_m + \theta_m\right) \tag{3.26}$$

and

$$g\left(f_0, \tau_0, \delta\right) = \sin\left(\delta T_b + f_0\tau_0 + \theta_0\right) - \sin\left(f_0\tau_0 + \theta_0\right), \tag{3.27}$$

then the above equation can be re-expressed as

$$
\begin{aligned}
y_0(t) = z &+ \frac{h_0}{4\sqrt{{d_0}^n}} \sum_{i=-\infty}^{+\infty} \sqrt{P_0} b_0(i) c_0 \\
&\times \int_0^{T_b} p_c\left((1+\Delta t)t + \tau_0 - lT_c - iT_b\right) \times \cos\left(f_0\tau_0 + \theta_0 + \delta t\right) dt \\
&+ \frac{1}{4} \sum_{m=1}^{M} \frac{h_m}{\sqrt{{d_m}^n}} \sum_{i=-\infty}^{+\infty} \sqrt{P_m} b_m(i) c_m \\
&\times \int_0^{T_b} p_c\left((1+\Delta t)t + \tau_m - lT_c - iT_b\right) \times \cos\left(f_m\tau_m + \theta_m + \delta t\right) dt \\
= z &+ \frac{h_0}{4\delta\sqrt{{d_0}^n}} \sum_{i=-\infty}^{+\infty} \sqrt{P_0} b_0(i) c_0 \times \frac{1}{1+\Delta t}\left(1 - \frac{\Delta t}{T_b}\right) \times \left[g\left(f_0, \tau_0, \delta\right)\right] \\
&+ \frac{1}{4\delta} \sum_{m=1}^{M} \frac{h_m}{\sqrt{{d_m}^n}} \sum_{i=-\infty}^{+\infty} \sqrt{P_m} b_m(i) c_m \times \frac{1}{1+\Delta t}\left(1 - \frac{\Delta t}{T_b}\right) \\
&\times \left[g\left(f_m, \tau_m, \delta\right)\right]. \qquad (3.28)
\end{aligned}
$$

3.2.2 Outage Performance

This section focuses on the SINR and outage performance of the considered drone swarm. The SINR inside the swarm measures the signal quality in the drone swarm.

3.2.2.1 SINR

SINR is used to measure the ratio between the relative strength of useful signals and interference and noise to assess the quality and reliability of a communication system, which is defined as

$$SINR = \frac{S}{I+N}, \qquad (3.29)$$

where S denotes the power of the target signal, I denotes the total power of the interference signal, N denotes the power of the noise, and the power is expressed in terms of the signal's energy.

In this model, the SINR of the received signal at the i-th information bit transmitted by S can be derived as

$$\gamma_0 = \frac{P_0 \frac{|h_0|^2}{{d_0}^n} \frac{\mathrm{g}(f_0,\tau_0,\delta)}{1+\Delta t}\left(1 - \frac{\Delta t}{T_b}\right)}{N_0 + \sum_{m=1}^{M} P_m \frac{|h_m|^2}{{d_m}^n} \frac{\mathrm{g}(f_m,\tau_m,\delta)}{1+\Delta t}\left(1 - \frac{\Delta t}{T_b}\right)}. \qquad (3.30)$$

3.2.2.2 OP

OP is often used to measure the probability that a signal transmission will be adversely affected in a particular communication scenario and will not successfully reach its intended target. These undesirable effects may include channel fading, interference, noise, and other factors. OP is defined as the probability that the SINR of a communication system falls below a certain threshold, i.e.,

$$P_{\gamma_0}{}^{\text{out}} = \Pr\{\gamma < \gamma_{th}\}. \tag{3.31}$$

When the channel undergoes Nakagami-m fading, $|h_m|^2$ obeys gamma distribution, and its CDF and PDF can be written respectively as

$$F_{|h_m|^2}(x) = \frac{1}{\Gamma(k)}\gamma\left(k, \frac{x}{\theta}\right) \tag{3.32}$$

and

$$f_{|h_m|^2}(x) = \frac{x^{k-1}}{\Gamma(k)\theta^k}\exp\left(-\frac{x}{\theta}\right), \tag{3.33}$$

respectively, where $\theta = \frac{\Omega}{k}$, k is the fading factor of the channel, Ω is the average power gain of the channel, $\Gamma(k)$ is the upper incomplete gamma function, $\gamma\left(k, \frac{x}{\theta}\right)$ is the lower incomplete gamma function, and $\frac{1}{\Gamma(k)}\gamma(k,t) = 1 - \exp(-t)\sum_{i=0}^{k}\frac{t^i}{i!}$.

Let $A_0 = \frac{g(f_0,\tau_0,\delta)}{1+\Delta t}\left(1 - \frac{\Delta t}{T_b}\right)$ and $A_m = \frac{g(f_m,\tau_m,\delta)}{1+\Delta t}\left(1 - \frac{\Delta t}{T_b}\right)$, then OP can be expressed as

$$\begin{aligned}
P_{\gamma_0}^{\text{out}} &= \Pr\{\gamma_0 < \gamma_{th}\} \\
&= \Pr\left\{\frac{P_0\frac{|h_0|^2}{{d_0}^n}A_0}{N_0 + \sum_{m=1}^{M} P_m\frac{|h_m|^2}{{d_m}^n}A_m} < \gamma_{\text{th}}\right\} \\
&= \Pr\left\{|h_0|^2 < \frac{{d_0}^n}{P_0}\sum_{m=1}^{M}\frac{\gamma_{th}}{A_0}P_m\frac{|h_m|^2}{{d_m}^n}A_m + \frac{{d_0}^n}{P_0}N_0\frac{\gamma_{th}}{A_0}\right\} \\
&= \frac{1}{\Gamma(k)}\gamma\left(k, \frac{X}{\theta}\right),
\end{aligned} \tag{3.34}$$

where $X = \frac{{d_0}^n}{P_0}\sum_{m=1}^{M}\frac{\gamma_{th}}{A_0}P_m\frac{|h_m|^2}{{d_m}^n}A_m + \frac{{d_0}^n}{P_0}N_0\frac{\gamma_{th}}{A_0}$.

Let $\alpha = \Gamma(k+1)^{-\frac{1}{k}}$, then the above equation can be simplified as

$$
\begin{aligned}
P_{\gamma_0}^{\text{out}} &\approx \left(1-\exp\left(-\alpha\frac{X}{\theta}\right)\right)^k \\
&= \sum_{j=0}^{k}\binom{k}{j}(-1)^j \exp\left(-\alpha j\frac{X}{\theta}\right) \\
&= \sum_{j=0}^{k}\binom{k}{j}(-1)^j \exp\left(-\frac{\alpha j {d_0}^n}{P_0\theta}\sum_{m=1}^{M}\frac{\gamma_{th}}{A_0}P_m\frac{|h_m|^2}{{d_m}^n}A_m\right) \\
&\quad\times \exp\left(-\frac{\alpha j {d_0}^n}{P_0\theta}N_0\frac{\gamma_{th}}{A_0}\right).
\end{aligned} \tag{3.35}
$$

Since the channel fading and the randomness of the drone position are considered here, the channel gain of the interfering signal and the distance from the interfering node to R are averaged to eliminate the effect of the randomness of the positions of these nodes.

Let $I_{gg}=\exp\left(-\frac{\alpha j {d_0}^n}{P_0\theta}\sum_{m=1}^{M}\frac{\gamma_{th}}{A_0}P_m\frac{|h_m|^2}{{d_m}^n}A_m\right)$, then we average over I_{gg} and it yields

$$
\begin{aligned}
I_{gg} &= E_{{d_m}^n}\left[E_{|h_m|^2}\left[\prod_{m=1}^{M}\exp\left(-\frac{\alpha j {d_0}^n}{P_0\theta}\frac{\gamma_{th}}{A_0}\frac{P_m|h_m|^2}{{d_m}^n}A_m\right)\right]\right] \\
&= E_{{d_m}^n}\left[\prod_{m=1}^{M}\int_0^{\infty}\exp\left(-\frac{\alpha j {d_0}^n\theta}{P_0\theta}\frac{\gamma_{th}}{A_0}\frac{P_m x}{{d_m}^n}A_m\right)f_{|h_m|^2}(x)dx\right] \\
&= E_{{d_m}^n}\left[\prod_{m=1}^{M}\left(\frac{\alpha j {d_0}^n}{P_0}\frac{\gamma_{th}}{A_0}\frac{P_m}{{d_m}^n}A_m+1\right)^{-k}\right].
\end{aligned} \tag{3.36}
$$

According to the Probability Generating Function $E\left[\prod_{x\in\Phi}f(x)\right]=\exp\left(-\lambda\int_{\mathbb{R}^2}(1-f(x))\,dx\right)$, using Chebyshev Gaussian quadrature, we can get

$$
\begin{aligned}
I_{gg} &= \exp\left(-\lambda\int_{\mathbb{R}_3}\left(1-\left(\frac{\alpha j {d_0}^n}{P_0}\frac{\gamma_{th}}{A_0}\frac{P_m}{{d_m}^n}A_m+1\right)^{-k}\right)dx\right) \\
&= \exp\left(-\lambda\int_0^r\int_0^{\pi}\int_0^{2\pi}\left(1-\left(\frac{\alpha j {d_0}^n}{P_0}\frac{\gamma_{th}}{A_0}\frac{P_m}{{d_m}^n}A_m+1\right)^{-k}\right)x^2\sin\phi\,d\psi\,d\phi\,dx\right) \\
&= \exp\left(-2\pi\lambda\int_0^r x^2\left(1-\left(\frac{\alpha j {d_0}^n}{P_0}\frac{\gamma_{th}}{A_0}\frac{P_m}{{d_m}^n}A_m+1\right)^{-k}\right)dx\int_0^{\pi}\sin\phi\,d\phi\right)
\end{aligned}
$$

$$= \exp\left(-4\pi\lambda \int_0^r x^2 \left(1 - \left(\frac{\alpha j {d_0}^n}{P_0} \frac{\gamma_{th}}{A_0} \frac{P_m}{{d_m}^n} A_m + 1\right)^{-k}\right) dx\right)$$
$$= \exp\left(-2\pi r\lambda \sum_{v=1}^{v} \sqrt{1 - {t_v}^2}\omega_v {v_v}^2 \left(1 - \left(\frac{\alpha j {d_0}^n}{P_0} \frac{\gamma_{th}}{A_0} \frac{P_m}{{d_m}^n} A_m + 1\right)^{-k}\right)\right), \tag{3.37}$$

where $v_v = \frac{r(t_v+1)}{2}$, $t_v = \cos\left(\frac{2v-1}{2V}\pi\right)$, and $\omega_v = \frac{\pi}{V}$.

Then, the expression for the OP can be finally given as

$$P_{\gamma_0}{}^{\text{out}} = \sum_{j=0}^{k} \binom{k}{j} (-1)^j I_{gg} \exp\left(-\frac{\alpha j {d_0}^n}{P_0 \theta} N_0 \frac{\gamma_{th}}{A_0}\right). \tag{3.38}$$

3.2.2.3 Asymptotic Analysis of the OP

As the SNR tends to infinity, the noise can be neglected. Thus, the SINR approximates the SNR as

$$\gamma_0 \approx \frac{P_0 \frac{|h_0|^2}{{d_0}^n} A_0}{\sum_{m=1}^{M} P_m \frac{|h_m|^2}{{d_m}^n} A_m}, \tag{3.39}$$

then the exponential function can be approximated by Taylor expansion, i.e., $\exp(-x) \approx 1 - x$, so the PDF of $|h_0|^2$ can be written as

$$f_{|h_0|^2}(x) \approx \frac{x^{k-1}}{\Gamma(k)\theta^k}\left(1 - \frac{x}{\theta}\right). \tag{3.40}$$

Therefore, OP can be expressed as

$$\begin{aligned} P_{\gamma_0}{}^{out} &= \Pr\{\gamma_0 < \gamma_{th}\} \\ &= \Pr\left\{\frac{P_0 \frac{|h_0|^2}{{d_0}^n} A_0}{\sum_{m=1}^{M} P_m \frac{|h_m|^2}{{d_m}^n} A_m} < \gamma_{th}\right\} \\ &= \Pr\left\{|h_0|^2 < \frac{\gamma_{th} {d_0}^n}{P_0 A_0} \sum_{m=1}^{M} P_m \frac{|h_m|^2}{{d_m}^n} A_m\right\}. \end{aligned} \tag{3.41}$$

Let $X = \frac{\gamma_{th} {d_0}^n}{P_0 A_0} \sum_{m=1}^{M} P_m \frac{|h_m|^2}{{d_m}^n} A_m$, then OP can be written as

$$
\begin{aligned}
P_{\gamma_0}{}^{out} &= \Pr\left\{|h_0|^2 < X\right\} \\
&= \int_0^X f_{|h_0|^2}(x)\,dx \\
&= \int_0^X \frac{x^{k-1}}{\Gamma(k)\,\theta^k}\left(1-\frac{x}{\theta}\right)dx \\
&= \frac{1}{k}\frac{X^k}{\Gamma(k)\,\theta^k} - \frac{1}{k+1}\frac{X^{k+1}}{\Gamma(k)\,\theta^{k+1}}.
\end{aligned} \tag{3.42}
$$

To eliminate the effects of the randomness of the channel gain and vehicles' positions, OP is averaged to obtain

$$
\begin{aligned}
E[P_{\gamma_0}{}^{out}] &= E\left[\frac{1}{k}\frac{X^k}{\Gamma(k)\,\theta^k} - \frac{1}{k+1}\frac{X^{k+1}}{\Gamma(k)\,\theta^{k+1}}\right] \\
&= \frac{1}{k}\frac{1}{\Gamma(k)\,\theta^k}E\left[X^k\right] - \frac{1}{k+1}\frac{1}{\Gamma(k)\,\theta^{k+1}}E\left[X^{k+1}\right].
\end{aligned} \tag{3.43}
$$

For $E[X^k]$, one can obtain

$$
\begin{aligned}
E[X^k] &= E\left[\left(\frac{\gamma_{th}{d_0}^n}{P_0 A_0}\sum_{m=1}^{M} P_m \frac{|h_m|^2}{{d_m}^n} A_m\right)^k\right] \\
&= \left(\frac{\gamma_{th}{d_0}^n}{P_0 A_0}\right)^k E\left[\left(\sum_{m=1}^{M} P_m \frac{|h_m|^2}{{d_m}^n} A_m\right)^k\right].
\end{aligned} \tag{3.44}
$$

Since the calculation of $E\left[\left(\sum_{m=1}^{M} P_m \frac{|h_m|^2}{{d_m}^n} A_m\right)^k\right]$ is complicated, we perform simulations to approximate the distribution of $\sum_{m=1}^{M} P_m \frac{|h_m|^2}{{d_m}^n} A_m$, and thus calculate the k-order moments of this variable. The parameters set in each of the two fits are given in Table 3.1.

We simulate and fit $\sum_{m=1}^{M} P_m \frac{|h_m|^2}{{d_m}^n} A_m$ as shown in Figs. 3.5 and 3.6. With parameters set to Table 3.1, the distribution of $\sum_{m=1}^{M} P_m \frac{|h_m|^2}{{d_m}^n} A_m$ approximately obeys

Table 3.1 Nakagami-m fitting parameters

Parameter	m	Ω	Radius of the sphere space r	Density of PPP λ
Parameter 1	12	1.05×10^{-4}	1×10^{-3}	1×10^{-8}
Parameter 2	66	1.2×10^{-3}	1×10^{-3}	1×10^{-7}

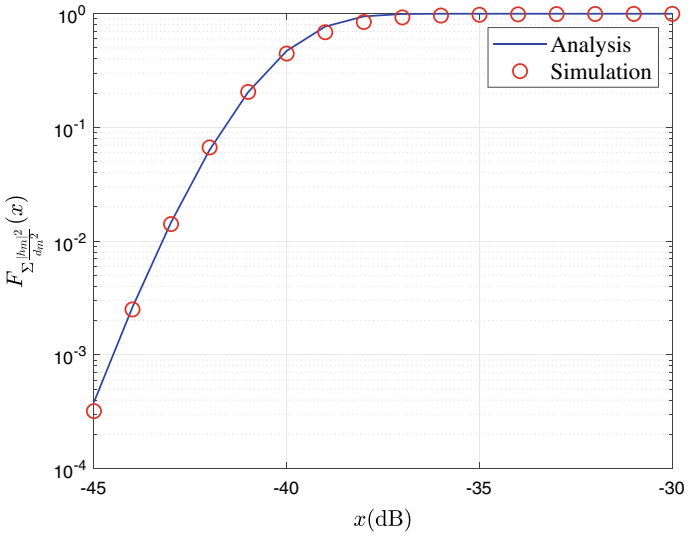

Fig. 3.5 Nakagami-*m* fitting results under parameter 1

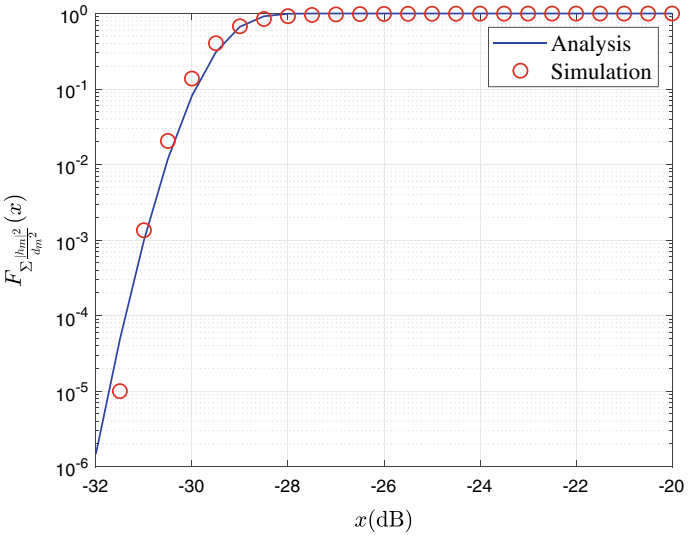

Fig. 3.6 Nakagami-*m* fitting results under parameter 2

Nakagami-m distribution, so the calculation continues using the Nakagami-m distribution function

$$\begin{aligned} E[X^k] &= \left(\frac{\gamma_{th} {d_0}^n}{P_0 A_0}\right)^k E\left[\left(\sum_{m=1}^{M} P_m \frac{|h_m|^2}{{d_m}^n} A_m\right)^k\right] \\ &= \left(\frac{\gamma_{th} {d_0}^n}{P_0 A_0}\right)^k \int_0^{+\infty} x^k \frac{2m^m}{\Gamma(m)\,\Omega^m} x^{2m-1} \exp\left(-\frac{m}{\Omega} x^2\right) dx \\ &= \left(\frac{\gamma_{th} {d_0}^n}{P_0 A_0}\right)^k \frac{\Gamma\left(m+\frac{k}{2}\right)\Omega^{\frac{k}{2}}}{\Gamma(m)\,m^{\frac{k}{2}}}. \end{aligned} \tag{3.45}$$

Based on the above results, the asymptotic expression for OP can be obtained as

$$\begin{aligned} {P_{\gamma_0}}^{out} =& \frac{1}{k} \frac{1}{\Gamma(k)\,\theta^k} \left(\frac{\gamma_{th} {d_0}^n}{P_0 A_0}\right)^k \frac{\Gamma\left(m+\frac{k}{2}\right)\Omega^{\frac{k}{2}}}{\Gamma(m)\,m^{\frac{k}{2}}} \\ &- \frac{1}{k+1} \frac{1}{\Gamma(k)\,\theta^{k+1}} \left(\frac{\gamma_{th} {d_0}^n}{P_0 A_0}\right)^{k+1} \frac{\Gamma\left(m+\frac{k+1}{2}\right)\Omega^{\frac{k+1}{2}}}{\Gamma(m)\,m^{\frac{k+1}{2}}}. \end{aligned} \tag{3.46}$$

3.2.3 Numerical Results

In the simulation process of OP, it is necessary to quantify the assumed model, study the transmission performance of the system based on numerical results, and validate the analysis model proposed in the previous sections. In addition, it is also necessary to simulate different parameters separately by controlling variables to explore the impact of different parameters on OP.

In the simulation, 10^5 Monte Carlo simulation experiments were conducted to model the possible effects of the randomness of the positions on the transmission performance. The main parameters are set as $k = 1$, $n = 2$, $S = 1000$, $\gamma_{th} = 1$, $\Omega_I = 1$ dBW, $T_b = 1.5 \times 10^{-4}$ s, $f_m = 150$ kHz, $P_0 = 30$ dBW, $P_m = 10$ dBW, $N_0 = -130$ dBW, $d_0 = 10000$ m, $\lambda = 5 \times 10^{-11}$, $T_c = 2 \times 10^{-6}$ s, $\tau_m = 2 \times 10^{-6}$ s, $\delta = 1$ Hz, $\theta_m = 0$, $\Delta t = 1 \times 10^{-5}$, and $r = 1000$ m.

Numerical results achieved by the derived analysis expressions presented in the previous section are compared with those obtained by Monte Carlo simulation to verify the accuracy of the proposed analysis models. From Fig. 3.7, it can be seen that the simulation results can be fitted with the theoretical ones. In contrast, the results of the asymptotic analysis are approximate to the theoretical results, thus proving the derivation results' accuracy.

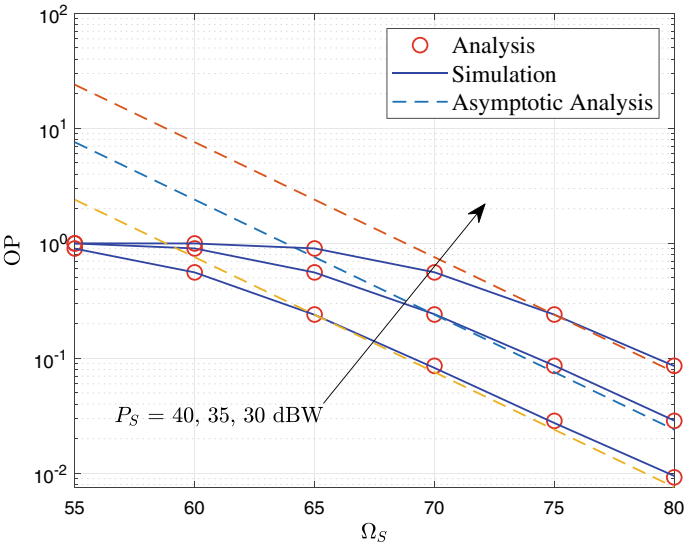

Fig. 3.7 Simulation and analysis results for OP

3.2.3.1 Numerical Results for OP

Figure 3.8 shows the simulation and theoretical results of the OP with different code chip periods. Observing this figure, it can be seen that the OP with different codebook cycles remains consistent, indicating that the chip period does not affect the OP of the considered system.

Figure 3.9 shows the simulation and analysis results of the OP under different chip delays. One can see that the OP of the system increases significantly with the increase of the chip delay. Therefore, reducing the chip delay can improve the outage performance.

Figure 3.10 shows the simulation and analysis results of the OP under different frequency compensation errors. We can see that when Ω_S is small, the frequency compensation error impacts the OP of the system. However, as Ω_S gradually becomes more significant, the OP under different frequency compensation errors slowly converges.

Figure 3.11 shows the simulation and analysis results of the OP with different random phases. As suggested in this figure, the OP of the system increases significantly with the increase of the random phase, which a large random phase will lead to bad receiving performance.

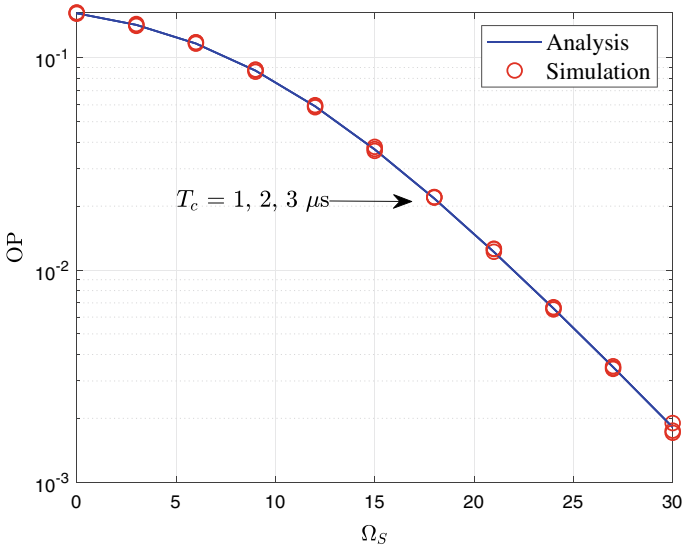

Fig. 3.8 OP for various chip periods T_c

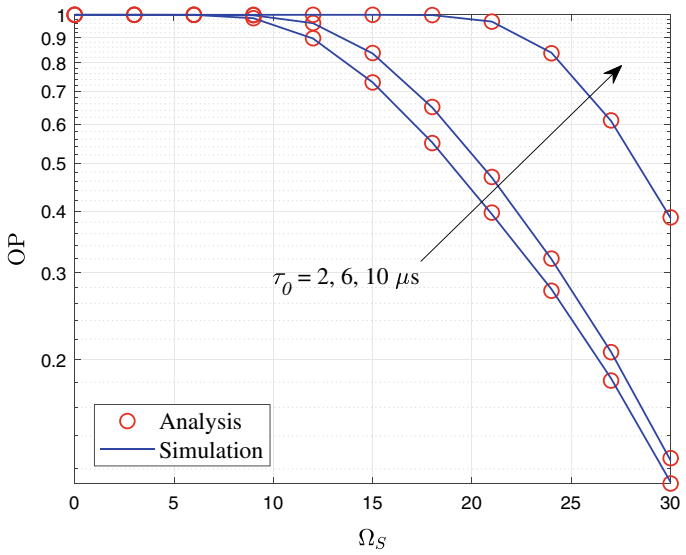

Fig. 3.9 OP for various chip delays τ_m

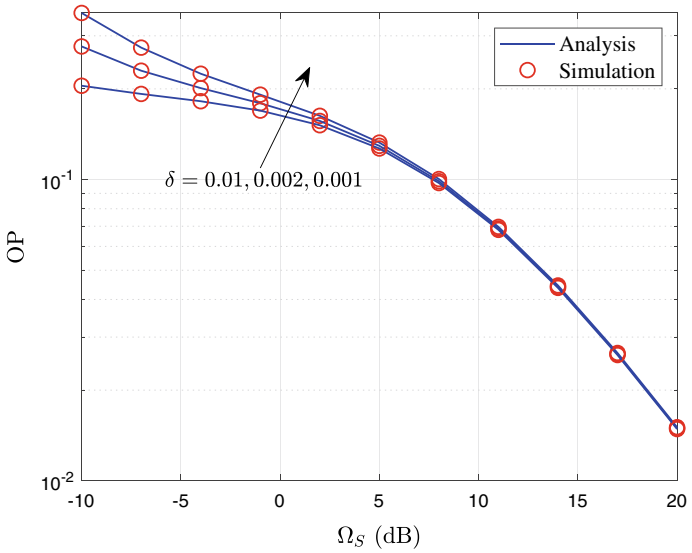

Fig. 3.10 OP for various frequency compensation errors δ

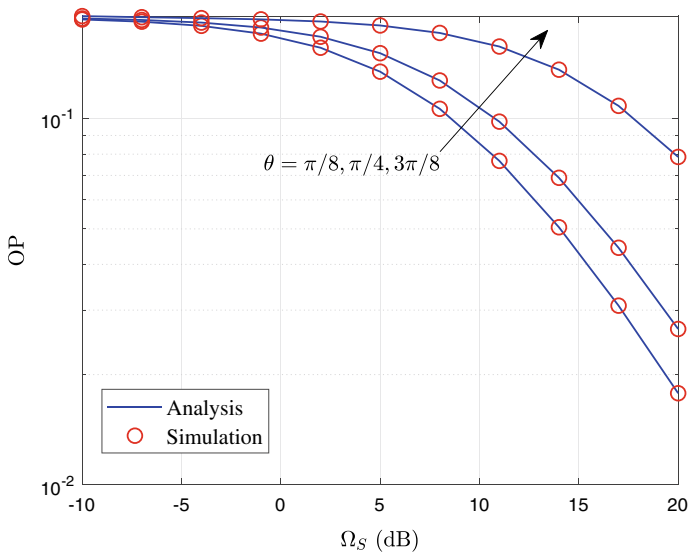

Fig. 3.11 OP for various random phases θ_m

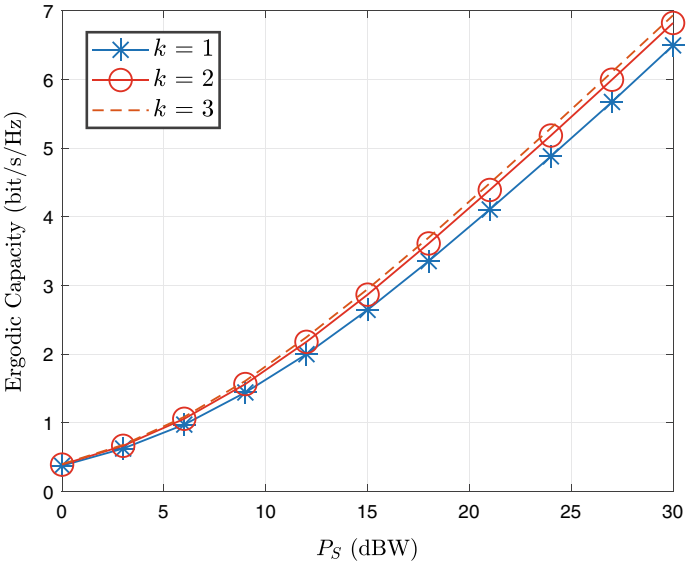

Fig. 3.12 Simulation results for traversing capacity

3.2.3.2 Numerical Results for EC

According to Shannon's theorem, the capacity of the system can be defined as

$$C = B\log_2(1+\gamma), \tag{3.47}$$

where B is the channel bandwidth and γ is the SNR at the receiver.

Figure 3.12 shows the simulation results of the EC with different channel fading factors under the default parameters above. As the figure shows, the EC gradually increases as the transmit power increases. When the fading parameter of Nakagami increases, the traversal capacity increases slightly but to a lesser extent.

3.2.4 Conclusion

This section focuses on the drone swarm's transmission performance, and the research's main content includes establishing the system signal model and deriving the analysis model for the OP.

The inter-drone-swarm transmission performance is an important direction in the research of drones. The current research on the drone swarm's transmission performance focuses on communication technology, network topology, routing and scheduling methods, data processing, and other related technologies. Combining the

randomness of the drone swarm with the anti-interference performance can help find a more suitable solution to tackle the interference problem within the swarm more comprehensively.

References

1. G. Pan, H. Lei, Z. Ding, Q. Ni, On 3-D hybrid VLC-RF systems with light energy harvesting and OMA scheme over RF links, in *GLOBECOM 2017-2017 IEEE Global Communications Conference* (2017), pp. 1–6
2. Y. Zeng, R. Zhang, T.J. Lim, Wireless communications with unmanned aerial vehicles: opportunities and challenges. IEEE Commun. Mag. **54**(5), 36–42 (2016)
3. I.S. Gradshteyn, I.M. Ryzhik, *Table of Integrals, Series and Products*, 7th edn. (Academic Press, San Diego, 2007)
4. A.P. Prudnikov, Yu.A. Brychkov, O.I. Marichev, *Integrals and Series of Elementary Functions* (Science, New York, 1992)
5. G. Zhang, Q. Wu, M. Cui, R. Zhang, Securing UAV communications via trajectory optimization, in *GLOBECOM 2017-2017 IEEE Global Communications Conference* (2017), pp. 1–6

Chapter 4
Satellite-UAV Communications

Yu Tian, Jiliang Zhang, Gaofeng Pan, and Mohamed-Slim Alouini

4.1 Stochastic Analysis of Cooperative Satellite-UAV Communications

This section considers a dual-hop cooperative satellite-UAV communication system including a satellite (S) and a group of cluster headers (CHs), respectively, with a group of uniformly distributed UAVs. Specifically, the CHs serve as aerial decode-and-forward (DF) relays to forward the information transmitted by the S to the UAVs. Moreover, free-space optical (FSO) and RF technologies are adopted over S-CH and CH-UAV links to exploit the high directivity of FSO over long-distance transmission and the omnidirectional coverage ability of RF. The positions of the CHs in the three-dimensional space follow the Matern hard-core point processes type II, in which each CH cannot be closer to another by less than a predefined distance. Three cases of CH-UAV links are considered during the performance modeling: Interference-free, interference-dominated, and interference-and-noise. Then, the coverage performance of the S-CH link and CH-UAV links in the three cases is studied, and the closed-form analytical expressions of the coverage probability (CP) over both links are derived. The asymptotic expressions for the CP over the S-CH link and CH-UAV link in the interference-free case are derived. Finally, numerical results are provided to validate our proposed analytical models, and thus, some meaningful conclusions are achieved.

Y. Tian · M.-S. Alouini
King Abdullah University of Science and Technology (KAUST), Thuwal, Saudi Arabia
e-mail: yu.tian@kaust.edu.sa

M.-S. Alouini
e-mail: slim.alouini@kaust.edu.sa

J. Zhang
Southwest University, Chongqing, China
e-mail: swuzhang@swu.edu.cn

G. Pan (✉)
Beijing Institute of Technology, Beijing, China
e-mail: gfpan@bit.edu.cn

G. Pan et al. (eds.), *UAV Communications: Modeling and Analyses*,
https://doi.org/10.1007/978-981-97-0383-8_4

The main contributions of Sect. 4.1 are summarized as follows.

(1) Compared with [1], in which (a) the distribution of UAVs with fixed numbers follow 3D BPP, (b) small-scale fading is not considered, and (c) the statistical randomness of the interfering signals in 3D space was approximated by using the Gamma distribution via the central limit theorem, in Sect. 4.1, (a) 3D MHCPP is utilized to make the system model more general, (b) Nakagami-*m* fading is employed to cover more network scenarios like troposphere and terrestrial spaces in which the impacts of multi-path propagation cannot be neglected, and (c) a more accurate moment generating function (MGF) of the summation of interfering signals over CH-UAV RF links is derived considering the randomness of the 3D locations of the CHs.
(2) Compared with [2, 3], we address the issue that path loss exponent $\alpha_r > 3$ in 3D MHCPP by introducing the maximum interference distributed range $D_{\max}$. α_r can be set as small as 2, which can accurately describe the LOS aerial communications. We also adopt the Nakagami-*m* fading model instead of the Rayleigh model to make the analysis more general.
(3) Compared with [2, 3], and [1], in which non-closed-form analytical expressions were presented for the performance indices while considering 3D interfering scenarios, in Sect. 4.1 closed-form analytical expressions are respectively derived for the CP over S-CH FSO links and CH-UAV RF links in interference-free, interference-dominated, and interference-and-noise cases.
(4) The asymptotic expressions for the CP are derived, and the diversity orders are calculated for the interference-free case of the S-CH FSO and CH-UAV RF links.

4.1.1 System Model

In Sect. 4.1, a dual-hop cooperative satellite-UAV communication system, which contains S and a group of CHs[1] that are respectively with a group of uniformly distributed UAVs, is considered, as shown in Fig. 4.1. Specifically, S first delivers its intensity-modulated optical signals to CHs by using multibeam wavelength division multiplexing-FSO technology [4]. Then each CH decodes its received signals by optical direct detection and forwards the recoded information to the UAVs within its serving space.[2,3]

[1] In practical, CHs can be common airplanes piloted by human or the UAVs with superior hardware resources, which is capable of providing data receiving, processing, and forwarding functionalities to serve as aerial relays between S and UAVs.

[2] This cluster-based CH-UAV network has the advantages of easy management and low operating cost, and is especially suitable for the highly dynamic scenarios with resource-constrained terminals.

[3] As most of the modulation schemes implemented in FSO systems are usually different from those adopted in RF communication systems, the DF technology is applied at the CHs rather than the amplify-and-forward technology.

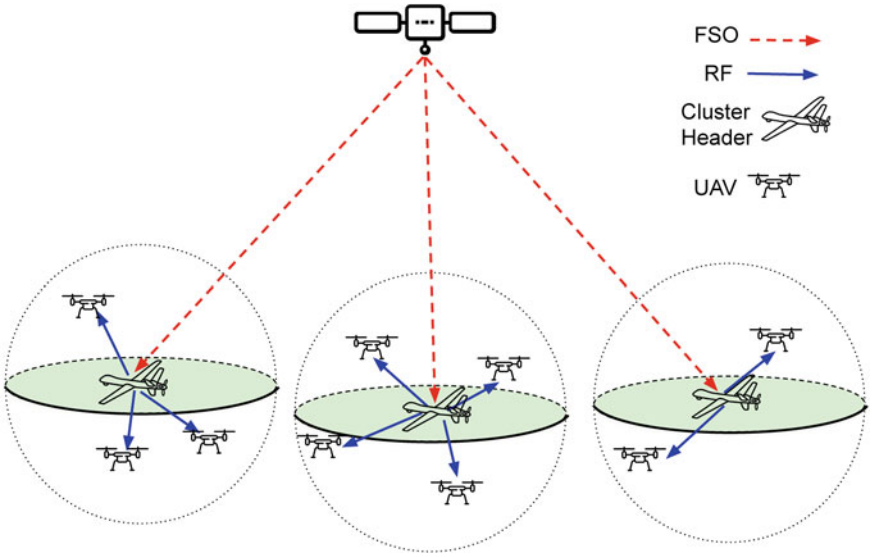

Fig. 4.1 System model

4.1.1.1 S-CH FSO Link

It is assumed that FSO communication technology is adopted over S-CH links to exploit its high directivity to minimize the probability that the transmitted information is wiretapped during long-distance transmission over S-CH links.[4] This assumption is reasonable as FSO technology has already been designed and implemented and is to be tested for inter-satellite and space-to-aerial communications benefiting from its own unique advantages, e.g., Space Development Agency plans to demonstrate optical communications from satellites to a military drone aircraft in the summer of 2021 [5].

Also, to reflect and meet practical aerial scenarios, in the considered system model, the locations of the CHs in 3D space are assumed to obey an MHCPP type-II,[5] denoted by Φ_{CH}, with an intensity of λ_{CH} and a minimum distance $D_{\min}$ between different CHs. To obtain the proposed MHCPP, a three-step thinning process is applied. Firstly, candidate points whose distribution follows an HPPP Φ_{P} with an intensity λ_{P} are

[4] Normally, the distance of satellite-aerial transmissions ranges from hundreds of to tens of thousands of kilometers, depending on the orbit height of the satellite.

[5] Here, we assume that the UAVs work in clusters and each cluster has its own working space. Moreover, one can easily see that if two clusters are too close to each other, they will merge into one cluster; otherwise, serious interference between/among two or more close UAV clusters will inevitably arise, resulting in the collapse of UAV systems.

generated in such a way that these points are uniformly distributed in the considered 3D space $\mathcal{V}$ and the number of candidate points $N_{\mathrm{P}} = |\Phi_{\mathrm{P}}|$ has a probability mass function of Poisson distribution with a mean $\lambda_{\mathrm{P}} V$ [6] expressed as

$$\mathbf{Pr}\{N_{\mathrm{P}} = n\} = \frac{(\lambda_{\mathrm{P}} V)^n}{n!} \exp\left(-\lambda_{\mathrm{P}} V\right), \tag{4.1}$$

where V is the volume of $\mathcal{V}$.

Then, secondly, each candidate point is assigned to an independent mark which obeys a uniform distribution ranging from 0 to 1. Thirdly, whether each candidate point is associated with the smallest mark is individually checked and compared with all other points around it within a distance, $D_{\min}$. The point can remain in Φ_{CH} if true. Otherwise, the point will be eliminated. This process shows that each CH exhibits a spherical repulsion space with the radius $D_{\min}$.

Thus, according to [6, Eq. (5.56)], the relationship between λ_{CH} and λ_{P} is given as

$$\lambda_{\mathrm{CH}} = \frac{1 - \exp\left(-\frac{4}{3}\pi D_{\min}^3 \lambda_{\mathrm{P}}\right)}{\frac{4}{3}\pi D_{\min}^3}. \tag{4.2}$$

As shown in Fig. 4.2, CHs are distributed inside a 3D space $\mathcal{V}$ that is defined by subtracting a spherical cone with radius R from another spherical cone with radius $R + H_{\mathrm{U}}$. The two spherical cones share the same center O and apex angle ξ_0. The volume of $\mathcal{V}$ is $V = \frac{2\pi}{3}(1 - \cos\xi_0)[(R + H_{\mathrm{U}})^3 - R^3]$.

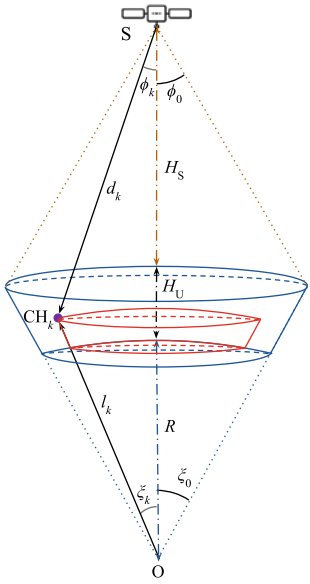

Fig. 4.2 S-CH system model

For the FSO link, the intensity modulated direct detection is utilized. According to [7, Eq. (3.1.27)], the electrical signal received by CH_k after photoelectric conversion is

$$y_k = \eta P_{\mathrm{S}} G_{\mathrm{S}} G_{\mathrm{R}} \left(\frac{\lambda}{4\pi d_k} \right)^2 h_p h_a h_l s_k + n_k, \tag{4.3}$$

where P_{S} is the transmit optical power, η is the effective photoelectric conversion ratio, G_{S} and G_{R} are the telescope gains of the transmitter and receiver, λ is the wavelength of the laser, d_k is the distance from the S to CH_k, h_p is the random attenuation caused by beam spreading and misalignment fading, h_a is the random attenuation caused by atmospheric turbulence, h_l is the atmospheric loss, s_k is the transmitted symbol with the average power of 1, and n_k is the AWGN of CH_k with power N_{F}.

In Sect. 4.1, we adopt the fading model mentioned in [8], which considers the atmospheric loss h_l, the atmospheric turbulence h_a with Gamma-Gamma distribution, and the misalignment fading h_p with a zero boresight pointing error model. Then, the CDF of the channel power gain $h = h_l h_a h_p$ can be given as

$$F_h(x) = \frac{\omega^2}{\Gamma(\alpha)\Gamma(\beta)} G_{2,4}^{3,1}\left(\frac{\alpha\beta}{A_0 h_l} x \,\middle|\, \begin{matrix} 1, \omega^2 + 1 \\ \omega^2, \alpha, \beta, 0 \end{matrix} \right), \tag{4.4}$$

where $\Gamma(\cdot)$ is the gamma function, α and β are the effective number of small-scale and large-scale eddies of the scattering environment, $G(\cdot|\cdot)$ is the Meijer-G function, A_0 is the fraction of power collected by the detector when there is no pointing error, and ω is the ratio between the equivalent beam radius and the standard deviation of pointing error displacement at the receiver.

In this context, the SNR of the signal received at CH_k is

$$\gamma_k = \frac{\eta^2 P_{\mathrm{S}}^2 G_{\mathrm{S}}^2 G_{\mathrm{R}}^2 \lambda^4 h^2}{(4\pi)^4 d_k^4 N_{\mathrm{F}}}. \tag{4.5}$$

Lemma 4.1 *Given d_k, the CDF of γ_k is*

$$F_{\gamma_k | d_k^2}(x) = \frac{\omega^2}{\Gamma(\alpha)\Gamma(\beta)} G_{2,4}^{3,1}\left(\Xi d_k^2 \sqrt{x} \,\middle|\, \begin{matrix} 1, \omega^2 + 1 \\ \omega^2, \alpha, \beta, 0 \end{matrix} \right), \tag{4.6}$$

where $\Xi = \frac{\alpha\beta(4\pi)^2\sqrt{N_{\mathrm{F}}}}{A_0 h_l \eta \lambda^2 P_{\mathrm{S}} G_{\mathrm{S}} G_{\mathrm{R}}}$.

Proof From Eqs. (4.4) and (4.5), we can get

$$\begin{aligned} F_{\gamma_k|d_k^2}(x) &= \mathbf{Pr}\{\gamma_k \le x\} = \mathbf{Pr}\left\{\frac{\eta^2 P_{\mathrm{S}}^2 G_{\mathrm{S}}^2 G_{\mathrm{R}}^2 \lambda^4 h^2}{(4\pi)^4 d_k^4 N_{\mathrm{F}}} \le x\right\} \\ &= \mathbf{Pr}\left\{h \le \frac{(4\pi)^2 d_k^2}{\eta\lambda^2}\frac{\sqrt{N_{\mathrm{F}}x}}{P_{\mathrm{S}}G_{\mathrm{S}}G_{\mathrm{R}}}\right\} \\ &= \frac{\omega^2}{\Gamma(\alpha)\Gamma(\beta)} G_{2,4}^{3,1}\left(\Xi d_k^2\sqrt{x}\,\middle|\,\begin{matrix}1, \omega^2+1\\ \omega^2, \alpha, \beta, 0\end{matrix}\right), \end{aligned} \tag{4.7}$$

where $\Xi = \frac{\alpha\beta(4\pi)^2\sqrt{N_{\mathrm{F}}}}{A_0 h_l \eta\lambda^2 P_{\mathrm{S}} G_{\mathrm{S}} G_{\mathrm{R}}}$. □

Proposition 4.1 *When $D_{\min} \ll \mathrm{V}^{\frac{1}{3}}$, CHs are approximately independently and uniformly distributed in $\mathcal{V}$.*

Proof Please refer to Appendix 3. □

Lemma 4.2 *The PDF of d_k^2 is*

$$f_{d_k^2}(x) = \frac{\pi}{2VL}\left[\tau_2^2(x) - \tau_1^2(x)\right], \tag{4.8}$$

where $d_{\min}^2 \le x \le d_{\max}^2$, $d_{\min} = H_{\mathrm{S}}$, $d_{\max} = \sqrt{R^2 + L^2 - 2RL\cos\xi_0}$, $L = H_{\mathrm{S}} + H_{\mathrm{U}} + R$, $\tau_2(x) = \min\left\{R + H_{\mathrm{U}}, L\cos\xi_0 - \sqrt{x - L^2\sin^2\xi_0}\right\}$, *and* $\tau_1(x) = \max\left\{R, L - \sqrt{x}\right\}$.

Proof Please refer to Appendix 4. □

Theorem 4.1 (4.1.1) *The CDF of γ_k is*

$$\begin{aligned} F_{\gamma_k}(x) =& \frac{\pi^2 b_1 \omega^2}{2M_f VL\Gamma(\alpha)\Gamma(\beta)} \sum_{i=1}^{M_f}\left[\tau_2^2(b_i) - \tau_1^2(b_i)\right]\sqrt{1-t_i^2} \\ &\times G_{2,4}^{3,1}\left(\Xi b_i\sqrt{x}\,\middle|\,\begin{matrix}1, \omega^2+1\\ \omega^2, \alpha, \beta, 0\end{matrix}\right), \end{aligned} \tag{4.9}$$

where M_f is the number of points of the Chebyshev-Gauss quadrature, $t_i = \cos\frac{2i-1}{2M_f}\pi$, $b_i = b_1 t_i + b_2$, $b_1 = \frac{d_{\max}^2 - d_{\min}^2}{2}$ and $b_2 = \frac{d_{\max}^2 + d_{\min}^2}{2}$.

Proof Using Eq. (4.6), the CDF of γ_k is

$$\begin{aligned} F_{\gamma_k}(x) &= \int_{d_{\min}^2}^{d_{\max}^2} F_{\gamma_k|d_k^2}(x|y) f_{d_k^2}(y) dy \\ &= \int_{d_{\min}^2}^{d_{\max}^2} \frac{\pi\omega^2}{2VL\Gamma(\alpha)\Gamma(\beta)}[\tau_2^2(y) - \tau_1^2(y)] G_{2,4}^{3,1}\left(\Xi x\sqrt{y}\,\middle|\,\begin{matrix}1, \omega^2+1\\ \omega^2, \alpha, \beta, 0\end{matrix}\right) dy. \end{aligned} \tag{4.10}$$

By setting $b_1 = \frac{d_{\max}^2 - d_{\min}^2}{2}$, $b_2 = \frac{d_{\max}^2 + d_{\min}^2}{2}$ and $t = \frac{y - b_2}{b_1}$ and employing the M_f-point Chebyshev-Gauss quadrature in the first case, Eq. (4.10) can be written as

$$\begin{aligned} F_{\gamma_k}(x) &= \frac{\pi b_1 \omega^2}{2VL\Gamma(\alpha)\Gamma(\beta)} \int_{-1}^{1} \left[\tau_2^2(b_1 t + b_2) - \tau_1^2(b_1 t + b_2)\right] \\ &\quad \times G_{2,4}^{3,1}\left(\Xi (b_1 t + b_2)\sqrt{x} \,\middle|\, \begin{matrix} 1, \omega^2 + 1 \\ \omega^2, \alpha, \beta, 0 \end{matrix} \right) dt \\ &= \frac{\pi^2 b_1 \omega^2}{2M_f VL\Gamma(\alpha)\Gamma(\beta)} \sum_{i=1}^{M_f} \left[\tau_2^2(b_i) - \tau_1^2(b_i)\right] \\ &\quad \times \sqrt{1 - t_i^2}\, G_{2,4}^{3,1}\left(\Xi b_i \sqrt{x} \,\middle|\, \begin{matrix} 1, \omega^2 + 1 \\ \omega^2, \alpha, \beta, 0 \end{matrix} \right), \end{aligned} \tag{4.11}$$

where $t_i = \cos \frac{2i-1}{2M_f}\pi$ and $b_i = b_1 t_i + b_2$. □

4.1.1.2 CH-UAV RF Link

RF communication is employed over CH-UAV links to utilize its omnidirectional coverage ability to realize information broadcasting in the local space of each CH. Moreover, in Sect. 4.1, we also assume that UAVs around the kth CH, CH_k, are uniformly distributed in its serving sphere, centered at CH_k with radius D_k. Their positions in 3D space obey an HPPP $\Phi_{k\mathrm{U}}$ with an intensity $\lambda_{k\mathrm{U}}$. CH_k forwards the recoded information with the transmit power P_k to the UAVs within its serving space.

In the second hop shown in Fig. 4.1, CH_k will transmit the recoded signals to the UAVs within its serving space, namely, the UAVs within the sphere with radius D_k centered at CH_k.[6]

To guarantee that there is no intersection between the serving spaces of any two CHs (CH_k and CH_j), $D_j + D_k < D_{\min}$ $(j \neq k)$ should be satisfied. The number of UAVs around CH_k, $N_{k\mathrm{U}}$, follows an HPPP with the density $\lambda_{k\mathrm{U}}$. The PMF of $N_{k\mathrm{U}}$ is $\mathbf{Pr}\{N_{k\mathrm{U}} = n\} = (\mu^n/n!)\exp(-\mu)$, where $\mu = \frac{4\pi D_k^3}{3}\lambda_{k\mathrm{U}}$ is the mean measure. To make the analysis tractable, we assume that all CHs have the same serving radius and the UAVs around them have the same density, namely, $D_k = D$ and $\lambda_{k\mathrm{U}} = \lambda_{\mathrm{U}}$ $(k = 1, \ldots, N_{\mathrm{CH}}, N_{\mathrm{CH}} = |\Phi_{\mathrm{CH}}|)$. Meanwhile, we assume that the communication channels from CH to UAVs suffer Nakagami-m fading.[7]

[6] In Sect. 4.1, a single antenna is considered at each UAV to reflect the rigorous hardware constraints of practical UAV systems, as well as to make Sect. 4.1 more concise. However, interested readers can easily expand our work to multi-antenna cases by exploiting the analysis method presented here.

[7] As suggested in Sect. 3.2.3 of [9], Nakagami-m can approximate Rician fading with the parameter K, which can be deduced by the fading parameter $m = (K+1)^2/(2K+1)$. In other words, Nakagami-m can represent the channel fading in the case of LoS transmission, which is the typi-

Then, the PDF and CDF of channel power gain g are shown as

$$f_g(x) = \left(\frac{m}{\Omega}\right)^m \frac{x^{m-1}}{(m-1)!} \exp\left(-\frac{m}{\Omega}x\right) \tag{4.12}$$

and

$$F_g(x) = 1 - \sum_{i=0}^{m-1} \left(\frac{m}{\Omega}\right)^{m_i} \frac{x^{m_i}}{m_i!} \exp\left(-\frac{m}{\Omega}x\right), \tag{4.13}$$

respectively, where Ω is the average received power, m is the fading parameter, and $m_i = m - i - 1$. Notably, to simplify the analysis, we only consider the scenario where m is an integer in the remainder of this section.

The free-space path-loss from CH_k to the jth $(0 < j \leq N)$ UAV marked as U_j can be given by $\rho d_{kj}^{\alpha_r}$, where ρ denotes the path loss at a distance $d = 1$ m and value of ρ depends on the carrier frequency, α_r is the path-loss exponent factor, and d_{kj} is the link distance between CH_k and U_j.

Lemma 4.3 *The PDF of d_{kj} are respectively given as*

$$f_{d_{kj}}(x) = \begin{cases} \frac{3}{D^3}x^2, & \text{if } 0 \leq x \leq D; \\ 0, & \text{else} \end{cases}. \tag{4.14}$$

Proof UAVs served by CH_k can be modeled as a set of independently and identically uniformly distributed points in a sphere centered at CH_k, denoted as W_k. According to [10], d_{kj} can be calculated from W_k, the PDF of which can be presented as

$$f_{W_k} = \frac{\lambda_{\mathrm{U}}}{\mu} = \frac{3}{4\pi D^3}. \tag{4.15}$$

Therefore, the CDF of d_{kj} can be calculated as

$$F_{d_{kj}}(x) = \int_0^x \int_0^\pi \int_0^{2\pi} \frac{3}{4\pi D^3} \sin\xi r^2 d\theta d\xi dr$$

$$= \begin{cases} 0, & \text{if } x < 0; \\ \frac{x^3}{D^3}, & \text{elseif } 0 \leq x \leq D; \\ 1, & \text{else} \end{cases}. \tag{4.16}$$

Then, the PDF of d_{kj} can be obtained though $f_{d_{kj}}(x) = \frac{dF_{d_{kj}}(x)}{dx}$. □

cal propagation scenario for the transmissions between CHs and UAVs. Also, when m approaches infinity, Nakagami-m can describe the case without fading.

4.1.2 Performance Analysis over S-CH FSO Links

4.1.2.1 Coverage Performance

CP is defined as the ergodic probability that the received SNR of a randomly selected receiver exceeds a specific threshold. Adopting Eq. (4.6) and given the SNR threshold γ_{th}, the CP of CH_k is given as

$$\begin{aligned} P_{\text{cov,SCH}_k}(\gamma_{\text{th}}) &= \mathbf{Pr}\{\gamma_k > \gamma_{\text{th}}\} \\ &= 1 - F_{\gamma_k}(\gamma_{\text{th}}) \\ &= 1 - \frac{\pi^2 b_1 \omega^2}{2M_f V L \Gamma(\alpha)\Gamma(\beta)} \sum_{i=1}^{M_f} \left[\tau_2^2(b_i) - \tau_1^2(b_i)\right] \\ &\quad \times \sqrt{1-t_i^2}\, \underbrace{G_{2,4}^{3,1}\left(\Xi b_i \sqrt{\gamma_{\text{th}}} \,\middle|\, \begin{matrix} 1, \omega^2+1 \\ \omega^2, \alpha, \beta, 0 \end{matrix}\right)}_{MG_0}. \end{aligned} \tag{4.17}$$

4.1.2.2 Asymptotic Coverage Performance

Theorem 4.2 (4.1.2) *The CP at high transmit SNR ($P_{\text{S}}^2/N_{\text{F}} \to \infty$) can be expressed as*

$$\begin{aligned} P_{\text{cov,SCH}_k}^{\infty}(\gamma_{\text{th}}) \approx 1 &- \frac{\pi^2 b_1 \omega^2}{2M_f V L \Gamma(\alpha)\Gamma(\beta)} \sum_{i=1}^{M_f} \sqrt{1-t_i^2}\left[\tau_2^2(b_i) - \tau_1^2(b_i)\right] \\ &\times \left[\left(\Xi b_i \sqrt{\gamma_{\text{th}}}\right)^{\omega^2} \frac{\Gamma(\alpha-\omega^2)\Gamma(\beta-\omega^2)}{\omega^2} + \left(\Xi b_i \sqrt{\gamma_{\text{th}}}\right)^{\alpha} \right. \\ &\left. \times \frac{\Gamma(\omega^2-\alpha)\Gamma(\beta-\alpha)}{\alpha\Gamma(\omega^2+1-\alpha)} + \left(\Xi b_i \sqrt{\gamma_{\text{th}}}\right)^{\beta} \frac{\Gamma(\omega^2-\beta)\Gamma(\alpha-\beta)}{\beta\Gamma(\omega^2+1-\beta)} \right]. \end{aligned} \tag{4.18}$$

Proof According to [11, Eq. (9.31.2)], MG_0 in Eq. (4.17) can be inverted as

$$MG_0 = G_{4,2}^{1,3}\left(\frac{1}{\Xi b_i \sqrt{\gamma_{\text{th}}}} \,\middle|\, \begin{matrix} 1-\omega^2, 1-\alpha, 1-\beta, 1 \\ 0, -\omega^2 \end{matrix}\right). \tag{4.19}$$

When $P_{\text{S}}^2/N_{\text{F}} \to \infty$, using the definition of Ξ in Eq. (4.7), we can get that $\frac{1}{\Xi b_i \sqrt{\gamma_{\text{th}}}} \to \infty$.

Resorting to [12, Eq. (17)], when $\frac{1}{\Xi b_i \sqrt{\gamma_{\text{th}}}} \to \infty$, MG_0 can be expanded as

$$\lim_{\frac{1}{\Xi b_i\sqrt{\gamma_{\text{th}}}}\to\infty} MG_0 = \left(\Xi b_i\sqrt{\gamma_{\text{th}}}\right)^{\omega^2} \frac{\Gamma(\alpha-\omega^2)\Gamma(\beta-\omega^2)}{\omega^2} + \left(\Xi b_i\sqrt{\gamma_{\text{th}}}\right)^{\alpha} \frac{\Gamma(\omega^2-\alpha)\Gamma(\beta-\alpha)}{\alpha\Gamma(\omega^2+1-\alpha)} + \left(\Xi b_i\sqrt{\gamma_{\text{th}}}\right)^{\beta} \frac{\Gamma(\omega^2-\beta)\Gamma(\alpha-\beta)}{\beta\Gamma(\omega^2+1-\beta)}. \tag{4.20}$$

Substituting Eqs. (4.20)–(4.17), (4.18) can be obtained. □

4.1.2.3 Diversity Order

In Sect. 4.1, the diversity order of the considered system is defined as

$$\Lambda = -\lim_{\bar{\gamma}\to\infty} \frac{\log(1-P_{\text{cov}})}{\log\bar{\gamma}}, \tag{4.21}$$

where $\bar{\gamma}$ is the average transmit SNR and P_{cov} is the CP.

Corollary 4.1 *The diversity order of the S-CH FSO link is* $\min\{\omega^2, \alpha, \beta\}$.

Proof From the definition of Ξ in Eq. (4.7), we know that $\bar{\gamma}\to\infty$ means $\Xi\to 0$. Three additive terms in the square brackets $[\cdot]$ in Eq. (4.18). When $\Xi\to 0$, it is obvious that the term with the minimum power index is dominant. According to Eq. (4.21), the diversity order can be reached as $\min\{\omega^2, \alpha, \beta\}$. □

4.1.3 Performance Analysis over CH-UAV RF Links

In this section, we investigate the coverage performance of CH-UAV links in three cases: interference-free case, interference-dominated case, and interference-and-noise case. These three cases can cover all the possibilities. When frequency division multiple access, CDMA, or time division multiple access is utilized, there is no interference between CHs, and it belongs to the interference-free case. When all CHs share the same communication resources (time slot, frequency, code, etc.) and the number of CHs is large, which makes the noise power negligible, an interference-dominated case should be used. When all CHs use the same communication resources and these CHs are sparsely distributed, the interfering power is comparable with the noise power, and the interference-and-noise case should be considered.

4.1.4 Interference-Free Case

We will first consider the case where there is no interference from other CHs, which represents the scenarios in which the interfering CHs are too far away from the receiver or the transmit power at the interfering CH is too low to incur effective interference at the target UAV.

Supposing that CH_k has the transmit power of P_{R}, the SNR at U_j in the serving space of CH_k can be expressed as

$$\gamma_{kj} = \frac{P_{\mathrm{R}} g_{kj}}{\rho d_{kj}^{\alpha_r} N_{\mathrm{R}}}, \tag{4.22}$$

where g_{kj} is the channel power gain of the CH_k-U_j link and N_{R} is the average power of the AWGN at U_j.

Theorem 4.3 (4.1.3) *The CDF of γ_{kj} can be calculated as*

$$F_{\gamma_{kj}}(x) = 1 - \frac{3}{\alpha_r D^3} \left(\frac{\Omega P_{\mathrm{R}}}{m \rho N_{\mathrm{R}}} \frac{1}{x} \right)^{\frac{3}{\alpha_r}} \sum_{i=0}^{m-1} \frac{1}{m_i!} \gamma \left(m_i + \frac{3}{\alpha_r}, \frac{m \rho N_{\mathrm{R}} D^{\alpha_r}}{\Omega P_{\mathrm{R}}} x \right). \tag{4.23}$$

Proof Using Eqs. (4.13) and (4.14), $F_{\gamma_{kj}}(z)$ can be expressed as

$$\begin{aligned}
F_{\gamma_{kj}}(x) &= \mathbf{Pr}\{\gamma_{kj} < x\} \\
&= \mathbf{Pr}\left\{ \frac{P_{\mathrm{R}} g_{kj}}{\rho d_{kj}^{\alpha_r} N_{\mathrm{R}}} < x \right\} \\
&= \mathbf{Pr}\left\{ g_{kj} < \frac{\rho d_{kj}^{\alpha_r} N_{\mathrm{R}}}{P_{\mathrm{R}}} x \right\} \\
&= \int_0^D F_g \left(\frac{\rho y^{\alpha_r} N_{\mathrm{R}}}{P_{\mathrm{R}}} x \right) f_{d_{kj}}(y) dy \\
&= 1 - \frac{3}{D^3} \sum_{i=0}^{m-1} \left(\frac{m \rho N_{\mathrm{R}}}{\Omega P_{\mathrm{R}}} x \right)^{m_i} \frac{1}{m_i!} \\
&\quad \times \underbrace{\int_0^D y^{\alpha_r m_i + 2} \exp\left(-\frac{m \rho N_{\mathrm{R}}}{\Omega P_{\mathrm{R}}} x y^{\alpha_r} \right) dy}_{I_0}.
\end{aligned} \tag{4.24}$$

Resorting to [11, Eq. (3.381.8)], I_0 can be given as

$$I_0 = \frac{1}{\alpha_r}\left(\frac{\Omega P_{\mathrm{R}}}{m\rho N_{\mathrm{R}} x}\right)^{m_i+\frac{3}{\alpha_r}} \gamma\left(m_i + \frac{3}{\alpha_r}, \frac{m\rho N_{\mathrm{R}} D^{\alpha_r}}{\Omega P_{\mathrm{R}}} x\right), \tag{4.25}$$

where $\gamma(\cdot,\cdot)$ is the lower incomplete gamma function.

Substituting Eq. (4.25) in Eq. (4.24), the CDF of γ_{kj} can be obtained as Eq. (4.23). □

Then, the CP, in this case, can be achieved as

$$\begin{aligned} P_{\mathrm{cov},kj}(\gamma_{\mathrm{th}}) &= 1 - F_{\gamma_{kj}}(\gamma_{\mathrm{th}}) \\ &= \frac{3}{\alpha_r D^3}\left(\frac{\Omega P_{\mathrm{R}}}{m\rho N_{\mathrm{R}}\gamma_{\mathrm{th}}}\right)^{\frac{3}{\alpha_r}} \sum_{i=0}^{m-1} \frac{1}{m_i!}\gamma\left(m_i + \frac{3}{\alpha_r}, \frac{m\rho N_{\mathrm{R}} D^{\alpha_r}\gamma_{\mathrm{th}}}{\Omega P_{\mathrm{R}}}\right). \end{aligned} \tag{4.26}$$

In a high SNR regime, the CDF of g in Nakagami-m fading is given as [13]

$$F_g^{\infty}(x) = \frac{m^{m-1}}{(m-1)!}\left(\frac{x}{\Omega}\right)^m. \tag{4.27}$$

Substituting Eq. (4.27) in Eq. (4.24), we can get the asymptotic coverage probability $P_{\mathrm{cov},kj}^{\infty}(\gamma_{\mathrm{th}})$ as

$$\begin{aligned} P_{\mathrm{cov},kj}^{\infty}(\gamma_{\mathrm{th}}) &= 1 - \int_0^D F_g^{\infty}\left(\frac{\rho N_{\mathrm{R}}\gamma_{\mathrm{th}}}{P_{\mathrm{R}}} y^{\alpha_r}\right) f_{d_{kj}}(y)dy \\ &= 1 - \frac{3}{D^3}\frac{m^{m-1}}{(m-1)!}\left(\frac{\rho N_{\mathrm{R}}\gamma_{\mathrm{th}}}{\Omega P_{\mathrm{R}}}\right)^m \int_0^D y^{\alpha_r m+2} dy \\ &= 1 - \frac{3m^{m-1}}{(m-1)!}\left(\frac{\rho N_{\mathrm{R}}\gamma_{\mathrm{th}}}{\Omega P_{\mathrm{R}}}\right)^m \frac{D^{\alpha_r m}}{\alpha_r m + 3}. \end{aligned} \tag{4.28}$$

Corollary 4.2 *The diversity order of the CH-UAV links in the interference-free case is m.*

Proof Substituting Eq. (4.28) into Eq. (4.21), we can obtain the diversity order as

$$\begin{aligned} &-\lim_{\frac{P_{\mathrm{R}}}{N_{\mathrm{R}}}\to\infty} \frac{\log\left[\frac{3m^{m-1}}{(m-1)!}\left(\frac{\rho N_{\mathrm{R}}\gamma_{\mathrm{th}}}{\Omega P_{\mathrm{R}}}\right)^m \frac{D^{\alpha_r m}}{\alpha_r m+3}\right]}{\log\left(\frac{P_{\mathrm{R}}}{N_{\mathrm{R}}}\right)} \\ &= \lim_{\frac{P_{\mathrm{R}}}{N_{\mathrm{R}}}\to\infty} \frac{\log\left[\frac{(m-1)!}{3m^{m-1}}\frac{\alpha_r m+3}{D^{\alpha_r m}}\right] + m\log\left(\frac{\Omega}{\rho\gamma_{\mathrm{th}}}\right) + m\log\left(\frac{P_{\mathrm{R}}}{N_{\mathrm{R}}}\right)}{\log\left(\frac{P_{\mathrm{R}}}{N_{\mathrm{R}}}\right)}. \end{aligned} \tag{4.29}$$

When $\frac{P_R}{N_R} \to \infty$, $\log\left[\frac{(m-1)!}{3m^{m-1}}\frac{\alpha_r m+3}{D^{\alpha_r m}}\right]$ and $m\log\left(\frac{\Omega}{\rho\gamma_{\text{th}}}\right)$ can be negligible. Finally, one can get the diversity order as m. □

4.1.4.1 Interference-Dominated Case

As the receivers of the UAVs have limited sensitivity, we consider that U_j is only disturbed by these CHs within the distance of $D_{\max}$ (usually, $D_{\max} \gg D$ and $D_{\max} \gg D_{\min}$).

To simplify the analysis, we assume that all CHs have the same transmit power P_R and the channel power gains between interfering CHs and U_j are independent and identically distributed random variables with parameters m and Ω. As the interfering power is much greater than the noise power [14], the signal-to-interference ratio (SIR) is considered in this case.

The received SIR at U_j around CH_k can be presented as

$$\gamma_{kj} = \frac{\frac{P_R g_{kj}}{\rho d_{kj}^{\alpha_r}}}{\sum_{i=1}^{N_I}\frac{P_R g_{jI_i}}{\rho d_{jI_i}^{\alpha_r}}} = \frac{\frac{g_{kj}}{d_{kj}^{\alpha_r}}}{I}, \tag{4.30}$$

where $I = \sum_{i=1}^{N_I}\frac{g_{jI_i}}{d_{jI_i}^{\alpha_r}}$, g_{jI_i} is the channel power gain between the I_ith interfering CH and U_j, and d_{jI_i} is the distance from the I_ith CH to U_j.

The CP of the RF link, in this case, can be written as

$$\begin{aligned} P_{\text{cov},kj}(\gamma_{\text{th}}) &= \mathbb{E}_{I,d_{kj}}\left[\mathbf{Pr}\{\gamma_{kj} \geq \gamma_{\text{th}}|I, d_{kj}\}\right] \\ &= \mathbb{E}_{I,d_{kj}}\left[\mathbf{Pr}\{g_{kj} \geq \gamma_{\text{th}} I d_{kj}^{\alpha_r}|I, d_{kj}\}\right]. \end{aligned} \tag{4.31}$$

Lemma 4.4 *$P_{\text{cov},kj}(\gamma_{\text{th}})$ can be expressed as*

$$P_{\text{cov},kj}(\gamma_{\text{th}}) = \sum_{i=0}^{m-1}\left(-\frac{m\gamma_{\text{th}}}{\Omega}\right)^{m_i}\frac{1}{m_i!}\mathbb{E}_{d_{kj}}\left\{d_{kj}^{\alpha_r m_i}\frac{d^{m_i}\mathbb{E}_I[e^{-sI}]}{ds^{m_i}}\right\}, \tag{4.32}$$

where $s = m\gamma_{\text{th}} d_{kj}^{\alpha_r}/\Omega$.

Proof According to Eq. (4.13) and the fact that I and d_{kj} are independent, Eq. (4.31) can be calculated as

$$
\begin{aligned}
P_{\mathrm{cov},kj}(\gamma_{\mathrm{th}}) &= \mathbb{E}_{I,d_{kj}}\left[\sum_{i=0}^{m-1}\left(\frac{m}{\Omega}\right)^{m_i}\frac{(\gamma_{\mathrm{th}} I d_{kj}^{\alpha_r})^{m_i}}{m_i!}\exp\left(-\frac{m\gamma_{\mathrm{th}} I d_{kj}^{\alpha_r}}{\Omega}\right)\right] \\
&= \sum_{i=0}^{m-1}\left(\frac{m}{\Omega}\right)^{m_i}\frac{\gamma_{\mathrm{th}}^{m_i}}{m_i!}\mathbb{E}_{I,d_{kj}}\left[(I d_{kj}^{\alpha_r})^{m_i}\exp\left(-\frac{m\gamma_{\mathrm{th}} I d_{kj}^{\alpha_r}}{\Omega}\right)\right] \\
&= \sum_{i=0}^{m-1}\left(\frac{m}{\Omega}\right)^{m_i}\frac{\gamma_{\mathrm{th}}^{m_i}}{m_i!}\mathbb{E}_{d_{kj}}\left\{d_{kj}^{\alpha_r m_i}\underbrace{\mathbb{E}_I\left[I^{m_i}\exp\left(-\frac{m\gamma_{\mathrm{th}} d_{kj}^{\alpha_r}}{\Omega} I\right)\right]}_{I_2}\right\}.
\end{aligned}
\tag{4.33}
$$

By setting $s = \frac{m\gamma_{\mathrm{th}} d_{kj}^{\alpha_r}}{\Omega}$, I_2 can be obtained as

$$
I_2 = \mathbb{E}_I\left[I^{m_i} e^{-sI}\right]. \tag{4.34}
$$

From the definition of the Laplace transform (LT), the LT of I can be given as $\mathcal{L}_I(s) = \int_0^\infty e^{-st} f_I(t)dt = \mathbb{E}_I[e^{-sI}]$, where $f_I(t)$ is the PDF of I.

By using the differential property of LT, I_2 can be achieved as

$$
\begin{aligned}
I_2 &= \int_0^\infty t^{m_i} e^{-st} f_I(t)dt \\
&= (-1)^{m_i}\frac{d^{m_i}\mathcal{L}_I(s)}{ds^{m_i}} \\
&= (-1)^{m_i}\frac{d^{m_i}\mathbb{E}_I[e^{-sI}]}{ds^{m_i}}.
\end{aligned}
\tag{4.35}
$$

Combining Eqs. (4.33) and (4.35), (4.32) can be obtained.

□

To continue calculating Eq. (4.32), we need to work on $\mathbb{E}_I\left[e^{-sI}\right]$ and $\frac{d^{m_i}\mathbb{E}_I[e^{-sI}]}{ds^{m_i}}$.

Lemma 4.5 $\mathbb{E}_I\left[e^{-sI}\right]$ *in Eq.* (4.32) *can be expressed as*

$$
\mathbb{E}_I\left[e^{-sI}\right] = \exp\left[\lambda_{\mathrm{CH}} V_1 (I_3 - 1)\right], \tag{4.36}
$$

where I_3 is present as

$$
\begin{aligned}
I_3 = \left(\frac{m}{\Omega s}\right)^m \frac{\pi}{2d_{kj}V_1}\Bigg[&\mathcal{F}\left(\frac{4}{\alpha_r}, d_{jI_1}^{\mathrm{g}_1}, d_{jI_1}^{\min}\right) + 2d_{kj}\mathcal{F}\left(\frac{3}{\alpha_r}, d_{jI_1}^{\mathrm{g}_1}, d_{jI_1}^{\min}\right) \\
&+ (d_{kj}^2 - D_{\min}^2)\mathcal{F}\left(\frac{2}{\alpha_r}, d_{jI_1}^{\mathrm{g}_1}, d_{jI_1}^{\min}\right) + 4d_{kj}\mathcal{F}\left(\frac{3}{\alpha_r}, d_{jI_1}^{\mathrm{g}_2}, d_{jI_1}^{\mathrm{g}_1}\right) \\
&- \mathcal{F}\left(\frac{4}{\alpha_r}, d_{jI_1}^{\max}, d_{jI_1}^{\mathrm{g}_2}\right) + 2d_{kj}\mathcal{F}\left(\frac{3}{\alpha_r}, d_{jI_1}^{\max}, d_{jI_1}^{\mathrm{g}_2}\right) \\
&+ (D_{\max}^2 - d_{kj}^2)\mathcal{F}\left(\frac{2}{\alpha_r}, d_{jI_1}^{\max}, d_{jI_1}^{\mathrm{g}_2}\right)\Bigg],
\end{aligned} \tag{4.37}
$$

where $d_{jI_1}^{\min} = (D_{\min} - d_{kj})^2$, $d_{jI_1}^{\mathrm{g}_1} = (D_{\min} + d_{kj})^2$, $d_{jI_1}^{\mathrm{g}_2} = (D_{\max} - d_{kj})^2$, $d_{jI_1}^{\max} = (D_{\max} + d_{kj})^2$, $\mathcal{F}(a, b, c) = \left[{}_2F_1\left(m, m+a; m+a+1; -\frac{m}{\Omega s}b^{\frac{\alpha_r}{2}}\right) b^{\frac{(m+a)\alpha_r}{2}} - {}_2F_1\left(m, m+a; m+a+1; -\frac{m}{\Omega s}c^{\frac{\alpha_r}{2}}\right) c^{\frac{(m+a)\alpha_r}{2}}\right]\frac{2}{(m+a)\alpha_r}$, $V_1 = \frac{4\pi}{3}(D_{\max}^3 - D_{\min}^3)$, *and* ${}_2F_1(\cdot,\cdot;\cdot;\cdot)$ *denotes Gauss hypergeometric function.*

Proof Please refer to Appendix 5. □

Lemma 4.6 *Resorting to* ***Lemma 5****,* $\frac{d^{m_i}\mathbb{E}_I[e^{-sI}]}{ds^{m_i}}$ *in Eq. (4.32) can be represented as*

$$
\frac{d^{m_i}\mathbb{E}_I[e^{-sI}]}{ds^{m_i}} = \exp\left(\mathcal{A}(s, d_{kj})\right)\left[1 + \mathbb{1}\{m_i > 0\}\sum_{n=1}^{m_i}\mathcal{B}(m_i, n, \mathcal{A}(s, d_{kj}))\right], \tag{4.38}
$$

where $\mathcal{A}(s, d_{kj}) = \lambda_{\mathrm{CH}}V_1(I_3 - 1)$,

$$
\mathcal{B}(m_i, n, \mathcal{A}(s, d_{kj})) = B_{m_i,n}\left(\mathcal{A}^{(1)}(s, d_{kj}), \ldots, \mathcal{A}^{(m_i-n+1)}(s, d_{kj})\right), \tag{4.39}
$$

$B_{m_i,n}(\cdot)$ *is the Bell polynomial, and* $\mathcal{A}^{(n)}(s, d_{kj})$ *is the nth derivative of* $\mathcal{A}(s, d_{kj})$.

Proof When $m_i = 0$,

$$
\frac{d^0}{ds^0}\exp\left(\mathcal{A}(s, d_{kj})\right) = \exp\left(\mathcal{A}(s, d_{kj})\right). \tag{4.40}
$$

When $m_i > 0$, according to Faádi Bruno's formula, we can obtain

$$
\frac{d^{m_i}}{ds^{m_i}}\exp\left(\mathcal{A}(s, d_{kj})\right) = \exp\left(\mathcal{A}(s, d_{kj})\right) \times \sum_{n=1}^{m_i}\mathcal{B}(m_i, n, \mathcal{A}(s, d_{kj})), \tag{4.41}
$$

where $\mathcal{B}(m_i, n, \mathcal{A}(s, d_{kj})) = B_{m_i,n}\left(\mathcal{A}^{(1)}(s, d_{kj}), \ldots, \mathcal{A}^{(m_i-n+1)}(s, d_{kj})\right)$, $B_{m_i,n}(\cdot)$ is the Bell polynomial, and $\mathcal{A}^{(n)}(s, d_{kj})$ is the nth derivative of $\mathcal{A}(s, d_{kj})$.

□

Lemma 4.7 *$\mathcal{A}^{(n)}(s, d_{kj})$ $(n > 0)$ in $\mathcal{B}(m_i, n, \mathcal{A}(s, d_{kj}))$ of Eq. (4.38) can be represented as*

$$\begin{aligned}\mathcal{A}^{(n)}(s, d_{kj}) = {} & \frac{\pi\lambda_{\mathrm{CH}}}{2d_{kj}}\left(\frac{m}{\Omega}\right)^m \sum_{l=0}^{n}\binom{n}{l}(-1)^{n-l}(m)_{n-l}s^{-m-n+l} \\ & \times\Bigg[\mathcal{F}^{(l)}\left(\frac{4}{\alpha_r}, d_{jI_1}^{\mathrm{g}_1}, d_{jI_1}^{\min}\right) + 2d_{kj}\mathcal{F}^{(l)}\left(\frac{3}{\alpha_r}, d_{jI_1}^{\mathrm{g}_1}, d_{jI_1}^{\min}\right) \\ & + (d_{kj}^2 - D_{\min}^2)\mathcal{F}^{(l)}\left(\frac{2}{\alpha_r}, d_{jI_1}^{\mathrm{g}_1}, d_{jI_1}^{\min}\right) + 4d_{kj}\mathcal{F}^{(l)}\left(\frac{3}{\alpha_r}, d_{jI_1}^{\mathrm{g}_2}, d_{jI_1}^{\mathrm{g}_1}\right) \\ & - \mathcal{F}^{(l)}\left(\frac{4}{\alpha_r}, d_{jI_1}^{\max}, d_{jI_1}^{\mathrm{g}_2}\right) + 2d_{kj}\mathcal{F}^{(l)}\left(\frac{3}{\alpha_r}, d_{jI_1}^{\max}, d_{jI_1}^{\mathrm{g}_2}\right) \\ & + (D_{\max}^2 - d_{kj}^2)\mathcal{F}^{(l)}\left(\frac{2}{\alpha_r}, d_{jI_1}^{\max}, d_{jI_1}^{\mathrm{g}_2}\right)\Bigg], \end{aligned} \tag{4.42}$$

where

$$\mathcal{F}^{(l)}(a, b, c) = \begin{cases} \mathcal{F}(a, b, c), & \text{if } l = 0; \\ \frac{2}{(m+a)\alpha_r}\left[b^{\frac{(m+a)\alpha_r}{2}}\Delta^{(l)}(s, a, b) - c^{\frac{(m+a)\alpha_r}{2}}\Delta^{(l)}(s, a, c)\right], & \text{if } l > 0 \end{cases}, \tag{4.43}$$

$$\begin{aligned}\Delta^{(l)}(s, a, b) = {} & \sum_{q=1}^{l}\frac{(m+a)(m)_q}{m+a+q}B_{l,q}\left(f_3^{(1)}(s, b), \ldots, f_3^{(l-q+1)}(s, b)\right) \\ & \times {}_2F_1\left(m+q, m+a+q; m+a+q+1; -\frac{mb^{\frac{\alpha_r}{2}}}{\Omega s}\right), \end{aligned} \tag{4.44}$$

$(m)_q = \prod_{k=0}^{q-1}(m-k)$ *is the rising Pochhammer symbol, and* $f_3^{(q)}(s, b) = (-1)^{q+1}q!\frac{mb^{\frac{\alpha_r}{2}}}{\Omega}s^{-1-q}$.

Proof Please refer to Appendix 6. □

Theorem 4.4 (4.1.4) *The CP of the RF link in the interference-dominated case can be expressed as*

$$\begin{aligned}P_{\mathrm{cov},kj}(\gamma_{\mathrm{th}}) \approx {} & \frac{3\pi}{2D^2M_r}\sum_{p=1}^{M_r}\sqrt{1-t_p^2}\sum_{i=0}^{m-1}\left(-\frac{m\gamma_{\mathrm{th}}}{\Omega}\right)^{m_i}\frac{b_p^{\alpha_r m_i+2}}{m_i!}\exp\left(\tilde{\mathcal{A}}(\gamma_{\mathrm{th}}, b_p)\right) \\ & \times\left[1 + \mathbb{1}\{m_i > 0\}\sum_{n=1}^{m_i}\mathcal{B}\left(m_i, n, \tilde{\mathcal{A}}(\gamma_{\mathrm{th}}, b_p)\right)\right], \end{aligned} \tag{4.45}$$

where $\tilde{\mathcal{A}}(\gamma_{\text{th}}, b_p) = \mathcal{A}\left(\frac{m\gamma_{\text{th}} b_p^{\alpha_r}}{\Omega}, b_p\right)$, $t_p = \cos\left(\frac{2p-1}{2M_r}\pi\right)$, $b_p = \frac{D}{2}(t_p + 1)$, $\mathcal{A}(\cdot,\cdot)$ *is defined in Lemma 4.6 and Eq. (4.37), and* $\mathcal{B}(\cdot,\cdot,\mathcal{A}(\cdot,\cdot))$ *is defined in Lemma 4.6 and Eq. (4.42).*

Proof Substituting Eqs. (4.14) and (4.38) in Eq. (4.32), and then substituting $s = m\gamma_{\text{th}} d_{kj}^{\alpha_r}/\Omega$, $P_{\text{cov},kj}(\gamma_{\text{th}})$ can expressed as

$$\begin{aligned} P_{\text{cov},kj}(\gamma_{\text{th}}) &= \sum_{i=0}^{m-1} \left(-\frac{m\gamma_{\text{th}}}{\Omega}\right)^{m_i} \frac{1}{m_i!} \mathbb{E}_{d_{kj}} \left\{ d_{kj}^{\alpha_r m_i} \exp\left(\mathcal{A}(s, d_{kj})\right) \right. \\ &\quad \left. \times \left[1 + \mathbb{1}\{m_i > 0\} \sum_{n=1}^{m_i} \mathcal{B}(m_i, n, \mathcal{A}(s, d_{kj}))\right] \right\} \\ &= \sum_{i=0}^{m-1} \left(-\frac{m\gamma_{\text{th}}}{\Omega}\right)^{m_i} \frac{1}{m_i!} \frac{3}{D^3} \int_0^D x^{\alpha_r m_i + 2} \exp\left(\tilde{\mathcal{A}}(\gamma_{\text{th}}, x)\right) \\ &\quad \times \left[1 + \mathbb{1}\{m_i > 0\} \sum_{n=1}^{m_i} \mathcal{B}\left(m_i, n, \tilde{\mathcal{A}}(\gamma_{\text{th}}, x)\right)\right] dx, \end{aligned} \tag{4.46}$$

where $\tilde{\mathcal{A}}(\gamma_{\text{th}}, x) = \mathcal{A}\left(\frac{m\gamma_{\text{th}} x^{\alpha_r}}{\Omega}, x\right)$.

By setting $t = \frac{2x-D}{D}$ and employing the M_r-point Chebyshev-Gauss quadrature in the first case, Eq. (4.46) can be written as

$$\begin{aligned} P_{\text{cov},kj}(\gamma_{\text{th}}) &= \sum_{i=0}^{m-1} \left(-\frac{m\gamma_{\text{th}}}{\Omega}\right)^{m_i} \frac{1}{m_i!} \frac{3}{D^3} \frac{D}{2} \int_{-1}^{1} \left[\frac{D}{2}(t+1)\right]^{\alpha_r m_i + 2} \\ &\quad \times \exp\left(\tilde{\mathcal{A}}(\gamma_{\text{th}}, \frac{D}{2}(t+1))\right) \left[1 + \mathbb{1}\{m_i > 0\}\right. \\ &\quad \left. \times \sum_{n=1}^{m_i} \mathcal{B}\left(m_i, n, \tilde{\mathcal{A}}(\gamma_{\text{th}}, \frac{D}{2}(t+1))\right)\right] dt \\ &= \sum_{i=0}^{m-1} \left(-\frac{m\gamma_{\text{th}}}{\Omega}\right)^{m_i} \frac{1}{m_i!} \frac{3}{2D^2} \frac{\pi}{M_r} \sum_{p=1}^{M_r} b_p^{\alpha_r m_i + 2} \exp\left(\tilde{\mathcal{A}}(\gamma_{\text{th}}, b_p)\right) \\ &\quad \times \sqrt{1 - t_p^2} \left[1 + \mathbb{1}\{m_i > 0\} \sum_{n=1}^{m_i} \mathcal{B}\left(m_i, n, \tilde{\mathcal{A}}(\gamma_{\text{th}}, b_p)\right)\right], \end{aligned} \tag{4.47}$$

where $t_p = \cos\left(\frac{2p-1}{2M_r}\pi\right)$ and $b_p = \frac{D}{2}(t_p + 1)$.

After reorganizing the components in Eq. (4.47), (4.45) can be obtained. □

Moreover, the CDF of γ_{kj} can be evaluated as

$$F_{\gamma_{kj}}(x) = 1 - P_{\mathrm{cov},kj}(x). \tag{4.48}$$

4.1.4.2 Interference-and-Noise Case

If both interference and noise are considered, the SINR is

$$\begin{aligned}\gamma_{kj} &= \frac{\frac{P_{\mathrm{R}} g_{kj}}{\rho d_{kj}^{\alpha_r}}}{\sum\limits_{i=1, i\neq k}^{N} \frac{P_{\mathrm{R}} g_{ij}}{\rho d_{ij}^{\alpha_r}} + N_{\mathrm{R}}} \\ &= \frac{\frac{g_{kj}}{d_{kj}^{\alpha_r}}}{I + \frac{\rho}{P_{\mathrm{R}}} N_{\mathrm{R}}}.\end{aligned} \tag{4.49}$$

Theorem 4.5 (4.1.5) *Considering interference and noise, the CP of the RF link in this case can be expressed as*

$$\begin{aligned}P_{\mathrm{cov},kj}(\gamma_{\mathrm{th}}) \approx & \frac{3\pi}{2D^2 M_r} \sum_{p=1}^{M_r} \sqrt{1-t_p^2} \sum_{i=0}^{m-1} \left(\frac{m\gamma_{\mathrm{th}}}{\Omega}\right)^{m_i} \frac{b_p^{\alpha_r m_i + 2}}{m_i!} \\ & \times \exp\left(-\frac{m\gamma_{\mathrm{th}} b_p^{\alpha_r} \rho N_{\mathrm{R}}}{\Omega P_{\mathrm{R}}} + \tilde{\mathcal{A}}(\gamma_{\mathrm{th}}, b_p)\right) \sum_{u=0}^{m_i} \binom{m_i}{u} \left(\frac{\rho N_{\mathrm{R}}}{P_{\mathrm{R}}}\right)^{m_i - u} \\ & \times (-1)^u \left[1 + \mathbb{1}\{u > 0\} \sum_{n=1}^{u} \mathcal{B}\left(u, n, \tilde{\mathcal{A}}(\gamma_{\mathrm{th}}, b_p)\right)\right].\end{aligned} \tag{4.50}$$

Proof To include noise, I should be replaced by $I + \frac{\rho}{P} N_{\mathrm{R}}$ in Eq. (4.34). According to [11, Eq. 1.111], we can obtain I_2 in this case as

$$\begin{aligned}I_2 &= \mathbb{E}_I \left[\left(I + \frac{\rho}{P_{\mathrm{R}}} N_{\mathrm{R}}\right)^{m_i} \exp\left(-sI - s\frac{\rho N_{\mathrm{R}}}{P_{\mathrm{R}}}\right)\right] \\ &= \exp\left(-s\frac{\rho N_{\mathrm{R}}}{P_{\mathrm{R}}}\right) \sum_{u=0}^{m_i} \binom{m_i}{u} \left(\frac{\rho N_{\mathrm{R}}}{P_{\mathrm{R}}}\right)^{m_i - u} \mathbb{E}_I\left[I^u \exp(-sI)\right].\end{aligned} \tag{4.51}$$

Combining Eqs. (4.14), (4.33), (4.34), (4.35), (4.38), and (4.51), and then employing the M_r-point Chebyshev-Gauss quadrature in the first case, the CP of the RF link in this case can be obtained as Eq. (4.50). □

4.1.5 The E2e Coverage Performance

We assume the DF relay scheme is implemented at all CHs in the considered system. Then, the equivalent e2e SNR from the S to terminal UAV can be given as $\gamma_{eq}^{\mathrm{DF}} = \min\{\gamma_k, \gamma_{kj}\}$.

Corollary 4.3 *The e2e CP for S-CH-UAV links can be finally achieved as*

$$P_{\mathrm{cov},e2e}(\gamma_{\mathrm{th}}) = P_{\mathrm{cov},\mathrm{SCH}_k}(\gamma_{\mathrm{th}}) P_{\mathrm{cov},kj}(\gamma_{\mathrm{th}}), \tag{4.52}$$

where $P_{\mathrm{cov},\mathrm{SCH}_k}(\gamma_{\mathrm{th}})$ *is presented as Eq.* (4.17) *and* $P_{\mathrm{cov},kj}(\gamma_{\mathrm{th}})$ *is given as Eqs.* (4.26), (4.45), *and* (4.50) *in interference-free case, interference-dominated case, and interference-and-noise case, respectively.*

Proof The CDF of the equivalent SNR under the DF scheme, $\gamma_{eq}^{\mathrm{DF}}$, is given as [15]

$$F_{\gamma_{eq}^{\mathrm{DF}}}(x) = 1 - \left[1 - F_{\gamma_k}(x)\right]\left[1 - F_{\gamma_{kj}}(x)\right]. \tag{4.53}$$

The CP here can be written as

$$\begin{aligned} P_{\mathrm{cov},e2e}(\gamma_{\mathrm{th}}) &= 1 - F_{\gamma_{eq}^{\mathrm{DF}}}(\gamma_{\mathrm{th}}) \\ &= \left[1 - F_{\gamma_k}(\gamma_{\mathrm{th}})\right]\left[1 - F_{\gamma_{kj}}(\gamma_{\mathrm{th}})\right] \\ &= P_{\mathrm{cov},\mathrm{SCH}_k}(\gamma_{\mathrm{th}}) P_{\mathrm{cov},kj}(\gamma_{\mathrm{th}}). \end{aligned} \tag{4.54}$$

□

Though the derived analytical expressions given in this and previous sections look a little complicated, considerable time can be saved compared to studying the system directly via Monte Carlo simulations, leading to greatly improved work/study efficiency for practical applications.

4.1.6 Numerical Results

This section will provide numerical results to assess the coverage performance of the considered satellite-UAV systems and verify the proposed analytical models. In the simulation, we run 1×10^6 trials of Monte Carlo simulations to model the randomness of the positions of the considered CHs and UAVs. Unless otherwise explicitly specified, the main parameters adopted in this section are set in Table 4.1.

4.1.6.1 S-CH FSO Links

In this subsection, we will study the coverage performance over S-CH links.

Table 4.1 Values of main parameters

Parameter definition	Value
Geometric parameters in Fig. 4.2	$H_U = 50$ km, $H_S = 35731$ km, $R = 6376$ km, $\xi_0 = \pi/800$ rad
Intensity of CHs in Eq. (4.2)	$\lambda_P = 0.001$
Parameters of FSO link in Eq. (4.3)	$P_S = 40$ dBm, $G_S = G_R = 107.85$ dB, $\lambda = 1550$ nm, $N_F = 10^{-10}$ mW, $\eta = 0.5$, $h_l = -0.35$ dB
Parameters in FSO fading model in Eq. (4.4)	$A_0 = 0.5$, $\omega = 1.1$, $\alpha = 2.902$, $\beta = 2.51$
Parameters in Nakagami-m fading model in Eq. (4.12)	$m = 5$, $\Omega = 1$
Geometric parameters in Fig. 4.14	$D = 1$ km, $D_{max} = 20$ km, $D_{min} = 2$ km
Transmit power of CH_k and noise power in Eq. (4.22)	$P_R = 30$ dBm, $N_R = 1.5 \times 10^{-11}$ W
Free-space path-loss exponent	$\alpha_r = 2$
Path loss at the distance of 1 m	$\rho = 38.5$ dB (Operating frequency = 2 GHz)

In Figs. 4.3, 4.4, and 4.5, the CP is presented for different turbulence, H_S, and pointing errors, respectively. One can easily see that CP decreases as γ_{th} increases, and coverage performance can be improved while P_S increases. The increase in CP is caused by the fact that a large γ_{th} represents a small probability of coverage events. The improvement in coverage performance can be explained by the large P_S generating a large average power for the received signals, leading to a larger received SNR.

Figure 4.3a shows that the CP with the weak turbulence outperforms the strong turbulence when γ_{th} is less than 20 dB. On the contrary, the opposite occurs when γ_{th} is greater than 20 dB. When γ_{th} is large, Fig. 4.3b depicts that the weak turbulence leads to a large $1 - P_{cov,SCH_k}$ (small P_{cov,SCH_k}) in the small P_S region, while the inverse observation is obtained in the large P_S region. When γ_{th} is small, $1 - P_{cov,SCH_k}$ in Fig. 4.3c presents the same conclusion compared with that in Fig. 4.3b.

In Fig. 4.4a and b, we can observe that H_S has a negative effect on the coverage performance. In other words, the CP degrades as the orbit height of the satellite increases, which denotes that path-loss increases because a large path-loss leads to a small received SNR at the CH, which results in a small CP.

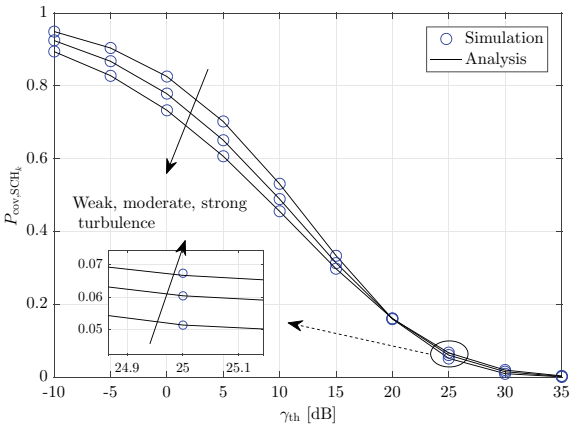

(a) $P_{\mathrm{cov,SCH}_k}$ versus γ_{th} with $P_{\mathrm{S}} = 40$ dBm

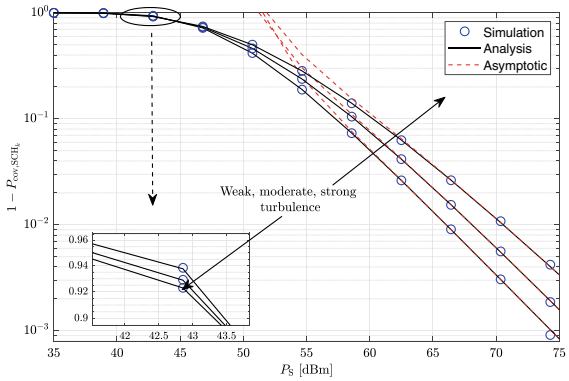

(b) $1 - P_{\mathrm{cov,SCH}_k}$ versus P_{S} with $\gamma_{\mathrm{th}} = 30$ dB

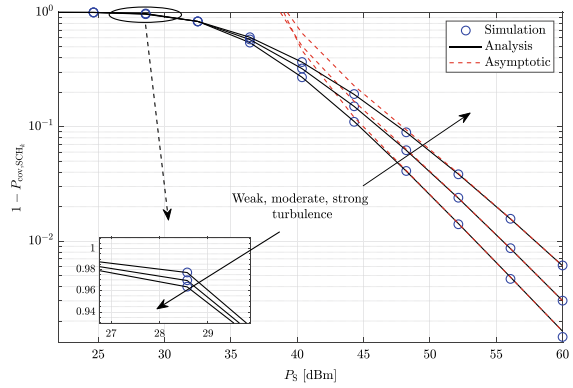

(c) $1 - P_{\mathrm{cov,SCH}_k}$ versus P_{S} with $\gamma_{\mathrm{th}} = 5$ dB

Fig. 4.3 $P_{\mathrm{cov,SCH}_k}$ and $1 - P_{\mathrm{cov,SCH}_k}$ over S-CH links for various kinds of turbulence (weak turbulence: $\alpha = 2.902$, $\beta = 2.51$; moderate turbulence: $\alpha = 2.296$, $\beta = 1.822$; strong turbulence: $\alpha = 2.064$, $\beta = 1.342$ [16])

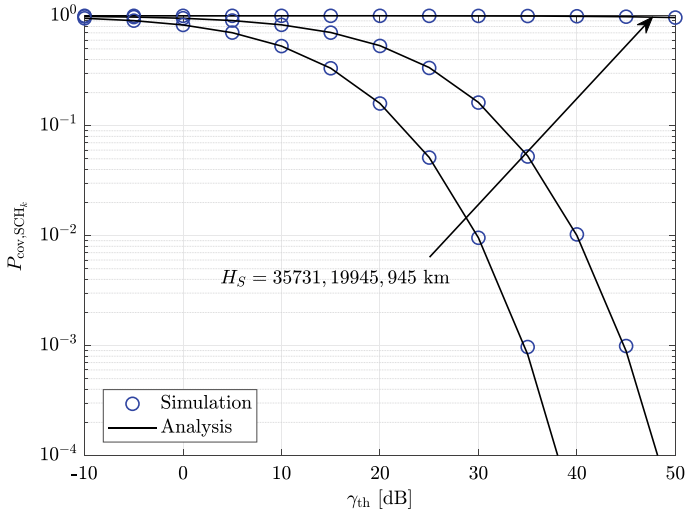

(a) $P_{\mathrm{cov,SCH}_k}$ versus γ_{th}

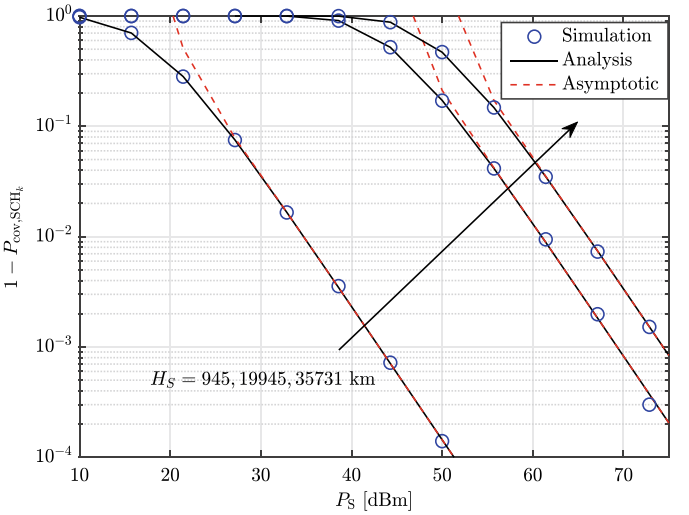

(b) $1 - P_{\mathrm{cov,SCH}_k}$ versus P_{S} with $\gamma_{\mathrm{th}} = 30$ dB

Fig. 4.4 $P_{\mathrm{cov,SCH}_k}$ and $1 - P_{\mathrm{cov,SCH}_k}$ over S-CH links for various H_{S}

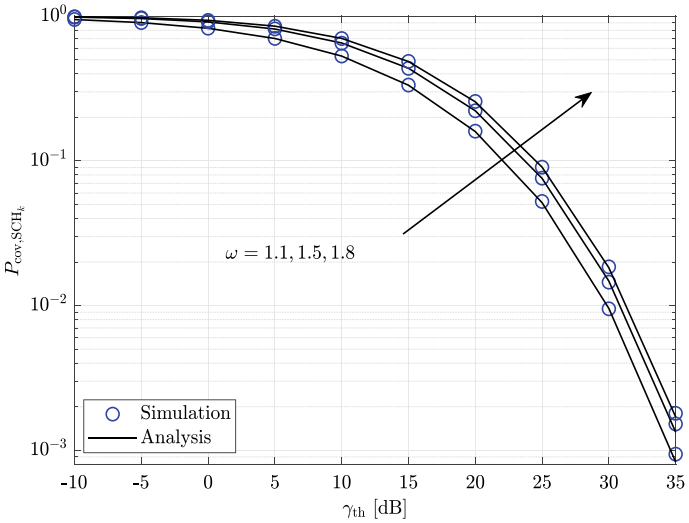

(a) $P_{\mathrm{cov,SCH}_k}$ versus γ_{th}

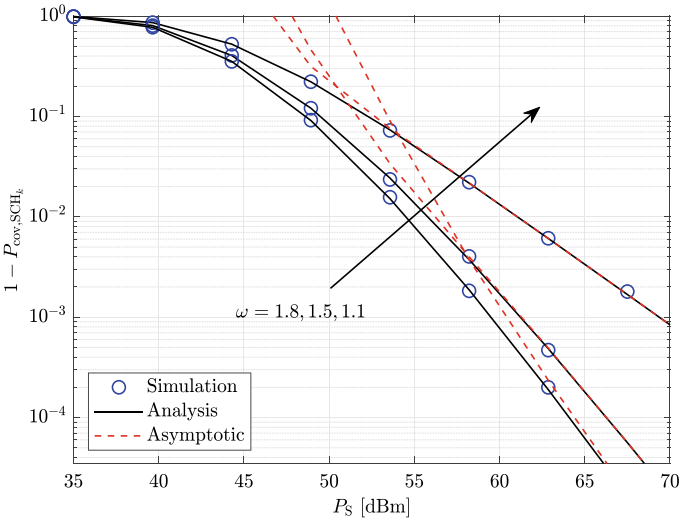

(b) $1 - P_{\mathrm{cov,SCH}_k}$ versus P_{S} with $\gamma_{\mathrm{th}} = 20$ dB

Fig. 4.5 $P_{\mathrm{cov,SCH}_k}$ and $1 - P_{\mathrm{cov,SCH}_k}$ over S-CH FSO links for various pointing errors

Figure 4.5 shows that increasing w leads to improved coverage performance. This observation can be explained by the fact that a large w denotes a slight standard deviation of pointing error displacement with a fixed equivalent beam radius at the receiver, resulting in a large average received power and SNR.

The asymptotic curves in Figs. 4.3b, c, and 4.4b have the same slopes in the high P_S region, as they show the same diversity order $\min\{\omega^2, \alpha, \beta\} = 1.21$. However, the asymptotic curves for $\omega = 1.1$ exhibit a different slope from the others in Fig. 4.5b because $\omega = 1.1$ results in $\min\{\omega^2, \alpha, \beta\} = 1.21$ and $\omega = 1.5$ or 1.9 leads to $\min\{\omega^2, \alpha, \beta\} = 1.9$, which cause different diversity orders.

4.1.6.2 CH-UAV RF Links

This section will investigate coverage performance for the 3 cases (interference-free, interference-dominated, and interference-and-noise cases) for various main parameters.

Figures 4.6 and 4.7 present the coverage performance for various m and D in the 3 cases. One can see that the CP with a large m outperforms the CP with a small m in the small γ_{th} region. The opposite observation is achieved for large γ_{th} region. Also, a large D leads to a small CP, which denotes a large distributed space for the UAVs, leading to a large path loss.

Figures 4.8 and 4.9 investigate the influence of $D_{\max}$ and $D_{\min}$, respectively. $D_{\max}$ clearly harms the CP, while $D_{\min}$ exhibits the opposite effect in this case. Also, a large $D_{\max}$ or a small $D_{\min}$ leads to more interfering CHs in the considered space,

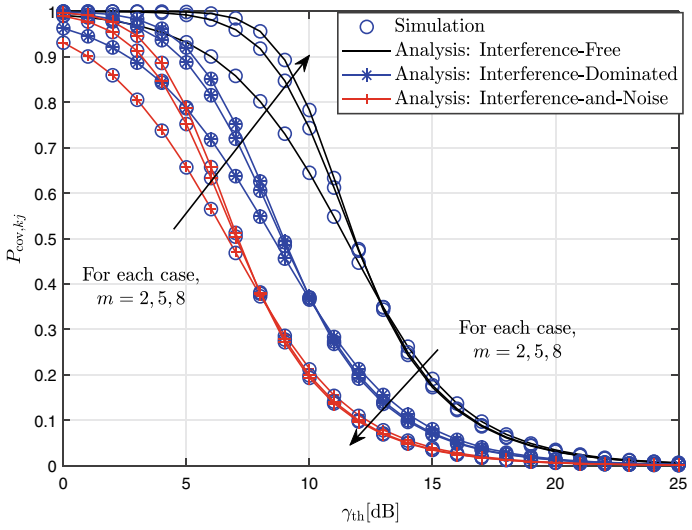

Fig. 4.6 $P_{\text{cov},kj}$ versus γ_{th} over CH-UAV links for different m in 3 cases

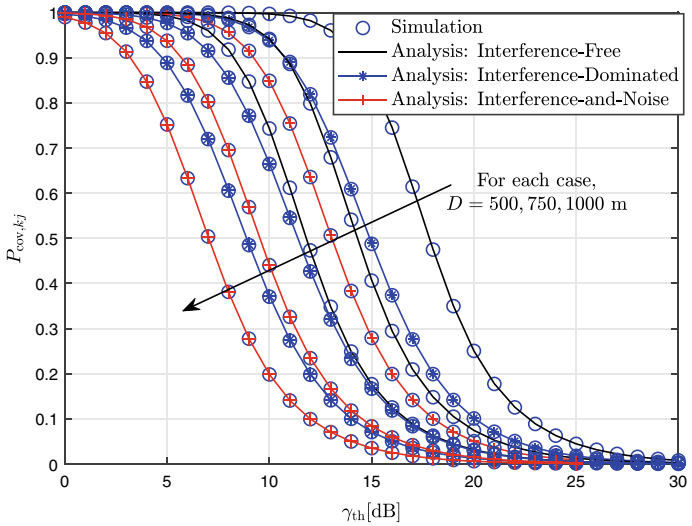

Fig. 4.7 $P_{\mathrm{cov},kj}$ versus γ_{th} over CH-UAV links for different D in 3 cases

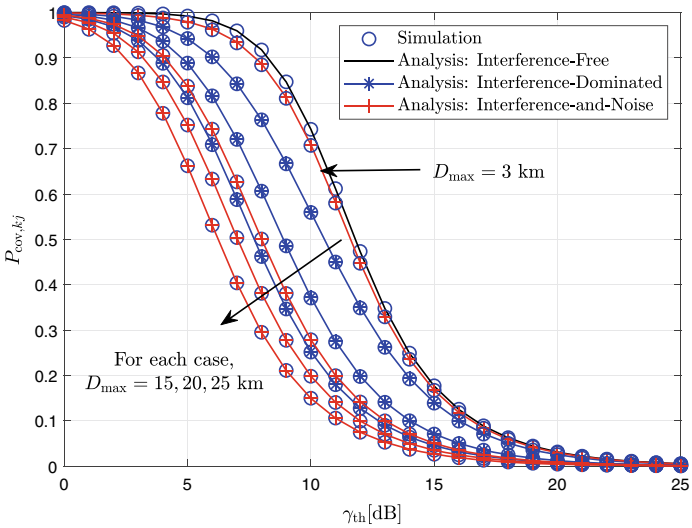

Fig. 4.8 $P_{\mathrm{cov},kj}$ versus γ_{th} over CH-UAV links for different $D_{\max}$ in the 3 cases

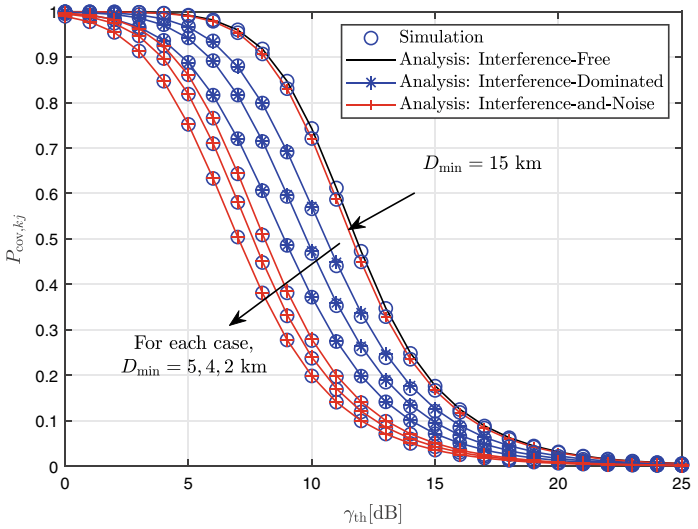

Fig. 4.9 $P_{\mathrm{cov},kj}$ versus γ_{th} over CH-UAV links for different $D_{\min}$ in the 3 cases

resulting in degradation of coverage performance. It can also be observed from these two figures that the interference-and-noise analysis curves with a small $D_{\max} = 3$ km and large $D_{\min} = 15$ km are very close to the interference-free curve. This is caused by the fact that a small $D_{\max}$ or a large $D_{\min}$ will shrink the distributed space and then reduce the number of interfering CHs. When $D_{\max} \approx D_{\min}$, the amount of interfering CHs is negligible, and the complex analysis model in the interference-and-noise case, Eq. (4.50), can be approximated to the simple model in the interference-free case, Eq. (4.23).

Figure 4.10 depicts the CP versus γ_{th} for different $P_{\mathrm{R}}/N_{\mathrm{R}}$. Obviously, for interference-free and interference-and-noise cases, a larger transmitting SNR $P_{\mathrm{R}}/N_{\mathrm{R}}$ will improve coverage performance. The analysis curve of the interference-and-noise case is very close to that of the interference-free case when $P_{\mathrm{R}}/N_{\mathrm{R}} = 97$ dB and the curve of the interference-dominated case when $P_{\mathrm{R}}/N_{\mathrm{R}} = 120$ dB. When $P_{\mathrm{R}}/N_{\mathrm{R}}$ is very small, $\gamma_{kj} = \frac{\frac{g_{kj}}{d_{kj}^{\alpha_r}}}{I + \frac{\rho}{P_{\mathrm{R}}} N_{\mathrm{R}}} \approx \frac{P_{\mathrm{R}} g_{kj}}{\rho d_{kj}^{\alpha_r} N_{\mathrm{R}}}$. Therefore, the analysis model of the interference-and-noise case, Eq. (4.50) can be approximated to the model of the interference-free case, Eq. (4.23). Meanwhile, when $P_{\mathrm{R}}/N_{\mathrm{R}}$ is very large, $\gamma_{kj} = \frac{\frac{g_{kj}}{d_{kj}^{\alpha_r}}}{I + \frac{\rho}{P_{\mathrm{R}}} N_{\mathrm{R}}} \approx \frac{g_{kj}}{I d_{kj}^{\alpha_r}}$ and, Eq. (4.50) can be approximated to the model of the interference-dominated case, Eq. (4.45).

Figure 4.11 shows the $1 - P_{\mathrm{cov},kj}$ versus $P_{\mathrm{R}}/N_{\mathrm{R}}$ for various γ_{th} in the interference-free case. It is easy to see that $1 - P_{\mathrm{cov},kj}$ decreases or $P_{\mathrm{cov},kj}$ increases when $P_{\mathrm{R}}/N_{\mathrm{R}}$ increases or γ_{th} decreases. These findings can be explained by the reasons proposed in the second paragraph of Sect. 4.1.6.1. We can also see that the three asymptotic

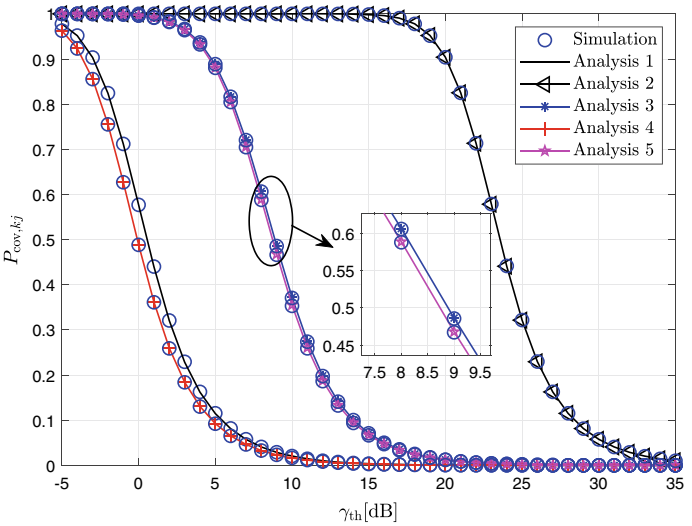

Fig. 4.10 $P_{\mathrm{cov},kj}$ versus γ_{th} over CH-UAV links for various $P_{\mathrm{R}}/N_{\mathrm{R}}$ (Analysis 1 and 2 are interference-free with $P_{\mathrm{R}}/N_{\mathrm{R}} = 97$ and 120 dB; Analysis 3 is interference-dominated; Analysis 4 and 5 are interference-and-noise with $P_{\mathrm{R}}/N_{\mathrm{R}} = 97$ and 120 dB)

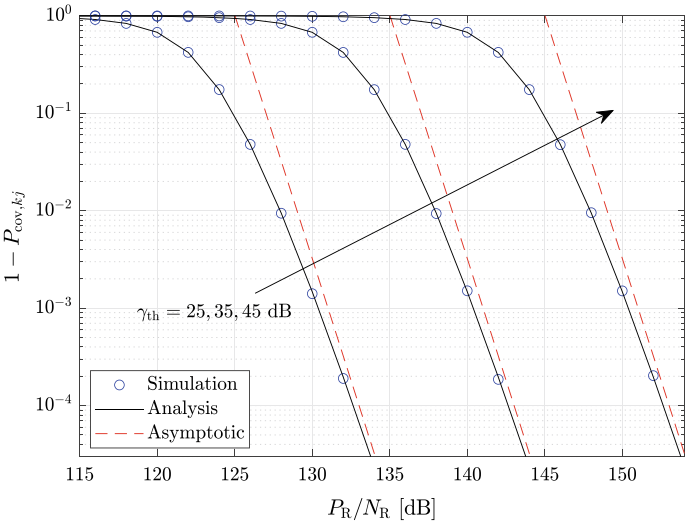

Fig. 4.11 $1 - P_{\mathrm{cov},kj}$ versus $P_{\mathrm{R}}/N_{\mathrm{R}}$ over CH-UAV links for different γ_{th} in the interference-free case

curves have the same slope in large P_R/N_R region because they share the same diversity order m.

Furthermore, one can clearly see from Figs. 4.3, 4.4, 4.5 and 4.11 that the simulation results agree very well with the results of the analysis, and the asymptotic curves converge to the simulation and analysis curves in the high P_S region, which verifies the accuracy of our proposed analytical and asymptotic models. The slopes of asymptotic curves show the correctness of the derived diversity order. The agreement between simulation and analysis curves for interference-dominated and interference-and-noise cases in Figs. 4.6, 4.7, 4.8, 4.9 and 4.10 indicates the rationality of the approximation shown in Fig. 4.14.

4.1.6.3 The E2e Coverage Performance

From Eq. (4.52), we know the e2e CP is the multiplication of S-CH CP and CH-UAV CP. The findings from Figs. 4.3, 4.4, 4.5 and 4.11 are also applicable to the e2e coverage performance over S-CH-UAV links.

4.1.7 Conclusion

In this section, we studied the coverage performance of a cooperative satellite-UAV communication system with a DF relay scheme while considering the randomness of the positions of the CHs and UAVs. Closed-form and approximated expressions for the CP over S-CH FSO links were derived. Moreover, the coverage performance over CH-UAV RF links was analyzed under three cases: interference-free, interference-dominated, and interference-and-noise. The analytical expressions for the CP under these three cases and the asymptotic under the interference-free case were presented. Finally, we show the closed-form analytical expression for the e2e CP over S-CH-UAV links.

Some valuable conclusions can be drawn from the numerical results as follows:

(1) The intensity of turbulence negatively influences the CP over the S-CH FSO link in the small γ_{th} or large P_S regions. In contrast, the opposite observation is found in the large γ_{th} or small P_S regions.
(2) The altitude of the satellite and pointing error negatively influence the CP over S-CH FSO links.
(3) The Nakagami-m fading parameter, m, has a positive effect on the CP over CH-UAV RF links in the small γ_{th} region and a negative effect in the large γ_{th} region.
(4) Over CH-UAV RF links, the coverage radius D and sensitivity radius D_{max} of the CP negatively influence the CP. In contrast, the hard-core radius D_{min} positively affects the CP.
(5) The diversity orders over S-CH FSO and CH-UAV links in the interference-free case are $\min\{\omega^2, \alpha, \beta\}$ and m, respectively.

(6) When $D_{\min} \approx D_{\max}$ or $P_{\mathrm{R}}/N_{\mathrm{R}}$ is very small, the analysis model of the interference-and-noise case, Eq. (4.50) can be approximated to the model of the interference-free case, Eq. (4.23).
(7) When $P_{\mathrm{R}}/N_{\mathrm{R}}$ is very large, the analysis model of the interference-and-noise case, Eq. (4.50) can be approximated to the model of the interference-dominated case (4.45).

Appendix 3: Proof of Proposition 1

As it is difficult to prove Proposition 1 mathematically, we use Monte Carlo simulation instead. Figs. 4.12 and 4.13 present the simulation and analysis results of the CDFs of l_k and d_k^2 with HPPP and MHCPP corresponding to different $D_{\min}$ in Eq. (4.2). The analysis curves are according to Eqs. (4.55) ($y = \xi_0$) and (4.64) in Appendix 4. The values of the other parameters adopted in this simulation are listed in Table 4.1 and $\mathrm{V}^{\frac{1}{3}} = 46.3$ km.

The MHCPP with a specific $D_{\min}$ is thinned from the HPPP by the rule introduced in Sect. 4.1.1. From the two figures, one can see that they present three same rules:

1. The simulation curve of the MHCPP gets close to that of the HPPP when $D_{\min}$ decreases;
2. The CDF curve of the MHCPP with $D_{\min} = 2$ km is identical to that of the HPPP;
3. The simulation curve matches the analysis curve very well.

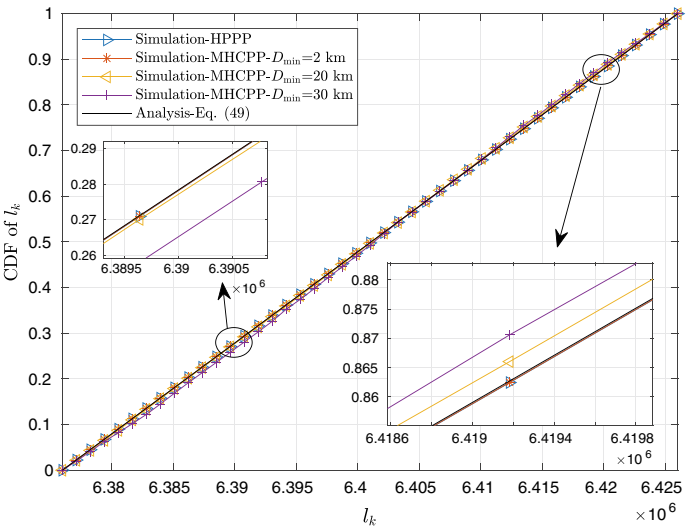

Fig. 4.12 CDF of l_k

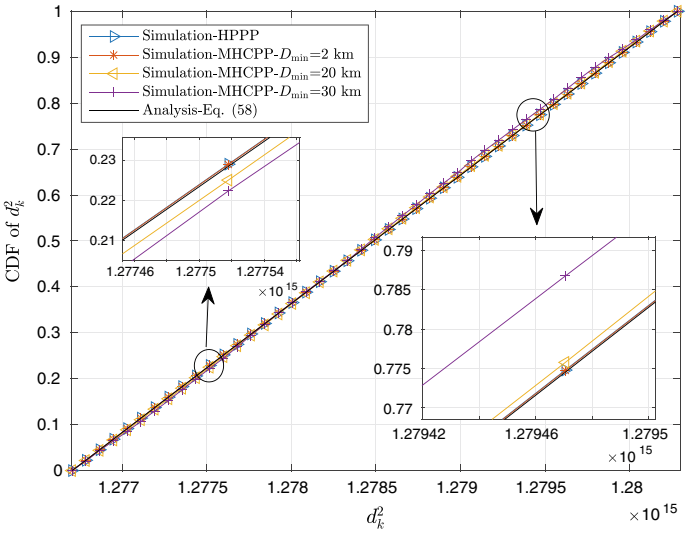

Fig. 4.13 CDF of d_k^2

These three observations verify the correctness of Proposition 1, Eq. (4.55) ($y = \xi_0$) and Eq. (4.64).

Appendix 4: Proof of Lemma 4.2

As CHs can be regarded as a set of independently and uniformly distributed points in $\mathcal{V}$ according to **Proposition 1**, the joint CDF of l_k and ξ_k is the ratio between the volumes of the two objects with red edges and blue edges in Fig. 4.2 which can be expressed as

$$F_{l_k,\xi_k}(x, y) = \frac{\int_0^{2\pi} d\theta \int_0^{y} \sin\xi d\xi \int_R^{x} r^2 dr}{V}$$

$$= \frac{2\pi(1-\cos y)(x^3 - R^3)}{3V}. \tag{4.55}$$

Then, the joint PDF of l_k and ξ_k can be written as

$$f_{l_k,\xi_k}(x, y) = \frac{\partial^2 F_{l_k,\xi_k}(x, y)}{\partial x \partial y}$$

$$= \frac{2\pi x^2 \sin y}{V}. \tag{4.56}$$

From Fig. 4.2, the relationships between l_k, ξ_k, and d_k^2 can be represented as

$$d_k^2 = l_k^2 + L^2 - 2l_k L\cos\xi_k, \tag{4.57}$$

where $L = H_S + H_U + R$.

It can be easily seen that

$$\begin{aligned} d_{\min} &= H_S \\ &\le d_k \le \sqrt{(R+H_U)^2 + L^2 - 2(R+H_U)L\cos\xi_0} \\ &= d_{\max}. \end{aligned} \tag{4.58}$$

To obtain the PDF of d_k^2, we first derive the joint PDF of d_k^2 and l_k.

According to the multivariate change of variables formula, the Jacobian determinant of the matrix
$\partial(d_k^2, l_k)/\partial(l_k, \xi_k)$ is

$$\begin{aligned} \left|\frac{\partial(d_k^2, l_k)}{\partial(l_k, \xi_k)}\right| &= \begin{vmatrix} 2l_k - 2L\cos\xi_k & 2l_k L\sin\xi_k \\ 1 & 0 \end{vmatrix} \\ &= 2l_k L\sin\xi_k. \end{aligned} \tag{4.59}$$

Then, the joint PDF of d_k^2 and l_k can be achieved as

$$\begin{aligned} f_{d_k^2, l_k}(x, y) &= \frac{f_{l_k,\xi_k}(x, y)}{\left|\frac{\partial(d_k^2, l_k)}{\partial(l_k, \xi_k)}\right|} \\ &= \frac{\pi y}{VL}, \end{aligned} \tag{4.60}$$

where $R \le y \le R + H_U$ and $\cos\xi_0 \le \cos\xi_k = \frac{y^2+L^2-x}{2Ly} \le 1$.

The PDF of d_k^2 can be acquired through the integration of Eq. (4.60) according to l_k as follows

$$\begin{aligned} f_{d_k^2}(x) &= \int_{\tau_1(x)}^{\tau_2(x)} f_{d_k, l_k}(x, y)dy \\ &= \frac{\pi}{2VL}\left[\tau_2^2(x) - \tau_1^2(x)\right]. \end{aligned} \tag{4.61}$$

Observing $R \le y \le R + H_U$ and $\cos\xi_0 \le \cos\xi_k = \frac{y^2+L^2-x}{2Ly} \le 1$, τ_1 and τ_2 can be obtained as

$$\tau_1(x) = \max\left\{R, L - \sqrt{x}\right\} \tag{4.62}$$

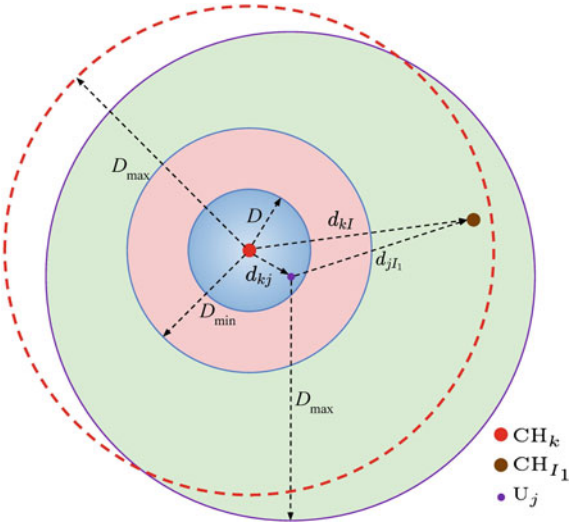

Fig. 4.14 CH-UAV link model

and

$$\tau_2(x) = \min\left\{R + H_{\mathrm{U}}, L\cos\xi_0 - \sqrt{x - L^2\sin^2\xi_0}\right\}, \tag{4.63}$$

respectively.

Furthermore, the CDF of d_k^2 can be achieved as

$$F_{d_k^2}(y) = \int_{d_{\min}^2}^{y} f_{d_k^2}(x)dx, \ d_{\min}^2 \le y \le d_{\max}^2. \tag{4.64}$$

Appendix 5: Proof of Lemma 4.5

As shown in Fig. 4.14, the inner blue sphere is the serving space of CH_k. The red and blue spaces are interference-free as their radii are smaller than or equal to $D_{\min}$ to CH_k. These CHs, including CH_{I_1}, which cause the interference to the typical UAV U_j, are located in the green space. d_{kj}, d_{jI_1}, and d_{kI_1} represent the distances between CH_k and U_j, U_j and CH_{I_1}, and U_k and CH_{I_1}, respectively.

To make the following derivation tractable, we estimate that CH_{I_1} is distributed in the sphere with a red dashed outline instead of the green sphere. This approximation is reasonable, as these two spheres mostly overlap, and the shift between them is less than D.

Similar to Lemma 4.2, we can obtain the joint PDF of $d_{jI_1}^2$ given d_{kj} as

$$f_{d_{jI_1}^2|d_{kj}}(x) = \frac{\pi[\tau_4^2(x, d_{kj}) - \tau_3^2(x, d_{kj})]}{2d_{kj}V_1}, \tag{4.65}$$

where $V_1 = \frac{4\pi}{3}(D_{\max}^3 - D_{\min}^3)$, $\tau_4(x, d_{kj}) = \min\{D_{\max}, \sqrt{x} + d_{kj}\}$, $\tau_3(x, d_{kj}) = \max\{D_{\min}, \sqrt{x} - d_{kj}\}$, and $d_{jI_1}^{\min} = (D_{\min} - d_{kj})^2 \le x \le (D_{\max} + d_{kj})^2 = d_{jI_1}^{\max}$.

It is easy to obtain that V_1 is the volume of the green space. The number of interfering CHs in this space has the probability $\mathbf{Pr}\{X = N_I\} = \frac{(\lambda_{\mathrm{CH}} V_1)^{N_I}}{N_I!} e^{-\lambda_{\mathrm{CH}} V_1}$, where $N_I = 0, \ldots, \infty$.

From the definition of s in Eq. (4.32), we know $s > 0$. Therefore, $\mathbb{E}_I[e^{-sI}]$ can be calculated as

$$\begin{aligned}
\mathbb{E}_I[e^{-sI}] &= \mathbb{E}_{N_I}\left\{\mathbb{E}_I\left[\exp\left(-s\sum_{i=1}^{N_I} g_{jI_i} d_{jI_i}^{-\alpha_r}\right)\right]\right\} \\
&\overset{(a)}{=} \mathbb{E}_{N_I}\left\{\prod_{i=1}^{N_I} \mathbb{E}_{g_{jI_i}, d_{jI_i}}\left[\exp\left(-s g_{jI_i} d_{jI_i}^{-\alpha_r}\right)\right]\right\} \\
&\overset{(b)}{=} \sum_{N_I=0}^{\infty} \frac{(\lambda_{\mathrm{CH}} V_1)^{N_I}}{N_I!} \exp\left(-\lambda_{\mathrm{CH}} V_1\right)\left\{\mathbb{E}_{g_{jI_1}, d_{jI_1}}\left[\exp\left(-s g_{jI_1} d_{jI_1}^{-\alpha_r}\right)\right]\right\}^{N_I} \\
&\overset{(c)}{=} \sum_{N_I=0}^{\infty} \frac{(\lambda_{\mathrm{CH}} V_1 I_3)^{N_I}}{N_I!} \exp\left(-\lambda_{\mathrm{CH}} V_1\right) \\
&\overset{(d)}{=} \exp\left(-\lambda_{\mathrm{CH}} V_1 + \lambda_{\mathrm{CH}} V_1 I_3\right),
\end{aligned} \tag{4.66}$$

where $I_3 = \int_{d_{jI_1}^{\min}}^{d_{jI_1}^{\max}} \mathbb{E}_{g_{jI_1}}\left[\exp\left(-s g_{jI_1} x^{-\frac{\alpha_r}{2}}\right)\right] f_{d_{jI_1}^2|d_{kj}}(x)dx$, (a) is based on the fact that g_{jI_i} and d_{jI_i} are both independent and identically distributed random variables, (b) is obtained by substituting the PMF of N_I, (c) is achieved by substituting Eq. (4.65), and (d) is deduced by using the Taylor series of $\exp\left(-\lambda_{\mathrm{CH}} V_1\right)$.

Using the MGF of the Nakagami-m function [17], $\mathbb{E}_{g_{jI_1}}\left[\exp\left(-s g_{jI_1} x^{-\frac{\alpha_r}{2}}\right)\right]$ can be obtained as

$$\mathbb{E}_{g_{jI_1}}\left[\exp\left(-s g_{jI_1} x^{-\frac{\alpha_r}{2}}\right)\right] = \left(\frac{\frac{m}{\Omega s} x^{\frac{\alpha_r}{2}}}{\frac{m}{\Omega s} x^{\frac{\alpha_r}{2}} + 1}\right)^m. \tag{4.67}$$

Substituting Eqs. (4.65) and (4.67) in I_3, we deduce

$$I_3 = \left(\frac{m}{\Omega s}\right)^m \frac{\pi}{2 d_{kj} V_1} \int_{d_{jI_1}^{\min}}^{d_{jI_1}^{\max}} \frac{x^{\frac{m\alpha_r}{2}}}{\left(\frac{m}{\Omega s} x^{\frac{\alpha_r}{2}} + 1\right)^m}\left[\tau_4^2\left(x, d_{kj}\right) - \tau_3^2\left(x, d_{kj}\right)\right] dy. \tag{4.68}$$

In the following, we will use τ_3 and τ_4 to represent $\tau_3\left(x, d_{kj}\right)$ and $\tau_4\left(x, d_{kj}\right)$, respectively, for convenience and discuss the integral interval in Eq. (4.68) in four cases according to the values of τ_3 and τ_4.

Case 1: When $\tau_4 = D_{\max}$ which means $D_{\max} < \sqrt{x} + d_{kj}$ and $\tau_3 = D_{\min}$ which means $\sqrt{x} - d_{kj} < D_{\min}$, we can get $(D_{\max} - d_{kj})^2 < x < (D_{\min} + d_{kj})^2$. However, as $D_{\max} \gg D_{\min}$, $D_{\max} \gg D > d_{kj}$, and $D_{\max} - D_{\min} \gg 2d_{kj}$, this case does not exist.

Case 2: When $\tau_4 = \sqrt{x} + d_{kj}$ which indicates $\sqrt{x} + d_{kj} < D_{\max}$ and $\tau_3 = D_{\min}$ which indicates $\sqrt{x} - d_{kj} < D_{\min}$, we can have $(D_{\min} - d_{kj})^2 < x < (D_{\min} + d_{kj})^2$ and $\tau_4^2 - \tau_3^2 = x + 2d_{kj}\sqrt{x} + d_{kj}^2 - D_{\min}^2$ can be obtained.

Case 3: When $\tau_4 = \sqrt{x} + d_{kj}$ which denotes $\sqrt{x} + d_{kj} < D_{\max}$ and $\tau_3 = \sqrt{x} - d_{kj}$ which denotes $D_{\min} < \sqrt{x} - d_{kj}$, we deduce $d_{jI_1}^{g_1} = (D_{\min} + d_{kj})^2 < x < (D_{\max} - d_{kj})^2 = d_{jI_1}^{g_2}$ and $\tau_4^2 - \tau_3^2 = 4d_{kj}\sqrt{x}$.

Case 4: When $\tau_4 = D_{\max}$ which shows $D_{\max} < \sqrt{x} + d_{kj}$ and $\tau_3 = \sqrt{x} - d_{kj}$ which shows $D_{\min} < \sqrt{x} - d_{kj}$, we can obtain $(D_{\max} - d_{kj})^2 < x < (D_{\max} + d_{kj})^2$ and $\tau_4^2 - \tau_3^2 = -x + 2d_{kj}\sqrt{x} + D_{\max}^2 - d_{kj}^2$.

By using [11, Eq. 3.194.1], I_3 can be represented as

$$
\begin{aligned}
I_3 = &\left(\frac{m}{\Omega s}\right)^m \frac{\pi}{2d_{kj}V_1}\Bigg\{ \int_{d_{jI_1}^{\min}}^{d_{jI_1}^{g_1}} \left[x^{\frac{m\alpha_r}{2}+1} + 2d_{kj}x^{\frac{m\alpha_r+1}{2}} + (d_{kj}^2 - D_{\min}^2)x^{\frac{m\alpha_r}{2}}\right] \\
&\times \frac{1}{\left(\frac{m}{\Omega s}x^{\frac{\alpha_r}{2}}+1\right)^m}dx + 4d_{kj}\int_{d_{jI_1}^{g_1}}^{d_{jI_1}^{g_2}} \frac{x^{\frac{m\alpha_r+1}{2}}}{\left(\frac{m}{\Omega s}x^{\frac{\alpha_r}{2}}+1\right)^m}dx \\
&+ \int_{d_{jI_1}^{g_2}}^{d_{jI_1}^{\max}} \frac{-x^{\frac{m\alpha_r}{2}+1} + 2d_{kj}x^{\frac{m\alpha_r+1}{2}} + (D_{\max}^2 - d_{kj}^2)x^{\frac{m\alpha_r}{2}}}{\left(\frac{m}{\Omega s}x^{\frac{\alpha_r}{2}}+1\right)^m}dx\Bigg\} \\
= &\left(\frac{m}{\Omega s}\right)^m \frac{\pi}{2d_{kj}V_1}\left\{\mathcal{F}\left(\frac{4}{\alpha_r}, d_{jI_1}^{g_1}, d_{jI_1}^{\min}\right) + 2d_{kj}\mathcal{F}\left(\frac{3}{\alpha_r}, d_{jI_1}^{g_1}, d_{jI_1}^{\min}\right)\right. \\
&+ (d_{kj}^2 - D_{\min}^2)\mathcal{F}\left(\frac{2}{\alpha_r}, d_{jI_1}^{g_1}, d_{jI_1}^{\min}\right) + 4d_{kj}\cdot\mathcal{F}\left(\frac{3}{\alpha_r}, d_{jI_1}^{g_2}, d_{jI_1}^{g_1}\right) \\
&- \mathcal{F}\left(\frac{4}{\alpha_r}, d_{jI_1}^{\max}, d_{jI_1}^{g_2}\right) + 2d_{kj}\mathcal{F}\left(\frac{3}{\alpha_r}, d_{jI_1}^{\max}, d_{jI_1}^{g_2}\right) \\
&\left.+ (D_{\max}^2 - d_{kj}^2)\mathcal{F}\left(\frac{2}{\alpha_r}, d_{jI_1}^{\max}, d_{jI_1}^{g_2}\right)\right\}, \qquad (4.69)
\end{aligned}
$$

where

$$
\begin{aligned}
\mathcal{F}(a,b,c) = &\Big[{}_2F_1\Big(m, m+a; m+a+1; -\frac{m}{\Omega s}b^{\frac{\alpha_r}{2}}\Big)\, b^{\frac{(m+a)\alpha_r}{2}} \\
&- {}_2F_1\Big(m, m+a; m+a+1; -\frac{m}{\Omega s}c^{\frac{\alpha_r}{2}}\Big)\, c^{\frac{(m+a)\alpha_r}{2}}\Big]\frac{2}{(m+a)\alpha_r}
\end{aligned}
$$

and ${}_2F_1(\cdot,\cdot;\cdot;\cdot)$ denotes the Gauss hypergeometric function.

Finally, Eq. (4.36) can be obtained by substituting Eq. (4.69) in Eq. (4.66).

Appendix 6: Proof of Lemma 4.7

According to the Leibnitz formula, $\mathcal{A}^{(n)}(s,d_{kj})$ $(n>0)$ can be expressed as

$$\mathcal{A}^{(n)}(s,d_{kj})=\frac{\pi\lambda_{\mathrm{CH}}}{2d_{kj}}\left(\frac{m}{\Omega}\right)^m\sum_{l=0}^{n}\binom{n}{l}f_1^{(n-l)}(s)f_2^{(l)}(s,d_{kj}), \tag{4.70}$$

where $f_1(s)=s^{-m}$ and $f_2(s,d_{kj})$ is represented as

$$\begin{aligned}f_2(s,d_{kj})=&\mathcal{F}\left(\frac{4}{\alpha_r},d_{jI_1}^{\mathrm{g}_1},d_{jI_1}^{\min}\right)+(d_{kj}^2-D_{\min}^2)\mathcal{F}\left(\frac{2}{\alpha_r},d_{jI_1}^{\mathrm{g}_1},d_{jI_1}^{\min}\right)\\&+2d_{kj}\mathcal{F}\left(\frac{3}{\alpha_r},d_{jI_1}^{\mathrm{g}_1},d_{jI_1}^{\min}\right)+4d_{kj}\mathcal{F}\left(\frac{3}{\alpha_r},d_{jI_1}^{\mathrm{g}_2},d_{jI_1}^{\mathrm{g}_1}\right)\\&-\mathcal{F}\left(\frac{4}{\alpha_r},d_{jI_1}^{\max},d_{jI_1}^{\mathrm{g}_2}\right)+2d_{kj}\mathcal{F}\left(\frac{3}{\alpha_r},d_{jI_1}^{\max},d_{jI_1}^{\mathrm{g}_2}\right)\\&+(D_{\max}^2-d_{kj}^2)\mathcal{F}\left(\frac{2}{\alpha_r},d_{jI_1}^{\max},d_{jI_1}^{\mathrm{g}_2}\right).\end{aligned} \tag{4.71}$$

It is easy to get the $(n-l)$th derivative of $f_1(s)$ as

$$f_1^{(n-l)}(s)=(-1)^{n-l}(m)_{n-l}s^{-m-n+l}, \tag{4.72}$$

where $(m)_{n-l}=\prod_{k=0}^{n-l-1}(m-k)$ is the rising Pochhammer symbol.

To get the lth derivative of $f_2(s,d_{kj})$, we should first calculate the lth derivative of $\Delta(s,a,b)={}_2F_1\left(m,m+a;m+a+1;-\frac{m}{\Omega s}b^{\frac{\alpha_r}{2}}\right)$.

When $l=0$, $\Delta^{(0)}(s,a,b)=\Delta(s,a,b)$ can be acquired.

When $l>0$, employing the Faadi Bruno's formula, $\Delta^{(l)}(s)$ can be obtained as

$$\begin{aligned}\Delta^{(l)}(s,a,b)=&\sum_{q=1}^{l}\frac{(m+a)(m)_q}{m+a+q}{}_2F_1\left(m+q,m+a+q;m+a+q+1;-\frac{mb^{\frac{\alpha_r}{2}}}{\Omega s}\right)\\&\times B_{l,q}\left(f_3^{(1)}(s,b),\ldots,f_3^{(l-q+1)}(s,b)\right),\end{aligned} \tag{4.73}$$

where $f_3(s,b)=-\frac{mb^{\frac{\alpha_r}{2}}}{\Omega}s^{-1}$, and $f_3^{(q)}(s,b)=(-1)^{q+1}q!\frac{mb^{\frac{\alpha_r}{2}}}{\Omega}s^{-1-q}$.

Furthermore, the lth derivative of $\mathcal{F}(a, b, c)$ can be achieved as

$$\mathcal{F}^{(l)}(a, b, c) = \frac{2}{(m+a)\alpha_r}\left[b^{\frac{(m+a)\alpha_r}{2}}\Delta^{(l)}(s, a, b) - c^{\frac{(m+a)\alpha_r}{2}}\Delta^{(l)}(s, a, c)\right]. \quad (4.74)$$

Combining Eqs. (4.71), (4.73), and (4.74), we can obtain the lth derivative of $f_2(s)$, $f_2^{(l)}(s)$. Then, Eq. (4.42) can be achieved by substituting Eq. (4.72) and $f_2^{(l)}(s)$ in Eq. (4.70).

4.2 Secrecy Outage Analysis for UAV Assisted Satellite-Terrestrial Simultaneous Wireless Information and Power Transfer (SWIPT) Systems with NOMA

This section studies the physical-layer security for a NOMA-based UAV-assisted hybrid satellite-terrestrial simultaneous wireless information and power transfer system. Specifically, a satellite sends confidential information on a NOMA basis to two terrestrial users through a UAV relay under the wiretapping of an eavesdropper. A power-splitting protocol coordinates information decoding and energy harvesting (EH). Assuming the satellite link experiences SR fading and the terrestrial links are subject to Nakagami-m fading, the analytical expressions for the SOP and the probability of strictly positive secrecy capacity for two users are derived, and Monte Carlo simulations verify the accuracy of the results.

We investigate the physical layer security for a NOMA-based UAV-assisted hybrid satellite-terrestrial SWIPT system. The main contributions are as follows:

(1) Assuming the satellite link undergoes SR fading and the terrestrial links experience Nakagami-m fading, we investigate the secrecy performance of a UAV-assisted hybrid satellite-terrestrial SWIPT system with NOMA. In particular, the analytical expressions of SOP and the probability of strictly positive secrecy capacity (SPSC) for both users are derived and verified with Monto-Carlo simulations.
(2) The influence of parameters such as power allocation coefficients, shadowing severity levels, path loss factors, power splitting (PS) ratio, and node distance on the system performance are considered.

4.2.1 System and Channel Models

As illustrated in Fig. 4.15, we assumed a UAV-assisted hybrid satellite-terrestrial SWIPT system with NOMA, which consists of a satellite (S), a DF UAV relay (R), a legitimate group of NOMA users (D_1 and D_2, with D_1 denoting the far user, and D_2 representing the near user), and an eavesdropper (E). The whole communication

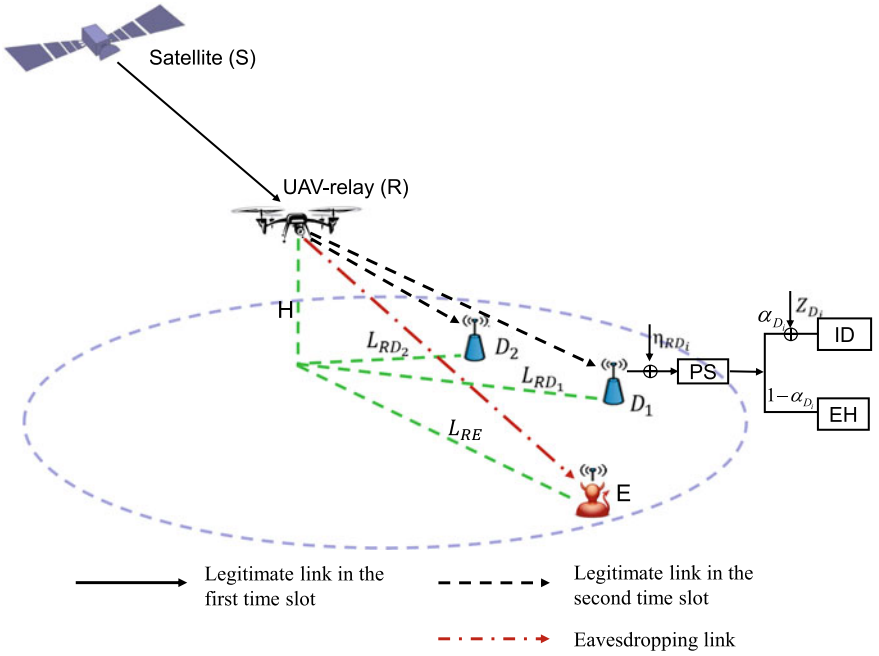

Fig. 4.15 System model

process can be divided into two equal time slots. S sends a confidential NOMA signal to R in the first time slot. In the second time slot, R first decodes the received signal and forwards the re-encoded NOMA signal to D_i ($i \in \{1, 2\}$) in the presence of E. Each user is assumed to be equipped with a rechargeable battery and a PS[8] protocol is performed to coordinate EH and information decoding (ID). Note that, in this analysis, we mainly focus on the scenario that both users are equipped with the PS receivers, meaning it is the destinations that can split the received signal from the UAV into two streams according to the PS ratios, i.e., one is for EH and the other is ID. In other words, the EH has little requirement for the UAV. Instead, it mainly depends on how the destination coordinates the received signal according to the PS factor rather than any constraint on the UAV. In addition, we assume that the S-R link experiences SR fading, and the terrestrial links, i.e., R-D_i, and R-E, are subject to Nakagami-m fading.

In the first time slot, the received signal at R is

[8] In literature, i.e., [18–20], both the time switching (TS) and the PS protocols are commonly used in the context of EH. The work of [18] shows that the PS protocol is more effective than the TS one in terms of energy efficiency and data transmission rate, and the PS protocol allows the receiver to complete EH and ID at the same stage without interruption over time [19]. In addition, compared with TS, the PS protocol is superior to it at high SNR regimes in terms of the achievable throughput [20]. Therefore, the PS protocol is adopted in this analysis.

$$y_{SR} = h_{SR}x + n_{SR}, \tag{4.75}$$

where $x = \sqrt{a_1 P_s}x_1 + \sqrt{a_2 P_s}x_2$[9] represents the NOMA signal and a_i is the power allocation coefficient with $a_1 + a_2 = 1$, and $a_1 \geq a_2$, n_{SR} represents the AWGN with zero mean and a variance of N_{SR}, and h_{SR} denotes the channel coefficient between S and R, which is expressed as

$$h_{SR} = \mathcal{F}_{SR} f_{SR}, \tag{4.76}$$

where f_{SR} represents the random SR fading coefficient and $\mathcal{F}_{SR}$ represents a scaling parameter, which includes free space loss and the antenna pattern [21], and it can be described as

$$\mathcal{F}_{SR} = \frac{C\sqrt{G_t G_r}}{4\pi f d\sqrt{K_B T_n B}}, \tag{4.77}$$

where C represents speed light, d is the distance between the satellite orbit and the receiver, f is the carrier frequency, K_B is the Boltzmann constant, T_n represents the noise temperature of the receiver, and B represents the carrier bandwidth. In addition, G_r is the receiving gain, and G_t denotes the satellite beam gain, which is approximately by [21]

$$G_t = G_{\max}\left(\frac{J_1(c)}{2c} + 36\frac{J_3(c)}{c^3}\right)^2, \tag{4.78}$$

with $G_{\max}$ is the maximal beam gain, $c = 2.07123\frac{\sin\phi}{\sin\phi_{3dB}}$, where ϕ is the angle between the receiver position and the beam center concerning the satellite, ϕ_{3dB} is the 3-dB angle, and $J_u(\cdot)$ represent the first-kind Bessel function of order u.

Next, perfect successive interference cancellation (SIC) [22],[10] x_1, and then removes x_1 from the received signal before decoding the signal of D_2, x_2. Therefore, the instantaneous SINR of decoding x_1 at R is

[9] Note that under the multi-user scenario, the power allocation coefficient assigned to each user depends on the channel power gain. If there are L users in the system, without loss of generality, we first order the channel power gain as $|h_{RD_1}|^2 \leq |h_{RD_2}|^2 \leq \ldots \leq |h_{RD_L}|^2$ and then give the power allocation coefficient to each user as $a_1 \geq a_2 \geq \ldots \geq a_L$, where $\sum_{\widetilde{i}=1}^{L} a_{\widetilde{i}} = 1$. Therefore, the general expression for the NOMA signal is $x = \sum_{\widetilde{i}=1}^{L}\sqrt{a_{\widetilde{i}} P_s}x_{\widetilde{i}}$, where $x_{\widetilde{i}}$ is the transmitted symbol for the $\widetilde{i}th$ user.

[10] Under the multi-user scenario with the perfect SIC principle, the decoding order is the increasing order of the channel power gain, which gives the instantaneous SINR of decoding the signal, $x_{\widetilde{m}}$, at R as $\gamma_{SR_{\widetilde{m}}} = \frac{P_s a_{\widetilde{m}}|h_{SR}|^2}{P_s|h_{SR}|^2\sum_{\widetilde{n}=\widetilde{m}+1}^{L} a_{\widetilde{n}} + N_{SR}}$ is performed to decode the signal. Hence, the R first decodes the signal of D_1, and the SNR of decoding the signal, x_L, as $\gamma_{SR_L} = \frac{P_s a_L|h_{SR}|^2}{N_{SR}}$.

$$\gamma_{SR_1} = \frac{P_s a_1 |h_{SR}|^2}{P_s a_2 |h_{SR}|^2 + N_{SR}} = \frac{a_1 \gamma_1}{a_2 \gamma_1 + 1}, \tag{4.79}$$

where $\gamma_1 = \frac{P_s \mathcal{F}_{SR}^2 |f_{SR}|^2}{N_{SR}} = \overline{\gamma}_1 |f_{SR}|^2$ and $\overline{\gamma}_1 = \frac{P_s \mathcal{F}_{SR}^2}{N_{SR}} = \overline{\gamma}_{SR} \mathcal{F}_{SR}^2$.

The instantaneous SNR of decoding x_2 can be given as

$$\gamma_{SR_2} = \frac{P_s a_2 |h_{SR}|^2}{N_{SR}} = a_2 \gamma_1. \tag{4.80}$$

After that, we have the PDF and CDF of γ_1 as [23]

$$f_{\gamma_1}(x) = \sum_{k=0}^{m_R - 1} \frac{\varsigma (1 - m_R)_k (-\delta_R)^k x^k}{\overline{\gamma}_1^{k+1} (k!)^2} \exp(-\lambda x) \tag{4.81}$$

and

$$F_{\gamma_1}(x) = 1 - \sum_{k=0}^{m_R - 1} \sum_{p=0}^{k} \frac{\varsigma (1 - m_R)_k (-\delta_R)^k x^p}{p! k! \lambda^{k-p+1} \overline{\gamma}_1^{k+1}} \exp(-\lambda x), \tag{4.82}$$

respectively, where $\lambda = \frac{\beta_R - \delta_R}{\overline{\gamma}_1}$, $\varsigma = \frac{1}{2b} \left(\frac{2bm_R}{2bm_R + \Omega_R} \right)^{m_R}$, $\beta_R = \frac{1}{2b}$, $\delta_R = \frac{\Omega_R}{2b(2bm_R + \Omega_R)}$ with m_R represents the fading severity parameter, $(\cdot)_k$ is the Pochhammer symbol, and Ω_R and $2b$ represent the average power of LoS and multipath components, respectively.

In the second time slot, the signals received at D_i and E are

$$y_{RD_i} = \sqrt{\alpha_{D_i}} \left(\frac{h_{RD_i}}{\sqrt{d_{RD_i}^{\eta}}} x + n_{RD_i} \right) + z_{Di} \tag{4.83}$$

and

$$y_{RE} = \sqrt{\alpha_E} \left(\frac{h_{RE}}{\sqrt{d_{RE}^{\eta}}} x + n_{RE} \right) + z_E, \tag{4.84}$$

respectively, where h_{RM} ($M \in \{D_i, E\}$) is the channel coefficient between R and M, α_M, $0 < \alpha_M < 1$, denote the PS ratio, n_{RM} is the AWGN with zero mean and a variance of N_{RM}, and z_M is the signal processing noise generated by the PS processing at the receiving ends, which is also modeled as AWGN with zero mean and a variance of δ_M^2 [24]. Furthermore, $d_{RM} = \sqrt{L_{RM}^2 + {H_R}^2}$ represents the distance between R

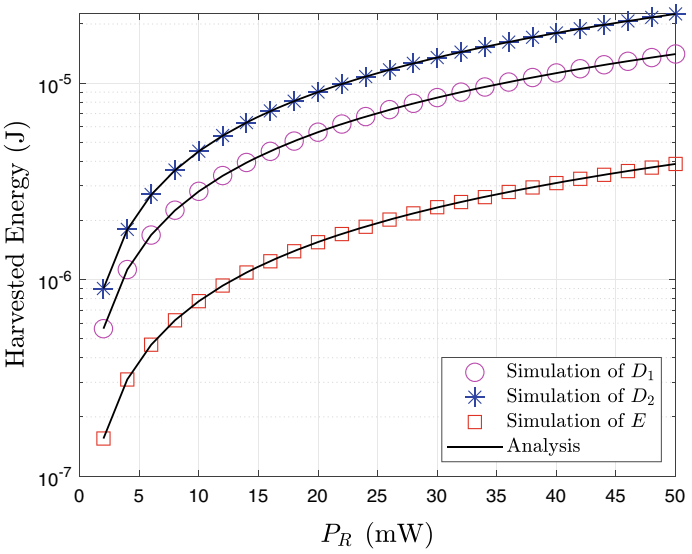

Fig. 4.16 Comparisons between the simulation and the analytical energy harvested with $T = 1s$, $\xi = 0.9$, $\alpha_{D_i} = \alpha_E = 0.5$, $L_{RD_1} = 20\,\text{m}$, $L_{RD_2} = 10\,\text{m}$, $L_{RE} = 50\,\text{m}$, and $H = 20\,\text{m}$

and M, H_R is the vertical height of R, L_{RM} is the horizontal distance between R and M, and η is the path loss exponent.

Since the linear EH mode[11] is of interest, the energy harvested at D_i and E can be expressed as

$$E_{RD_i} = \frac{\xi(1-\alpha_{D_i})P_R|h_{RD_i}|^2T/2}{d_{RD_i}^{\eta}} \tag{4.85}$$

and

$$E_{RE} = \frac{\xi(1-\alpha_E)P_R|h_{RE}|^2T/2}{d_{RE}^{\eta}}, \tag{4.86}$$

respectively, where ξ $(0 < \xi < 1)$ is the energy conversion efficiency and T is the transmission time. Figure 4.16 shows the comparisons between the simulation and the analytical energy harvested by users and the eavesdropper. It is observed that

[11] Noted from [25] that a practical EH model should be a sensitivity-based logistic model. With such a model, the harvested energy should be $E(P_M) = \{\frac{P_{\max}}{\exp(-\tau_0 P_0+\nu_0)}(\frac{1+\exp(-\tau_0 P_0+\nu_0)}{1+\exp(-\tau_0 P_M+\nu_0)} - 1)T/2\}^+$, where $P_M = \frac{(1-\alpha_M)P_R|h_{RM}|^2}{d_{RM}^{\eta}}$, $\{x\}^+ = \max\{x, 0\}$, P_0 is the harvester's sensitivity threshold, the parameters τ_0 and ν_0 control the steepness of the function $E(P_M)$, and $P_{\max}$ is the saturation threshold of the harvester.

more energy can be harvested at a higher transmit power value under the linear EH mode considered in this analysis.

Next, perfect SIC is performed at the near user, D_2, which first decodes and subtracts x_1 from the received signal and then decodes its information. Therefore, the received instantaneous SNR at D_2 is

$$\gamma_{RD_2} = \frac{\alpha_{D_2} a_2 \rho_2 |h_{RD_2}|^2}{(\alpha_{D_2} + \mu_2) d_{RD_2}^{\eta}} \tag{4.87}$$

while for the far user, D_1, it detects its own information directly by regarding x_2 as interference with the instantaneous SINR denoted as

$$\gamma_{RD_1} = \frac{\alpha_{D_1} a_1 \rho_1 |h_{RD_1}|^2}{(\alpha_{D_1} a_2 \rho_1 |h_{RD_1}|^2 + \alpha_{D_1} + \mu_1) d_{RD_1}^{\eta}}, \tag{4.88}$$

where $\rho_i = \frac{P_R}{N_{RD_i}}$ and $\mu_i = \frac{\delta_D^2}{N_{RD_i}}$.

Similar to [26, 27], the worst-case scenario is considered with the assumption that E has the largest decoding capability and parallel interference cancellation (PIC) is adopted, meaning it decodes x_1 (x_2) without considering the interference of x_2 (x_1). Therefore, the instantaneous SNR at E for decoding the signal of D_i is

$$\gamma_{E_i} = \frac{\alpha_E a_i \rho_e |h_{RE}|^2}{(\alpha_E + \mu_E) d_{RE}^{\eta}}, \tag{4.89}$$

where $\rho_e = \frac{P_R}{N_E}$ and $\mu_E = \frac{\delta_E^2}{N_E}$.

Since the terrestrial links are assumed to be with Nakagami-m fading, the PDF and CDF of h_{RM} can be expressed as [27]

$$f_{|h_{RM}|^2}(x) = \frac{\beta^m x^{m-1}}{\Gamma(m)} \exp(-\beta x) \tag{4.90}$$

and

$$F_{|h_{RM}|^2}(x) = 1 - \sum_{j=0}^{m-1} \frac{\beta^j x^j}{j!} \exp(-\beta x), \tag{4.91}$$

respectively, where $\beta = \frac{m}{\Omega}$, m is the fading parameter, Ω is the channel mean power, and $\Gamma(\cdot)$ is the gamma function.

From Eqs. (4.86), (4.87) and (4.90), the CDFs of γ_{RD_1} and γ_{RD_2} can be derived as

$$F_{\gamma_{RD_1}}(x) = \begin{cases} 1 - \sum\limits_{j_1=0}^{m_{D_1}-1} \dfrac{\beta_1^{j_1} C_1^{j_1} x^{j_1}}{j_1!(A_1 - A_2 x)^{j_1}} \exp\left(-\dfrac{\beta_1 C_1 x}{A_1 - A_2 x}\right), & \text{if } x < \dfrac{a_1}{a_2 d_{RD_1}^{\eta}}, \\ 1, & \text{else} \end{cases} \tag{4.92}$$

and

$$F_{\gamma_{RD_2}}(x) = 1 - \sum_{j_2=0}^{m_{D_2}-1} \frac{\beta_2^{j_2} C_2^{j_2} x^{j_2}}{j_2! B_1^{j_2}} \exp\left(-\frac{\beta_2 C_2 x}{B_1}\right), \tag{4.93}$$

respectively, where $A_1 = \alpha_{D_1} a_1 \rho_1$, $A_2 = \alpha_{D_1} a_2 \rho_1 d_{RD_1}^{\eta}$, $C_1 = (\alpha_{D_1} + \mu_1) d_{RD_1}^{\eta}$, $B_1 = \alpha_{D_2} a_2 \rho_2$, and $C_2 = (\alpha_{D_2} + \mu_2) d_{RD_2}^{\eta}$.

Next, Eqs. (4.88), (4.90) and (4.91), the CDF and PDF of γ_{E_i} can be derived as

$$\begin{aligned} F_{\gamma_{E_i}}(x) &= \Pr\left\{\gamma_{E_i} < x\right\} \\ &= F_{|h_{RE}|^2}\left(\frac{(\alpha_E + \mu_E) d_{RE}^{\eta} x}{\alpha_E a_i \rho_e}\right) \\ &= F_{|h_{RE}|^2}\left(\frac{T_e x}{U_i}\right) \end{aligned} \tag{4.94}$$

and

$$\begin{aligned} f_{\gamma_{E_i}}(x) &= \frac{T_e}{U_i} f_{|h_{RE}|^2}\left(\frac{T_e x}{U_i}\right) \\ &= \frac{\beta_e^{m_e} T_e^{m_e} x^{m_e - 1}}{\Gamma_{(m_e)} U_i^{m_e}} \exp\left(-\frac{\beta_e T_e x}{U_i}\right), \end{aligned} \tag{4.95}$$

respectively, where $T_e = (\alpha_E + \mu_E) d_{RE}^{\eta}$ and $U_i = \alpha_E a_i \rho_e$.

4.2.2 Secrecy Performance Analysis

In this section, we will present the derivations of SOP and the probability of SPSC for both users.

4.2.2.1 SOP and the Probability of SPSC at D_1

The instantaneous secrecy capacity (SC) of D_1 for the S-R and R-D_1 links are

$$C_{SR_1} = \frac{1}{2}\log_2(1+\gamma_{SR_1}) \tag{4.96}$$

and

$$C_{RD_1} = \left\{\frac{1}{2}[\log_2(1+\gamma_{RD_1}) - \log_2(1+\gamma_{E_1})]\right\}^+, \tag{4.97}$$

respectively, where $\{x\}^+ = \max\{x, 0\}$. From the capacity point of view, the relaying network adopting DF protocol is similar to a series system, which means that the worse hop dominates the system capacity [28]. Hence, the instantaneous SC of D_1 is

$$C_{D_1} = \min\{C_{SR_1}, C_{RD_1}\}. \tag{4.98}$$

SOP is a probability when the instantaneous SC is below a target capacity, C_{th_1}. Therefore, it has the SOP for D_1 as

$$\begin{aligned} P_{SOP}^{D_1} &= \Pr\{C_{D_1} < C_{th_1}\} \\ &= \Pr\{\min\left\{C_{SR_1}, C_{RD_1}\right\} < C_{th_1}\} \\ &= 1 - \Pr\{C_{SR_1} \geq C_{th_1}\}\Pr\{C_{RD_1} \geq C_{th_1}\} \\ &= 1 - \Pr\{\gamma_{SR_1} \geq \varepsilon_1 - 1\}\Pr\{\gamma_{RD_1} \geq \varepsilon_1(1+\gamma_{E_1}) - 1\} \\ &= 1 - M_1 M_2, \end{aligned} \tag{4.99}$$

where

$$\begin{aligned} M_1 &= 1 - \Pr\left\{\gamma_1 < \frac{\varepsilon_1 - 1}{a_1 - a_2\varepsilon_1 + a_2}\right\} \\ &= 1 - F_{\gamma_1}\left(\frac{\varepsilon_1 - 1}{a_1 - a_2\varepsilon_1 + a_2}\right) \\ &= \sum_{k=0}^{m_R-1}\sum_{p=0}^{k} \frac{\varsigma(1-m_R)_k(-\delta_R)^k(\varepsilon_1-1)^p}{p!k!\lambda^{k-p+1}\overline{\gamma}_1^{k+1}(a_1 - a_2\varepsilon_1 + a_2)^p} \exp\left(-\frac{\lambda(\varepsilon_1-1)}{a_1 - a_2\varepsilon_1 + a_2}\right), \end{aligned} \tag{4.100}$$

and

$$
\begin{aligned}
M_2 &= 1 - \left[\int_0^{t_1} f_{\gamma_{E_1}}(x) F_{\gamma_{RD_1}}(\varepsilon_1 + \varepsilon_1 x - 1) dx + \int_{t_1}^{\infty} f_{\gamma_{E_1}}(x) dx\right] \\
&= \int_0^{t_1} f_{\gamma_{E_1}}(x)\left[1 - F_{\gamma_{RD_1}}(\varepsilon_1 + \varepsilon_1 x - 1)\right] dx \\
&= \int_0^{t_1} \frac{\beta_e^{m_e} T_e^{m_e} x^{m_e - 1}}{\Gamma_{(m_e)} U_1^{m_e}} \exp\left(-\frac{\beta_e T_e x}{U_1}\right) \sum_{j_1=0}^{m_{D_1}-1} \frac{\beta_1^{j_1} C_1^{j_1} (\varepsilon_1 + \varepsilon_1 x - 1)^{j_1}}{j_1! [A_1 - A_2(\varepsilon_1 + \varepsilon_1 x - 1)]^{j_1}} \\
&\quad \times \exp\left(-\frac{\beta_1 C_1 (\varepsilon_1 + \varepsilon_1 x - 1)}{A_1 - A_2(\varepsilon_1 + \varepsilon_1 x - 1)}\right) dx, \qquad (4.101)
\end{aligned}
$$

in which $\varepsilon_1 = 2^{2C_{th_1}}$ and $t_1 = \frac{a_1}{a_2 d_{RD_1}^{\eta} \varepsilon_1} + \frac{1}{\varepsilon_1} - 1$.

Note that the closed-form expression of (4.101) is complicated to obtain. Therefore, the Gauss-Chebyshev quadrature method [29] is applied to get the approximate expression as

$$
\begin{aligned}
M_2 =& \frac{\beta_e^{m_e} T_e^{m_e}}{\Gamma_{(m_e)} U_1^{m_e}} \sum_{j_1=0}^{m_{D_1}-1} \frac{t_1 \pi}{2N_1} \frac{(\beta_1 C_1)^{j_1}}{j_1!} \sum_{n_1=1}^{N_1} \frac{(\varepsilon_1 + \varepsilon_1 \tau_1 - 1)^{j_1} \tau_1^{m_e - 1}}{[A_1 - A_2(\varepsilon_1 + \varepsilon_1 \tau_1 - 1)]^{j_1}} \\
&\times \exp\left(-\frac{\beta_1 C_1 (\varepsilon_1 + \varepsilon_1 \tau_1 - 1)}{A_1 - A_2(\varepsilon_1 + \varepsilon_1 \tau_1 - 1)}\right) \exp\left(-\frac{\beta_e T_e \tau_1}{U_1}\right) \sqrt{1 - \phi_1^2}, \qquad (4.102)
\end{aligned}
$$

in which $\phi_1 = \cos(\frac{2n_1 - 1}{2N_1}\pi)$, $\tau_1 = \frac{t_1 \phi_1 + t_1}{2}$, and N_1 is the number of the Gaussian-Chebyshev terms.

After that, substituting Eqs. (4.100) and (4.102), into Eq. (4.99), it has

$$
\begin{aligned}
P_{SOP}^{D_1} =& 1 - \sum_{k=0}^{m_R - 1} \sum_{p=0}^{k} \frac{\varsigma (1 - m_R)_k (-\delta_R)^k (\varepsilon_1 - 1)^p}{p! k! \lambda^{k-p+1} \overline{\gamma}_1^{k+1} (a_1 - a_2 \varepsilon_1 + a_2)^p} \\
&\times \exp\left(-\frac{\lambda(\varepsilon_1 - 1)}{a_1 - a_2 \varepsilon_1 + a_2}\right) \frac{\beta_e^{m_e} T_e^{m_e}}{\Gamma_{(m_e)} U_1^{m_e}} \sum_{j_1=0}^{m_{D_1}-1} \frac{t_1 \pi}{2N_1} \frac{(\beta_1 C_1)^{j_1}}{j_1!} \\
&\times \sum_{n_1=1}^{N_1} \frac{(\varepsilon_1 + \varepsilon_1 \tau_1 - 1)^{j_1} \tau_1^{m_e - 1}}{[A_1 - A_2(\varepsilon_1 + \varepsilon_1 \tau_1 - 1)]^{j_1}} \exp\left(-\frac{\beta_1 C_1 (\varepsilon_1 + \varepsilon_1 \tau_1 - 1)}{A_1 - A_2(\varepsilon_1 + \varepsilon_1 \tau_1 - 1)}\right) \\
&\times \exp\left(-\frac{\beta_e T_e \tau_1}{U_1}\right) \sqrt{1 - \phi_1^2}. \qquad (4.103)
\end{aligned}
$$

Next, the probability of SPSC is defined as a probability when the instantaneous SC is greater than zero. Therefore, it has the probability of SPSC for D_1 as

$$\begin{aligned} P_{SPSC}^{D_1} &= \Pr\{(C_{D_1} > 0)\} \\ &= \Pr\{\min\left(C_{SR_1}, C_{RD_1}\right) > 0\} \\ &= \Pr\{C_{SR_1} > 0\} \Pr\{C_{RD_1} > 0\}, \end{aligned} \tag{4.104}$$

where

$$\begin{aligned} \Pr\{C_{SR_1} > 0\} &= \Pr\left\{\frac{1}{2}\log_2(1+\gamma_{SR_1}) > 0\right\} \\ &= \Pr\{\gamma_{SR_1} > 0\} \\ &= 1, \end{aligned} \tag{4.105}$$

and

$$\begin{aligned} \Pr\{C_{RD_1} > 0\} &= \Pr\left\{\frac{1}{2}[\log_2(1+\gamma_{RD_1}) - \log_2(1+\gamma_{E_1})] > 0\right\} \\ &= 1 - \Pr\left\{\gamma_{RD_1} \le \gamma_{E_1}\right\} \\ &= 1 - \int_0^{\infty} F_{\gamma_{RD_1}}(x) f_{\gamma_{E_1}}(x) dx \\ &= \int_0^{t_1} f_{\gamma_{E_1}}(x)\left[1 - F_{\gamma_{RD_1}}(x)\right] dx \\ &= \frac{\beta_e^{m_e} T_e^{m_e}}{\Gamma_{(m_e)} U_1^{m_e}} \sum_{j_1=0}^{m_{D_1}-1} \frac{t_1 \pi}{2N_2} \frac{(\beta_1 C_1)^{j_1}}{j_1!} \sum_{n_2=1}^{N_2} \frac{\tau_2^{j_1+m_e-1}}{[A_1 - A_2\tau_2)]^{j_1}} \\ &\quad \times \exp\left(-\frac{\beta_1 C_1 \tau_2}{A_1 - A_2\tau_2} - \frac{\beta_e T_e \tau_2}{U_1}\right)\sqrt{1-\phi_2^2}, \end{aligned} \tag{4.106}$$

in which $\phi_2 = \cos(\frac{2n_2-1}{2N_2}\pi)$, $\tau_2 = \frac{t_1\phi_2+t_1}{2}$, and N_2 is the number of the Gaussian-Chebyshev terms.

4.2.2.2 SOP and the Probability of SPSC at D_2

The instantaneous SC for D_2 is

$$C_{D_2} = \min\left\{C_{SR_2}, C_{RD_2}\right\}, \tag{4.107}$$

with

$$C_{SR_2} = \frac{1}{2}\log_2(1+\gamma_{SR_2}), \tag{4.108}$$

and

$$C_{RD_2} = \left\{ \frac{1}{2} \left[\log_2(1+\gamma_{RD_2}) - \log_2(1+\gamma_{E_2}) \right] \right\}^+. \tag{4.109}$$

Therefore, it has the SOP of D_2 as

$$\begin{aligned} P_{SOP}^{D_2} &= \Pr\{C_{D_2} < C_{th_2}\} \\ &= \Pr\{\min\left\{C_{SR_2}, C_{RD_2}\right\} < C_{th_2}\} \\ &= 1 - \Pr\{C_{SR_2} \geq C_{th_2}\} \Pr\{C_{RD_2} \geq C_{th_2}\} \\ &= 1 - \Pr\{\gamma_{SR_2} \geq \varepsilon_2 - 1\} \Pr\{\gamma_{RD_2} \geq \varepsilon_2(1+\gamma_{E_2}) - 1\} \\ &= 1 - I_1 I_2, \end{aligned} \tag{4.110}$$

where

$$\begin{aligned} I_1 &= 1 - F_{\gamma_1}\left(\frac{\varepsilon_2 - 1}{a_2}\right) \\ &= \sum_{k=0}^{m_R-1} \sum_{p=0}^{k} \frac{\varsigma(1-m_R)_k(-\delta_R)^k(\varepsilon_2-1)^p}{p!k!\lambda^{k-p+1}\overline{\gamma}_1^{k+1}a_2^p} \exp\left(-\frac{\lambda(\varepsilon_2-1)}{a_2}\right), \end{aligned} \tag{4.111}$$

and

$$\begin{aligned} I_2 &= \int_0^\infty f_{\gamma_{E_2}}(x)\left[1 - F_{\gamma_{RD_2}}(\varepsilon_2(1+x)-1)\right]dx \\ &= \int_0^\infty \frac{\beta_e^{m_e} T_e^{m_e} x^{m_e-1}}{\Gamma_{(m_e)} U_2^{m_e}} \exp\left(-\frac{\beta_e T_e x}{U_2}\right) \sum_{j_2=0}^{m_{D_2}-1} \frac{\beta_2^{j_2} C_2^{j_2} (\varepsilon_2(1+x)-1)^{j_2}}{j_2! B_1^{j_2}} \\ &\times \exp\left(-\frac{\beta_2 C_2(\varepsilon_2(1+x)-1)}{B_1}\right) dx \\ &= \frac{\beta_e^{m_e} T_e^{m_e}}{\Gamma_{(m_e)} U_2^{m_e}} \exp\left(-\frac{\beta_2 C_2(\varepsilon_2-1)}{B_1}\right) \sum_{j_2=0}^{m_{D_2}-1} \frac{\beta_2^{j_2} C_2^{j_2}}{j_2! B_1^{j_2}} \\ &\times \sum_{q=0}^{j_2} \binom{j_2}{q} (\varepsilon_2-1)^{j_2-q} \varepsilon_2^q \frac{\Gamma_{(m_e+q)}}{[\frac{\beta_2 C_2 \varepsilon_2}{B_1} + \frac{\beta_e T_e}{U_2}]^{m_e+q}}, \end{aligned} \tag{4.112}$$

in which $\varepsilon_2 = 2^{2C_{th_2}}$.

After that, substituting Eqs. (4.111) and (4.112) into Eq. (4.110), it has

$$P_{SOP}^{D_2} = 1 - \left\{ \sum_{k=0}^{m_R-1} \sum_{p=0}^{k} \frac{\varsigma(1-m_R)_k(-\delta_R)^k(\varepsilon_2-1)^p}{p!k!\lambda^{k-p+1}\overline{\gamma}_1^{k+1}a_2^p} \exp\left(-\frac{\lambda(\varepsilon_2-1)}{a_2}\right) \right\}$$
$$\times \left\{ \frac{\beta_e^{m_e}T_e^{m_e}}{\Gamma_{(m_e)}U_2^{m_e}} \exp\left(-\frac{\beta_2 C_2(\varepsilon_2-1)}{B_1}\right) \sum_{j_2=0}^{m_{D_2}-1} \frac{\beta_2^{j_2}C_2^{j_2}}{j_2!B_1^{j_2}} \right.$$
$$\left. \times \sum_{q=0}^{j_2} \binom{j_2}{q} (\varepsilon_2-1)^{j_2-q}\varepsilon_2^q \frac{\Gamma_{(m_e+q)}}{\left[\frac{\beta_2 C_2\varepsilon_2}{B_1} + \frac{\beta_e T_e}{U_2}\right]^{m_e+q}} \right\}. \tag{4.113}$$

Next, we have the probability of SPSC for D_2 as

$$\begin{aligned} P_{SPSC}^{D_2} &= \Pr\{(C_{D_2} > 0)\} \\ &= \Pr\{\min\left\{C_{SR_2}, C_{RD_2}\right\} > 0\} \\ &= \Pr\{C_{SR_2} > 0\}\Pr\{C_{RD_2} > 0\}, \end{aligned} \tag{4.114}$$

where

$$\begin{aligned} \Pr\{C_{SR_2} > 0\} &= \Pr\left\{\frac{1}{2}\log_2(1+\gamma_{SR_2}) > 0\right\} \\ &= \Pr\{\gamma_{SR_2} > 0\} \\ &= 1 \end{aligned} \tag{4.115}$$

and

$$\begin{aligned} \Pr\{C_{RD_2} > 0\} &= 1 - \Pr\{\gamma_{RD_2} \le \gamma_{E_2}\} \\ &= 1 - \int_0^\infty F_{\gamma_{RD_2}}(x) f_{\gamma_{E_2}}(x) dx \\ &= \frac{\beta_e^{m_e}T_e^{m_e}}{\Gamma_{(m_e)}U_2^{m_e}} \sum_{j_2=0}^{m_{D_2}-1} \frac{\beta_2^{j_2}C_2^{j_2}}{j_2!B_1^{j_2}} \frac{\Gamma_{(m_e+j_2)}}{\left[\frac{\beta_2 C_2}{B_1} + \frac{\beta_e T_e}{U_2}\right]^{m_e+j_2}}. \end{aligned} \tag{4.116}$$

4.2.3 Performance Evaluation

4.2.3.1 Numerical Results and Discussions

This section will present and discuss the numerical results of both users. Following [21, 23], some commonly used system parameters and channel shadowing severities are illustrated in Tables 4.2 and 4.3. Unless otherwise specified, the channel of frequent heavy shadowing are used, and some other parameters are set as follows: $\overline{\gamma}_{SR}$

Table 4.2 System parameters [21]

Parameters	Value
Satellite orbit	GEO
Boltzmann constant	1.38×10^{-23} J/m
Frequency band	2 GHz
Maximum beam gain	48 dB
3dB angle	0.8°
Receive gain	4 dB
Link bandwidth	15 MHz
Noise temperature	300 K

Table 4.3 Satellite channel shadowing severities [23]

Shadowing	m_R	b	Ω_R
Frequent heavy shadowing (FHS)	1	0.063	8.94×10^{-4}
Average shadowing (AS)	10	0.126	0.835
Infrequent light shadowing (ILS)	19	0.158	1.29

= 20 dB, $\rho_e = 5$ dB, $a_1 = 0.8$, $a_2 = 0.2$, $\eta = 2$, $H_R = 50$ m, $L_{RD_1} = 80$ m, $L_{RD_2} = 60$ m, $L_{RE} = 150$ m, $m_{D_1} = m_{D_2} = m_e = 2$, $\Omega_{D_1} = \Omega_{D_2} = \Omega_e = 1$, $\alpha_{D_1} = \alpha_{D_2} = 0.7$, $\alpha_E = 0.5$, $\mu_i = \mu_E = 1$, $C_{th_1} = 0.0002$ bits/s/Hz, $C_{th_2} = 0.001$ bits/s/Hz, and $N_1 = N_2 = 30$.

As illustrated in Fig. 4.17, SOP versus ρ_1 for D_1 under various a_1 is presented. It is observed that the value of SOP keeps decreasing with the increase of ρ_1 until ρ_1 exceeds a particular value, i.e., $\rho_1 > 40$ dB. After that, the SOP value almost remains constant. This is because, in this case, the SOP performance of the system with a DF protocol is mainly dominated by the worse hop, i.e., the first hop. Furthermore, it is also observed that the secrecy performance of the higher a_1 is better than that of the lower one. This is because a higher a_1 indicates that more power will be allocated to D_1, which leads to better secrecy performance.

Figure 4.18 depicts the SOP performance of D_2 versus ρ_2 with different a_2. It is noticed that the secrecy performance improves as ρ_2 increases. However, we observe a flat area in this figure when $\rho_2 > 45$ dB at which the SOP performance remains unchanged. This is because the S-R link under such conditions controls the SOP performance. Moreover, it is also noticed that a higher a_2 leads to better secrecy performance for D_2.

Figures 4.19 and 4.20 present the effect of various UAV altitudes on SOP performance for D_1 and D_2, respectively. Observed from these two figures, one can find that the value of SOP increases with the increase of H_R. A higher H_R leads to a more significant path loss.

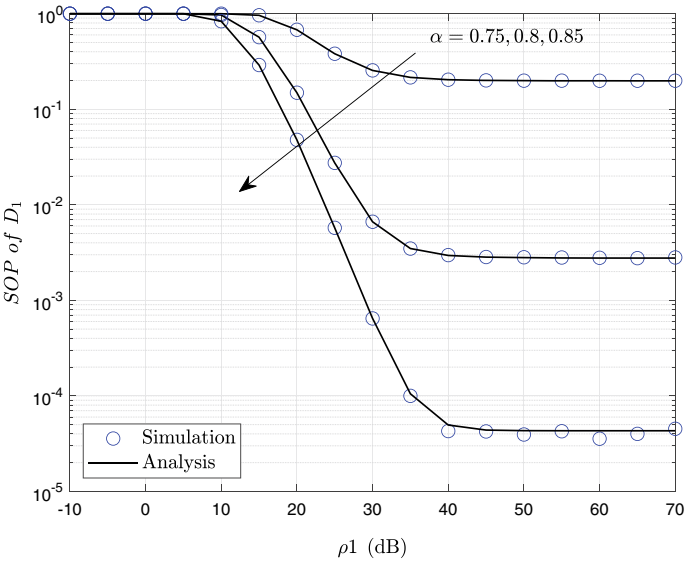

Fig. 4.17 SOP of D_1 versus ρ_1 under various a_1

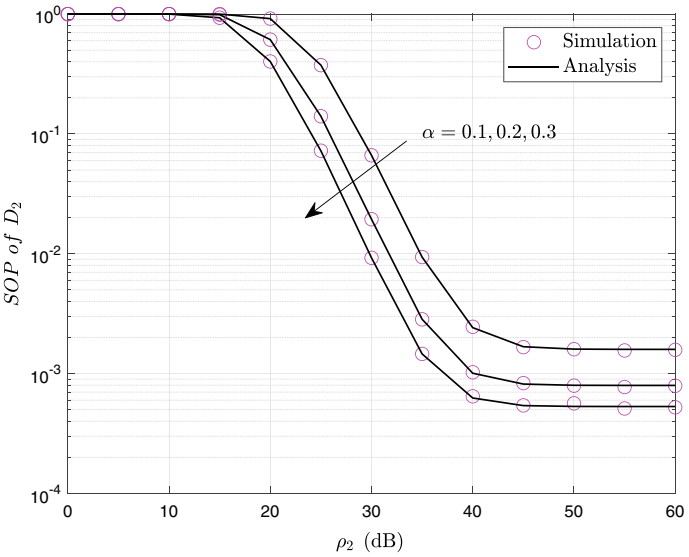

Fig. 4.18 SOP of D_2 versus ρ_2 under various a_2

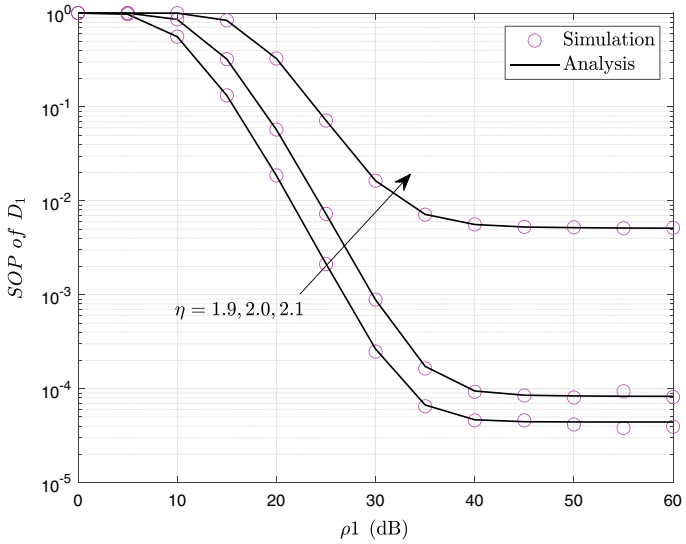

Fig. 4.19 SOP of D_1 versus ρ_1 under various UAV altitude

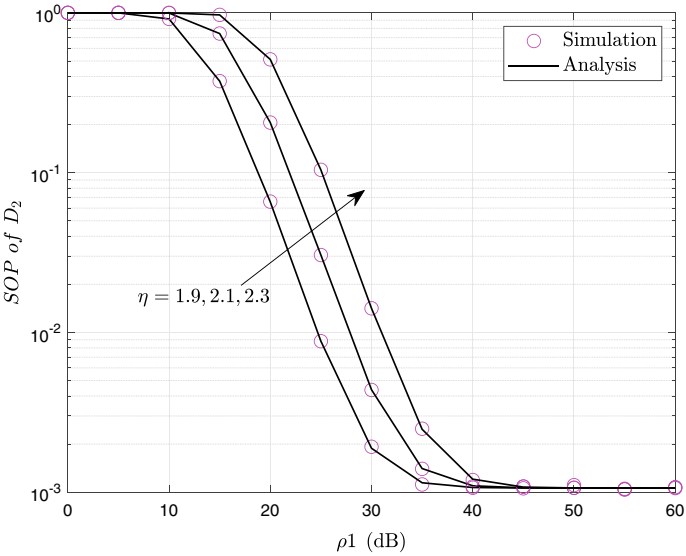

Fig. 4.20 SOP of D_2 versus ρ_2 under various UAV altitude

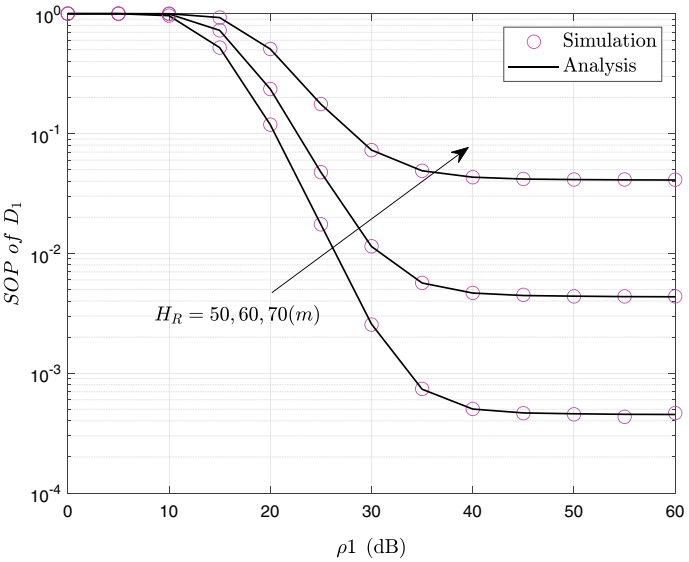

Fig. 4.21 SOP of D_1 versus ρ_1 under various η with a_1=0.85 and ρ_e=7 dB

Figures 4.21 and 4.22 plot the SOP versus ρ_1 and ρ_2 for D_1 and D_2 under various η. We can notice that the SOP performance decreases as η increases. This is because a larger value of η means more path loss, leading to worse SOP performance.

Figures 4.23 and 4.24 depict the SOP performance for D_1 and D_2 versus ρ_1 and ρ_2 under various α_{D_1}, α_{D_2} and α_E. One can observe that a higher value of α_{D_1} and α_{D_2} can result in better secrecy performance. This is because more power is used to decode information on the user side. In addition, we can also notice that the value of SOP increases with the increase of α_E. This is because the eavesdropper allocates more power to decode the wiretapping information.

Figures 4.25 and 4.26 show the three typical shadowing conditions of the satellite link on SOP performance for both users. One can see that ILS gives the best secrecy performance, and FHS can lead to the worst performance when $\overline{\gamma}_{SR}$ is in low-to-medium ranges, which means the secrecy performance of the system improves as the shadowing severity decreases.

As illustrated in Figs. 4.27 and 4.28, the probability of SPSC for D_1 and D_2 versus ρ_1 and ρ_2 under various ρ_e are presented. Observed from these two figures, one can find that the system performance improves when ρ_e decreases, as the *R*-D_1 and *R*-D_2 links becomes better than the *R*-*E* link.

Next, as a benchmark, we also compare the PS protocol with the TS one regarding the SOP performance in our proposed model, illustrated in Fig. 4.29. This figure shows that the PS protocol is superior to the TS one under the conditions considered, consistent with the results presented in [18, 20].

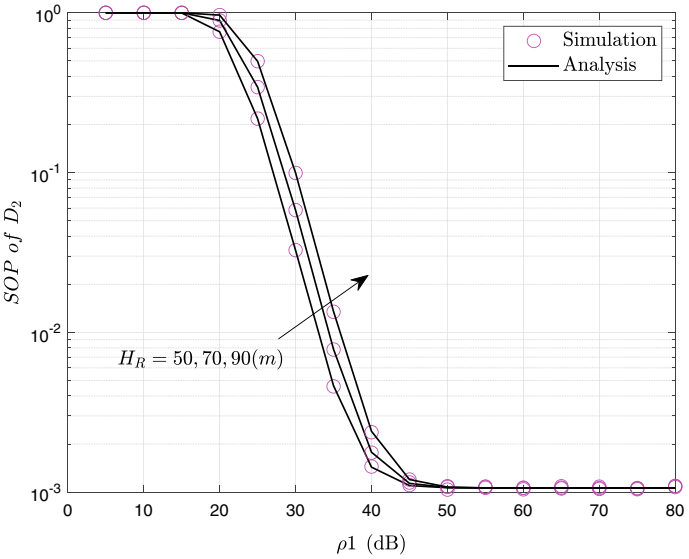

Fig. 4.22 SOP of D_2 versus ρ_2 under various η

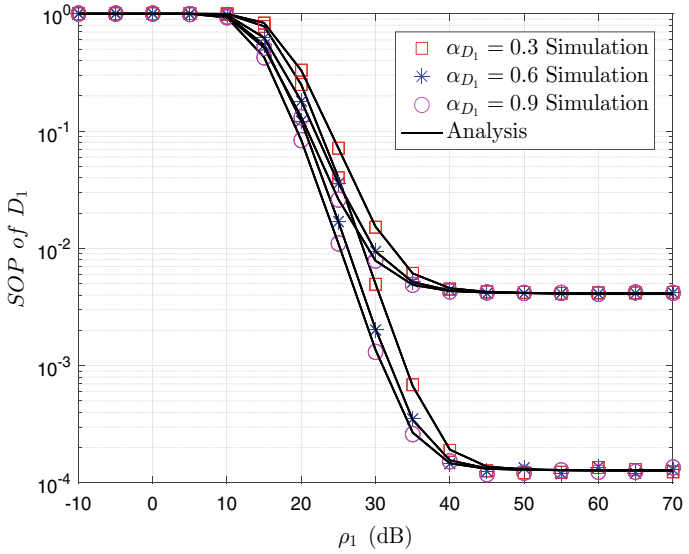

Fig. 4.23 SOP of D_1 versus ρ_1 under various α_{D_1} and α_E

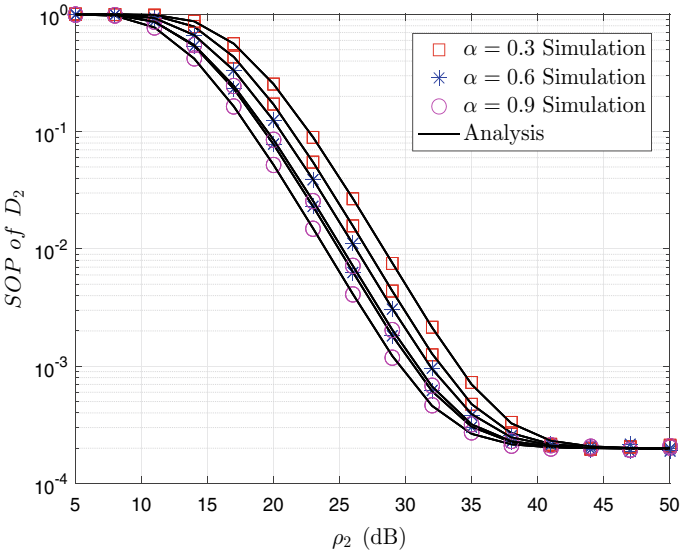

Fig. 4.24 SOP of D_2 versus ρ_2 under various α_{D_2} and α_E with $H_R = 20\,\text{m}$ and $L_{RE} = 60\,\text{m}$

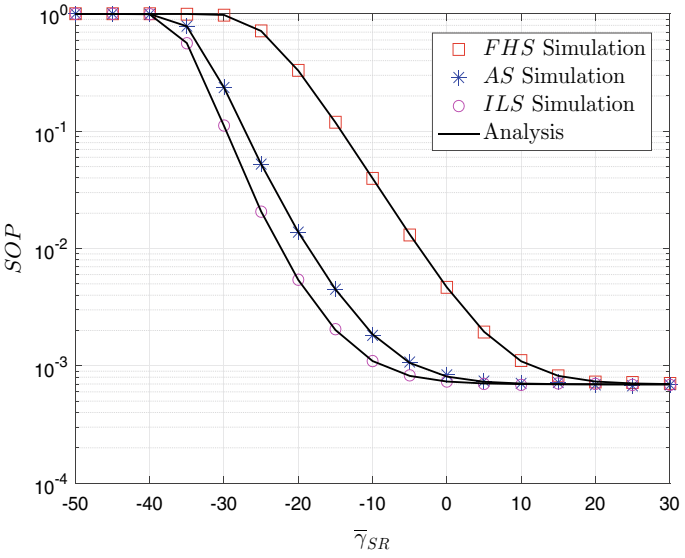

Fig. 4.25 SOP of D_1 versus $\overline{\gamma}_{SR}$ with ρ_1 = 35 dB and C_{th_1} = 0.0002 bits/s/Hz

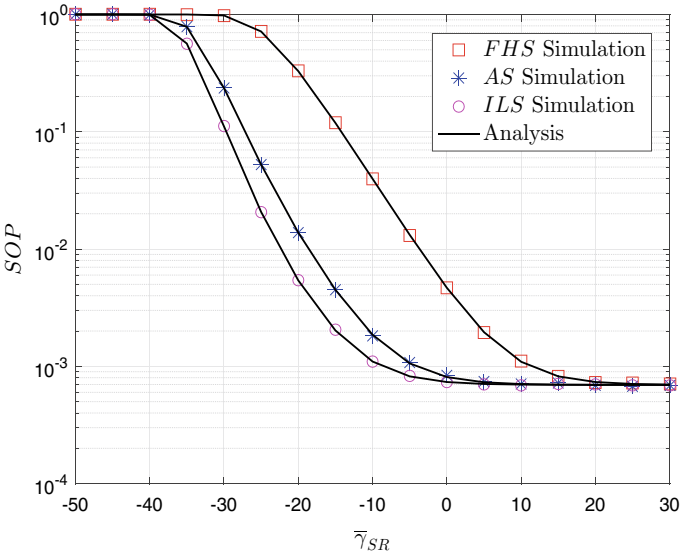

Fig. 4.26 SOP of D_2 versus $\overline{\gamma}_{SR}$ with ρ_2 = 35 dB and C_{th_2} = 0.0002 bits/s/Hz

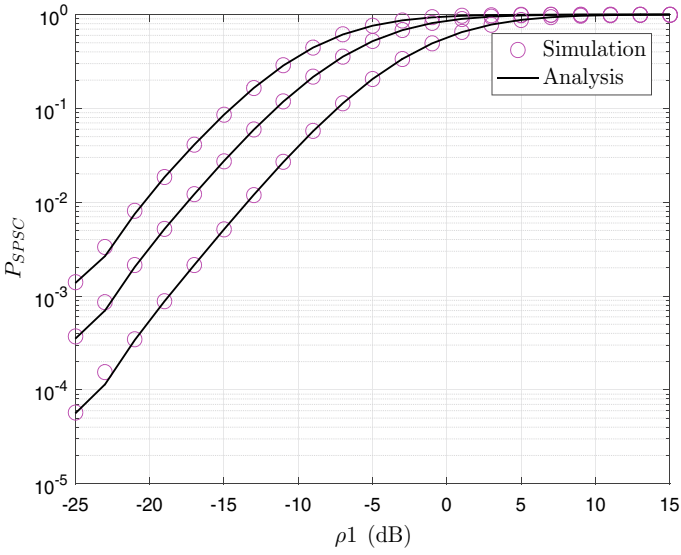

Fig. 4.27 Probability of SPSC for D_1 versus ρ_1 under various ρ_e

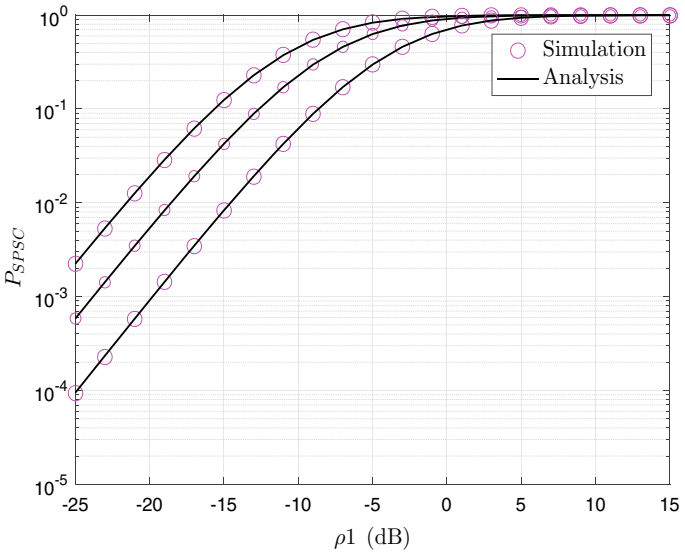

Fig. 4.28 Probability of SPSC for D_2 versus ρ_2 under various ρ_e

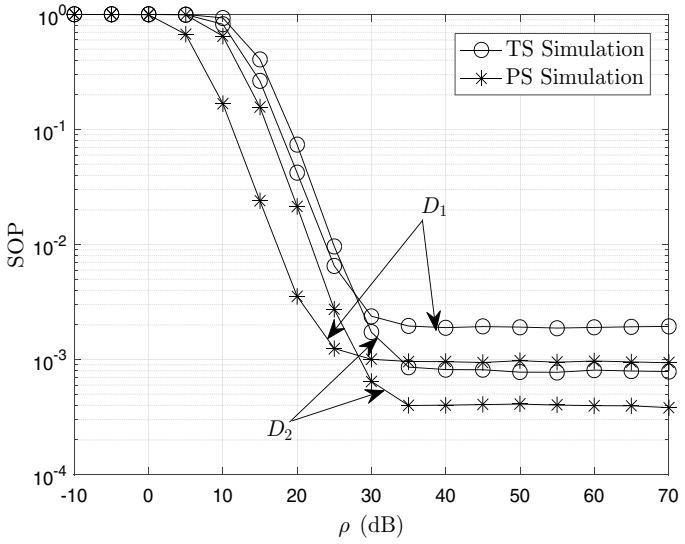

Fig. 4.29 Comparisons of the PS and TS protocols with a_1=0.6, $\rho_1 = \rho_2 = \rho$, $H = 30$ m, $L_{RD_1} = 45$ m, $L_{RD_2} = 20$ m, and a TS factor of 0.5

4.2.3.2 SOP for the UAV with a Constant Speed

This section presents the mobility of the UAV on the SOP performance. To simplify the analysis, we consider a simple scenario where the UAV flies horizontally along with the y-axis to the right with a constant speed v as shown in Fig. 4.30. Without loss of generality, it is assumed that the initial positions of R, D_i, and E in the three-dimensional (3D) coordinate axis are represented by (x_R, y_R, z_R), $(x_{D_i}, y_{D_i}, z_{D_i})$, and (x_E, y_E, z_E), respectively. Therefore, as the UAV is flying, the instantaneous coordinate of R is $(x_R, y_R + vt, z_R)$, in which t is the flight time. Next, it has the distance between R and D_i, E can be expressed as

$$d_{RD_i} = \sqrt{(x_R - x_{D_i})^2 + (y_R + vt - y_{D_i})^2 + (z_R - z_{D_i})^2} \tag{4.117}$$

and

$$d_{RE} = \sqrt{(x_R - x_E)^2 + (y_R + vt - y_E)^2 + (z_R - z_E)^2}. \tag{4.118}$$

The results are presented in Fig. 4.31. It is observed that the SOP performance for both users are first improved and then decreases as the UAV flies. This is because the UAV first approaches and then flies away from the users, which in turn makes the distance between the UAV and users decrease and then increase.

Finally, the Monte Carlo simulation results are consistent with the analysis results, which shows the accuracy of the derived analysis expression.

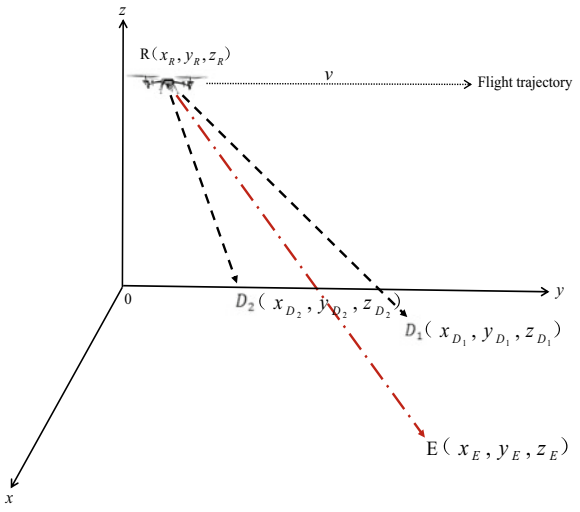

Fig. 4.30 The flying trajectory of the UAV with a constant speed of v

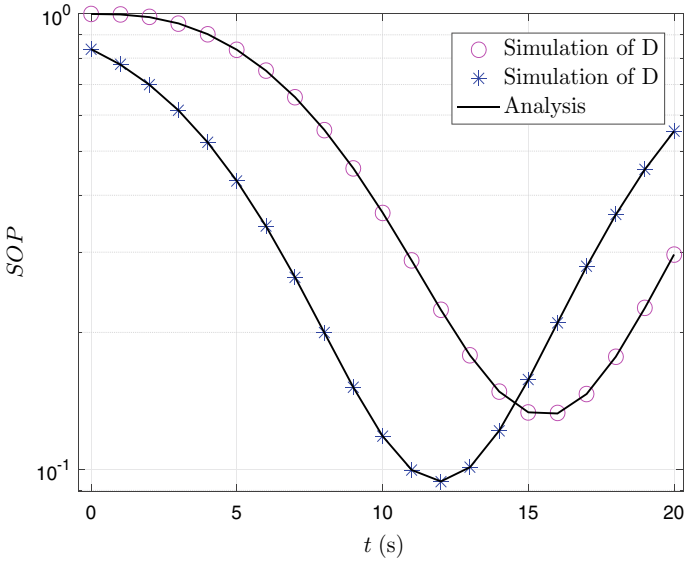

Fig. 4.31 SOP versus the trajectory of the UAV with $a_1 = 0.7$, $\rho_1 = \rho_2 = \rho_e = 15$ dB, initial coordinates of R(0,0,25), D_1(25,80,0), D_2(0,60,0), E(110,110,0) in meter, and $v = 5\text{m/s}$

4.2.4 Conclusion

In this section, we have investigated the secrecy performance of a UAV-assisted hybrid satellite-terrestrial SWIPT system based on NOMA, in which the satellite link experiences SR fading and the terrestrial links are subject to Nakagami-*m* fading distribution. Considering the influence of power allocation coefficients, the distance of the nodes, PS ratio, path loss, and shadowing severity levels, the analytical expressions of SOP and the probability of SPSC for both users have been derived. Numerical results indicate that the system performance increases significantly with the increasing of $\overline{\gamma}_{SR}$, ρ_1, and ρ_2 in the low-to-medium regimes. Furthermore, the results also indicate that it is better to properly adjust the power distribution coefficient and PS ratio to result in the best secrecy performance.

References

1. Y. Li, N.I. Miridakis, T.A. Tsiftsis, G. Yang, M. Xia, Air-to-Air communications beyond 5G: a novel 3D CoMP transmission scheme. IEEE Trans. Wireless Commun. **19**(11), 7324–7338 (2020)
2. S. Bachtobji, A. Omri, R. Bouallegue, K. Raoof, Modelling and performance analysis of mmWaves and radio-frequency based 3D heterogeneous networks. IET Commun. **12**(3), 290–296 (2018)

3. A. Omri, M.O. Hasna, Modeling and Performance analysis of D2D communications with interference management in 3-D HetNets, in *2016 IEEE Global Communications Conference (GLOBECOM)* (2016), pp. 1–7
4. M. Grover, P. Singh, P. Kaur, C. Madhu, Multibeam WDM-FSO system: an optimum solution for clear and hazy weather conditions. Wirel. Pers. Commun. **97**(4), 5783–5795 (2017)
5. R.A. Williamson, The Landsat legacy: remote sensing policy and the development of commercial remote sensing. Photogramm. Eng. Remote Sens. **63**(7), 877–885 (1997)
6. S.N. Chiu, D. Stoyan, W.S. Kendall, J. Mecke, *Stochastic Geometry and its Applications* (Wiley, New York, 2013)
7. S. Karp, R.M. Gagliardi, S.E. Moran, L.B. Stotts, *Optical Channels: Fibers, Clouds, Water and the Atmosphere* (Taylor & Francis, London, 1989)
8. E. Zedini, A. Kammoun, M. SAlouini, Performance of multibeam very high throughput satellite systems based on FSO feeder links with HPA nonlinearity. IEEE Trans. Wirel. Commun. **19**(9), 5908–5923 (2020)
9. A. Goldsmith, *Wireless Communications* (Cambridge University Press, Cambridge, 2005)
10. G. Pan, H. Lei, Z. Ding, Q. Ni, On 3-D hybrid VLC-RF systems with light energy harvesting and OMA scheme over RF links, in *2017 IEEE Global Communication Conference* (2017), pp. 1–6
11. I.S. Gradshteyn, I.M. Ryzhik, *Table of Integrals, Series, and Products* (Academic press, New York, 2014)
12. I.S. Ansari, F. Yilmaz, M.-S. Alouini, Performance analysis of FSO links over unified gamma-gamma turbulence channels, in *2015 IEEE 81st Vehicular Technology Conference (VTC Spring)* (2015), pp. 1–5
13. X. Lei, L. Fan, D.S. Michalopoulos, P. Fan, R.Q. Hu, Outage probability of TDBC protocol in multiuser two-way relay systems with Nakagami-m fading. IEEE Commun. Lett. **17**(3), 487–490 (2013)
14. A.M. Hunter, J.G. Andrews, S. Weber, Transmission capacity of ad hoc networks with spatial diversity. IEEE Trans. Wirel. Commun. **7**(12), 5058–5071 (2008)
15. Y. Ai, A. Mathur, M. Cheffena, M.R. Bhatnaga, H. Lei, Physical layer security of hybrid satellite-FSO cooperative systems. IEEE Photonics J. **11**(1), 1–14 (2019)
16. X. Liu, M. Lin, W.-P. Zhu, J.-Y. Wang, P.K. Upadhyay, Outage performance for mixed FSO-RF transmission in satellite-aerial-terrestrial networks. IEEE Photonics Technol. Lett. **32**(21), 1349–1352 (2020)
17. M.K. Simon, M.-S. Alouini, *Digital Communication over Fading Channels*, 2nd edn. (Wiley, New York, 2005)
18. H.Q. Tran, C.V. Phan, Q.T. Vien, Power splitting versus time switching based cooperative relaying protocols for SWIPT in NOMA systems. Phys. Commun. **41**, 101098 (2020) https://doi.org/10.1016/j.phycom.2020.101098
19. Z. Xu, S. Wang, D. Liu, Z. Wen, Joint beamforming and power-splitting optimization for SWIPT-enabled MISO full-duplex two-way cooperative NOMA systems. Phys. Commun. **45**, 101257 (2021). https://doi.org/10.1016/j.phycom.2020.101257
20. Y. Gu, S. Aissa, RF-based energy harvesting in decode-and-forward relaying systems: ergodic and outage capacities. IEEE Trans. Wirel. Commun. **14**(11), 6425–6434 (2025). https://doi.org/10.1109/TWC.2015.2453418
21. K. Guo, M. Lin, B. Zhang, J. Ouyang, W. Zhu, Secrecy performance of satellite wiretap channels with multi-user opportunistic scheduling. IEEE Wirel. Commun. Lett. **7**(6), 1054–1057 (2018). https://doi.org/10.1109/LWC.2018.2859385
22. S. Arzykulov, T.A. Tsiftsis, G. Nauryzbayev, M.M. Abdallah, G. Yang, Outage performance of underlay CR-NOMA networks with detect-and-forward relaying, in *2018 10th International Conference on Wireless Communications and Signal Processing (WCSP)* (2018), pp. 1–6
23. Y. Ai, A. Mathur, M. Cheffena, M.R. Bhatnagar, H. Lei, Physical layer security of hybrid satellite-FSO cooperative systems. IEEE Photonics J. **11**(1), 1–14 (2019). https://doi.org/10.1109/JPHOT.2019.2892618

24. S. Zhong, H. Huang, R. Li, Outage probability of power splitting SWIPT two-way relay networks in Fakagami-m fading. EURASIP Wirel. Commun. Netw. 1–8 (2018) https://doi.org/10.1186/s13638-017-1006-0
25. S. Wang, M. Xia, K. Huang, Y.-C. Wu, Wirelessly powered two-way communication with nonlinear energy harvesting model: rate regions under fixed and mobile relay. IEEE Trans. Wirel. Commun. **16**(12), 8190–8204 (2017). https://doi.org/10.1109/TWC.2017.2758767
26. Y. Zhang, H. Wang, Q. Yang, Z. Ding, Secrecy sumrate maximization in non-orthogonal multiple access. IEEE Commun. Lett. **20**, 930–933 (2016). https://doi.org/10.1109/LCOMM.2016.2539162
27. C. Yu, H. Ko, X. Peng, W. Xie, Secrecy outage performance analysis for cooperative NOMA over Nakagami-m channel. IEEE Access **7**, 79866–79876 (2019). https://doi.org/10.1109/ACCESS.2019.2923450
28. H. Lei, Z. Dai, I.S. Ansari, K. Park, G. Pan, M. Alouini, On secrecy performance of mixed RF-FSO systems. IEEE Photonics J. **9**, 1–14 (2017). https://doi.org/10.1109/JPHOT.2017.2723422
29. J. Zhang, X. Zheng, G. Pan, Y. Xie, On secrecy analysis of UAV-enabled relaying NOMA systems. Phys. Commun. **45**, 101263 (2021). https://doi.org/10.1016/j.phycom.2020.101263

Chapter 5
UAV Relay Communications

Xinyu Zheng, Jiliang Zhang, and Gaofeng Pan

5.1 On Secrecy Analysis of Underlay Cognitive UAV-Aided NOMA Systems with Transmit Antenna Selection/Maximal-Ratio Combining (TAS/MRC)

This section investigates the secrecy performance of a UAV-aided NOMA network in the context of underlay CR. Specifically, a multi-antenna secondary source (S) transmits a mixed signal incorporated with NOMA to two multi-antenna secondary destinations (D_i) via a UAV-enabled DF relay in the presence of an eavesdropper (E). In addition, both a transmit antenna selection scheme at S and a maximal ratio combining protocol at D_i and E are considered. Considering all the links undergo Nakagami-m fading with path loss, we analyze the secrecy performance in terms of SOP for both users. Moreover, we also use Monte Carlo simulations to verify those expressions.

The main contributions are as follows:

(1) We study the secrecy performance for an underlay CR UAV-aided NOMA system. The scenario of a TAS scheme at a secondary source, the MRC protocol at the destinations, and the parallel PIC at the eavesdropper are considered.
(2) The PDF and CDF of all links are first characterized when all the links experience both large-scale and small-scale fading. Then, utilizing those expressions, we derive both users' closed-form expressions of the SOP.
(3) We also investigate the impact of several parameters, i.e., the number of antennas, power distribution coefficient, the height of the UAV, and interference power threshold, on the secrecy performance.

X. Zheng · J. Zhang
Southwest University, Chongqing, China
e-mail: swuzhang@swu.edu.cn

G. Pan (✉)
Beijing Institute of Technology, Beijing, China
e-mail: gfpan@bit.edu.cn

G. Pan et al. (eds.), *UAV Communications: Modeling and Analyses*,
https://doi.org/10.1007/978-981-97-0383-8_5

(4) Finally, we analyze the effect of the hovering position of the UAV and the flight trajectory on the secrecy performance.

5.2 System and Channel Models

As shown in Fig. 5.1, an underlay CR UAV-aided NOMA system is considered in this analysis, which includes a L_S-antenna secondary source (S), a single antenna UAV-relay (R), two multi-antenna secondary destinations, i.e., a L_{D_1}-antenna far user (D_1) and a L_{D_2}-antenna near user (D_2), and a L_E-antenna eavesdropper (E). Note that the UAV is a relay in this system to link the information transmission from S to destinations.

Unlike the traditional ground relaying system, due to the advantage of mobility, it is easier and faster to deploy the UAV-enabled relaying system, especially in natural disasters. Furthermore, the LoS link is more likely to be established with the UAV-enabled relay [1, 2]. It is assumed that there is no direct link between S and both two users due to deep fading and/or obstacle blocking.

We also assume that E can only overhear the second hop, and this assumption is reasonable. In a practical scenario, it may be difficult for E to find a suitable position to wiretap both hops as the UAV is allocated in a proper deployment position to build reliable links to serve both users well. Therefore, from the eavesdropping point of view and to guarantee that it can overhear the information of both users, E may adopt a strategy to locate itself on the destination side. The symbol, $d_{Rg} = \sqrt{K_{Rg}^2 + H^2}$, is used to indicate the distance between nodes R and g, where $g \in \{S,\ D_i,\ E\}$, and H and K_{Rg} denote the vertical distance of node R to the ground and the horizontal

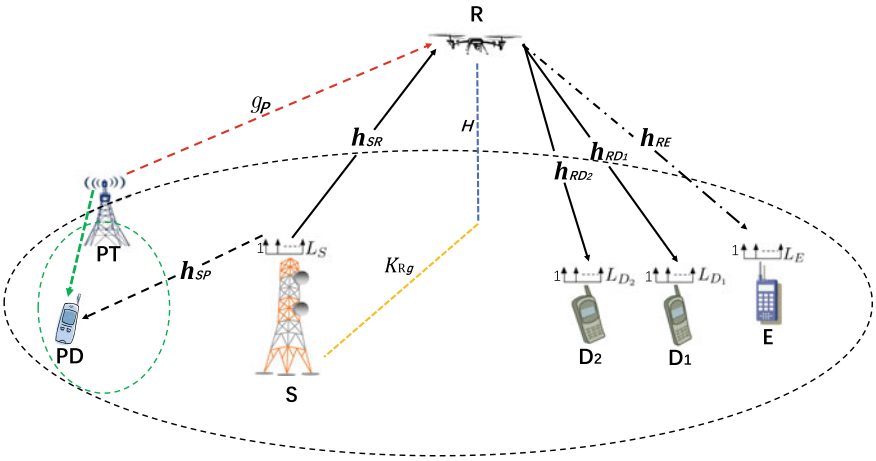

Fig. 5.1 System model

distance to node g, respectively. It is noted that the measured results from [3, 4] showed that in the suburban/open filed environment, the performance of the UAV communication system is significantly affected by path loss.

Moreover, according to the experimental results, the UAV channels in low-altitude applications can be more appropriately modeled as Nakagami-m distributions [5]. Therefore, all links are assumed to undergo Nakagami-m fading with a path loss, and h_{ab} ($a, b \in \{P,\ S,\ R,\ D_i,\ E\}$) is used to denote the channel coefficient between nodes a and b with a fading parameter m_{ab} and an average channel power gain $\Omega_{ab} = E\{|h_{ab}|^2\}$. Therefore, the channel power gains, $|h_{ab}|^2$, follows a gamma distribution with the PDF and CDF expressed as

$$f_{|h_{ab}|^2}(x) = \frac{\beta_{ab}^{m_{ab}} x^{m_{ab}-1}}{\Gamma(m_{ab})} \exp(-\beta_{ab} x) \tag{5.1}$$

and

$$F_{|h_{ab}|^2}(x) = 1 - \sum_{i=0}^{m_{ab}-1} \frac{\beta_{ab}^i x^i}{i!} \exp(-\beta_{ab} x), \tag{5.2}$$

where $\beta_{ab} = \frac{m_{ab}}{\Omega_{ab}}$ and $\Gamma(\cdot)$ is defined as gamma function shown by [6, Eq. (8.339.1)].

In the first time slot, S adopts the selected antenna after performing the TAS scheme to transmit a mixed signal $x_{SR} = \sum_{i=1}^{2} \sqrt{\alpha_i P_s} x_i$ to R under the underlay cognitive radio model, where α_i means the power allocation factor satisfying $\alpha_1 + \alpha_2 = 1$ and $\alpha_1 > \alpha_2$, and x_i means the signal of D_i with $\mathrm{E}|x_i|^2 = 1$. The transmit power of S is denoted as $P_s = \frac{I_{th}}{|h_{SP}|^2}$, where I_{th} is the interference threshold at the primary destination.

Similar to [7, 8], the interference signal from the primary transmitter is modeled as AWGN to simplify the theoretical analysis. Thus, the signal received by R is denoted as

$$y_{SR} = \frac{h_{SR}^{\max}}{\sqrt{d_{SR}^{\theta}}} x_{SR} + n_R + g_P, \tag{5.3}$$

where n_R is the zero mean AWGN with a variance of N_R, and g_P is the interference signal from PT, which is with $\mathcal{CN}(0, \eta N_R)$, and η is the scaling coefficient of g_P, $|h_{SR}^{\max}| = \max_{1 \le l_S \le L_S} \left| h_{SR}^{l_S} \right|$, with $h_{SR}^{l_S}$ means the channel coefficient between l_S-th antenna of S and R, and θ is the path loss exponent.

Similar to [9, 10], perfect SIC is employed in this analysis. Therefore, the far user's signal, x_1, is first decoded at R, and then x_1 is removed from the mixed signal before decoding x_2. Hence, it has the SNR and SINR for D_2 and D_1 at R as

$$\gamma_{SR}^{D_2} = \frac{\alpha_2 \rho_{SR} |h_{SR}^{\max}|^2}{(\eta + 1) d_{SR}^{\theta}} \tag{5.4}$$

and

$$\gamma_{SR}^{D_1} = \frac{\alpha_1 \rho_{SR} |h_{SR}^{\max}|^2}{\alpha_2 \rho_{SR} |h_{SR}^{max}|^2 + (\eta + 1) d_{SR}^{\theta}}, \tag{5.5}$$

respectively, where $\rho_{SR} = \frac{P_s}{N_R}$.

Next, the CDF of $|h_{SR}^{max}|^2$ can be obtained as

$$F_{|h_{SR}^{max}|^2}(x) = \left[1 - \sum_{i=0}^{m_{SR}-1} \frac{\beta_{SR}^i x^i}{i!} \exp(-\beta_{SR} x) \right]^{L_S}. \tag{5.6}$$

In the second time slot, the DF protocol, which eliminates the influence of the first hop on the second hop in the dual-hop communication, is adopted at R to process the received signal. Therefore, R first decodes the received signal and then forwards the re-encoded one to D_i in the presence of E. Hence, the received signals at l_{D_i}-th antenna of D_i and at l_E-th antenna of E can be written as

$$y_{RD_i}^{l_{D_i}} = \frac{h_{RD_i}^{l_{D_i}}}{\sqrt{d_{RD_i}^{\theta}}} x_{RD} + n_{D_i} \tag{5.7}$$

and

$$y_{RE}^{l_E} = \frac{h_{RE}^{l_E}}{\sqrt{d_{RE}^{\theta}}} x_{RD} + n_E, \tag{5.8}$$

respectively, where n_{D_i} and n_E are the zero mean AWGN with variances of N_{D_i} and N_E at D_i and E, and $x_{RD} = \sum_{i=1}^{2} \sqrt{\alpha_i P_R} x_i$, and P_R is the transmit power at R. Moreover, $h_{RD_i}^{l_{D_i}}$ and $h_{RE}^{l_E}$ denote the channel coefficients for the l_{D_i}-th antenna of the D_i and l_E-th antenna of E, respectively.

Next, D_i adopts the MRC scheme to process the received signals. Meanwhile, SIC is also performed. Specifically, the far user D_1 decodes its signal while treating D_2's signal as interference. While the near user, D_2, first decodes and subtracts D_1's signal and then processes its signal.

Therefore, it has the instantaneous SINR at D_1 and the SNR at D_2 as

$$\gamma_{RD_1} = \frac{\rho_{RD_1} \alpha_1 |h_{RD_1}|^2}{\alpha_2 \rho_{RD_1} |h_{RD_1}|^2 + d_{RD_1}^{\theta}} \tag{5.9}$$

and

$$\gamma_{RD_2} = \frac{\rho_{RD_2}\alpha_2|h_{RD_2}|^2}{d_{RD_2}^{\theta}}, \tag{5.10}$$

respectively, where $\rho_{RD_i} = \frac{P_R}{N_{D_i}}$ and $|h_{RD_i}|^2 = \sum_{l_{D_i}=1}^{L_{D_i}} |h_{RD_i}^{l_{D_i}}|^2$.

Making use of Eqs. (5.2), (5.9), and (5.10), the CDFs of γ_{RD_1} and γ_{RD_2} can be obtained as

$$F_{\gamma_{RD_1}}(x) = \begin{cases} 1 - \sum_{i=0}^{m_{RD_1}L_{D_1}-1} \frac{(d_{RD_1}^{\theta}\beta_{RD_1})^i x^i}{[\rho_{RD_1}(\alpha_1-\alpha_2 x)]^i i!} \exp\left(-\frac{\beta_{RD_1} d_{RD_1}^{\theta} x}{\rho_{RD_1}(\alpha_1-\alpha_2 x)}\right), & \text{if } x < \frac{\alpha_1}{\alpha_2}; \\ 1, & \text{else} \end{cases} \tag{5.11}$$

and

$$F_{\gamma_{RD_2}}(x) = 1 - \sum_{j=0}^{m_{RD_2}L_{D_2}-1} \frac{(\beta_{RD_2} d_{RD_2}^{\theta})^j x^j}{(\alpha_2\rho_{RD_2})^j j!} \exp\left(-\frac{\beta_{RD_2} d_{RD_2}^{\theta} x}{\alpha_2\rho_{RD_2}}\right), \tag{5.12}$$

respectively.

In addition, we conduct this analysis under the assumption that E has the largest decoding ability. Specifically, the MRC technique is applied at E to process the received signal. The PIC is also employed to decode the superimposed signals, i.e., the interference from x_1 (x_2) can be eliminated when decoding x_2 (x_1). Hence, the SNRs for the signals of D_1 and D_2 at E can be expressed as

$$\gamma_{RE}^{D_1} = \frac{\alpha_1\rho_{RE}|h_{RE}|^2}{d_{RE}^{\theta}} = \alpha_1\gamma_{RE} \tag{5.13}$$

and

$$\gamma_{RE}^{D_2} = \frac{\alpha_2\rho_{RE}|h_{RE}|^2}{d_{RE}^{\theta}} = \alpha_2\gamma_{RE}, \tag{5.14}$$

where $\rho_{RE} = \frac{P_R}{N_E}$, $|h_{RE}|^2 = \sum_{l_E=1}^{L_E} |h_{RE}^{l_E}|^2$, and $\gamma_{RE} = \frac{\rho_{RE}|h_{RE}|^2}{d_{RE}^{\theta}}$ with the PDF of γ_{RE} denoted as

$$f_{\gamma_{RE}}(x) = \frac{(\beta_{RE} d_{RE}^{\theta})^{m_{RE}L_E} x^{m_{RE}L_E-1}}{\rho_{RE}{}^{m_{RE}L_E}\Gamma(m_{RE}L_E)} \exp\left(-\frac{\beta_{RE} d_{RE}^{\theta} x}{\rho_{RE}}\right). \tag{5.15}$$

5.3 Secrecy Performance Analysis

In this section, the derivation of SOPs for two users is presented.

5.3.1 SOP Analysis

5.3.1.1 SOP of D_1

The instantaneous SC of D_1 for the two links can be expressed as

$$C_{SR}^{D_1} = \frac{1}{2}\log_2\left(1+\gamma_{SR}^{D_1}\right) \tag{5.16}$$

and

$$C_{RD_1} = \left\{\frac{1}{2}\log_2\frac{1+\gamma_{RD_1}}{1+\gamma_{RE}^{D_1}}\right\}^+, \tag{5.17}$$

where$\{x\}^+ = \max\{x, 0\}$.

The worst hop in the DF relaying system dominates the system capacity. Hence, the SC of D_1 as

$$C_{D_1} = \min\left\{C_{SR}^{D_1}, C_{RD_1}\right\}. \tag{5.18}$$

A secrecy outage occurs when the instantaneous SC exceeds the user's threshold requirement, C_{th_1}. Therefore, it has the SOP of D_1 as

$$\begin{aligned} P_{SOP}^{D_1} &= \Pr\left\{C_{D_1} < C_{th_1}\right\} \\ &= \Pr\left\{\min\left\{C_{SR}^{D_1}, C_{RD_1}\right\} < C_{th_1}\right\} \\ &= 1 - \Pr\left\{C_{SR}^{D_1} \geq C_{th_1}, C_{RD_1} \geq C_{th_1}\right\} \\ &= 1 - \Pr\left\{C_{SR}^{D_1} \geq C_{th_1}\right\}\Pr\left\{C_{RD_1} \geq C_{th_1}\right\} \\ &= 1 - \Pr\left\{\gamma_{SR}^{D_1} \geq C_{T_1} - 1\right\}\Pr\left\{\gamma_{RD_1} \geq C_{T_1}(1+\gamma_{RE}^{D_1}) - 1\right\}, \end{aligned} \tag{5.19}$$

where $C_{T_1} = 2^{2C_{th_1}}$.

Based on Eqs. (5.1), (5.5), and (5.6), we have

$$\begin{aligned}\Pr\left\{\gamma_{SR}^{D_1} \geq C_{T_1} - 1\right\} &= \Pr\left\{|h_{SR}^{\max}|^2 \geq \gamma_{th_1}|h_{SP}|^2\right\} \\ &= \int_0^\infty \left[1 - F_{|h_{SR}^{\max}|^2}(\gamma_{th_1}x)\right] f_{|h_{SP}|^2}(x)dx \\ &= 1 - \int_0^\infty \frac{\beta_{SP}^{m_{SP}} x^{m_{SP}-1}}{\Gamma(m_{SP})} \exp(-\beta_{SP}x) \\ &\quad \times \underbrace{\left[1 - \exp(-\beta_{SR}\gamma_{th_1}x) \sum_{i=0}^{m_{SR}-1} \frac{(\beta_{SR}\gamma_{th_1}x)^i}{i!}\right]^{L_S}}_{J} dx,\end{aligned} \tag{5.20}$$

where $\gamma_{th_1} = \frac{(C_{T_1}-1)(\eta+1)d_{SR}^{\theta}}{\rho_I(\alpha_1-\alpha_2(C_{T_1}-1))}$ and $\rho_I = \frac{I_{th}}{N_R}$.

Applying the binomial theorem to the term, J, in Eq. (5.20), it has

$$\begin{aligned}J &= \sum_{k=0}^{L_S} \binom{L_S}{k} (-1)^k \exp(-k\beta_{SR}\gamma_{th_1}x) \left[\sum_{i=0}^{m_{SR}-1} \frac{(\beta_{SR}\gamma_{th_1}x)^i}{i!}\right]^k \\ &= \sum_{k=0}^{L_S} \binom{L_S}{k} (-1)^k \exp(-k\beta_{SR}\gamma_{th_1}x) \prod_{i=0}^{m_{SR}-2} \left(\frac{(\beta_{SR}\gamma_{th_1})^i}{i!}\right)^{k_{i+1}} \\ &\quad \times \sum_{k_1=0}^{k} \sum_{k_2=0}^{k-k_1} \cdots \sum_{k_{m_{SR}-1}=0}^{k-k_1-\cdots-k_{m_{SR}-2}} \binom{k}{k_1}\binom{k-k_1}{k_2}\cdots\binom{k-k_1-\cdots-k_{m_{SR}-2}}{k_{m_{SR}}-1} \\ &\quad \times \left(\frac{(\beta_{SR}\gamma_{th_1})^{m_{SR}-1}}{(m_{SR}-1)!}\right)^{k-k_1-\cdots-k_{m_{SR}-1}} x^{\Theta},\end{aligned} \tag{5.21}$$

where $\Theta = (m_{SR}-1)(k-k_1) - (m_{SR}-2)k_2 - \cdots - 2k_{m_{SR}-2} - k_{m_{SR}-1}$.

Defining

$$\Phi = \sum_{k_1=0}^{k} \sum_{k_2=0}^{k-k_1} \cdots \sum_{k_{m_{SR}-1}=0}^{k-k_1-\cdots-k_{m_{SR}-2}} \binom{k}{k_1}\binom{k-k_1}{k_2}\cdots\binom{k-k_1-\cdots-k_{m_{SR}-2}}{k_{m_{SR}}-1}, \tag{5.22}$$

$$\Psi_1 = \left(\frac{(\beta_{SR}\gamma_{th_1})^{m_{SR}-1}}{(m_{SR}-1)!}\right)^{k-k_1-\cdots-k_{m_{SR}-1}} \prod_{i=0}^{m_{SR}-2} \left(\frac{(\beta_{SR}\gamma_{th_1})^i}{i!}\right)^{k_{i+1}}, \tag{5.23}$$

and substituting Eq. (5.21) into Eq. (5.20), we have

$$\begin{aligned}\Pr\left\{\gamma_{SR}^{D_1} \geq C_{T_1} - 1\right\} &= 1 - \int_0^{\infty} \sum_{k=0}^{L_S} \binom{L_S}{k} (-1)^k \exp(-k\beta_{SR}\gamma_{th_1} x) \Phi \Psi_1 x^{\Theta} \\ &\quad \times \frac{\beta_{SP}^{m_{SP}} x^{m_{SP}-1}}{\Gamma(m_{SP})} \exp(-\beta_{SP} x) dx \\ &= 1 - \sum_{k=0}^{L_S} \binom{L_S}{k} (-1)^k \Phi \Psi_1 \frac{\beta_{SP}^{m_{SP}}}{\Gamma(m_{SP})} \\ &\quad \times \int_0^{\infty} x^{\Theta + m_{SP} - 1} \exp\left[-(k\beta_{SR}\gamma_{th_1} + \beta_{SP}) x\right] dx \\ &= 1 - \sum_{k=0}^{L_S} \binom{L_S}{k} (-1)^k \Phi \Psi_1 \frac{\beta_{SP}^{m_{SP}}}{\Gamma(m_{SP})} (\Theta + m_{SP} - 1)! \\ &\quad \times (k\beta_{SR}\gamma_{th_1} + \beta_{SP})^{-\Theta - m_{SP}}.\end{aligned} \tag{5.24}$$

Based on Eqs. (5.11), and (5.15), it has

$$\begin{aligned}\Pr\left\{\gamma_{RD_1} \geq C_{T_1}(1 + \gamma_{RE}^{D_1}) - 1\right\} &= 1 - \left[\int_0^t F_{\gamma_{RD_1}}(C_{T_1}(1 + \alpha_1 x) - 1) f_{\gamma_{RE}}(x) dx \right. \\ &\quad \left. + \int_t^{\infty} f_{\gamma_{RE}}(x) dx\right] \\ &= \int_0^t \left[1 - F_{\gamma_{RD_1}}(C_{T_1}(1 + \alpha_1 x) - 1)\right] f_{\gamma_{RE}}(x)\, dx \\ &= \int_0^t \exp\left[-\frac{\beta_{RD_1} d_{RD_1}^{\theta}(C_{T_1} - 1 + C_{T_1}\alpha_1 x)}{\rho_{RD_1}(\alpha_1 - \alpha_2(C_{T_1} - 1 + C_{T_1}\alpha_1 x))}\right] \\ &\quad \cdot \sum_{j=0}^{m_{RD_1} L_{D_1} - 1} \frac{\beta_{RD_1}^j (d_{RD_1}^{\theta})^j (C_{T_1} - 1 + C_{T_1}\alpha_1 x)^j}{j!(\rho_{RD_1}(\alpha_1 - \alpha_2(C_{T_1} - 1 + C_{T_1}\alpha_1 x)))^j} \\ &\quad \cdot \frac{(\beta_{RE} d_{RE}^{\theta})^{m_{RE} L_E} x^{m_{RE} L_E - 1}}{\rho_{RE}^{m_{RE} L_E} \Gamma(m_{RE} L_E)} \exp\left(-\frac{\beta_{RE} d_{RE}^{\theta} x}{\rho_{RE}}\right) dx,\end{aligned} \tag{5.25}$$

where $t = \frac{\frac{\alpha_1}{\alpha_2} + 1 - C_{T_1}}{\alpha_1 C_{T_1}}$.

Since the closed-form expression for Eq. (5.25) is difficult to obtain, the Gaussian Chebyshev quadrature [6] is applied to obtain an approximated expression as

$$\Pr\left\{\gamma_{RD_1} \geq C_{T_1}(1+\gamma_{RE}^{D_1})-1\right\} = \frac{(\beta_{RE} d_{RE}^{\theta})^{\mu_{RE}}}{\rho_{RE}^{\mu_{RE}}\Gamma(\mu_{RE})} \sum_{j=0}^{\mu_{RD_1}-1} \frac{(\beta_{RD_1} d_{RD_1}^{\theta})^{j}}{j!} \frac{t}{2}\frac{\pi}{N}$$
$$\cdot \sum_{n=1}^{N} \frac{(C_{T_1}-1+C_{T_1}\alpha_1\tau)^{j}}{\left[\rho_{RD_1}(\alpha_1-\alpha_2(C_{T_1}+C_{T_1}\alpha_1\tau-1))\right]^{j}}$$
$$\cdot \exp\left[\frac{(1-C_{T_1}-C_{T_1}\alpha_1\tau)\beta_{RD_1} d_{RD_1}^{\theta}}{\rho_{RD_1}(\alpha_1-\alpha_2(C_{T_1}+C_{T_1}\alpha_1\tau-1))}\right]$$
$$\cdot \exp\left(-\frac{\beta_{RE} d_{RE}^{\theta}}{\rho_{RE}}\tau\right)\tau^{\mu_{RE}-1}\sqrt{1-\phi^2}, \tag{5.26}$$

where N is a factor of the Gaussian-Chebyshev term, and $\phi = \cos(\frac{2n-1}{2N}\pi)$, $\tau = \frac{t}{2}(\phi+1)$, $\mu_{RD_i} = m_{RD_i} L_{D_i}$, $\mu_{RE} = m_{RE} L_E$.

Applying Eqs. (5.21), and (5.25), we express the analytical expression of SOP for D_1 as

$$P_{SOP}^{D_1} = 1 - \left[1 - \sum_{k=0}^{L_S}\binom{L_S}{k}(-1)^k \Phi\Psi_1 \frac{\beta_{SP}^{m_{SP}}}{\Gamma(m_{SP})}(\Theta+m_{SP}-1)!\right.$$
$$\left.\times (k\beta_{SR}\gamma_{th_1}+\beta_{SP})^{-\Theta-m_{SP}}\right] \frac{(\beta_{RE} d_{RE}^{\theta})^{\mu_{RE}}}{\rho_{RE}^{\mu_{RE}}\Gamma(\mu_{RE})} \sum_{j=0}^{\mu_{RD_1}-1} \frac{(\beta_{RD_1} d_{RD_1}^{\theta})^{j}}{j!}$$
$$\times \frac{t}{2}\frac{\pi}{N}\sum_{n=1}^{N} \frac{(C_{T_1}-1+C_{T_1}\alpha_1\tau)^{j}}{\left[\rho_{RD_1}(\alpha_1-\alpha_2(C_{T_1}+C_{T_1}\alpha_1\tau-1))\right]^{j}}$$
$$\times \exp\left[\frac{(1-C_{T_1}-C_{T_1}\alpha_1\tau)\beta_{RD_1} d_{RD_1}^{\theta}}{\rho_{RD_1}(\alpha_1-\alpha_2(C_{T_1}+C_{T_1}\alpha_1\tau-1))}\right]$$
$$\times \exp\left(-\frac{\beta_{RE} d_{RE}^{\theta}}{\rho_{RE}}\tau\right)\tau^{\mu_{RE}-1}\sqrt{1-\phi^2}. \tag{5.27}$$

5.3.1.2 SOP of D_2

The instantaneous SC for D_2 is

$$C_{D_2} = \min\left\{C_{SR}^{D_2}, C_{RD_2}\right\}, \tag{5.28}$$

where

$$C_{SR}^{D_2} = \frac{1}{2}\log_2\left(1+\gamma_{SR}^{D_2}\right) \tag{5.29}$$

and

$$C_{RD_2} = \left\{ \frac{1}{2}\log_2 \frac{\left(1+\gamma_{RD_2}\right)}{\left(1+\gamma_{RE}^{D_2}\right)} \right\}^+. \tag{5.30}$$

Next, the SOP of D_2 is expressed as

$$\begin{aligned} P_{SOP}^{D_2} &= \Pr\left\{C_{D_2} < C_{th_2}\right\} \\ &= \Pr\left\{\min(C_{SR}^{D_2}, C_{RD_2}) < C_{th_2}\right\} \\ &= 1 - \Pr\left\{C_{SR}^{D_2} \geq C_{th_2}, C_{RD_2} \geq C_{th_2}\right\} \\ &= 1 - \Pr\left\{C_{SR}^{D_2} \geq C_{th_2}\right\} \Pr\left\{C_{RD_2} \geq C_{th_2}\right\} \\ &= 1 - \Pr\left\{\gamma_{SR}^{D_2} \geq C_{T_2} - 1\right\} \Pr\left\{\gamma_{RD_2} \geq C_{T_2}(1+\gamma_{RE}^{D_2}) - 1\right\}, \end{aligned} \tag{5.31}$$

where $C_{T_2} = 2^{2C_{th_2}}$ and C_{th_2} is the capacity threshold of D_2.

From Eqs. (5.1), (5.4), and (5.6), we have

$$\begin{aligned} \Pr\left\{\gamma_{SR}^{D_2} \geq C_{T_2} - 1\right\} &= \Pr\left\{|h_{SR}^{max}|^2 \geq \gamma_{th_2}|h_{SP}|^2\right\} \\ &= \int_0^\infty \left[1 - F_{|h_{SR}^{max}|^2}(\gamma_{th_2} x)\right] f_{|h_{SP}|^2}(x) dx \\ &= 1 - \sum_{k=0}^{L_S} \binom{L_S}{k} (-1)^k \Phi \Psi_2 \frac{\beta_{SP}^{m_{SP}}}{\Gamma(m_{SP})} (\Theta + m_{SP} - 1)! \\ &\quad \times (k\beta_{SR}\gamma_{th_2} + \beta_{SP})^{-\Theta - m_{SP}}, \end{aligned} \tag{5.32}$$

where $\Psi_2 = \prod_{i=0}^{m_{SR}-2} \left(\frac{(\beta_{SR}\gamma_{th_2})^i}{i!}\right)^{k_{i+1}} \left(\frac{(\beta_{SR}\gamma_{th_2})^{m_{SR}-1}}{(m_{SR}-1)!}\right)^{k-k_1-\cdots-k_{m_{SR}-1}}$ and $\gamma_{th_2} = \frac{(C_{T_2}-1)(\eta+1)d_{SR}^{\theta}}{\rho_I \alpha_2}$.

After that, from Eqs. (5.12) and (5.15), and (3.326.2) in [6], it has

$$\begin{aligned}\Pr\left\{\gamma_{RD_2} \geq C_{T_2}(1+\gamma_{RE}^{D_2})-1\right\} &= \int_0^{\infty}\left[1-F_{\gamma_{RD_2}}(C_{T_2}(1+\alpha_2 x)-1)\right] f_{\gamma_{RE}}(x)\,dx \\ &= \int_0^{\infty}\sum_{j=0}^{\mu_{RD_2}-1}\frac{(\beta_{RD_2}d_{RD_2}^{\theta})^j (C_{T_2}-1+C_{T_2}\alpha_2 x)^j}{(\alpha_2\rho_{RD_2})^j\, j!} \\ &\quad \cdot \exp\left(-\frac{\beta_{RD_2}d_{RD_2}^{\theta}(C_{T_2}-1+C_{T_2}\alpha_2 x)}{\alpha_2\rho_{RD_2}}\right) \\ &\quad \cdot \frac{\beta_{RE}^{\mu_{RE}}(d_{RE}^{\theta})^{\mu_{RE}} x^{\mu_{RE}-1}}{\rho_{RE}^{\mu_{RE}}\Gamma(\mu_{RE})}\exp\left(-\frac{\beta_{RE}d_{RE}^{\theta}x}{\rho_{RE}}\right)dx \\ &= \frac{(\beta_{RE}d_{RE}^{\theta})^{\mu_{RE}}}{\rho_{RE}^{\mu_{RE}}\Gamma(\mu_{RE})}\exp\left(-\frac{\beta_{RD_2}d_{RD_2}^{\theta}(C_{T_2}-1)}{\alpha_2\rho_{RD_2}}\right) \\ &\quad \cdot \sum_{j=0}^{\mu_{RD_2}-1}\frac{(\beta_{RD_2}d_{RD_2}^{\theta})^j}{(\alpha_2\rho_{RD_2})^j\, j!}\sum_{q=0}^{j}\binom{j}{q}(C_{T_2}-1)^{j-q} \\ &\quad \times (C_{T_2}\alpha_2)^q \frac{\Gamma(\mu_{RE}+q)}{\left(\beta_{RD_2}d_{RD_2}^{\theta}\frac{C_{T_2}}{\rho_{RD_2}}+\frac{\beta_{RE}d_{RE}^{\theta}}{\rho_{RE}}\right)^{\mu_{RE}+q}}.\end{aligned} \tag{5.33}$$

Finally, from Eqs. (5.31) and (5.32), the SOP of D_2 can be derived as

$$\begin{aligned}P_{SOP}^{D_2} &= 1-\left(1-\sum_{k=0}^{L_S}\binom{L_S}{k}(-1)^k \Phi\Psi_2\frac{\beta_{SP}^{m_{SP}}}{\Gamma(m_{SP})}(\Theta+m_{SP}-1)!\right. \\ &\quad \left.\times (k\beta_{SR}\gamma_{th_2}+\beta_{SP})^{-\Theta-m_{SP}}\right)\frac{(\beta_{RE}d_{RE}^{\theta})^{\mu_{RE}}}{\rho_{RE}^{\mu_{RE}}\Gamma(\mu_{RE})} \\ &\quad \times \exp\left(-\frac{\beta_{RD_2}d_{RD_2}^{\theta}(C_{T_2}-1)}{\alpha_2\rho_{RD_2}}\right)\sum_{j=0}^{\mu_{RD_2}-1}\frac{(\beta_{RD_2}d_{RD_2}^{\theta})^j}{(\alpha_2\rho_{RD_2})^j\, j!}\sum_{q=0}^{j}\binom{j}{q} \\ &\quad \times (C_{T_2}-1)^{j-q}(C_{T_2}\alpha_2)^q\frac{\Gamma(\mu_{RE}+q)}{\left(\beta_{RD_2}d_{RD_2}^{\theta}\frac{C_{T_2}}{\rho_{RD_2}}+\frac{\beta_{RE}d_{RE}^{\theta}}{\rho_{RE}}\right)^{\mu_{RE}+q}}.\end{aligned} \tag{5.34}$$

5.3.2 *Asymptotic Analysis*

To enhance the study, a theoretical insight in terms of asymptotic analysis for both users is provided in this section to show the significance of the analytical results in the high SNR regimes, revealing the system's performance limits.

For D_1, let $\rho_I \to \infty$ (i.e.,$\gamma_{th_1} \to 0$), while ρ_{RD_1} keeps fixed and finite, it has $\lim_{\gamma_{th_1}\to 0} \exp(-k\beta_{SR}\gamma_{th_1}x) = 1$. Therefore, the asymptotic expression can be obtained as

$$
\begin{aligned}
P_{SOP_1}^{\rho_I\to\infty} = 1-\Big(1-\sum_{k=0}^{L_S}\binom{L_S}{k}(-1)^k\beta_{SP}^{m_{SP}}(k\beta_{SR}\gamma_{th_1}+\beta_{SP})^{-m_{SP}}\Big) \\
\times \frac{(\beta_{RE}d_{RE}^{\theta})^{\mu_{RE}}}{\rho_{RE}^{\mu_{RE}}\Gamma(\mu_{RE})}\sum_{j=0}^{\mu_{RD_1}-1}\frac{(\beta_{RD_1}d_{RD_1}^{\theta})^j}{j!}\frac{t}{2}\frac{\pi}{N} \\
\times \sum_{n=1}^{N}\frac{(C_{T_1}-1+C_{T_1}\alpha_1\tau)^j}{\big[\rho_{RD_1}(\alpha_1-\alpha_2(C_{T_1}+C_{T_1}\alpha_1\tau-1))\big]^j} \\
\times \exp\left[\frac{(1-C_{T_1}-C_{T_1}\alpha_1\tau)\beta_{RD_1}d_{RD_1}^{\theta}}{\rho_{RD_1}(\alpha_1-\alpha_2(C_{T_1}+C_{T_1}\alpha_1\tau-1))}\right] \\
\times \exp\left(-\frac{\beta_{RE}d_{RE}^{\theta}}{\rho_{RE}}\tau\right)\tau^{\mu_{RE}-1}\sqrt{1-\phi^2}. \qquad (5.35)
\end{aligned}
$$

Next, let $\rho_{RD_1} \to \infty$ while ρ_I keeps fixed and finite. Making use of the first two terms of the Taylor series expansion, the asymptotic expression of D_1 can be obtained as

$$
\begin{aligned}
P_{SOP_1}^{\rho_{RD_1}\to\infty} = 1-\Big(1-\sum_{k=0}^{L_S}\binom{L_S}{k}(-1)^k\Phi\Psi_1\frac{\beta_{SP}^{m_{SP}}}{\Gamma(m_{SP})} \\
\times (\Theta+m_{SP}-1)!(k\beta_{SR}\gamma_{th_1}+\beta_{SP})^{-\Theta-m_{SP}}\Big) \\
\times \frac{(\beta_{RE}d_{RE}^{\theta})^{\mu_{RE}}}{\rho_{RE}^{\mu_{RE}}\Gamma(\mu_{RE})}\sum_{j=0}^{\mu_{RD_1}-1}\frac{(\beta_{RD_1}d_{RD_1}^{\theta})^j}{j!}\frac{t}{2}\frac{\pi}{N} \\
\times \sum_{n=1}^{N}\frac{(C_{T_1}-1+C_{T_1}\alpha_1\tau)^j}{\big[\rho_{RD_1}(\alpha_1-\alpha_2(C_{T_1}+C_{T_1}\alpha_1\tau-1))\big]^j} \\
\times \left[1+\frac{(1-C_{T_1}-C_{T_1}\alpha_1\tau)\beta_{RD_1}d_{RD_1}^{\theta}}{\rho_{RD_1}(\alpha_1-\alpha_2(C_{T_1}+C_{T_1}\alpha_1\tau-1))}\right] \\
\times \exp\left(-\frac{\beta_{RE}d_{RE}^{\theta}}{\rho_{RE}}\tau\right)\tau^{\mu_{RE}-1}\sqrt{1-\phi^2}. \qquad (5.36)
\end{aligned}
$$

Applying the approaches, we can respectively obtain the asymptotic expressions when $\rho_I \to \infty$ and $\rho_{RD_2} \to \infty$ for D_2 as

$$
\begin{aligned}
P_{SOP_2}^{\rho_I \to \infty} = 1 - \Big(1 - \sum_{k=0}^{L_S} \binom{L_S}{k} (-1)^k \beta_{SP}^{m_{SP}} \\
\times (k\beta_{SR}\gamma_{th_2} + \beta_{SP})^{-m_{SP}}\Big) \\
\times \frac{(\beta_{RE} d_{RE}^{\theta})^{\mu_{RE}}}{\rho_{RE}^{\mu_{RE}} \Gamma(\mu_{RE})} \exp\left(-\frac{\beta_{RD_2} d_{RD_2}^{\theta} (C_{T_2} - 1)}{\alpha_2 \rho_{RD_2}}\right) \\
\times \sum_{j=0}^{\mu_{RD_2}-1} \frac{(\beta_{RD_2} d_{RD_2}^{\theta})^j}{(\alpha_2 \rho_{RD_2})^j j!} \sum_{q=0}^{j} \binom{j}{q} (C_{T_2} - 1)^{j-q} \\
\times (C_{T_2}\alpha_2)^q \frac{\Gamma(\mu_{RE} + q)}{\left(\beta_{RD_2} d_{RD_2}^{\theta} \frac{C_{T_2}}{\rho_{RD_2}} + \frac{\beta_{RE} d_{RE}^{\theta}}{\rho_{RE}}\right)^{\mu_{RE}+q}}
\end{aligned} \tag{5.37}
$$

and

$$
\begin{aligned}
P_{SOP_2}^{\rho_{RD_2} \to \infty} = 1 - \Big(1 - \sum_{k=0}^{L_S} \binom{L_S}{k} (-1)^k \Phi \Psi_2 \frac{\beta_{SP}^{m_{SP}}}{\Gamma(m_{SP})} \\
\times (\Theta + m_{SP} - 1)! (k\beta_{SR}\gamma_{th_2} + \beta_{SP})^{-\Theta - m_{SP}}\Big) \\
\times \frac{(\beta_{RE} d_{RE}^{\theta})^{\mu_{RE}}}{\rho_{RE}^{\mu_{RE}} \Gamma(\mu_{RE})} \left(1 - \frac{\beta_{RD_2} d_{RD_2}^{\theta} (C_{T_2} - 1)}{\alpha_2 \rho_{RD_2}}\right) \\
\times \sum_{j=0}^{\mu_{RD_2}-1} \frac{(\beta_{RD_2} d_{RD_2}^{\theta})^j}{(\alpha_2 \rho_{RD_2})^j j!} \sum_{q=0}^{j} \binom{j}{q} (C_{T_2} - 1)^{j-q} \\
\times (C_{T_2}\alpha_2)^q \frac{\Gamma(\mu_{RE} + q)}{\left(\frac{\beta_{RE} d_{RE}^{\theta}}{\rho_{RE}}\right)^{\mu_{RE}+q}}.
\end{aligned} \tag{5.38}
$$

5.4 Performance Evaluation

5.4.1 Numerical Results and Discussions

In this section, we discuss the numerical and simulation results. The parameters are set as $\rho_I = 15\,\text{dB}$, $\rho_{RE} = 10\,\text{dB}$, $\alpha_1 = 0.85$, $\alpha_2 = 0.15$, $\theta = 2$, $K_{SR} = 80\,\text{m}$, $K_{RD_1} = 80\,\text{m}$, $K_{RD_2} = 60\,\text{m}$, $K_{RE} = 280\,\text{m}$, $H = 60\,\text{m}$, $m_{SP} = m_{SR} = m_{RD_1} = m_{RD_2} = m_{RE} = 2$, $\Omega_{SP} = \Omega_{SR} = \Omega_{RD_1} = \Omega_{RD_2} = \Omega_{RE} = 1$, $C_{th_1} = 0.0005$ bits/s/Hz, $C_{th_2} = 0.001$ bits/s/Hz, $N = 50$, and $L_S = L_{D_1} = L_{D_2} = L_E = 2$.

Figures 5.2 and 5.3 plot the impact of ρ_{RD_1} and ρ_{RD_2} on the SOP performance for D_1 and D_2 under different H, respectively. We can observe from those two figures that the secrecy performance is enhanced as ρ_{RD_1} (ρ_{RD_2}) increases due to the channel advantage of the legitimate link over the eavesdropping one. Furthermore,

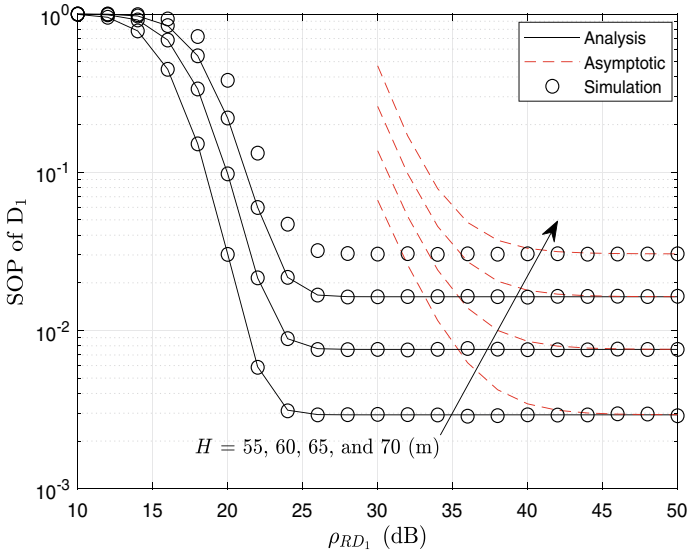

Fig. 5.2 SOP of D_1 versus ρ_{RD_1} for various H

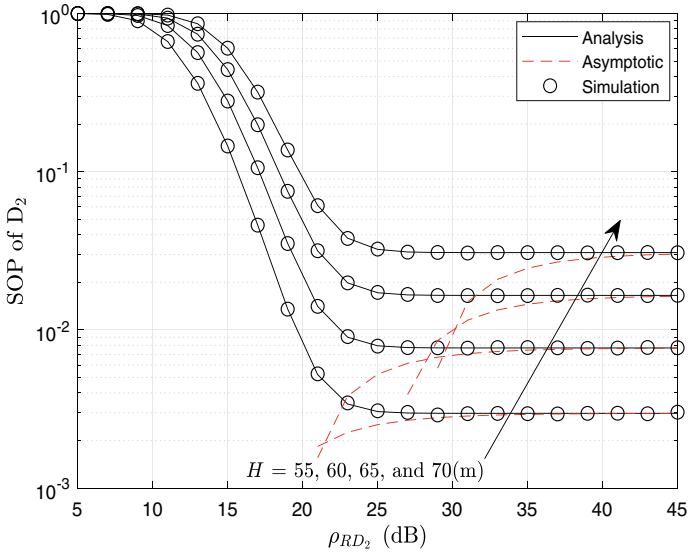

Fig. 5.3 SOP of D_2 versus ρ_{RD_2} for various H

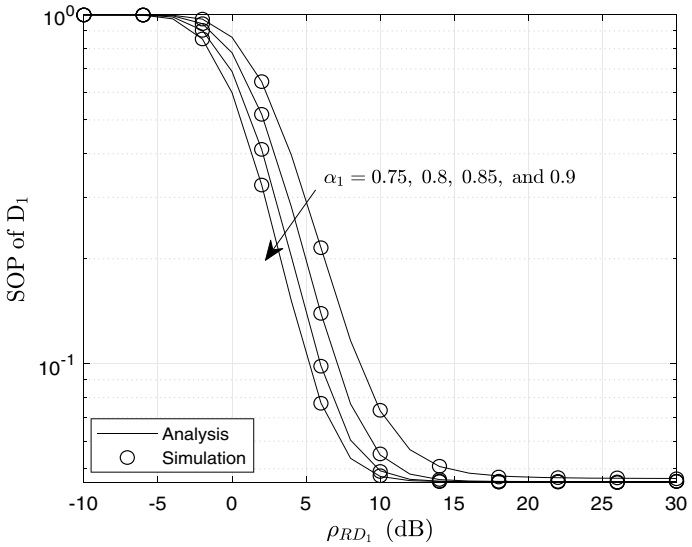

Fig. 5.4 SOP of D_1 versus ρ_{RD_1} for various α_1

the asymptotic results are approximate with the exact ones at the high SNR regions. However, it is also observed that when ρ_{RD_1} and ρ_{RD_2} are in the comparably high SNR region, i.e., $\rho_{RD_1} > 28\,\text{dB}$ in Fig. 5.2 and $\rho_{RD_2} > 24\,\text{dB}$ in Fig. 5.3, the SOP performance almost remains unchanged with ρ_{RD_1} (ρ_{RD_2}) increases. This is because the worst hop dominates the performance in the dual-hop link. In addition, one can see that a larger value of H corresponds to a worse SOP performance as a higher path loss resulted.

The SOP performance versus ρ_{RD_1} and ρ_{RD_2} for varying α_1 and α_2 are presented in Figs. 5.4 and 5.5. One can observe that the SOP performance enhances as $\alpha_1(\alpha_2)$ increases. A higher $\alpha_1(\alpha_2)$ means more power is allocated to the corresponding user.

The SOP versus ρ_I for D_1 and D_2 under various ρ_{RD_1} and ρ_{RD_2} are depicted in Figs. 5.6 and 5.7. We can see that the SOP performance enhances with the increase of ρ_I, as more power can be used for information transmission at S. Furthermore, as expected, the asymptotic results are approximate with the exact ones at the high SNR regimes.

Figures 5.8 and 5.9 plot the SOP versus ρ_{RE} for varying ρ_{RD_1} and ρ_{RD_2}. One can reveal that the SOP performance improves as the ρ_{RE} value decreases. This is because a smaller value of ρ_{RE} means a poorer natural communication environment for the eavesdropper.

The impact of the number of antennas on the SOP performance is illustrated in Figs. 5.10 and 5.11. One can see that the value of SOP decreases as L_{D_i} increases when $\rho_{RD_1} < 24\,\text{dB}$ in Fig. 5.10 and $\rho_{RD_2} < 36\,\text{dB}$ in Fig. 5.11. This is because a higher diversity gain can be obtained when more antennas are available on the device. When ρ_{RD_i} exceeds a certain value, i.e., $\rho_{RD_1} > 24\,\text{dB}$ and $\rho_{RD_2} > 36\,\text{dB}$, the secrecy

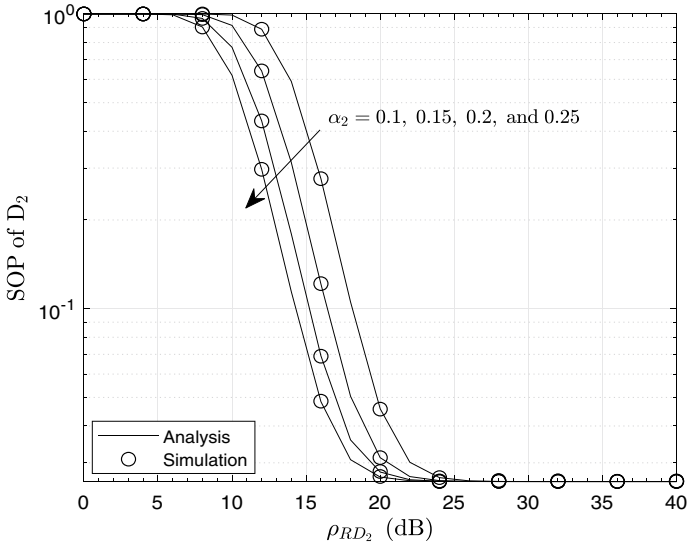

Fig. 5.5 SOP of D_2 versus ρ_{RD_2} for various α_2

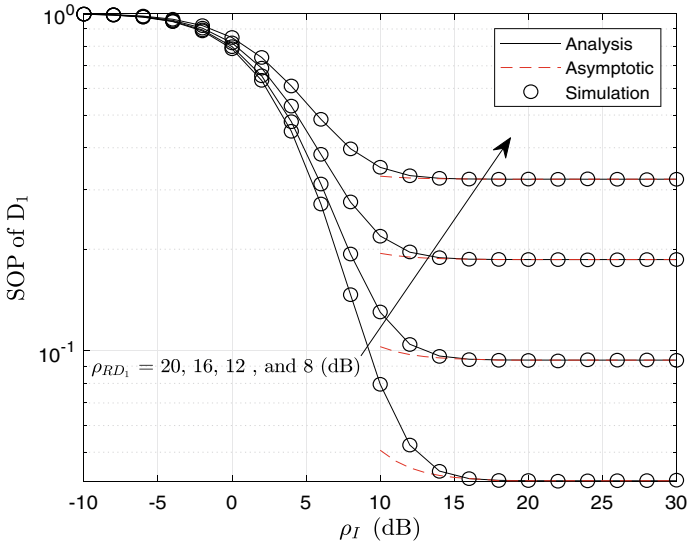

Fig. 5.6 SOP of D_1 versus ρ_I for various ρ_{RD_1}

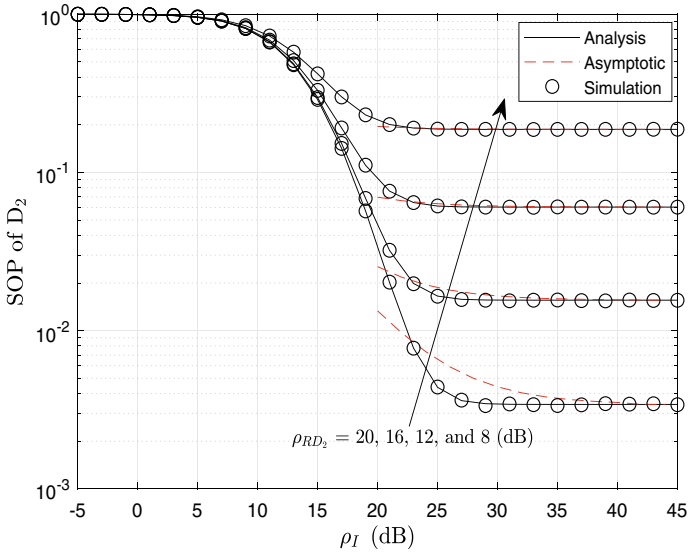

Fig. 5.7 SOP of D_2 versus ρ_I for various ρ_{RD_2}

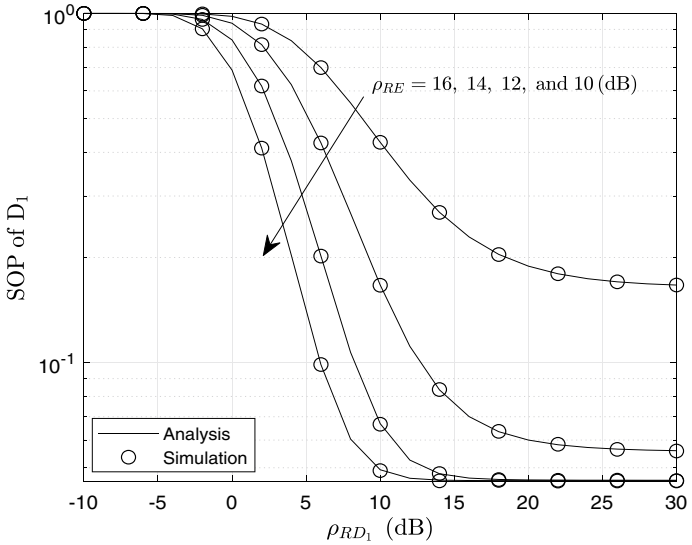

Fig. 5.8 SOP of D_1 versus ρ_{RD_1} for various ρ_{RE}

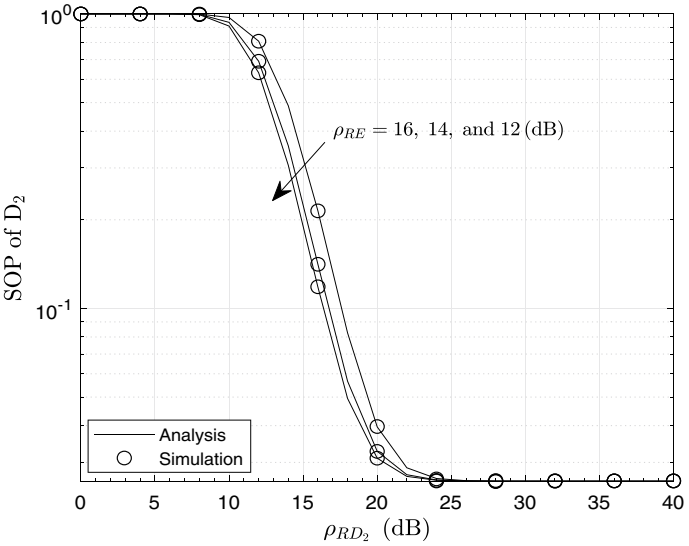

Fig. 5.9 SOP of D_2 versus ρ_{RD_2} for various ρ_{RE}

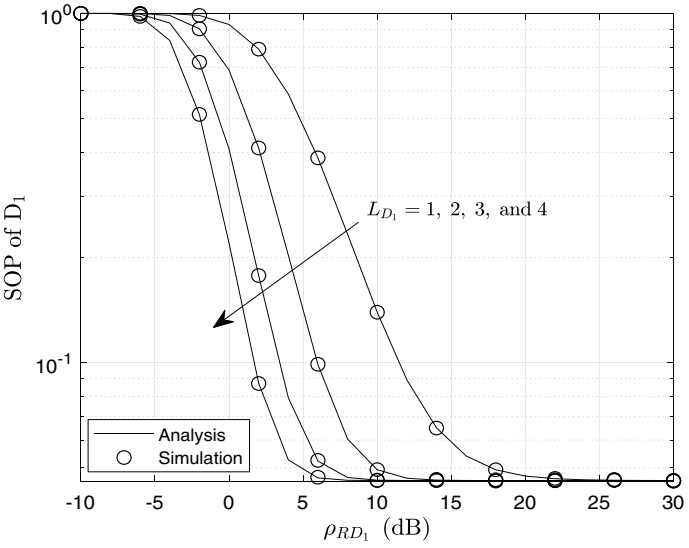

Fig. 5.10 SOP of D_1 versus ρ_{RD_1} for various L_{D_1}

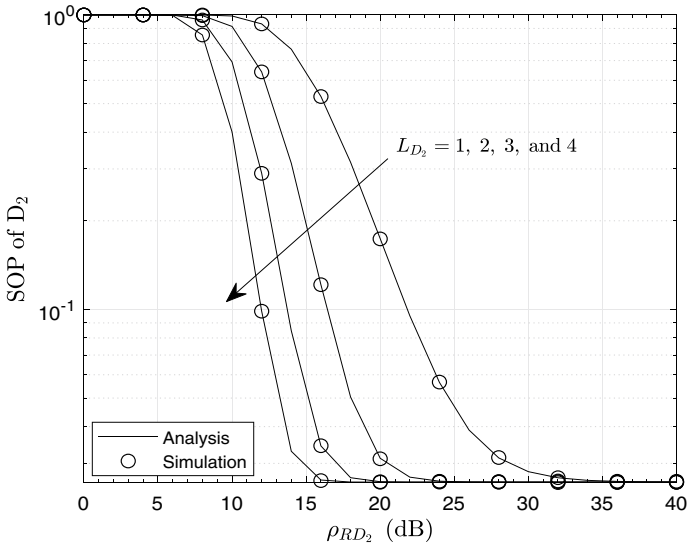

Fig. 5.11 SOP of D_2 versus ρ_{RD_2} for various L_{D_2}

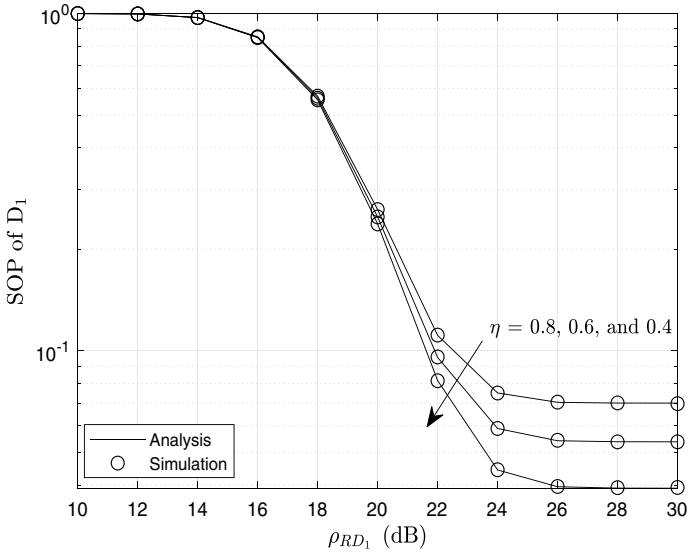

Fig. 5.12 SOP of D_1 versus ρ_{RD_1} for various η

performance is almost similar for the different number of antennas, which is because the first hop dominates the system performance.

The impact of scaling coefficient η on the SOP performance is presented in Figs. 5.12 and 5.13. As illustrated in those two figures, it is observed that the SOP

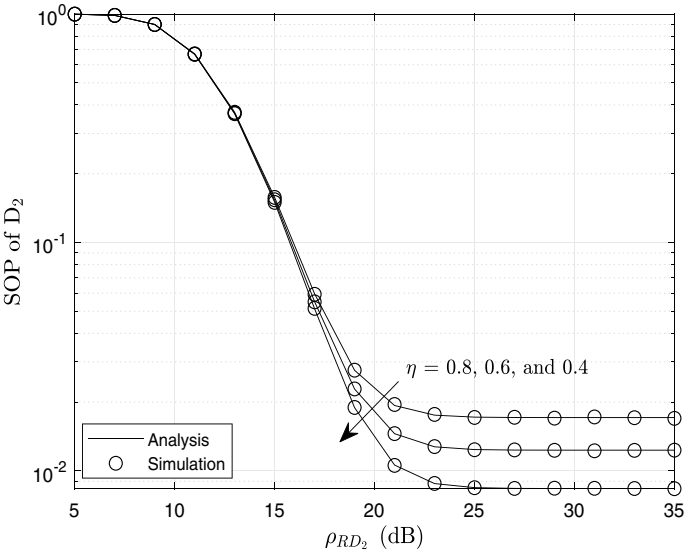

Fig. 5.13 SOP of D_2 versus ρ_{RD_2} for various η

performance improves as the value of η decreases. This is because a smaller value of η means less interference from the primary transmitter, which can result in better SOP performance.

5.4.2 SOP for the UAV with Different Spatial Positions and a Constant Speed

This section presents the SOP performance when the UAV has different spatial positions and flies at a constant speed. For convenience, as shown in Fig. 5.14, the positions of S, R, D_i, and E are presented in a three-dimensional coordinate, which are (x_S, y_S, z_S), (x_R, y_R, z_R), $(x_{D_i}, y_{D_i}, z_{D_i})$, and (x_E, y_E, z_E). Unless otherwise specified, the initial coordinates of those nodes are set as S (0, 0, 0), R (30, 30, 60), D_1 (90, 90, 0), D_2 (70, 70, 0), and E (230, 230, 0), and the unit is meter (m).

Scenario 1: UAV is with different spatial positions.
In this scenario, the distance between the UAV and the node g ($g \in \{S, D_1, D_2, E\}$) can be re-expressed using the three-dimensional coordinates as

$$d_{Rg} = \sqrt{(x_R - x_g)^2 + (y_R - y_g)^2 + (z_R - z_g)^2}. \tag{5.39}$$

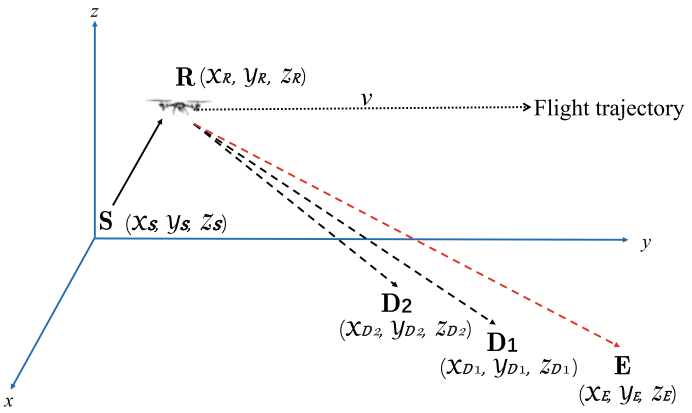

Fig. 5.14 Three-dimensional coordinate model and the flight trajectory of the UAV with a constant speed

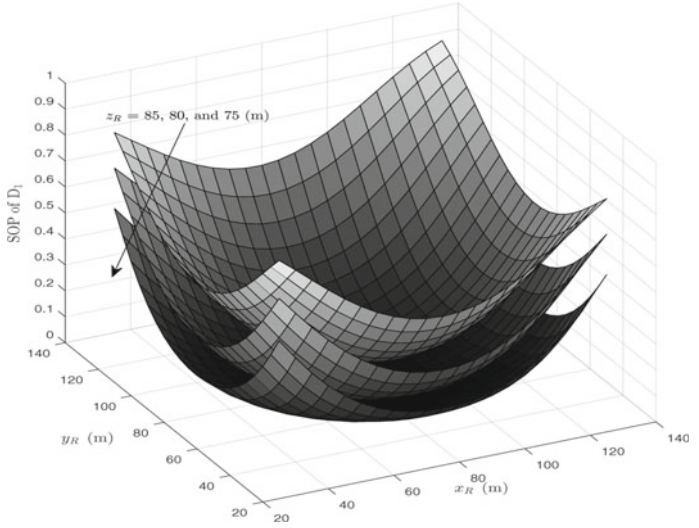

Fig. 5.15 SOP of D_1 versus the UAV deployment position under various z_R with $\alpha_1 = 0.8$

The results are presented in Figs. 5.15 and 5.16. Those two figures show that an optimal UAV deployment position exists for each curve in which the secrecy outage performance is the best.

Scenario 2: UAV flies with a constant speed.
As shown in Fig. 5.14, a simple scenario in which the UAV flies horizontally along with the y-axis to the right with a constant speed v is considered. Therefore, the distance between the UAV and the node g is

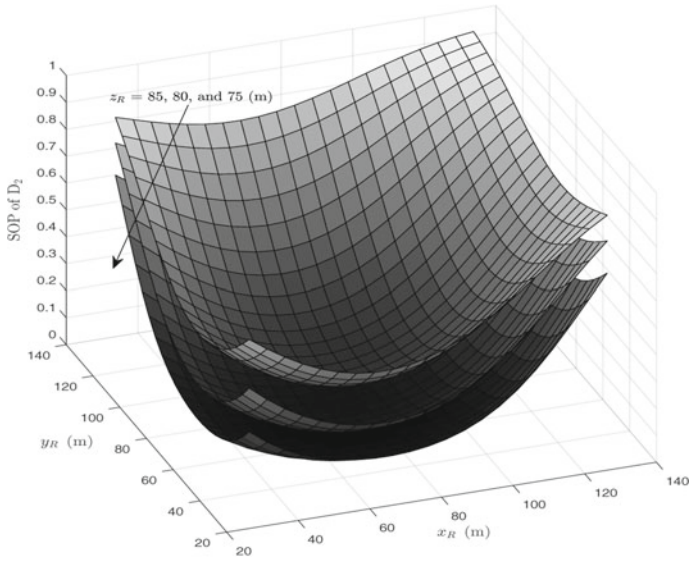

Fig. 5.16 SOP of D_2 versus the UAV deployment position under various z_R with $\alpha_1 = 0.8$

$$d_{Rg} = \sqrt{(x_R - x_g)^2 + (y_R + vt - y_g)^2 + (z_R - z_g)^2}, \tag{5.40}$$

where t is the flight time. As illustrated in Fig. 5.17, one can observe that the SOP performance for both users first improves and then decreases as the UAV flies. This is because the UAV first approaches and then flies away from the users, which decreases the distance between the UAV and the users and increases.

From the above two scenarios, we can conclude that it is better to allocate the UAV in a proper position to result in the best secrecy performance of the system.

Last but not least, compared with previous works on multi-antenna scenarios for UAV-NOMA systems, it is noted that the purpose of adopting multi-antenna is to cover different sectors [11], or to realize the beamforming [12–14], or to employ directional modulation [15]. Unlike those previous works, our focus of employing multi-antenna in this study is on diversity-combining techniques regarding SOP performance, i.e., both TAS at the source and MRC at the destinations. The primary technical challenge of the analysis includes but is not limited to obtaining the PDF and CDF expressions for the TAS output in the presence of underlay cognitive radio and the MRC output, as well as doing the asymptotic analysis. Numerical results from the analytical and asymptotic expressions show that the asymptotic results approximate the exact ones at the high SNR regions. Furthermore, it is also found that those figures have an error floor because another hop with fixed SNRs dominates the system performance.

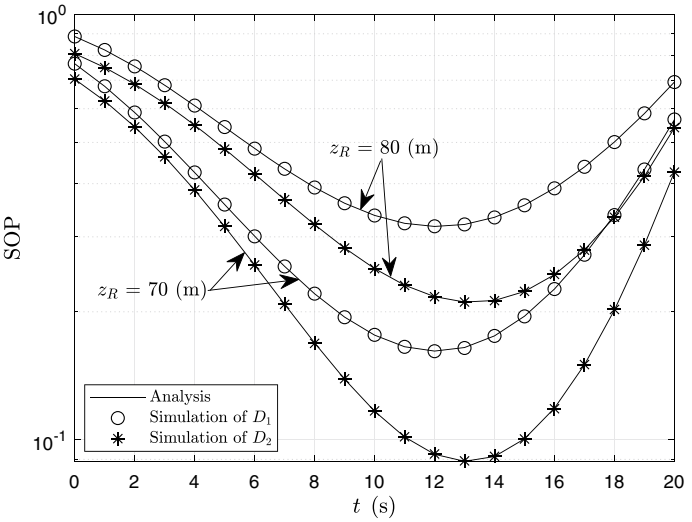

Fig. 5.17 SOP versus the trajectory of the UAV with D_1 (90, 70, 0), and $v = 5$ m/s

5.5 Conclusion

This section analyzes the secrecy performance for an underlay CR-based UAV-aided NOMA system over Nakagami-*m* fading channels. Both users' analytical and asymptotic expressions of SOP have been obtained when the TAS scheme is adopted at a secondary source and the MRC protocol is deployed at the destinations. Furthermore, we have analyzed the effects of the number of antennas, power distribution coefficient, height of the UAV, and interference power threshold on the secrecy performance. Numerical results illustrate that increasing the average SNR can enhance the secrecy performance, and the worse hop dominates the secrecy performance of the whole link. Moreover, increasing the number of receiving antennas, interference power threshold, and power distribution coefficient can also enhance the SOP performance of the system. In contrast, the system performance deteriorates as the height of the UAV increases. In addition, an optimal UAV deployment position makes the secrecy outage performance the best.

References

1. Y. Zeng, R. Zhang, T.J. Lim, Wireless communications with unmanned aerial vehicles: opportunities and challenges. IEEE Commun. Mag. **54**(5), 36–42 (2016)
2. L. Gupta, R. Jain, G. Vaszkun, Survey of important issues in UAV communication networks. IEEE Commun. Surv. Tuts. **18**(2), 1123–1152 (2016)

3. A.A. Khuwaja, Y. Chen, N. Zhao, M.-S. Alouini, P. Dobbins, A survey of channel modeling for UAV communications. IEEE Commun. Surv. Tuts. **20**(4), 2804–2821 (2018)
4. X. Cai et al., *Low Altitude UAV Propagation Channel Modelling*, in 2017 11th European Conference on Antennas and Propagation (EUCAP) (2017), pp. 1443–1447
5. W. Khawaja, I. Guvenc, D. Matolak, *UWB Channel Sounding and Modeling for UAV Air-to-ground Propagation Channels*, in 2016 IEEE Global Communications Conference (GLOBECOM) (2016), pp. 1–7
6. I.S. Gradshteyn, I.M. Ryzhik, *Table of Integrals, Series, and Products*, 7th edn. (Academic press, San Diego, 2007)
7. S. Arzykulov, G. Nauryzbayev, T.A. Tsiftsis, B. Maham, Performance analysis of underlay cognitive radio nonorthogonal multiple access networks. IEEE Trans. Veh. Technol. **68**(9), 9318–9322 (2019)
8. D.-T. Do, A.-T. Le, B.M. Lee, NOMA in cooperative underlay cognitive radio networks under imperfect SIC. IEEE Access **8**, 86180–86195 (2020)
9. W. Han, J. Ge, J. Men, Performance analysis for NOMA energy harvesting relaying networks with transmit antenna selection and maximal-ratio combining over Nakagami-*m* fading. IET Commun. **10**(18), 2687–2693 (2016)
10. Z. Wei, D.W.K. Ng, J. Yuan, Joint pilot and payload power control for uplink MIMO-NOMA with MRC-SIC receivers. IEEE Commun. Lett. **22**(4), 692–695 (2018)
11. T.M. Nguyen, W. Ajib, C. Assi, A novel cooperative NOMA for designing UAV-assisted wireless backhaul networks. IEEE J. Sel. Areas Commun. **36**(11), 2497–2507 (2018)
12. T. Hou, Y. Liu, Z. Song, X. Sun, Y. Chen, Multiple antenna aided NOMA in UAV networks: a stochastic geometry approach. IEEE Trans. Commun. **67**(2), 1031–1044 (2019)
13. N. Rupasinghe, Y. Yapici, I. Guvenc, Y. Kakishima, Non-orthogonal multiple access for mmWave drone networks with limited feedback. IEEE Trans. Commun. **67**(1), 762–777 (2019)
14. Y. Yapici, N. Rupasinghe, I. Guvenc, H. Dai, A. Bhuyan, Physical layer security for NOMA transmission in mmWave drone networks. IEEE Trans. Veh. Technol. **70**(4), 3568–3582 (2021)
15. X. Sun, W. Yang, Y. Cai, Secure communication in NOMA-assisted millimeter-wave SWIPT UAV networks. IEEE Internet Things J. **7**(3), 1884–1897 (2020)

Chapter 6
Conclusion

Gaofeng Pan, Xiaqing Miao, Xuanhe Yang, and Ziyi Yang

UAVs have become increasingly prevalent in various industries and applications, ranging from military and surveillance operations to commercial and humanitarian uses. Efficient and reliable communication is critical to UAV operations, enabling control, data transmission, and situational awareness.

Over the years, significant advancements have been made in UAV communication systems, resulting in improved range, bandwidth, security, and reliability. Several communication technologies, including RF, satellite, and cellular networks, are commonly used for UAV operations. Each technology has advantages and limitations; the choice depends on the mission's requirements.

RF communication remains the primary UAV control and telemetry method, particularly in the form of dedicated data links. It offers low latency, high bandwidth, and LOS operation, making it suitable for short-range and real-time applications. However, RF communication has a limited range and can be affected by interference and signal degradation.

Satellite communication provides global coverage and is ideal for long-range UAV operations, remote sensing, and BLOS applications. It offers high bandwidth and reliable connectivity but may suffer from higher latency due to the longer transmission distances. Satellites equipped with high-frequency bands, such as Ka-band, can provide even greater data rates for UAV communication.

Cellular networks, specifically 4G and emerging 5G networks, are being increasingly explored for UAV communication. They offer extensive coverage in urban and populated areas, allowing UAVs to leverage existing infrastructure. Cellular networks provide high data rates, low latency, and advanced features like network

G. Pan (✉) · X. Miao · X. Yang · Z. Yang
Beijing Institute of Technology, Beijing, China
e-mail: gfpan@bit.edu.cn

Z. Yang
e-mail: yziyi@bit.edu.cn

G. Pan et al. (eds.), *UAV Communications: Modeling and Analyses*,
https://doi.org/10.1007/978-981-97-0383-8_6

slicing and edge computing. However, their coverage is limited to areas with cellular infrastructure, and signal quality may vary depending on the location.

To ensure robust and secure communication, UAVs often employ encryption techniques and protocols to protect data integrity and confidentiality. Additionally, measures like frequency hopping, anti-jamming mechanisms, and redundancy in communication links are implemented to enhance reliability and mitigate interference.

In conclusion, UAV communications have witnessed significant advancements, enabling more sophisticated and complex operations. RF communication, satellite communication, and cellular networks play vital roles in different scenarios, providing UAVs with diverse options for reliable and efficient communication. As technology continues to evolve, we can expect further improvements in UAV communication systems, enabling even more advanced and innovative applications in the future.

In this book, we mainly elaborated the following content.

6.1 UAV-Terrestrial Communications

6.1.1 Secure UAV Systems with Linear Trajectory

The mentioned section investigates the secrecy outage performance of a UAV system with a linear trajectory. In this system, a UAV, denoted as S, flies in a straight line and transmits its information over the downlink to a legitimate receiver, D, on the ground. However, there is also an eavesdropping UAV denoted as E that attempts to overhear the data being transmitted between S and D. Additionally, there is information being transmitted over the uplink from D to S, such as commanding messages to control S's detecting operations, which can also be eavesdropped by E. The locations of S, D, and E are randomly distributed.

The first step in the investigation is to characterize the statistical characteristics, such as CDFs and PDFs, of the received SNR for both the downlink and the uplink. The SNR is a critical parameter that determines the quality of the communication links. By analyzing the statistical characteristics of the SNR, the researchers can gain insights into the system's performance and vulnerability to eavesdropping attacks.

Next, closed-form analytical expressions are derived for the lower boundary of the SOP for both the downlink and the uplink. SOP represents the probability that eavesdropper E successfully decodes the transmitted information, compromising the system's security. By deriving these analytical expressions, the researchers can evaluate the system's secrecy performance and assess the effectiveness of countermeasures to protect against eavesdropping.

To validate the proposed analytical models, Monte Carlo simulations are conducted. Monte Carlo simulations involve using random sampling to estimate the behavior and performance of a system. By comparing the simulation results with the derived analytical expressions, the researchers can verify the accuracy and effectiveness of their proposed models.

In summary, the secrecy outage performance of a UAV system with a linear trajectory has been investigated while considering the presence of an eavesdropping UAV. The statistical characteristics of the SNR are analyzed, and closed-form analytical expressions for the lower boundary of the SOP are derived for both the downlink and the uplink. Monte Carlo simulations are performed to validate the proposed analytical models. This research contributes to understanding secure communication in UAV systems with linear trajectories and provides analytical tools to evaluate the system's secrecy performance.

6.1.2 Secure UAV-to-Vehicle Communications

This work investigates the secrecy performance of a UAV-to-vehicle (UAV-2-V) communication system, addressing the security concerns associated with UAV communications. In this system, communication occurs between a UAV denoted as S, acting as a temporary aerial BS, and a legitimate vehicle denoted as D, which moves along a road. However, an eavesdropping vehicle denoted as E, also on the same road, attempts to overhear the information transmitted between S and D.

The locations of S, D, and E are assumed to be uniformly distributed. S is in the sky, while D and E are on the highway. The statistical characteristics of the received SNR, including the CDF and PDF, are characterized separately for both the downlink and uplink. Understanding the statistical characteristics of the SNR is crucial for assessing the system's performance and vulnerability to eavesdropping attacks.

For the downlink, closed-form expressions are derived for both the approximate and asymptotic SOP. SOP represents the probability that the eavesdropper E successfully decodes the transmitted information, compromising the system's security. The downlink channels are assumed to experience Rician fading, a common model for wireless channels that includes a LOS component. The derived expressions provide insights into the system's secrecy performance under Rician fading conditions.

Furthermore, the secrecy outage performance of the uplink is investigated. The uplink refers to the communication from D to S. Closed-form expressions for the exact and asymptotic SOP are derived for two cases: when the eavesdropping channel experiences Rician fading and when it follows a Weibull fading model. Weibull fading is a more generalized fading model that encompasses various fading environments.

Monte Carlo simulations are conducted to validate the proposed analytical models. By comparing the simulation results with the derived analytical expressions, the researchers can assess the accuracy and effectiveness of their models in representing the system's secrecy performance.

In summary, this work investigates the secrecy performance of a UAV-2-V communication system, considering the presence of an eavesdropping vehicle. The statistical characteristics of the SNR are analyzed, and closed-form expressions for the SOP are derived for both the downlink and the uplink under different fading conditions. Monte Carlo simulations are performed to validate the proposed models. This

research enhances the understanding of secure communication in UAV-2-V systems and provides analytical tools for evaluating the system's secrecy performance.

6.1.3 Power Adaptation Schemes in Aerial-Terrestrial Communications

This part focuses on studying the transmission capacity performance of an aerial-terrestrial communication system. In this system, an unmanned aerial vehicle denoted as S transmits information bits to a terrestrial receiver denoted as D. The transmit power of S is adaptively controlled based on the instantaneous CSI to optimize the transmission capacity.

Three adaptive transmission schemes are considered in this work. The first scheme is optimal simultaneous power and rate adaptation, where S adjusts its transmit power and transmission rate based on the channel conditions. The second scheme is optimal rate adaptation with constant transmit power, where S adapts only the transmission rate while keeping the transmit power constant. The third scheme is truncated channel inversion with a fixed rate, where S adjusts the transmit power using channel inversion while maintaining a fixed transmission rate.

Closed-form expressions for the EC are derived under these adaptive transmission schemes, taking into account the randomness of the location of the terrestrial receiver D. The EC represents the average achievable transmission capacity over multiple channel realizations. By deriving closed-form expressions, the researchers can gain insights into the system's capacity performance under different adaptive transmission schemes and random location scenarios.

Furthermore, asymptotic expressions for the EC are derived to obtain additional insights into the system's performance. Asymptotic analysis allows for understanding the system's behavior as specific parameters, such as the SNR or the number of antennas, tend to infinity or approach extreme values.

Numerical results are presented to compare the performance of the considered power adaptation methods and to validate the accuracy of the proposed analytical models. These numerical results provide quantitative assessments of the different adaptive transmission schemes and confirm the effectiveness of the derived closed-form expressions.

In summary, the transmission capacity performance of an aerial-terrestrial communication system with adaptive transmission schemes has been studied. Closed-form expressions for the EC are derived, considering the randomness of the terrestrial receiver's location. Asymptotic expressions are also obtained to gain further insights. Numerical results are provided to compare power adaptation methods and validate the proposed analytical models. This research contributes to understanding and optimizing the capacity performance of aerial-terrestrial communication systems.

6.2 UAV-to-UAV Communications

In the mentioned work, the focus is on investigating the secrecy performance of a UAV-to-UAV system. In this system, one UAV is the source (S) transmitting information to a legitimate UAV receiver. At the same time, a group of other UAVs attempts to eavesdrop on the information being transmitted between S and the legitimate UAV receiver. The locations of both the legitimate UAV receiver and the eavesdropping UAVs are randomly distributed within the coverage space of S.

The first step in the investigation is to characterize the statistical characteristics of the SNR over the links from S to the legitimate UAV receiver. The SNR is an essential factor that determines the quality and reliability of the communication link. By analyzing the statistical characteristics of the SNR, the researchers gain insights into the system's performance and vulnerability to eavesdropping attacks.

Next, we present closed-form analytical expressions for the SOP and the average secrecy capacity. SOP represents the probability that the eavesdroppers successfully decode the transmitted information, breaching the system's security. On the other hand, the average secrecy capacity quantifies the average amount of secure data that can be reliably transmitted from S to the legitimate UAV receiver while keeping it confidential from the eavesdroppers.

To validate the proposed analytical models, Monte Carlo simulations are conducted. Monte Carlo simulations involve using random sampling to estimate the behavior and performance of a system. By comparing the simulation results with the derived analytical expressions, the researchers can verify the accuracy and effectiveness of their proposed models.

In summary, we investigate the secrecy performance of a UAV-to-UAV system, considering the presence of eavesdropping UAVs. The statistical characteristics of the SNR are analyzed, and closed-form analytical expressions for the SOP and the average secrecy capacity are derived. Monte Carlo simulations are performed to validate the proposed analytical models. This research contributes to understanding secure communication in UAV systems and provides analytical tools to evaluate the system's secrecy performance.

6.3 Satellite-UAV Communications

The investigation of the impacts of small-scale fading over the aerial-terrestrial channel and the randomness of the position of the terrestrial terminal on the capacity performance of a SISO aerial-terrestrial system under three different adaptive transmission schemes (OSPRA, ORA, and TIFR) can provide valuable insights into the system's efficiency and reliability.

Small-scale fading refers to the rapid fluctuations in the received signal strength caused by multipath propagation and interference effects in wireless communication channels. It can significantly impact the quality and reliability of the received signal.

Small-scale fading can affect the system's capacity in the context of the aerial-terrestrial system, where signals are transmitted between an aerial UAV or drone and a terrestrial terminal.

The randomness of the position of the terrestrial terminal introduces spatial variability into the channel characteristics. As the terrestrial terminal moves within its coverage area, the received signal strength and quality can vary due to changes in the channel conditions. This randomness adds another layer of complexity to the system's capacity performance.

The three adaptive transmission schemes, OSPRA, ORA, and TIFR schemes, are likely designed to mitigate the effects of small-scale fading and adapt the transmission parameters to optimize capacity. OSPRA (Optimal Spatial Random Access) is a scheme that aims to maximize the system capacity by dynamically selecting the best transmission mode based on channel conditions. ORA (Opportunistic Relaying Algorithm) is a relaying scheme that exploits the available relay nodes to improve the overall system capacity. TIFR (Time-Invariant Feedback Rate) is a scheme that adapts the feedback rate based on channel quality, optimizing the system capacity under varying channel conditions.

By studying the capacity performance under these adaptive transmission schemes, the investigation can provide insights into how these schemes cope with small-scale fading and the randomness of the terrestrial terminal's position. It can evaluate their effectiveness in maximizing capacity, adapting to changing channel conditions, and maintaining reliable communication in the aerial-terrestrial system.

The findings of this investigation can be used to enhance the design and optimization of future aerial-terrestrial communication systems. It can guide the development of adaptive transmission schemes that better handle small-scale fading and spatial variability in the terrestrial terminal's position. Additionally, the results can help understand the limitations and potential trade-offs associated with each adaptive transmission scheme, allowing for informed decision-making in system design and deployment.

The mentioned work also focuses on improving the accuracy and analytical modeling of interfering signals in a three-dimensional (3D) space within the context of CH-UAV RF and S-CH FSO links. The previous approach approximated the statistical randomness of interfering signals using the Gamma distribution, a commonly used approximation based on the central limit theorem. However, the current work aims to provide a more accurate representation by deriving the moment-generating function of the summation of interfering signals while considering the randomness of the 3D locations of CHs (Cluster Heads).

By considering the randomness of the 3D locations of CHs, the work accounts for the spatial variability of the interference signals in a more precise manner. This approach provides a more realistic representation of the interfering scenarios in 3D space. Furthermore, the work goes beyond presenting non-closed-form analytical expressions for performance indices. It achieves closed-form analytical expressions for the coverage probability over S-CH FSO and CH-UAV RF links.

The derived closed-form analytical expressions for the coverage probability are valuable as they allow a more straightforward evaluation of the system's perfor-

mance under different interference scenarios. The coverage probability is a critical performance metric that indicates the probability of achieving a reliable connection or communication link in the presence of interference.

The closed-form expressions presented in this work cover various interference scenarios, including interference-free, interference-dominated, and interference-and-noise cases. This comprehensively analyzes the system's performance under different interference conditions.

Overall, this work contributes to the understanding and analysis of CH-UAV RF links and S-CH FSO links by incorporating accurate modeling of interfering signals in 3D space and deriving closed-form analytical expressions for the coverage probability. The improved modeling and analytical expressions enhance the evaluation and optimization of these communication links, enabling better design and deployment decisions in practical scenarios.

6.4 UAV Relay Communications

The first contribution is the proposal of a mixed RF and underwater optical communication network, where a UAV acts as a mobile source to transmit a signal to an underwater terminal. This transmission is achieved through a surface relay. Integrating RF and underwater optical communication allows for communication between aerial and underwater nodes, which can be useful in various applications.

Furthermore, the analytical expressions of OP were derived for both amplified-and-forward and DF protocols in this mixed RF-underwater optical communication network. OP is a performance metric representing the probability of a communication link failing to meet a certain quality-of-service requirement. The system's performance can be evaluated, optimized, and compared under different protocols and scenarios by deriving analytical expressions for OP.

The second contribution is proposing a resource optimization scheme for a UAV-NOMA network. This scheme aims to enhance the EE and spectrum efficiency of the system. EE refers to the system's achievable throughput ratio to energy consumption, and spectrum efficiency refers to the data transmitted over a given bandwidth. By optimizing resource allocation in the UAV-NOMA network, the scheme aims to improve the system's energy and spectrum utilization, leading to more efficient and effective communication.

In summary, the contributions include the proposal of a mixed RF-underwater optical communication network with a UAV as a mobile source, the derivation of analytical expressions for OP under different protocols, and the development of a resource optimization scheme for a UAV-NOMA network to enhance energy and spectrum efficiency. These contributions advance the understanding and optimization of communication systems in challenging environments and pave the way for more efficient and reliable communication in aerial, underwater, and NOMA networks.

6.5 Future of UAV Communications

UAVs have already revolutionized industries such as agriculture, construction, logistics, and delivery services. In the future, we can expect to see further advancements in these areas, with drones becoming more efficient, autonomous, and capable of carrying heavier payloads. This could lead to increased adoption of UAVs for tasks like aerial inspections, crop monitoring, and last-mile deliveries. Moreover, Urban Air Mobility (UAM) refers to using drones for personal transportation within cities. In the future, we might witness the development of advanced drone taxis and air shuttles, enabling convenient and efficient transportation. These autonomous aerial vehicles could help alleviate traffic congestion, reduce commuting times, and enhance urban mobility. What's more, UAVs will continue to evolve with improved autonomous capabilities. Future drones might possess advanced computer vision systems and machine learning algorithms. Here are also a few key areas that are likely to shape the future of UAV communication:

1. BLOS Communication: Currently, UAVs are often limited to operating within the line of sight (LOS) of the operator or a ground station. However, future advancements in communication technology, such as satellite links, high-frequency radio waves, and advanced networking protocols, can enable UAVs to communicate beyond the LOS, expanding their operational range and capabilities.
2. Swarm Communication: Swarm technology, where multiple UAVs operate cooperatively and coordinated, is gaining traction. In the future, enhanced communication systems will allow for seamless coordination and communication among swarm members, enabling them to effectively perform complex tasks, share information, and adapt to dynamic environments.
3. Improved Data Transmission: UAVs generate vast amounts of data through various sensors, cameras, and other onboard systems. Future communication systems must support high-speed data transmission and low-latency links to facilitate real-time data analysis, remote control, and command and control operations.
4. Security and Privacy: As UAVs become more prevalent in various industries, ensuring secure and private communication will be crucial. Advanced encryption techniques, authentication protocols, and anti-jamming technologies will significantly protect UAV communications from cyber threats.
5. Integration with Existing Communication Infrastructure: Integrating UAV communications seamlessly into existing communication infrastructure, such as cellular networks or dedicated UAV communication networks, will be essential. This integration will allow UAVs to leverage existing infrastructure for communication, enhancing their reliability and enabling efficient airspace management.
6. Spectrum Management: With the increasing number of UAVs in operation, efficient spectrum management will become critical to avoid interference and congestion. Regulatory bodies and communication authorities must develop frameworks to allocate dedicated frequency bands or implement dynamic spectrum-sharing mechanisms to support UAV communication.

7. Artificial Intelligence (AI) and Machine Learning (ML): AI and ML technologies will play a crucial role in UAV communications by enabling autonomous decision-making, adaptive communication protocols, and intelligent routing algorithms. These technologies can enhance communication efficiency, optimize network resources, and improve overall UAV mission performance.

It's important to note that advancements will influence the future of UAV communications in communication technology, regulatory frameworks, industry requirements, and the evolving needs of various sectors, such as agriculture, logistics, emergency response, and surveillance.